Master Thesis, Department of Geosciences

COMPACTION, ROCK PROPERTIES EVALUATION, ROCK PHYSICS DIAGNOSTICS, AVO MODELING AND SEISMIC INVERSION IN THE SNØHVIT FIELD, SW BARENTS SEA

Md Jamilur Rahman

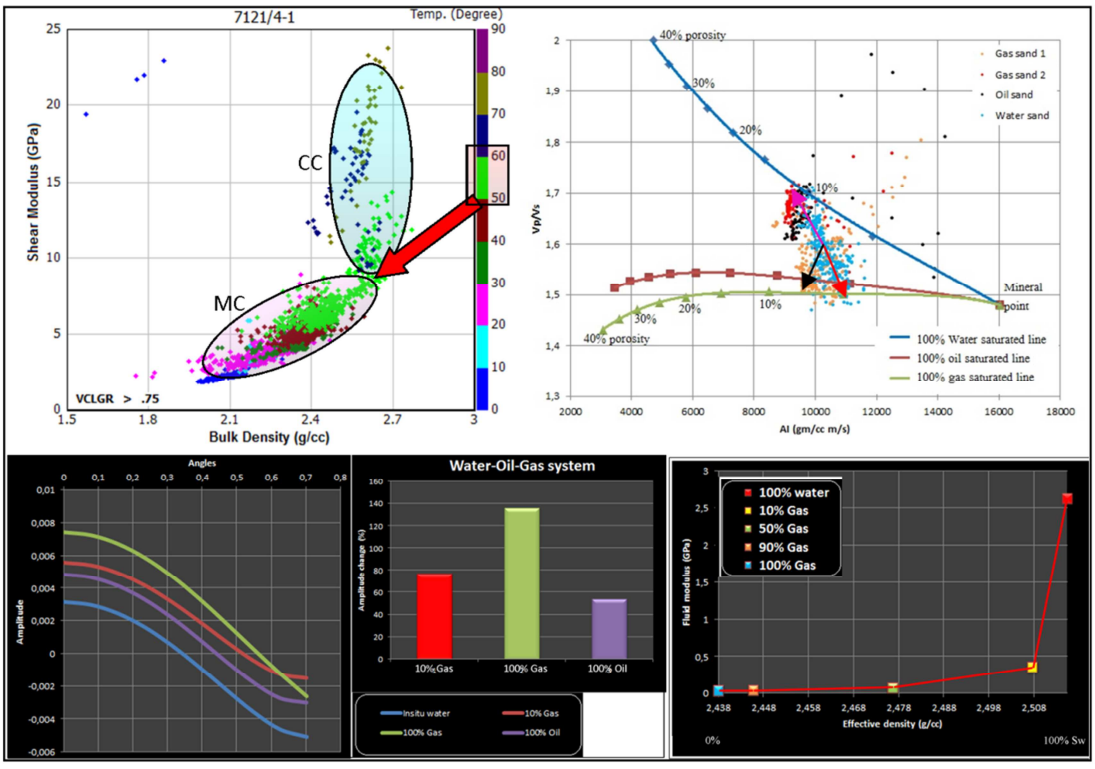

UNIVERSITY OF OSLO

FACULTY OF MATHEMATICS AND NATURAL SCIENCES

COMPACTION, ROCK PROPERTIES EVALUATION, ROCK PHYSICS DIAGNOSTICS, AVO MODELING AND SEISMIC INVERSION IN THE SNØHVIT FIELD, SW BARENTS SEA

Md Jamilur Rahman

Master Thesis in Geosciences

Discipline: Geology

Department of Geosciences

Faculty of Mathematics and Natural Sciences

University of Oslo

01.06.2012

Preface

This thesis is part of the BarRock project and is submitted to the Department of Geosciences, University of Oslo (UiO), in candidacy of the M.Sc. Degree.

This research has been performed at the Department of Geosciences, University of Oslo, during the period of August 2011 – May 2012 under the supervision of Md Nazmul Haque Mondol and Jens Jahren, Associate Professors, Department of Geosciences, University of Oslo, Norway

Acknowledgements

I would like to express my sincere gratitude to my supervisor Md Nazmul Haque Mondol, and Co-supervisor Jens Jahren, Associate Professors, Department of Geosciences, University of Oslo for their continuous supervision throughout the research with valuable suggestions, guidance and encouragement. I am also thankful to them for their constructive and valuable criticism during reviewing the manuscript.

I wish to express my special gratitude to Michael Heeremans and IT staff, department of Geosciences for their technical support and assisting me in various ways during the research. I am also grateful to all academic and administrative members of the Department of Geosciences for their generous help and co-operation during the research.

Many thanks are dedicated to people who are working on BarRock project specially Mohammad Koochak Zadeh, Mohsen Kalani, Sirikarn Narongsirikul and Oluwakemi Yetunde Ogebule for their constructive discussions in this research.

I would like to convey my special gratitude and love to my parents who have always supported me in my whole life.

I am also grateful to my study group mates, Danial Farvardini, Arif Butt and Mohsen Fardi. Your team spirit, constructive discussions, academic and social life never be forgotten. I also want to acknowledge my course mates who made up a significant diversity and also developed an open minded culture.

Lastly, thanks to my all friends who came from different countries around the world. Your moral and emotional supports relish me throughout my life.

Abstract

Snøhvit field is located in the SW Barents Sea and comprises a reservoir in Lower to Middle Jurassic sandstones of Stø Formation containing gas with thin oil lag. The sandstones of Upper Triassic to Lower Jurassic Nordmela and Tubåen Formations have also shown gas in few wells. Several stages of uplift and erosion of the entire region resulted in dramatic changes in reservoir rock properties and petroleum system. Hence, analysis of this sedimentary basin as a normally subsiding basin would mislead the exploration results. An integrated approach that incorporates compaction analysis, rock physics diagnostics, AVO modeling and post-stack seismic inversion has been carried out to predict reservoir properties of the Snøhvit field. Six exploration wells drilled in the study area and three 2D seismic lines have been considered for detail compaction, AVO modeling inversion and detail rock physics analyses.

Naturally compacted rocks in the well 7121/5-1 indicate transformation in compaction domain (MC to CC) at present depth 1922 m (BSF) corresponding to present day temperature of 66°C. An abrupt velocity increase at this depth is inferred as a result of grain framework stiffening related to precipitation of micro-quartz cement. The higher velocity-depth gradient of this sediment than laboratory experimental curves is related to the burial history and subsequent uplift. However, the estimated exhumation in the studied area varies between 300 and 760 m. The present day temperature of well 7121/5-1 at transition depth after exhumation is 93°C which is quite enough to change the rock stiffness. But, the present day temperature (50°C) at transition depth in well 7120/5-1 indicates the paleo-temperature history in this basin was different.

The velocity of the Stø Formation in the eastern well is lower than the western well. The eastern well is located more close to the shore line which may control deposition of coarse and well sorted sediments. Hence, the influence of compaction (both mechanical and chemical) is lower in the east than west. However, the reservoir quality of the Stø Formation is decreasing from east to west. Moreover, the reservoir quality is changing because of vertical lithological alterations. The rock physics template is not good for lithology identification, but good enough for fluid separation. The stø reservoir in the studied area has been overconsolidated. Hence, the fluid separation using the rock physics template is very difficult and risky (in exploration phase).

The sensitivity analysis of different fluid saturations indicates substantial change of effective rock properties when added only 10% gas into a gas-water system, mainly because of changing the effective fluid modulus. Higher gas saturation (50 and 90%) has slightly changed the fluid modulus as resulted from synthetic seismic traces. The lateral variation of the cap rock (Fuglen Formation) elastic properties greatly controls the AVO characteristics of the reservoir rock (Stø Formation). Lithological heterogeneity and lateral thickness variation changed the AVO response. The diagenetic changes (different depth level reservoirs) within reservoirs also affect AVO responses. Moreover, the AVO gas sand classes based on reflectivity and intercept-gradient cross-plots have given a quick preliminary AVO evaluation of the Stø reservoirs.

The post-stack seismic inversion shows the low impedance within the reservoir (Stø Formation) zone compared to the upper and lower units. Moreover, inversion is useful to track laterally the lower impedance hydrocarbon filled reservoirs. Thus, it can be concluded that the geophysical techniques help to understand the reservoir, leading to its proper management and better evaluation of new structural and stratigraphic prospects for exploration and development planning.

Nomenclature

AI: Acoustic Impedance

AVO: Amplitude versus Offset

BHT: Bottom Hole Temperature

BSF: Below Sea Floor

CC: Chemical Compaction

FRM: Fluid Replacement Model

HC: Hydrocarbon

HR: Hampson Russell

I_{GR}: Gamma Ray Index

IP: Interactive Petrophysics

K: Bulk modulus

MC: Mechanical Compaction

MD: Measured Depth

MPa: Mega Pascal

PR: Poisson's Ratio

RKB: Relative to Kelly Bushing

RPT: Rock Physics Template

R^2: Correlation Coefficient

S_w: Water saturation

TTI: Time Temperature Integral

TVD: Total Vertical Depth

Vp: P-Wave velocity

V_{sh}: Volume of shale

Vs: S-Wave velocity

μ: Shear modulus

Table of Contents

Chapter 4 Materials and Methods

Chapter 5 Compaction and Rock Property evaluation

List of Figures

Chapter 1 Introduction

Chapter 2 Geological framework

Chapter 3 Theoretical Background

Chapter 4 Materials and Methods

Chapter 5 Compaction and rock properties evaluation

Chapter 6 Rock physics analysis

Chapter 7 AVO modeling

Chapter 8 Seismic inversion

List of tables

Chapter 2 Geological framework

Chapter 3 Theoretical background

Chapter 4 Materials and methods

Chapter 5 Compaction and rock properties evaluation

Chapter 7 AVO modeling

Chapter 8 Seismic inversion

Chapter 1: Introduction

1.1 Background
1.2 Motivation
1.3 Research objectives
1.4 Study area
1.5 Chapter descriptions
1.6 Limitation, future work and implications

UNIVERSITY OF OSLO

FACULTY OF MATHEMATICS AND NATURAL SCIENCES

Chapter 1: Introduction

1.1 Background

The Norwegian Continental Shelf is divided into three main provinces; North Sea, Mid-Norwegian continental margin and Western Barents Sea for hydrocarbon exploration (inset map in Fig. 1.1). Before continental break-up these provinces were part of a larger epicontinental sea which was lying between the continental masses of Fennoscandia, Svalbard and Greenland (Faleide et al., 2010). The portion of the Norwegian Barents Sea covers 230000 km^2 which is more than one and a half times the area of the Norwegian sector of the North Sea (Dore, 1995). The greater Barents Sea is bordered by the Norwegian Sea in the west, the islands of Svalbard (Norway) in the northwest, the islands of Franz Josef land and Novaya Zemlya in the northeast and east and in the south Norway and Russian main land (Fig. 1.1).

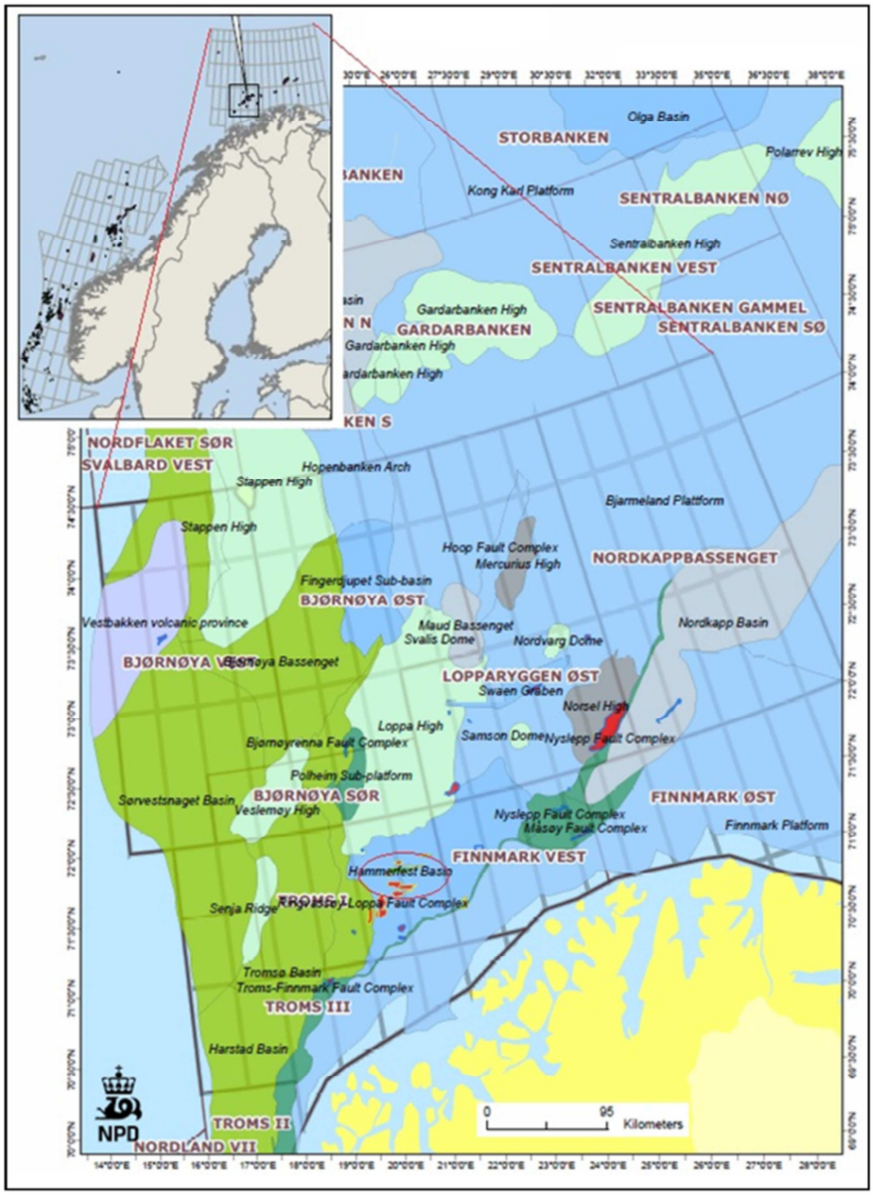

Fig. 1.1: Structural elements of the Norwegian Barents Sea (Source: NPD) and the Norwegian Continental Shelf shows hydrocarbon exploration blocks (inset map).

The Norwegian Barents Sea was opened for exploration in 1980. Untill now approximately 94 exploration wells have been drilled. However, almost 25 discoveries have been made and most of them are in the Hammerfest Basin (Fig. 1.2). The success rate roughly one in three in the Norwegian Barents Sea is higher compare to the Norwegian North Sea. The reason for high success rate is the presence of several petroleum systems (Ohm et al., 2008; Faleide et al., 2010). A great variety of traps (fault and salt structures, stratigraphic pinch-out) and seals, multiple source rocks from the Carboniferous to the Cretaceous in age () and good quality reservoir rocks from Permian to Paleocene age are present in the area. Though the success rate is higher but it is commercially disappointing mainly because of the gas discoveries (eg. Snøhvit, Askeladd, Tronarose etc.) compared to a few small oil discoveries (eg. Goliat, Nacula). In the year 2011-2012, two major oil discoveries (Skrugard and Havis) proved this area as oil prone which is an important break-through for future exploration activities in the SW Barents Sea.

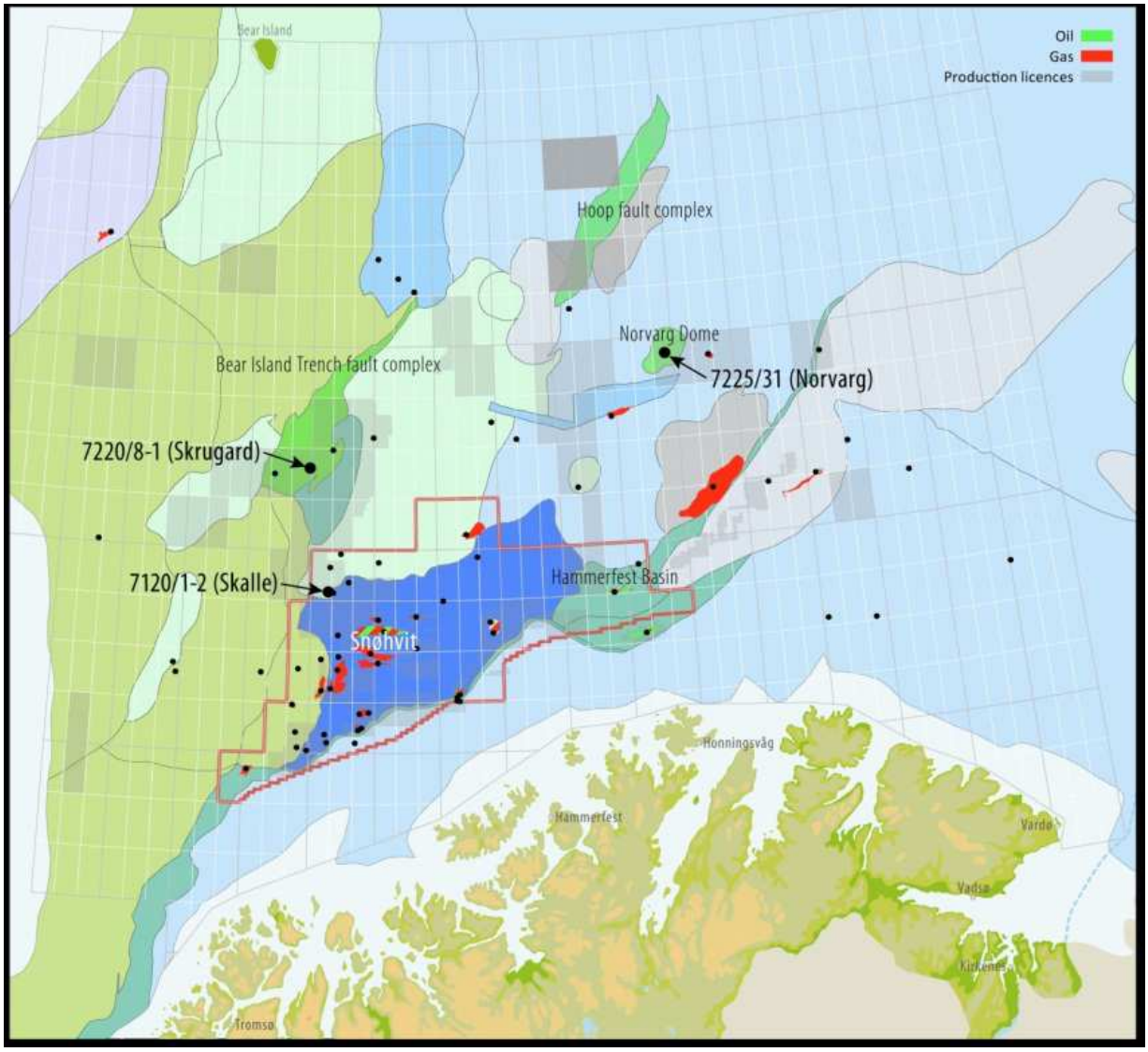

Fig. 1.2: Map shows exploration wells and discoveries in the SW Barents Sea (Source: NPD).

Though the Norwegian Barents Sea is promising for high success rate and variety of petroleum systems already proved, it is still difficult to find commercial petroleum accumulation because of uplift and erosions. The Barents Sea area experienced several phases of uplift and erosion since Paleocene. The maximum uplift is about 3000 m in the northwest

towards the Stappen High (Dore and Jensen, 1996) whereas minimum values are 0 to 500 m in the Hammerfest and Tromsø Basin (Nyland et al., 1992). Dore and Jensen (1996) discussed the following negative effects of Late Cenozoic uplift and erosion that make the area more challenging in hydrocarbon exploration as well as production:

- Changes in structural attitude.
- Gas expansion due to pressure release force the oil below spill points.
- Failure of seals.
- Cooling of source rock subsequently stop the hydrocarbon generation.
- Reservoir quality deterioration because of maximum burial and diagenetic effects.

Residual oil in many dry wells proves oil generation and accumulation in the past that gives hope for future exploration. But advance technology and thinking are necessary for exploration success in the uplifted area like Barents Sea. Exact uplift estimation will definitely help to interpret source rock maturation and reservoir quality prediction which is very important for exploration success. The better understanding of rock properties (velocity, density, porosity etc.) will provide a better solution for uplifted basin which is related to detail compaction studies and integration of rock physics techniques. In addition, AVO modeling and seismic inversion will help to discriminate lithology and pore fluid in reservoir rocks.

1.2 Motivation

As we know the Barents Sea area is tectonically very complex. The area has suffered several events like subsidence, upliftment, erosion and reburial. It is very important to know the actual depth of burial of source and reservoir rocks because of their maturation history and reservoir property characterization like porosity, permeability, hydrocarbon saturation etc. Moreover uplift and erosion influenced the sealing capacity of the cap rocks. These complexities of uplifted basin motivate to carry out this research. By integrating different techniques like compaction, rock physics diagnostics, AVO modeling and seismic inversion it can help to understand better those complexities. The study area, the Snøhvit field, is located in the central part of the Hammerfest Basin. Since several exploration wells have been drilled and 2- and 3D seismic are also available, the area is therefore an ideal choice to carry rock physics research. Most of the rock physics models are related to normally subsidence basins whereas the Hammerfest Basin has significant uplift history that makes the rock property studies complex and more challenging. The established rock physics models also vary significantly from basin to basin and rock property behavior should be different for uplifted basins compared to normally subsided basin. Several issues discussed above give strong motivation to carry a research which has significant challenge to find out solution of rock property evolution in an uplifted area like the Snøhvit field.

1.3 Research objectives

The aim of the research is to integrate the compaction behavior and rock property evolution of Plio-Pleistocene to Triassic sediments and rocks penetrated by six exploration wells (7120/5-1, 7120/6-1, 7120/6-2S, 7121/4-1, 7121/4-2 and 7121/5-1) in the Snøhvit field (Fig. 1.3c). In addition, rock physics diagnostics, AVO modeling and post-stack seismic inversion are carried out for characterization of Triassic and Jurassic reservoirs in the Hammerfest Basin. The emphasis is given to find link between geological processes and seismic/sonic log

responses of reservoir rocks. Rock physics make a bridge between those parameters. The detail objectives of the thesis can be highlighted as follows:

- To investigate the compaction behavior and rock property evolution of whole sedimentary succession penetrated by the studied wells.
- To identify the generalized compaction trends of sands and shales.
- To identify transition zone of mechanical and chemical compaction and to determine the Cenozoic uplift and erosion.
- Rock physics diagnostics, AVO modeling and post-stack seismic inversion of reservoir rocks to get better understanding of net-to-gross, porosity, cementation and discrimination of lithology and pore fluids.

1.4 Study area

The Snøhvit Field is located in the central part of the Hammerfest basin, SW Barents Sea at a water depth of 310-340 m (Fig. 1.3). The area is highly faulted due to tectonic resulted several stages of uplift and erosion (Fig. 1.3b). The reservoirs contain gas, condensate and oil in Lower and Middle Jurassic sandstones of the Stø and Nordmela Formations (Source: NPD). SO far, it is the only producing field in the Norwegian Barents Sea. The development comprises 21 wells and covers the Snøhvit, Askeladd, Askeladd Vest, Askeladd Sentral and Albatross discoveries (Fig. 1.3b). The new small discovery Skalle (25 km north from the Snøhvit area) is also developed with involvement with the existing Snøhvit installation. The Snøhvit development is operated by Statoil on behalf of six gas companies owning licenses: Petoro (30%), Total E&P (18.40%), GDF SUEZ E&P (12%), Statoil (33.53%), Hess (3.26%) and RWE Dea (2.81%) (Source: NPD). As mentioned earlier, six exploration wells 7120/5-1, 7120/6-1, 7120/6-2S, 7121/4-1, 7121/4-2 and 7121/5-1 (Fig. 1c) have been included in the study. . Except 7120/5-1 (brine saturated) and 7121/4-2 (only gas saturated), four others wells have gas saturation with thin layers of oil lags below the gas exists. Though thin layer of oil is present but the development does not include producing it. The recovery strategy is pressure depletion and only developed for gas. The producing natural gas (CO_2, NGL and condensate) has been transported through a 160 km long pipeline to the processing plant at Melkøya. The CO2 content is sent back to the field for re-injection in a deeper formation whereas processed LNG, LPG and condensate are shipped to the market. The Snøhvit field has started production in 2007 with a planned to produce in next 30 years.

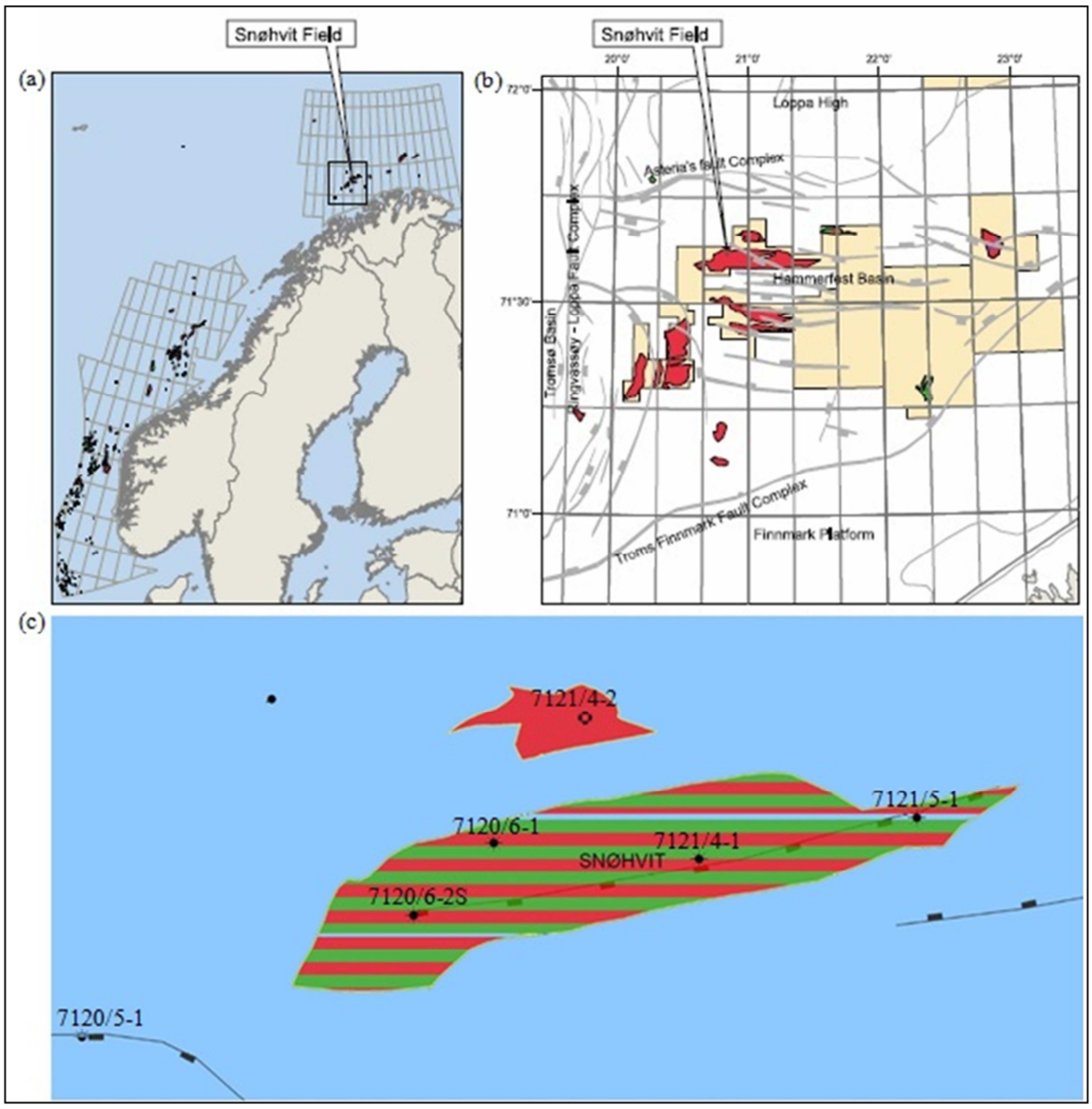

Fig. 1.3: (a) Location of the Snøhvit field, (b) the main structural elements of the Hammerfest Basin (Source: Wennberg et al., 2008) and (c) the location of the six studied wells (Source: NPD Factmaps).

1.5 Chapter descriptions

The thesis has subdivided into 9 different chapters. The first chapter is given a general introduction of the study area. It addition it discussed motivation of the research objectives and give an overview of the Snøhvit field. Limitation of the research is also included in the chapter 1.

Chapter two describes the structure, tectonic and geological frameworks of the greater Barents Sea with a special emphasis on the Hammerfest Basin, Norwegian Barents Sea. It also describes briefly the geological evolution, stratigraphy and petroleum system in the study area.

A brief theoretical background of all four methods (compaction, rock physics, AVO and seismic inversion) has been given in the chapter 3. Different theories are described under different subheading following an order from compaction to seismic inversion. These theories have been used later to discussion findings of the research.

Chapter 4 focuses exclusively the materials and methods. First the database (well logs, seismic and published compaction trends) included this study explained briefly and later a detail explanation of different datasets and methodologies given.

Compaction and rock property evaluation is belongs to the chapter five. The description and discussion of different topics like general trends of different rock parameters (velocity, porosity, density, gamma ray etc.), transition zone from mechanical to chemical, exhumation and sand-shale trends are presented in this chapter.

The rock physics analysis and use of rock physics diagnostic in the reservoir and source rocks are the main focus for chapter six.

Chapter seven has described AVO modeling. The effect of different geological parameters on AVO response for reservoir and cap rocks is explained in this chapter. Synthetic seismic analysis is also incorporated here.

Post-stack seismic inversion is carried out in this study and describe in chapter eight with special emphasis on theoretical background, results and discussion.

Finally, a summary of the entire research and major conclusions are given in the last chapter (chapter nine).

1.6 Limitation, future work and implications

This research is time limited which does not allow me to do the mineralogy analysis of different reservoir, source and cap rocks. No thin sections data have been used in this study. Though all steps used in this research are somehow related to depositional sequences which is mainly dependent on lithology, grain size distribution and sortings but because of lack of thin section, I have to dependent on well logs which are uncertain most of the time. Another important parameter in rock physics analysis is the effective porosity which in logs may not be accurate. In this study I used the average porosity calculated from density and neutron porosity logs. These porosity logs are also not always giving the actual effective porosity which could be a major limitation of this study. Shear velocity is crucial for rock physics diagnostics and AVO modeling although it is not easy to find in the log suite. I had only one well (7120/6-2S) with shear wave velocity data and for others wells I used the empirical equations that may not reflect the original scenario of shear wave behavior in the study area. The pre-stack seismic data are needed for AVO analysis. Because of no pre-stack data seismic AVO analysis was not performed though it is a powerful tool in hydrocarbon exploration.

To show a more comprehensive reservoir characterization and compaction behavior of sedimentary sequences, one can extend this work even further by combining two other theses focusing on two neighboring discoveries (Albatross and Snøhvit) in the Hammerfest Basin. Till now most of rock physics templates (RPT) are given very nice results with unconsolidated reservoirs. But in case of consolidated sandstones these RPTs have not given robust result. The Hammerfest Basin is an uplifted basin and the main reservoir rock (Stø

Formation) is overconsolidated. Hence, this basin is a very nice platform to generate RPTs which have given robust result in uplifted and overconsolidated reservoirs. In this research, few attempted have been carried out to generate such kind of RPTs but was not successful due to time limitation.

The rock physics relationships found in this study can be useful for petroleum industry in hydrocarbon exploration in other part of the Barents Sea. The results found in this study can also be tested for other basins that have upliftment history.

Chapter 2: Geological Framework

UNIVERSITY OF OSLO

FACULTY OF MATHEMATICS AND NATURAL SCIENCES

Chapter 2: Geological Framework

The geological framework of an area gives an idea about the quality and quantity of the source, reservoir and cap rocks and helps to evaluate hydrocarbon prospects. The geology of the Barents Sea is more complex compared to the North Sea due to several stages of tectonic events which influence significantly the petroleum system of the area. Though this area has multiple source and reservoir rocks with great seal potentials, it has far less exploration activities compared to the North Sea or the Norwegian Sea. The geological evolution of the area gives understanding about paleo-depositional environments and the actual depth of burial of reservoir and source rocks. The following sections focus on tectonic setting, geological evolution, stratigraphy, depositional history and petroleum systems of greater Barents Sea with more focus on the Snøhvit field in the Hammerfest Basin.by time and temperature.

2.1 Tectonic setting

The greater Barents Sea was an intracratonic basin and has been affected by several phases of tectonic events since the Caledonian orogenic movements terminated in Early-Devonian times. These phases are Late Devonian?-Carboniferous, Middle Jurassic-Early Cretaceous and Early Tertiary and each of this phase has several pulses which were migrated westward (Faleide et al., 2010). The structural trend of the Caledonian orogeny on the Norwegian mainland is from NE to SW whereas the Barents Sea continental shelf is dominated by ENE-WSW to NE-SW and NNE-SSW to NNW-WSW trends with local influence of WNW-ESE striking elements (Berglund et al., 1986). In the south-western part of the Barents Sea, a zone of ENE-WSW trending defined by the major fault complexes bordering the Hammerfest and Nordkapp basins. The orientation of the Hammerfest basin itself is also ENE-WSW. According to Berglund et al. (1986) the Hammerfest basin was outlined by five different fault complexes. These are: (i) Troms-Finmark fault complex in the south, (ii) Ringvassøy-Loppa fault complex in the east to west which characterized by north-south faults, (iii) Southern Loppa High fault complex in the south, (iv) Hammerfest basin fault types within the basin (south) and (v) Local shallow faults within the basin (north) (Fig. 2.1).

The Hammerfest basin is a graben like feature (150 km long and 70 km wide) which was developed from Late Jurassic to Early Cretaceous time (Berglund et al., 1986). This basin is lying among the Loppa high in the north, the Tromsø basin in the west, Troms-Finnmark platform to the south and eastward the structural relief gradually dies out as the basin narrows and shallows (Fig. 2.2). According to Linjordet et al. 1992 the basin is symmetrical and more widens and deepens westward. In the western margin of the basin originally far beyond of its present limits but because of north-south trending easterly rotated fault blocks, the Ringvassøy-Loppa Fault Complex (RLFC), possible westerly continuation is buried under the thick Cretaceous sediments of the Tromsø Basin (Berglund et al. 1986). The basin was affected by a doming parallel to the basin axis during Middle Jurassic to Early Barremian (Fig. 2.2). The main subsidence occurred along the north and south margins (Linjordet et al., 1992). Because of flexural extension which is related to the doming, the E-W trending fault system was formed in the central part of the basin. Horsts and grabens formed along the crest of the dome because a majority of these faults dip toward the basin axis. In the Late Paleocene to Early Eocene subsidence and sedimentation occurred in the western part of the Barents Sea but after the early-Eocene time, the opening of the Norwegian-Greenland Sea, the area was uplifted and eroded.

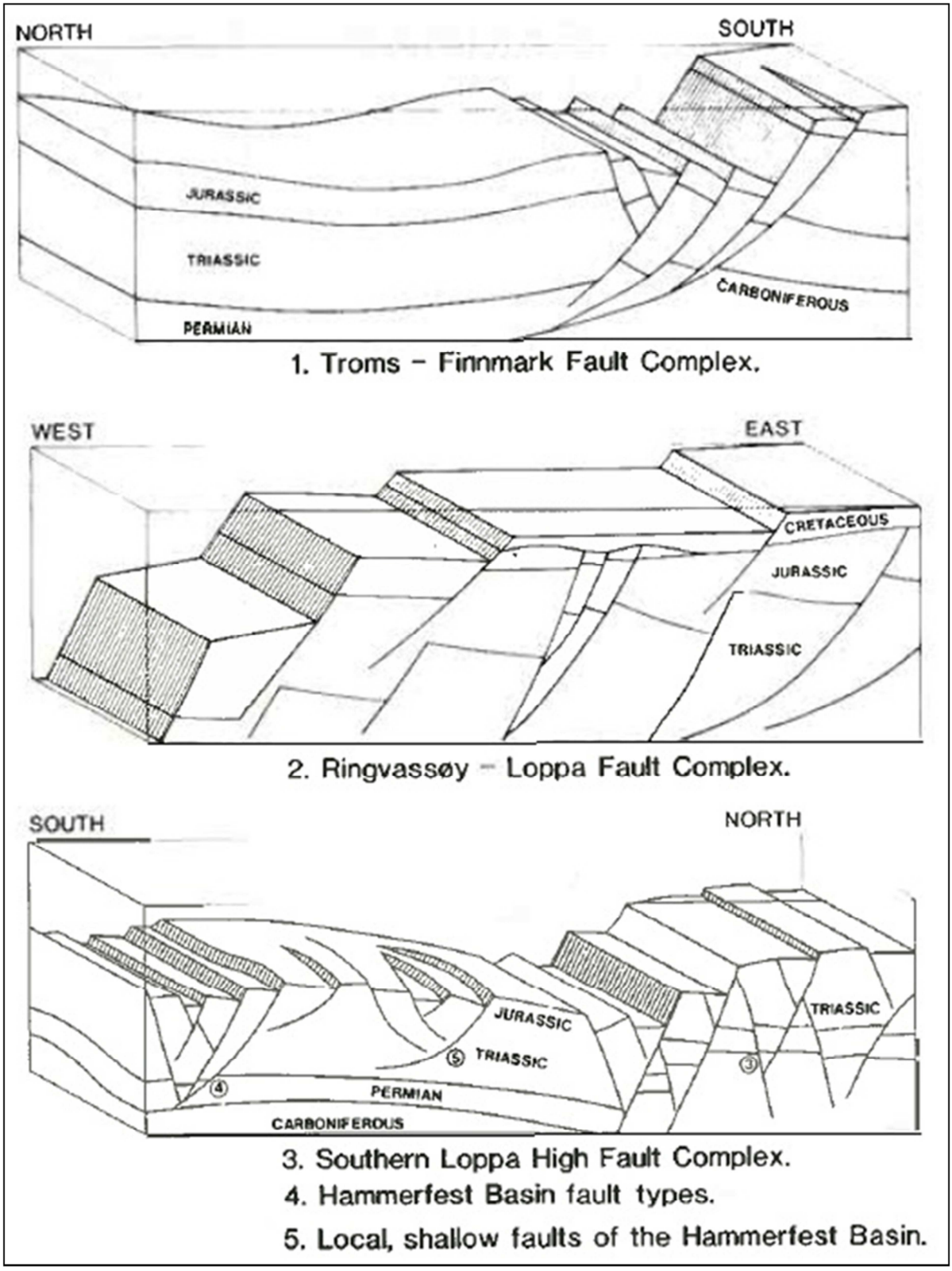

Fig. 2.1: Different faults system around Hammerfest Basin (modified after Berglund et al., 1986).

Because of updoming in the central part of the Hammerfest basin created a series of east-west oriented normal fault. The Snøhvit accumulation occurs in three of these normal faults blocks which were east-west oriented horst and dipping gently to the west (Fig. 2.2). The Hammerfest basin including the Snøhvit field has been affected by several phases of

exhumation during Tertiary which influences the reservoir and source rocks in the Snøhvit area (Faleide et al., 1996). The maximum depth was greater than the current burial depth, which changes the reservoir and source rock properties significantly.

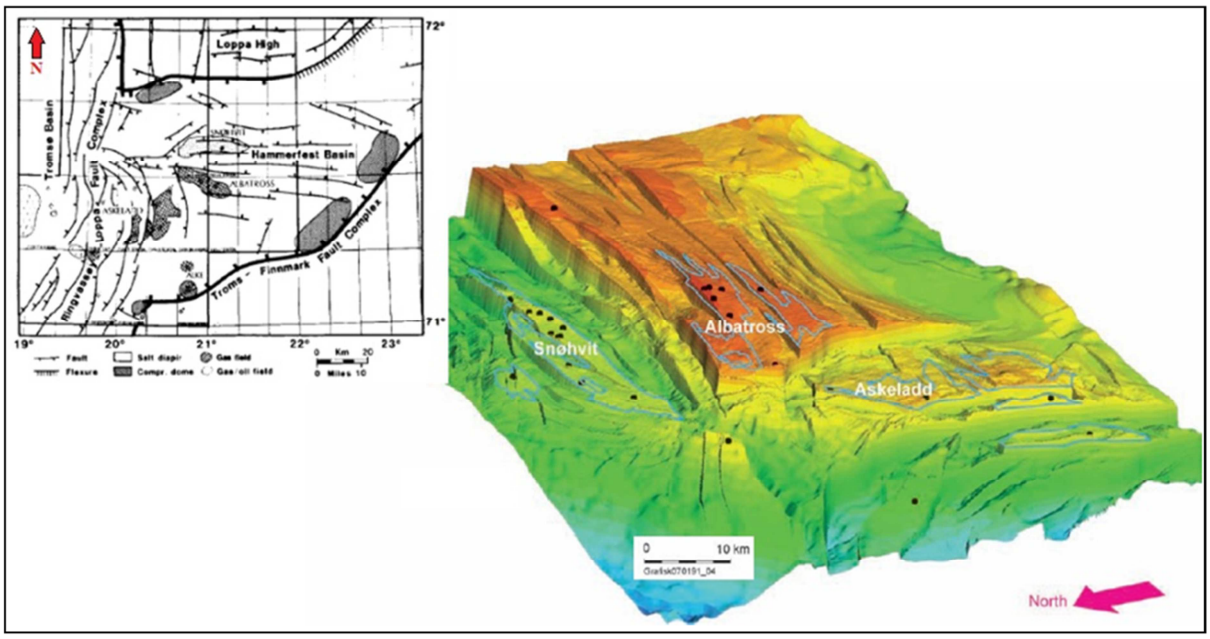

Fig. 2.2: The structural diagram of Snøhvit field at Middle Jurassic level. The blue lines show the outlines of the hydrocarbon pools (modified after Spencer et al., 2008). Structural elements of the Hammerfest basin (inset Figure) with fields (modified after Linjordet et al., 1992).

2.2 Geological evolution

The geological evolution started in Early Paleozoic time (600 Ma) began to open an ocean called Iapetus (Berglund et al., 1986). From that time the greater Barents Sea and surrounding areas have been experienced four major stages of evolution (Fig. 2.3). During Late Silurian to Early Devonian time the caledonides basement were consolidated which was later eroded and deposited as red molasses sediments into the rapidly subsiding intramontane basins of Ireland, Scotland, Western Norway, Eastern Greenland and Svalbard. During Late Devonian time the trans-pression and trans-tension activity led to folding and graben formation in this area.

In the Late Devonian-Early Carboniferous time the dominant faults (extensional) direction were NE-SW and WNW-ESE to NW-SE, one of which represents the present western limit of the Loppa high (Berglund et al., 1986) northeasterly trend which were aligned along the pre-existing Caledonian structures. The Upper Devonian basin was probably filled with the mixture of clastics, carbonates and evaporites similar in the Pechora basin in the eastern part of Barents Sea. The Lower Carboniferous deposits were more widespread clastic sequence possibly contains coal seam in the west and north but carbonate sedimentation was dominated to the east (Faleide et al., 1984). The middle Carboniferous-Lower Permian sequence indicates a quiet tectonic period in most of the area. In the Nordkapp Basin and Tromsø Basin evaporitic depositions were developed during this period (Berglund et al., 1986). At the end of Early Permian regional lithology was changed from carbonate to terrigeneous marine clastics. The Late Permian sediments were deposited on a widespread shelf sequence because of the upliftment in the south and east. The depocentres of Permian times were in the north-eastern and in the south-western part of the present Hammerfest Basin (Berglund et al., 1986).

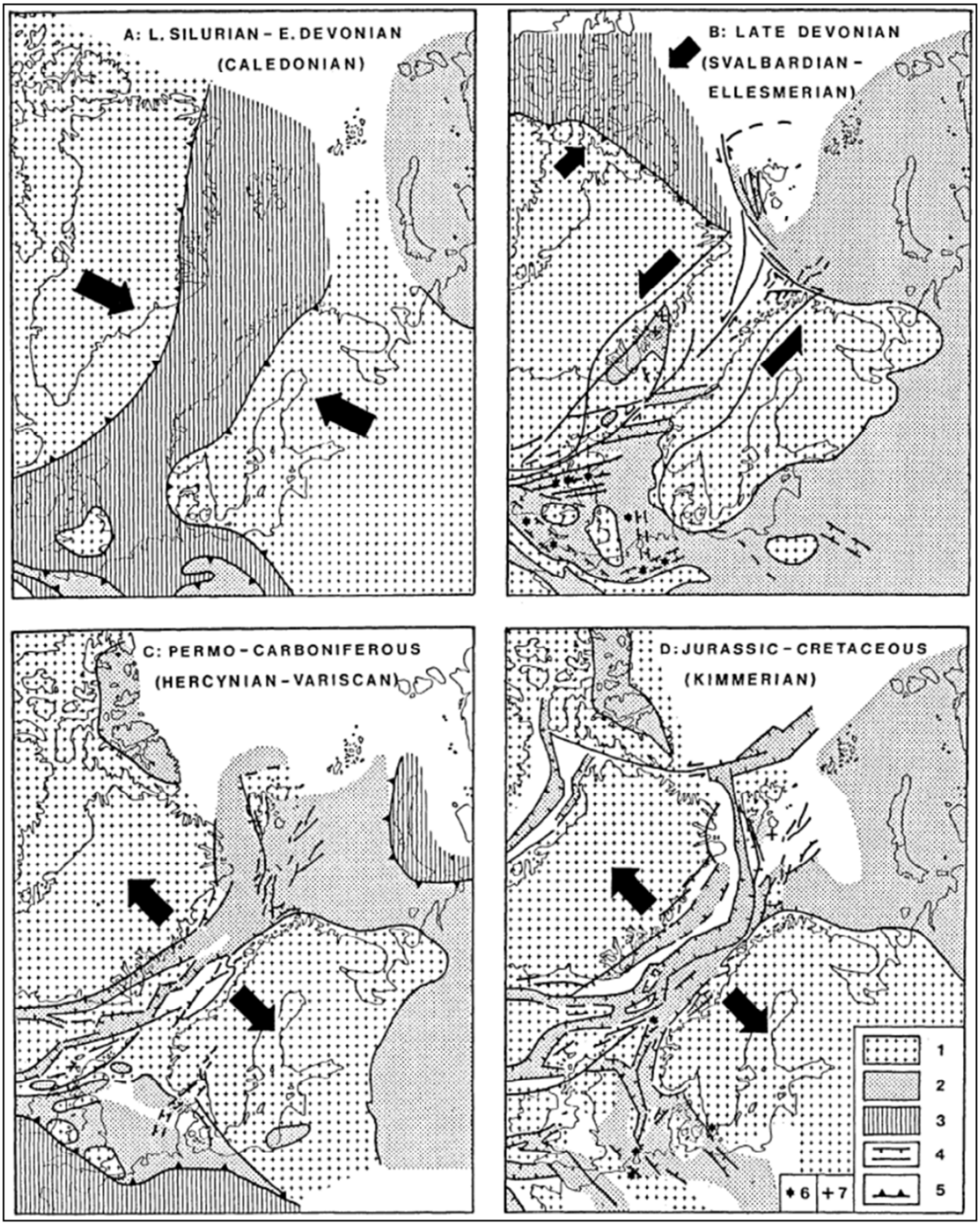

Fig. 2.3: Main stages in the evolution of the western Barents Sea and surrounding areas. (Continental fit after: Faleide et al., 1984). 1, stable elements – continental cratons and intrabasinal highs; 2, sedimentary basins; 3, active foldbelts; 4, normal and wrench faults; 5, deformation front of active foldbelts; 6, intrusions; 7, volcanics

The Permo-Triassic boundary marks a regional change to lower impedance marine sediments. At this time the whole area was tectonically inactive and a thick package of sediments mainly marine shale, siltstone and sandstone were deposited. In the Early to middle Triassic the subsidence was more pronounced in the east than west (Faleide et al., 1984) and the westerly

prograding sequences are more coarse and proximal into the eastern part of the Hammerfest basin because probably related to the Uralian orogeny far to the east (Berglund et al., 1986). The Middle and Upper Triassic interval is composed of repetitive upward-coarsening clastic sequences which represents cyclic changes from open marine to continental deposits and the lithology is mainly siltstone, sandstone, claystone and shale with thin coal beds (Berglund et al. 1986). But at the end of the middle Triassic a regional unconformity was generated because of relative upliftment in the east (Faleide et al., 1984) shifting the area of the maximum sediment accumulation to the west. The alteration continental shaly sediments and shallow marine sandy sediments in Late Triassic to Middle Jurassic sequences was controlled by a complex interplay of tectonic subsidence, eustatic sea-level changes and local sediment input (Berglund et al., 1986). Towards the end of the Triassic shallower conditions were established and interbedded onshore and offshore sediments were deposited.

According to Faleide et al. (1984) during Jurassic period a more or less transgressional phase indicates a slightly higher rate of relative subsidence then deposition. During the Early Kimmerian tectonics at the Triassic-Jurassic transition the Barents Sea region was relatively undisturbed but significant rifting was initiated during Mid Kimmerian phase in the Middle Jurassic time. In this phase faults were in high angle normal fault but limited penetration into the sequence below. The faulting was more intense in the southwest part. The mid Kimmerian phase comprises a number of discrete pulses during Middle and Late Jurassic. In the Middle Jurassic times the general relative rise in sea-level led to the deposition of the Stø formation (Berglund et al., 1986) which is the good reservoir rocks in the SW Barents sea region. The Lower and Middle Jurassic sequences have been deposited before the onset of tectonic movements which lead to the formation of Hammerfest basin (Berglund et al., 1986) indicating pre-rift sediments. During the Late Jurassic a relatively thin transgressive layer was syn-tectonically deposited within these rift basins and because of stagnant and reducing regime this Upper Jurassic clays are rich in organic matter, which makes it an excellent source rocks in the Barents Sea area. The Late Kimmerian tectonic regime was started during the time of jurassic-Cretaceous transition. The Caledonian basement zone of weakness reactivates again and a series of deep-seated normal faults were created. Compressional and also transpressional force have been active in the Late Kimmerian fault blocks in the hinge zone on the southwestern Barents Sea.

During Aptian-Albian time when the Late Kimmerian movements had ceased, the regional basin province subsidence relative to the Svalbard Platform upliftment. Because of strong differential subsidence in the west, the main structural elements were formed. The Loppa High was invested between the subsidence of Bjørnøya and Hammerfest basins. The rate of subsidence in the west was much faster than eastern part of the Loppa High fault complex.

In the Base of Tertiary during Laramide phase, the Kimmerian wrench system was activated again and the Hammerfest and Nordkapp basins were uplifted and Upper Cretaceous sediments were eroded (Faleide et al., 1984). During Late Paleocene – Early Eocene in the southern Barents Sea a relatively uniform and widespread sequence was deposited. A transform system exited between the young Lofoten-Greenland basin and the Arctic Ocean which initiated subsidence and westward tilting of the shelf sequences. The margin was uplifted, truncated and intensely faulted near the present continent – ocean boundary which led to generation of new oceanic crust along the whole Barents Sea margin. During this period whole Barents shelf was uplifted and acted as a source area for marginal wedge. Top layer of the Barents Sea sediments were mainly Pliocene-Pleistocene glacio-marine and moraine deposits.

2.3 Stratigraphy

The Barents shelf stratigraphic succession showed two distinct lithologies in its geologic history. The Devonian, Carboniferous and Permian time is dominated by carbonates whereas Mesozoic and Cenozoic are mainly represented by clastic sediments. On the other hand within clastic sediments based on their tectonic activity they showed two distinct lithologies. Kapp Toscana group represents sandstones which is Triassic and Jurassic in age whereas Adventdalen Group represents shales which is Lower Jurassic and younger. A rifting events mark in the Middle Jurassic in age which is the key factor for different lithologies (Fig. 2.4). It also represents the paleo-depositional environments in which before rifting deltaic, shallow marine conditions and after rifting deep sea condition exits. Several source rocks have been encountered within this stratigraphy from Carboniferous to Cretaceous (Ohm et al., 2008).

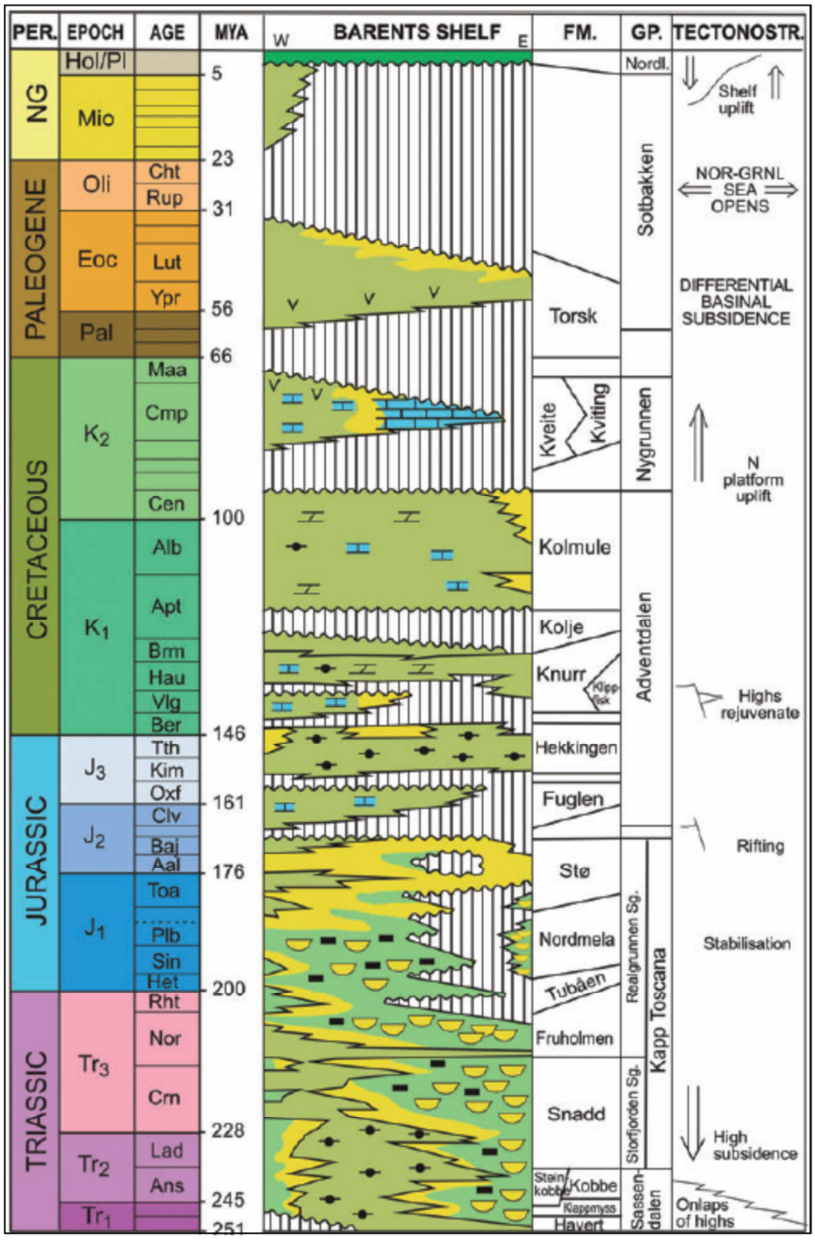

Fig. 2.4: The Mesozoic and Cenozoic development of the south-western Barents Sea (modified from Nøttvedt et al., 1993), with the geological time scale based on Gradstein et al. (2004) (cited in Worsley, 2008).

The Snøhvit area consists Lower to Middle Jurassic sandstones which extends throughout the Hammerfest basin (Fig. 2.5). The main reservoir is Lower-Middle Jurassic Stø formation which is clean sandstone. In Nordmela and Tubåen formation in some wells also encounter gas-water contact (GWC) or oil-water contact (OWC). The Triassic and Late Jurassic organic shales are possibly the source rock of this accumulation.

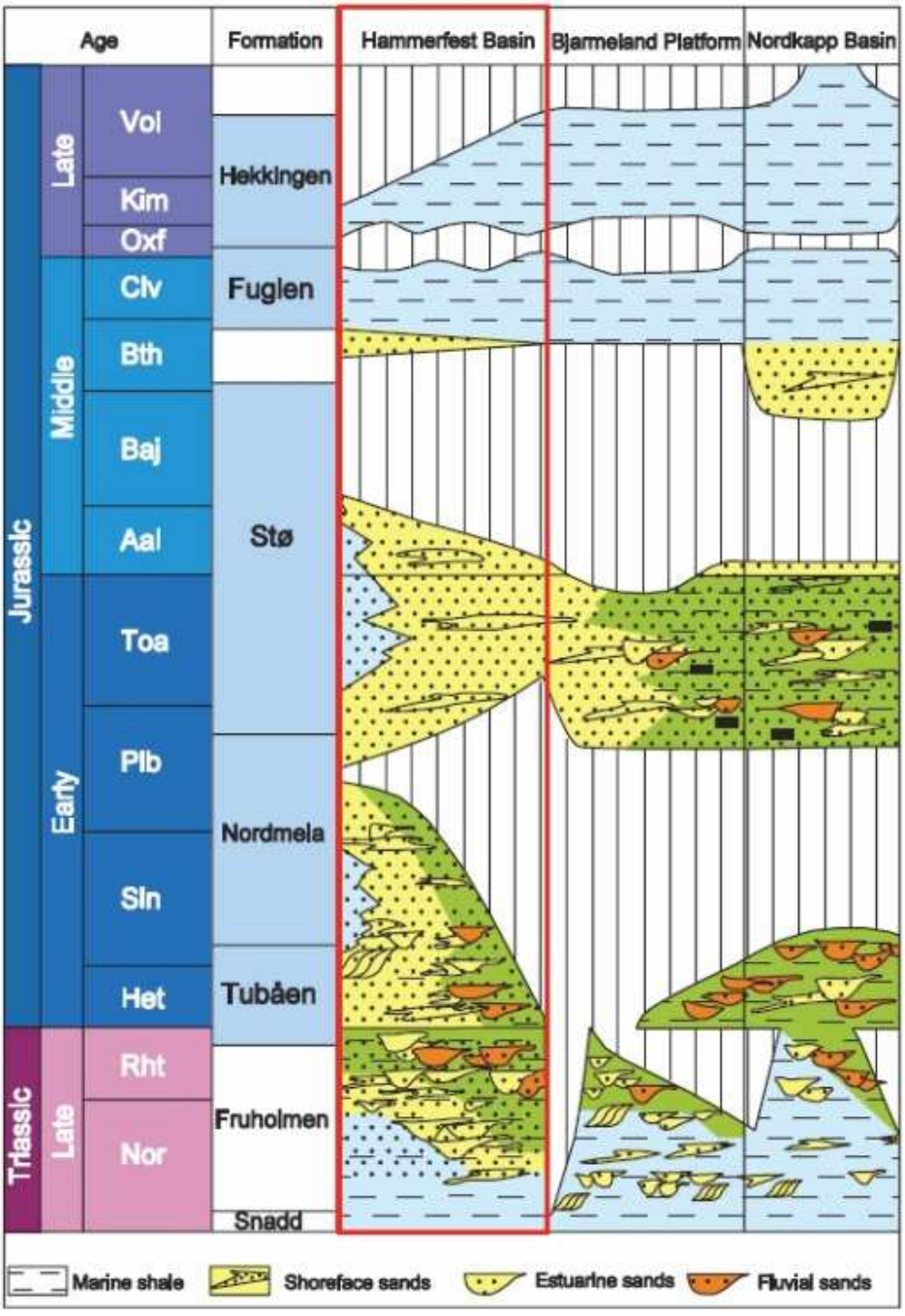

Fig. 2.5: Triassic-Jurassic stratigraphy of Hammerfest basin (Source: Wennberg et al., 2008).

The deepest well in Snøhvit field is 7121/6-2S which drilled the oldest stratigraphic formation Snadd in Late-Triassic age. All six wells used in this study are shown in the Table 2.1 with the oldest formation, penetration depth and age. All are encounter the target reservoirs Stø, Nordmela and Tubåen formation. The brief stratigraphic description of the target Formations are given below:

Table 2.1: Wells with corresponding oldest unit of penetration.

Well Name	Total depth (m) RKB	Oldest unit	Age
7120/5-1	2699	Fruholmen FM	Late Triassic
7120/6-1	2820	Tubåen FM	Late Triassic
7121/6-2S	3035	Snadd FM	Late Triassic
7121/4-1	2609	Fruholmen FM	Late Triassic
7121/4-2	2799	Fruholmen FM	Late Triassic
7121/5-1	3197	Snadd FM	Late Triassic

2.3.1 Kapp Toscana Group

2.3.1.1 Storfjorden subgroup (Late Triassic)

The Kapp Toscana Group is locally rich in sandstones of varying origins. But the lower part Snadd Formation is basically prodeltaic shales which deposited in front of the north-westerly prograding system (Worsley, 2008). Interbeded siltstones and sandstones are also found. Thin coaly lenses are developed locally further up (Dalland et al., 1988). In the Hammerfest basin this formation is 1300 m thick.

2.3.1.2 Realgrunnen Subgroup (Latest Triassic to Middle Jurassic)

This subgroup is present throughout the Hammerfest basin and probably thickens markedly into the Tromsø basin. This subgroup is also deposited in Loppa high and Troms-Finnmark platform which was eroded during Kimmerian movements (Dalland et al., 1988). The average thickness in Hammerfest basin is 450 m. This group comprises 4 formations. These are:

- **Fruholmen Formation**

  The older formation of this subgroup and comprises grey to dark grey shales which gradually upwards into interbedded sandstones, shales and coals (Dalland et al., 1988). The thickness of this formation is 250 m. Because of Rhaetian transgression the whole area is covered by water and open marine shale was deposited.

- **Tubåen Formation**

  This formation is dominated by sandstones with subordinate shales and minor coals. Coals are most abundant southeast basinal margins and die out to the northwest (Dalland et al., 1988). This formation is relatively thin 65-87 m respectively.

- **Nordmela Formation**

  The formation consists of interbedded siltstones, sandstones, shales and claystones with minor coal. Sandstones become more prominent towards the top (Dalland et al., 1988). The formation was deposited in tidal flat to flood plain environments.
- **Stø Formation**

The dominant rocks are sandstones which are moderate to well sorted and mineralogically mature (Dalland et al., 1988). Thin units of shale and siltstone are also present. This formation is thickest in the southwestern part of the Hammerfest basin and gradually thinning eastward. The sands were deposited in a prograding coastal regime whereas shale/siltstone intervals represent regional transgressive pulses.

2.3.2 Adventdalen Group (Mid-Jurassic to Mid-Cretaceous)

This group represents a regional transgression which cut off the supply of coarse clastics and marine black shale was deposited (Worsley D., 2008). All highs and platforms were submerged but thickness was varied between highs and basins. There are five formations in this group. These are:

- **Fuglen Formation**

  Fuglen formation is the lower unit of the Adventdalen group. It consists pyritic mudstone with interbedded thin limestones. The shales are dark brown in color.

- **Hekkingen Formation**

  This Upper Jurassic formation is an excellent source rock quality in the Barent Sea which contains organic contents upto 20% (Worsley D., 2008). The formation consists of brownish-grey to very dark grey shale and claystone with occasional thin interbeds of limestone, dolomite, siltstone and sandstone.

- **Knurr Formaton**

  This formation also consists of dark grey to greyish brown claystone but because of lowering of sea level and better bottom circulation (Worsley D., 2008) is not a good source rock. Thin sandstones layers are also seen in this formation.

- **Kolje Formation**

  This formation was deposited in distal open marine conditions with good water circulation and consists of dark brown to dark grey shale and claystone with minor interbedded limestones and dolomites.

- **Kolmule Formation**
  Continuation of Kolje formation consists of dark grey to green claystone and shale with limestone and dolomite stringers. Traces of gluconite and pyrite were also occurred (Dalland et al., 1988).

2.4 Depositional environment

It is very important to know the provenance and depositional environment of a sedimentary sequence to carry out the compaction and rock physics analyses. Depositional environments affect the petrophysical behavior of rocks. Here, the discussion is only focused on the depositional environments of reservoir and source rocks of studied area. The best reservoir

rock in the Hammerfest Basin is the Stø Formation whereas the Tubåen and Nordmela Formation also have good reservoir potential. Figure 2.6 shows the depositional environments of Nordmela and Stø formations.

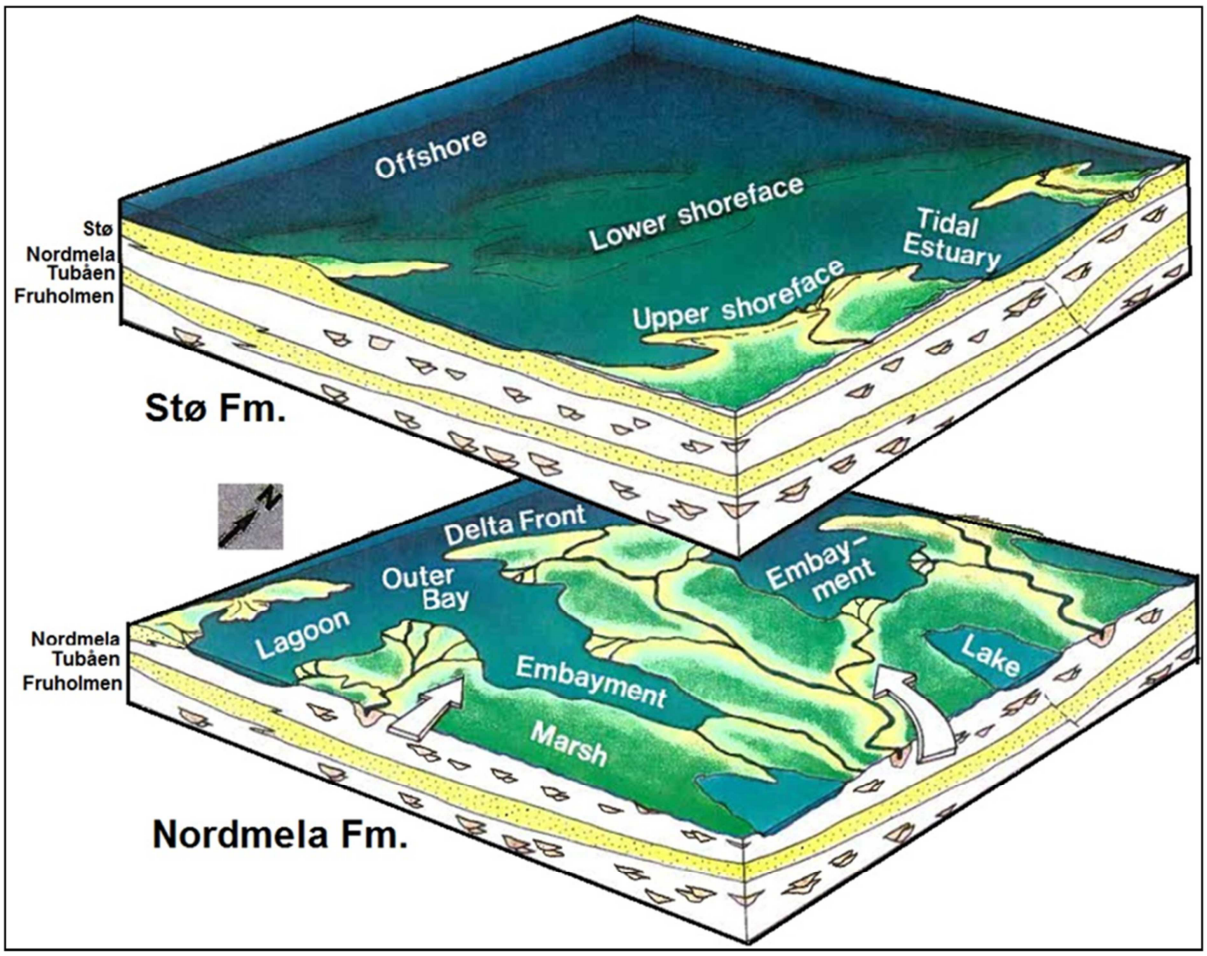

Fig. 2.6: Paleogeography and depositional model for Stø and Nordmela formations (modified after Berglund et al., 1986).

The Nordmela formation consists mainly of deltaic environment where the sub-environments were lagoon, marsh, embayment lake, delta front, channels etc. It represents a broad alteration of fine-grained sandstones, siltstones, mudstones and thin coals. The channels were mainly anastomosing pattern which was responsible for thick and coarse sandstones constitute less than 20% of the total lithology (Berglund et al., 1986). The average thickness of Nordmela formation is more or less similar in the Snøhvit area (Fig. 2.7). The global Sea level started to rise and the Stø formation was deposited in a shoreline and nearshore depositional environments which is strongly influenced by storm-wave processes and bioturbation. The source of south and east were still active and fine- to medium grained sandstones was deposited over a large area. The whole formation represents several episodes of sea level changes but the upper part shows more distal marine facies (Lower shoreface-offshore) compare to lower part (Berglund et al., 1986). On the other hand from east to west the facies changed from proximal to distal because of the eastward provinces. The thickness of the formation also varied from east to west (Fig. 2.7). Major transgressions changed the shoreface environments into deep sea anoxic conditions which was the time for deposition of Hekkingen formation, the major source rock in Hammerfest basin. The thickness of this

formation from east to west also revel this condition (thin in the distal part compare to proximal).

The overall trend of the early Middle Jurassic depositional environment in the Hammerfest basin is represents an upward transgression from upper delta plain (Tubåen Fm.) through lower delta plain (Nordmela Fm.) to delta front or shoreface (Stø Fm.) to deep sea (Hekkingen Fm.) environments. The gradual proximal facies onlaping on the east/south-east direction with gradual thinning eastward suggest a basin margin in the same direction (Berglund et al., 1986). These geological complexities from east to west around the Snøhvit field influence the rock properties.

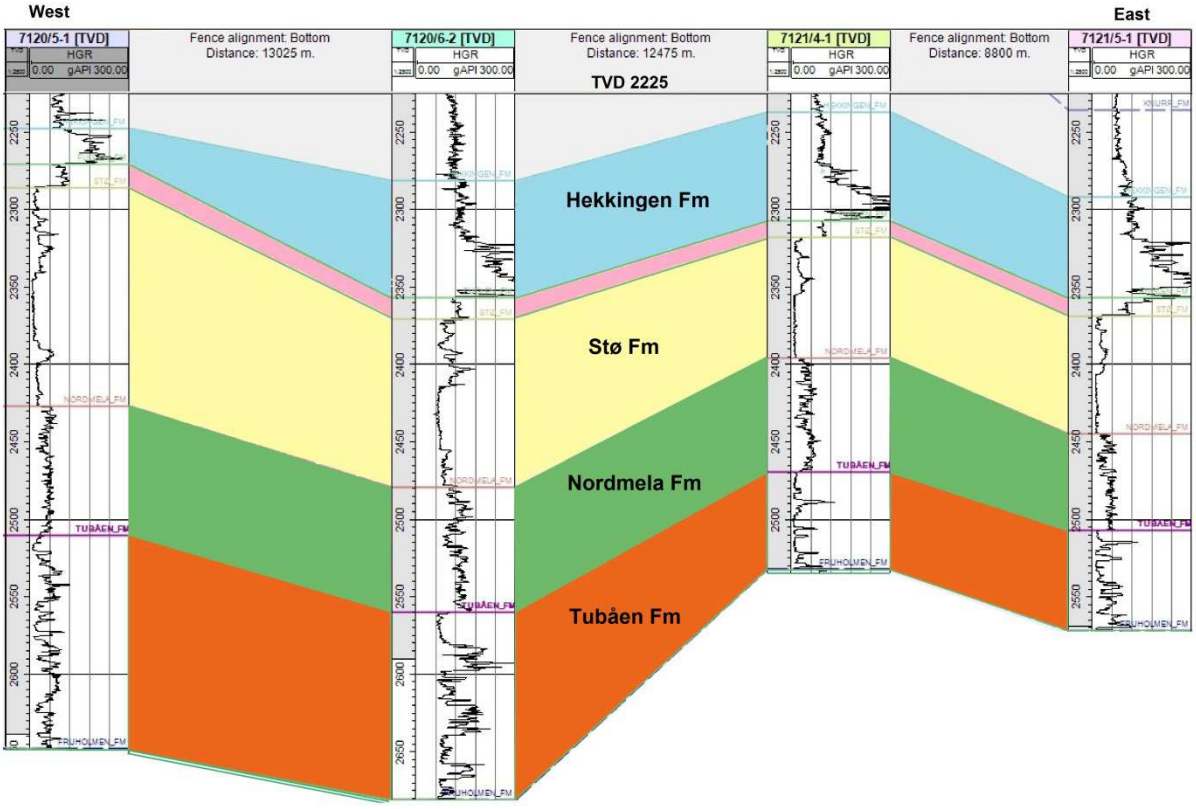

Fig. 2.7: A litho-stratigraphic correlation of Kapp Toscana Group of four studied wells.

2.5 Petroleum system

Three different petroleum systems: Paleozoic, Early-Middle Triassic and Late Jurassic exit in the greater Barents Sea whereas in the Hammerfest basin it belongs to the Late Jurassic and mixed systems (Fig. 2.8) (Henriksen et al., 2011). The important parameters in petroleum system is the reservoir rock, source rock, seal and time of migration which I discussed detail here. In uplifted basin theses parameters are more complicated compare to normally subsided basin. Uplift influences reservoir quality, source rock maturation and seal. Since Hammerfest basin is an uplifted area, proper care should be taken when someone explain the petroleum system.

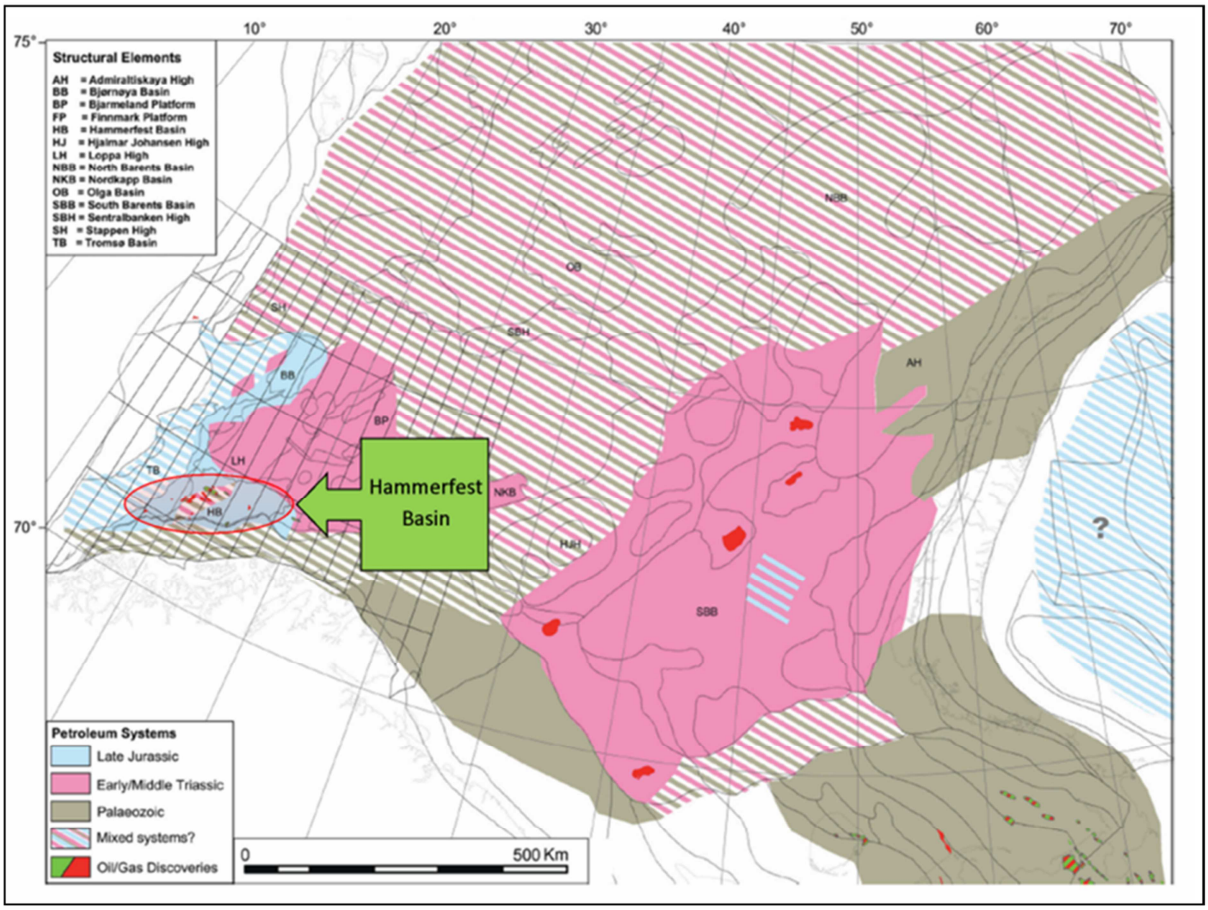

Fig. 2.8: Petroleum systems in the greater Barents Sea. The map is based on inferred presence of source rocks and modeled maturity and is calibrated to the distribution and geochemistry of hydrocarbons in wells in the Norwegian Barents Sea (modified after Henriksen et al., 2011).

2.5.1 Reservoir rocks

The most significant reservoir rocks in the Hammerfest Basin lie within the strata of Jurassic age and the major discoveries in that area have a principal reservoir rock of Lower to Middle Jurassic Stø Formation (Dore, 1995). The Lower Jurassic Nordmela and Tubåen formation have also good reservoir characteristics. The depositional environments of these are coastal, deltaic, marine to shore face settings. The two different subunits of Stø formation have been shown in the Figure 2.9. The upper part of this formation is poorly sorted compare to lower part and represents good reservoir quality. The energy condition also influences the sorting as well as bioturbation. In low energy with highly bioturbation condition, poorly sorted sediments have been deposited which has poor reservoir quality. On the other hand, high energy well sorted sediments have low bioturbation and preserve better reservoir quality.

The Nordmela formation is deposited in subtidal or tidal channel environments which represents lenticular and flaser bedding (Fig. 2.10). The vertical fluid flow is restricted but horizontally distributed channel sand is very good quality reservoirs. On the other hand, Tubåen formation has better reservoir quality which is fine to medium grained sandstones. Because of greater burial depth in the past and uplift the diagenetic history deteriorate reservoir quality more in the Tubåen formation compare to the Stø formation. However, those reservoir rocks in the Hammerfest basin are promising though the basin has uplift history.

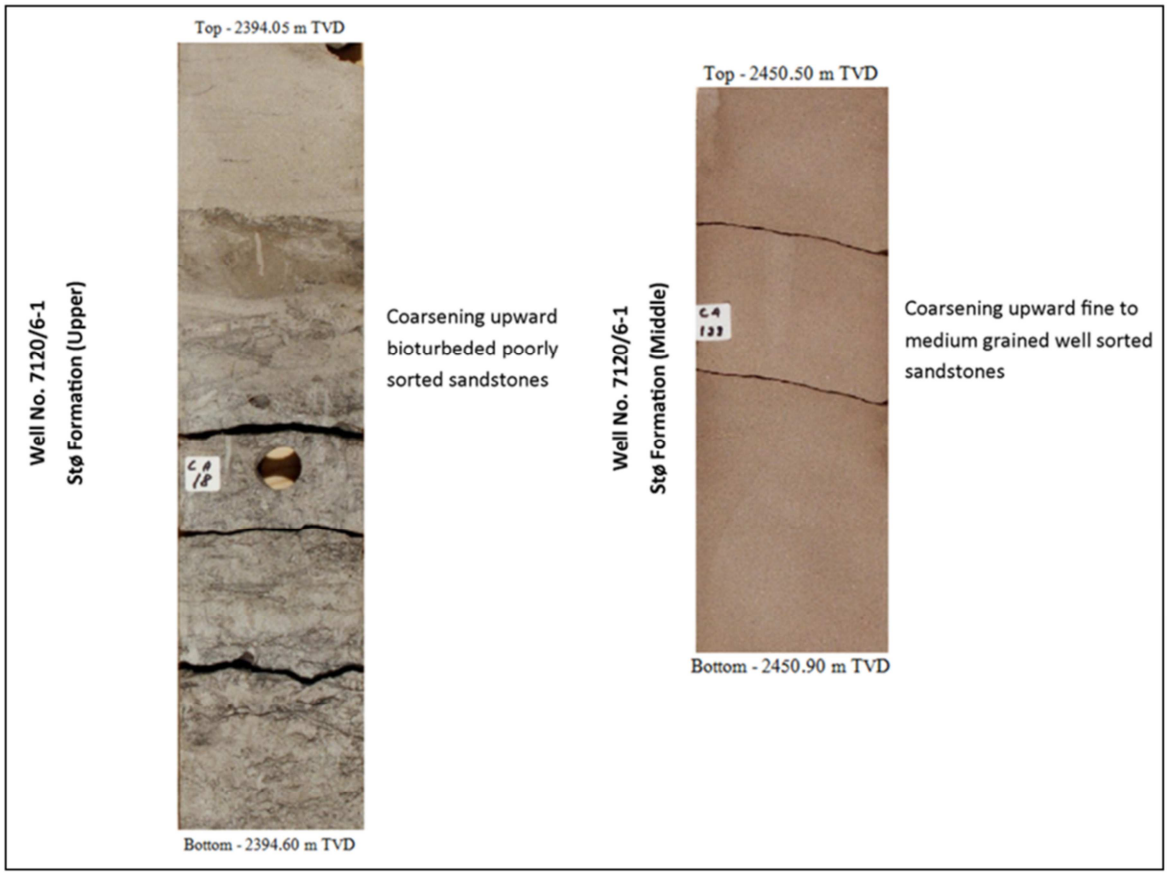

Fig. 2.9: Core photographs of the Stø formation from the well 7120/6-1 show the variation of depositional environments (Source: NPD).

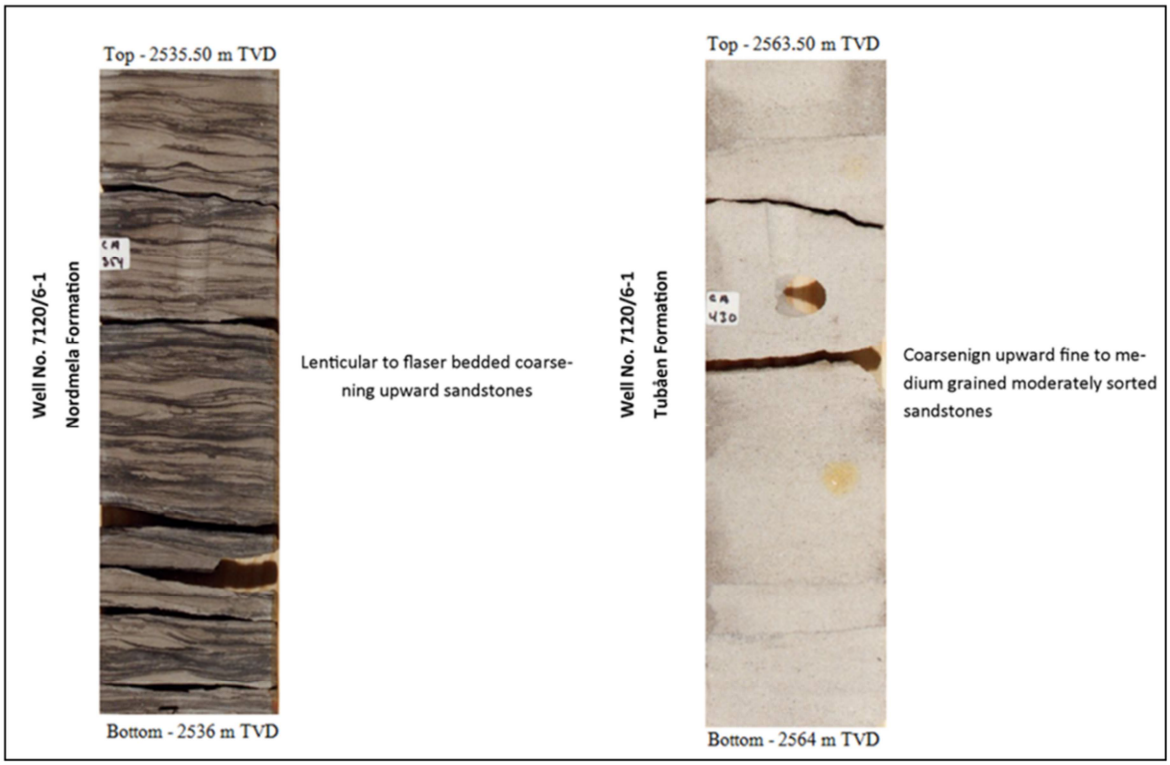

Fig. 2.10: Core photographs of Nordmela and Tubåen formation from the well 7120/6-1 showing different sedimentary structures indicate variation of depositional environments (Source: NPD).

2.5.2 Source rocks

The term source rock denotes a sedimentary unit that capable of generating hydrocarbons that subsequently migrate into a reservoir. A typical source rock contains greater than usual abundance of organic matter (>1% TOC in clastic rock). Craking of Kerogen takes place in deep burial (around 2.5 Km, depends on geothermal gradient) and higher temperature (70 to 80°C) which produce hydrocarbons. Terrestial kerogene has a tendency to generate gas whereas marine kerogen is oil prone.

A series of petroleum source rocks were deposited in the greater Barents shelf area during Silurian to Cretaceous time. Silurian and Late Devonian source rocks are most significant in the Timan-Pechora basin, whereas Triassic and Jurassic age are commom in Southern Barents Sea. Further to the west, Late Permian, Triassic, Late Jurassic and Early Cretaceous marine source rocks are present (Henriksen et al., 2011). The south western Hammerfest basin consist Permian to Early Cretaceous multi-sourced system which make this area as an overfilled petroleum basin (Ohm et al., 2008). The Snøhvit area has three possible source rocks which are: the Late Jurassic-Early Cretaceous anaerobic shales of the Hekkingen Formation, the Early Jurassic Nordmela Formation and the Triassic shales (Linjordet et al., 1992). The Hekkingen Formation is the best source rock and has good potential to generate light oil, condensate and gas whereas terrestrial Nordmela formation and over-matured Triassic shales have generated condensate and gas. The Hekkingen formation in the Barents Sea is the equivalent of the Kimmeridge clay formation in the North Sea which is deposited in anoxic deep marine restricted basin conditions (Dalland et al., 1988). The formation is most prolific because of its total organic carbon (TOC) and the hydrocarbon generative potential (Fig. 2.11). The Nordmela and Triassic shales are mainly sub-tidal to tidal terrestrial shales which are not too prolific for oil but good for gas. In the Hammerfest basin most Triassic source rocks entered into the gas window whereas the Hekkingen formation is in oil window. During upliftment the temperature of the Hekkingen formation may crossed above the oil window and stop to generate hydrocarbon which is a negative consequences for hydrocarbon generation in an uplifted basin. However, evidence of non-cogenetic system gas has been documented in this area indicating the presence of a live petroleum system in the area (Ohm et al., 2008).

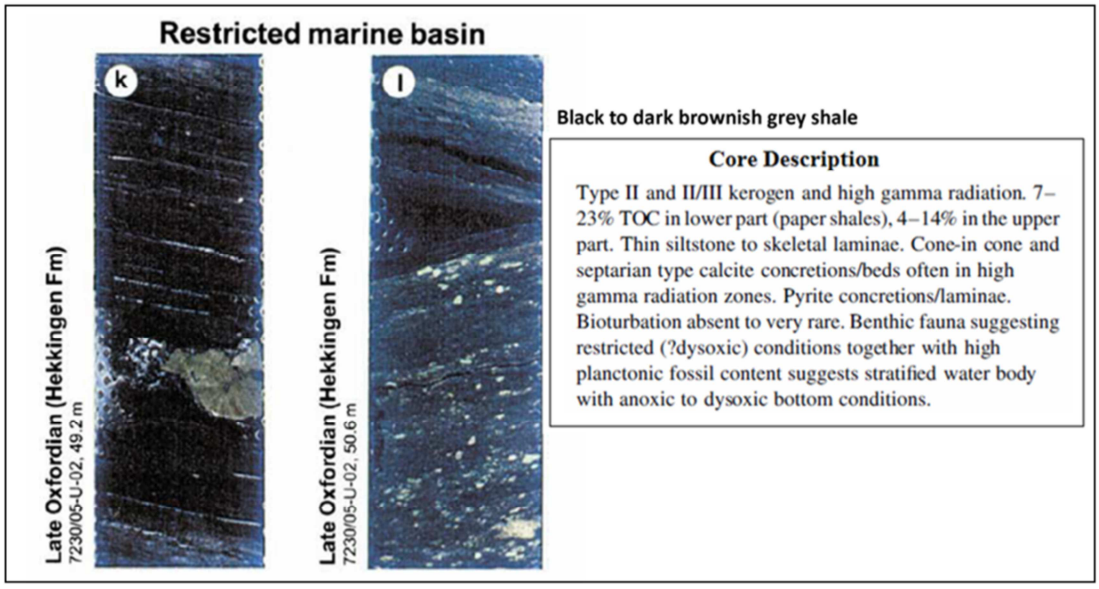

Fig. 2.11: Core description of the Hekkingen formation (Modified after Bugge et al., 2002).

2.5.3 Trap and Seal

The Hammerfest basin was tectonically highly active and experienced several phases of uplift that created many fault related traps like hanging wall roll-over anticlines, antithetic faults or sealing faults. In Hammerfest Basin most of the discoveries are fault- bounded positive blocks traps (Dore, 1995). The Stø Formation, main Snøhvit reservoir, is also bounded by three east-west oriented normal faults with several smaller faults oriented in various directions (Fig. 2.12). In the Upper Albian interval horizontal stress direction was north-south that closed off the east-west oriented major faults before the time of hydrocarbon migration and makes the trap for Snøhvit accumulation (Linjordet et al., 1992).

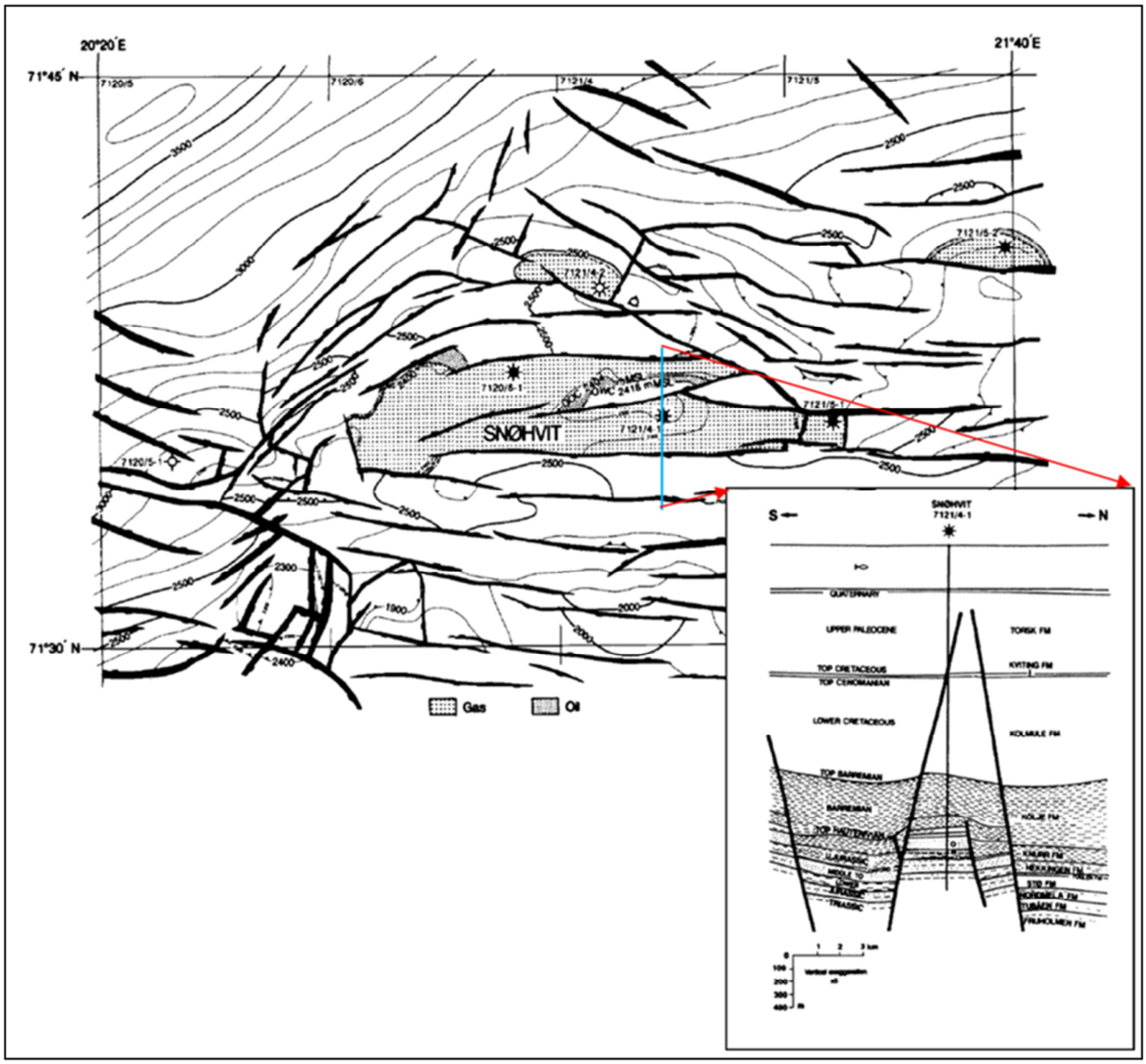

Fig. 2.12: Structural depth map on the top of the Stø Formation with a north-south geologic section through the discovery well 7121/4-1 shows in the inset Figure (modified after Linjordet et al., 1992).

The Snøhvit field has two excellent seals: the Fuglen Formation and the Hekkingen Formation that sealing the hydrocarbon (Fig. 2.13). The Fuglen formation is a thin mudstone layer (11 to 30 m thick) compare to Hekkingen formation (65 to 112 m thick) where the thickness of both formations increased northward. The lower part of the Hekkingen formation showed very high gamma ray value as well as low P-wave velocity can be interpreted by

combine effects of high gas content and high pore pressure. Therefore, the lower part of the Hekkingen formation represents the best seal. Moreover, the mechanical strength and brittleness also suggested the formation is a good seal rocks (Linjordet et al., 1992).

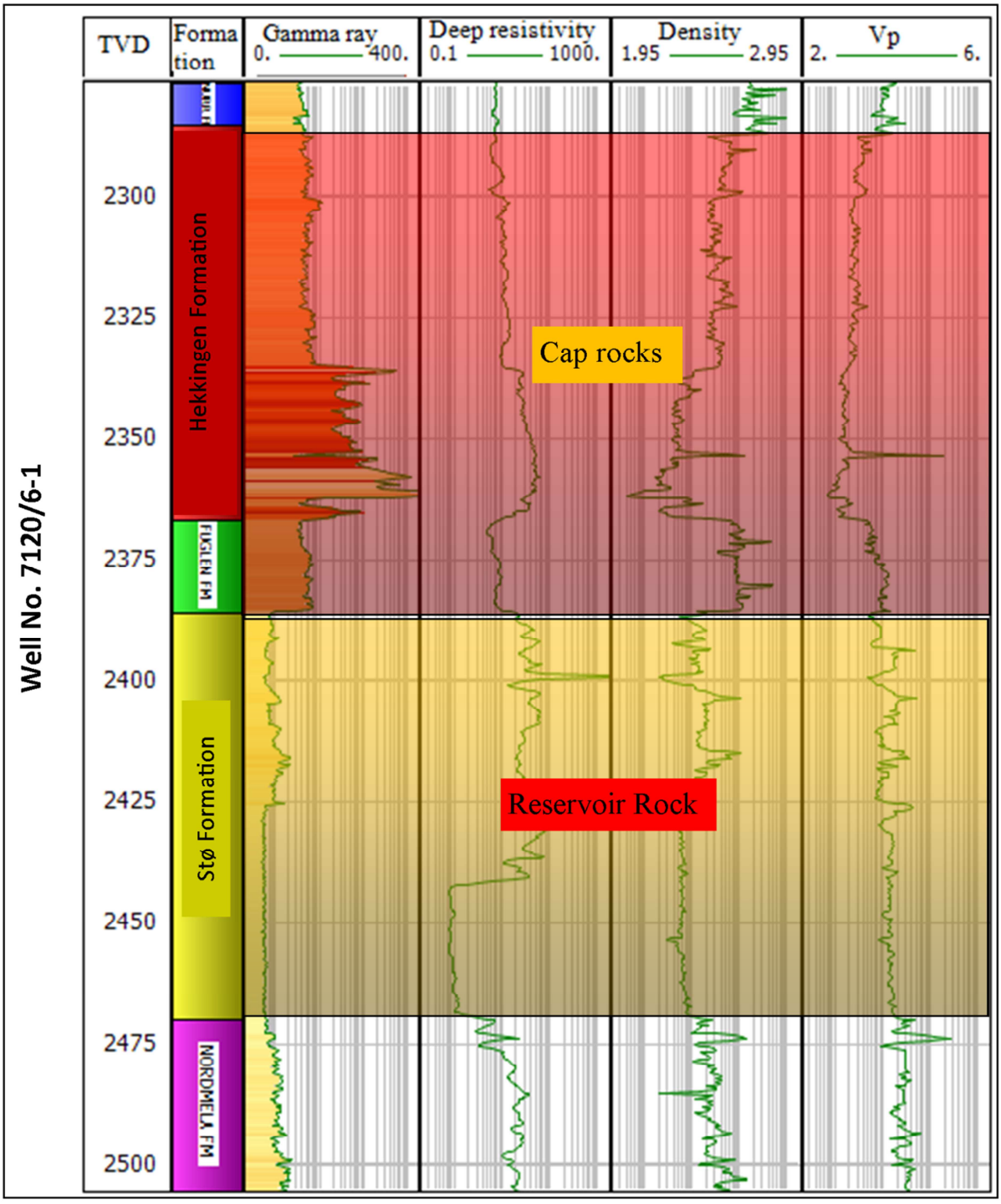

Fig. 2.13: Gamma, resistivity, P-wave velocity and density log response of the Fuglen and Hekkingen Formations, the main cap/seal rocks in the study area.

Chapter 3: Theoretical Background

UNIVERSITY OF OSLO

FACULTY OF MATHEMATICS AND NATURAL SCIENCES

Chapter 3: Theoretical Background

3.1 Compaction

The properties of sediments and rocks are continuously changing from the time of deposition, through burial at the greater depth and also during uplift. There are several diagenetic processes acting on the reservoir rocks just after their deposition to the present. Compaction and evolution of rock physical and acoustic properties influence significantly by their primary composition. Therefore, it is very important to linked diagenetic model to provinance and depositional systems (facies models and sequence stratigraphy) (Bjørlykke and Jahren, 2010). According to Bjørlykke and Jahren (2010) the main diagenetic processes are mechanical (stress dependent) and chemical (temperature and time dependent) compactions. In shallow burial the main porosity destruction mechanism is mechanical, while at deep burial chemical compaction takes over and porosity is lost by the precipitation of quartz cement. Near surface diagenesis is also common. At very shallow burial depth (less than 10 m) sediments may react with the air or water both by fluid flow and diffusion and change their bulk composition more than at greater burial (Bjørlykke and Jahren, 2010). The soil forming processes and precipitation of carbonate and silicates in the desert environments are also the example of early diagenesis (Bjørlykke & Jahren, 2010). These evaporation processes on desert environments make coatings of red or yellow iron oxides and clays on desert sand which prevent quartz cementation at greater depth and preserved porosity.

3.1.1 Mechanical Compaction

Mechanical compaction depends on the effective stress which is the difference between lithostatic pressure and pore pressure (Eq. 3.2). The magnitude of mechanical compaction is depended on the effective stress and the mechanical strength of the sediment grains and their framework (Fig. 3.1). The rate of compaction depends on permeability which controls the buildup of pore pressure (Bjørlykke and Høeg, 1997). On the other hand, permeability is depended on grain size and the specific surface areas of rock forming minerals. The volume reduction or porosity loss is due to the reorientation, cleavage and fracturing of brittle grains and pseudo-plastic deformation of ductile grains (Bjørlykke et al., 1989).

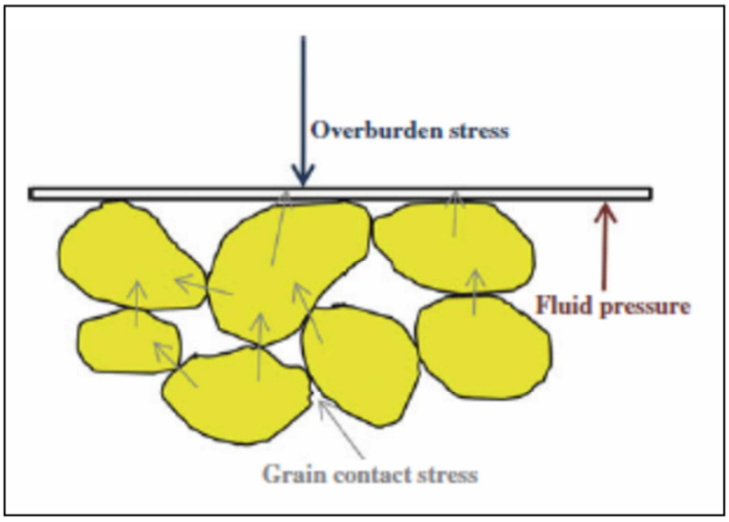

Fig. 3.1: The effective stress from the overburden (σ'_v) is carried by the mineral grain framework (solid phase) and the pore pressure (fluid phase) (source: Bjørlykke and Jahren, 2010).

Mechanical compaction of a sedimentary layer dominates in the shallow part of the basin down to 2-4 km depth (80-100^{0}C), depending on the geothermal gradient (Chuhan et al., 2002; Mondol et al., 2007). The direction of the principal stress is normally vertical but in compressive regimes the major principal stress axis can be horizontal (Chuhan et al., 2002). The weight of the overburden sediments and fluids in the pore space produce a vertical stress. For a sedimentary basin the total vertical stress (lithostatic stress) can be calculated as follows:

$$\sigma_v = \rho_b \, gh \quad \text{..... (3.1)}$$

Where ρ_b is the average bulk density of overburden sediments, g is the gravitational force and h is the thickness of the overburden sediments. The effective stress (σ'_v) is the difference between the total vertical stress (σ_v) and the pore pressure (Pp) and it increases linearly with depth (under hydrostatic pore pressure conditions):

$$\sigma'_v = \sigma_v - Pp \quad \text{..... (3.2)}$$

This effective stress is the main control of mechanical compaction which occurs via frictional slippage, rotation and sliding (Chuhan et al., 2002) and reorientation (Bjørlykke and Jahren, 2010) of the grains. If the pore pressure increases, it reduces the vertical effective stress and hence mechanical and will preserve porosity though the grains are in greater depth (Bjørlykke and Jahren, 2010). Mechanical compaction also depends on some other geological parameters like grain size, sorting and the rate of fluid expulsion from the compacting sediments (Waples and Couples, 1998; Bjørlykke et al., 2004). Sand and shales have different compaction trends both in mechanical and chemical compaction zones. After a certain depth in the mechanical compaction zone shales compact more compared to sands. The compaction of sands varies because of grain size and sorting. The coarse grained sand compacts more due to grain crushing than the fine grained sand (Bjørlykke and Jahren, 2010) because of stress per grain contact which results in higher porosity losses in the coarser sand than finer one (Chuhan et al., 2002) (Fig. 3.2). In fine-grained sands the grain contact is more compared to coarse-grained sands and prevents the grain crushing because more grain contact means low stress per contact. Well sorted sand preserved more porosity compare to poorly sorted sand because fine particles in poorly sorted sand filled porosity during compaction.

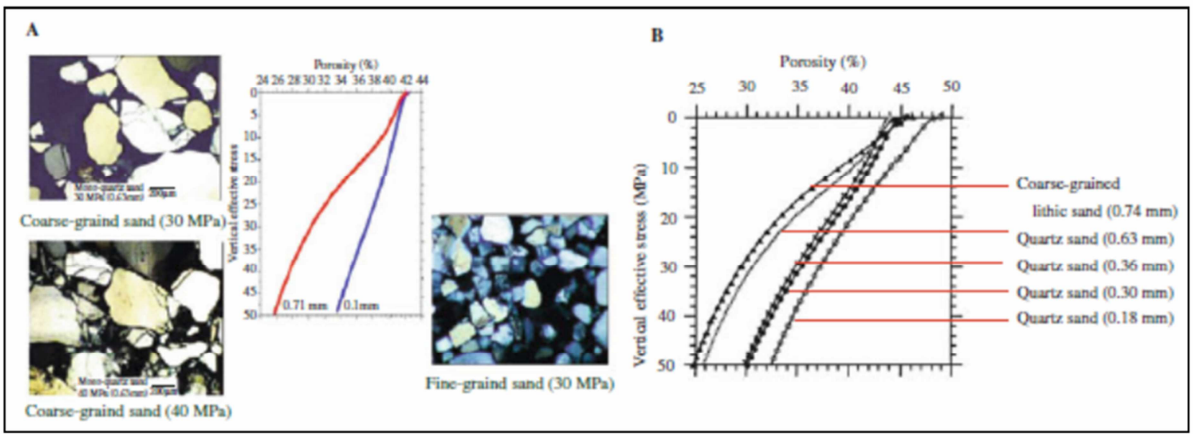

Fig. 3.2: (a) Experimental compaction of fine-grained and coarse-grained sand showing that well sorted fine-grained sands are less compressible compared to the coarse-grained sands, (b) The porosity loss as a function of grain size due to more grain crushing (modified after Bjørlykke & Jahren, 2010).

Similar trend follow the shales as well, coarse grain shale compact more compare to fine grain shales (Storvoll et al., 2005; Mondol et al., 2007; Marcussen et al., 2009; Thyberg et al., 2009). Smectite is finer than kaolinite which does not expelled fluid easily during compaction. These pressured fluid increased pore pressure (Overpressure) which decline the effective stress of this zone and preserved more porosity in smectite compared to than kaolinite (Mondol et al., 2007). The porosity reduction of clays or clay-rich sediments started even during first decimeter to a few meters of burial, whereas in sandstones due to reorientation, fracturing and deformation of grains require higher overburden stress (Bjørlykke et al., 1989).

3.1.2 Chemical Compaction

Chemical compaction usually occurs at deeper parts of the sedimentary basins, normally started from 2 to 2.5 km (depends on temperature gradient). It is the result of mineral dissolution and precipitation of minerals and is functions of mineral stability (thermodynamics) and kinetics (Peltonen et al., 2008). It is temperature dependent and control by many factors such as primary mineral composition, pore-fluid composition and time-temperature history etc. (Bjørlykke, 1998; Peltonen et al., 2008). At initial phase of chemical compaction a small amount of cement at the grain contacts will significantly increase the stiffness (Vernik and Nur, 1992; Dvorkin and Nur, 1996) and ceased the stress dependent mechanical compaction even the cement is relatively soft (Dvorkin et al., 1994). This zone is called the transition zone (Fig. 3.3). In the uplifted basin the chemical compaction will continue as long as the temperature below 70-80^0 C but the rate is lower because of the lowering of temperature due to upliftment (Bjørlykke and Jahren, 2010) (Fig. 3.3).

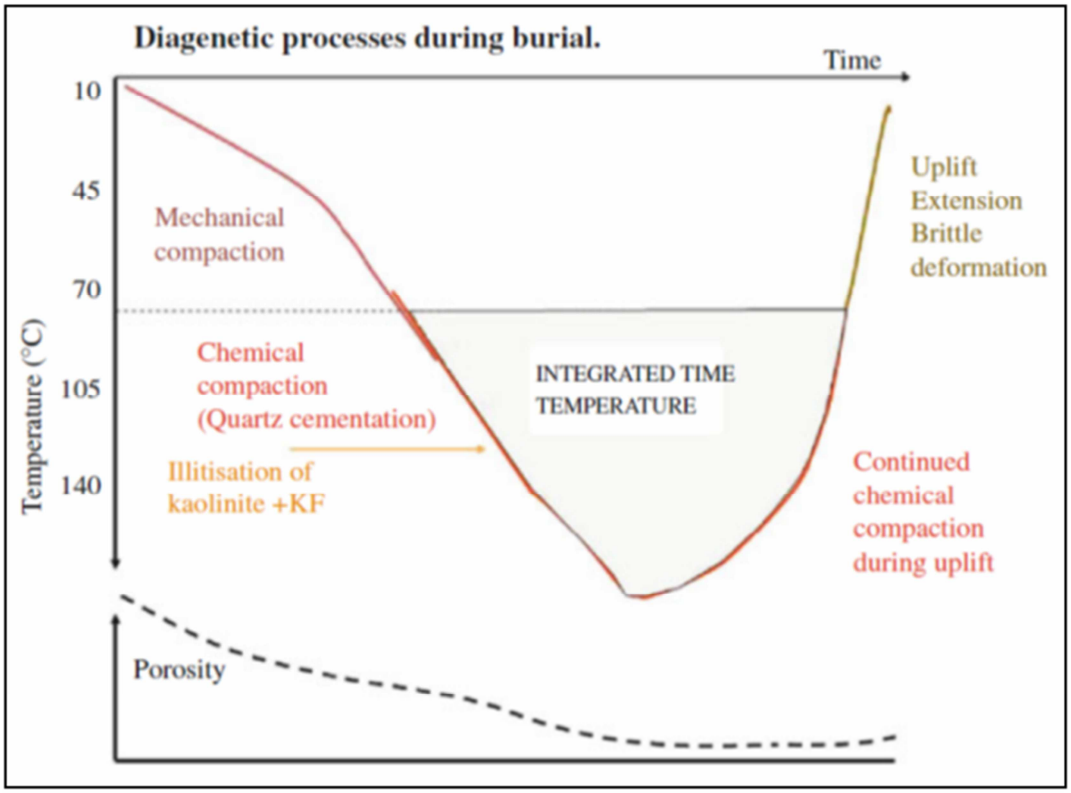

Fig. 3.3: Diagenetic processes mainly quartz cementation as a function of temperature and time. Note that quartz cementation will continue also during uplift as long as the temperature exceeds 70-80^{0}C (modified after Bjørlykke and Jahren, 2010)

The transition from mechanical to chemical compaction in mudstones and sandstones are different. In sandstones the transition starts from 70-80^0 C whereas in shales it does not simply occur at a specific depth or temperature, but is rather a function of the stability of the primary minerals and burial history (Bjørlykke, 1998; Peltonen et al., 2008). It depends on the mineral alteration processes from smectite to illite and /or chlorite which started from 60-70^{0}C.

Smectite + K-feldspar = Illite + Quartz…….. (3.3)

In shales another chemical reaction is the transition of kaolinite to illite which started at 120-130^0 C (Storvoll and Brevik, 2008):

K-feldspar + Kaolinite = Illite + Quartz…….. (3.4)

This precipitated quartz sometimes act as a coating of sand grains and prevent quartz cementation which preserve porosity in great depth. This micro-quartz also precipitated at low temperature (60-80^{0}C) when the pore water is supersaturated with respect to quartz through the dissolution of Opal A or Opal CT which is also coated the grain and preserved porosity (Bjørlykke and Jahren, 2010). This micro-quartz is the only possible form of quartz cement in a high silica supersaturation system, since the growth rate of quartz is very low at this low temperature (Thyberg et al., 2009). As we know different mudstone lithologies showed different mechanical compaction trends (Storvoll et al., 2005; Mondol et al., 2007; Marcussen et al., 2009; Thyberg et al., 2009), the illitization process of smectite results in the formation of smaller and stiffer crystal (micro-quartz) influenced the mudstones physical properties (Bjørlykke, 1998). This process may also reduce the permeability in mudstone which leading to create overpressure formation (Thyberg et al., 2009). In this process smectite releases significant amounts of silica (Bjørlykke, 1998; Peltonen et al., 2009; Thyberg et al., 2009) but the amount of silica released will depend on the composition of smectite present (e.g. trioctahedral or dioctrahedral) (Peltonen et al., 2009; Thyberg et al., 2009).

Another important parameter for quartz cementation is the surface area available for precipitation (Walderhaus, 1996). The coatings (Fig. 3.4) such as chlorite, illite, detrital clay, iron oxide (haematite), micro-quartz and bitumen do not give any surface for quartz precipitation or retarded quartz cementation and preserved porosity even at greater depth. Storvoll et al. (2002) concluded that in order to be the effective grain-coating some criteria must be fulfilled:

- The clay minerals must cover the grains before significant quartz cementation starts (greater than 2-3 km)
- The coating must be continuous and cover the entire grain surface
- The coating must be present on most of the grains in the sample

But the coated grain when subjected to 40-50 Mpa effective stress which caused pervasive grain crushing (Chuhan et al., 2002; Bjørlykke and Jahren, 2010) and these newly created fractures provided suitable sites for quartz nucleation (Chuhan et al., 2001).

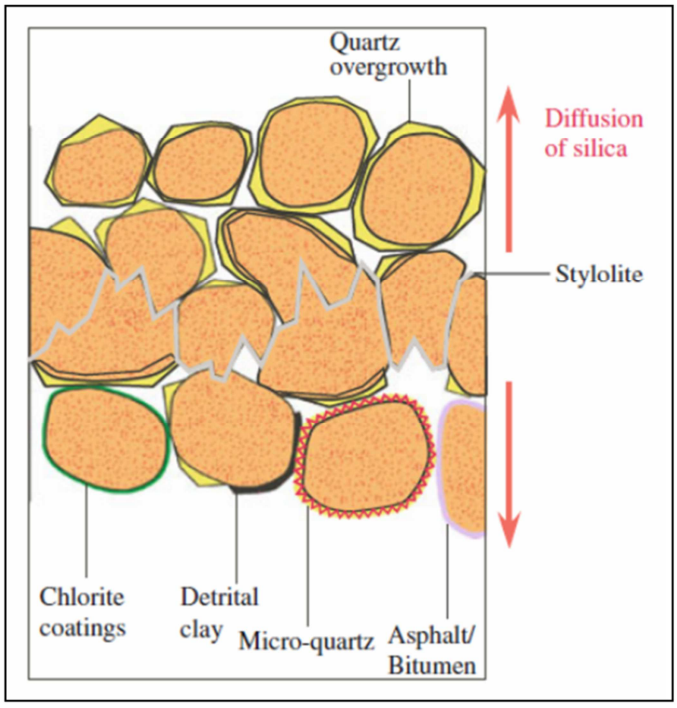

Fig. 3.4: Schematic illustration of a stylolite. The dissolved silica is transported away from the clay-rich stylolite by diffusion. This makes more long distance and advective transport of silica difficult. The rate of precipitation of quartz cement is a function of the surface area available. Grain coatings such as chlorite, illite, detrital clay, iron oxide (haematite), micro-quartz and bitumen prevent or retard quartz cementation (modified after Bjørlykke and Jahren, 2010)

The stylolites are formed at greater depth where sandstone grains are faced combined effects of mechanical and chemical compaction which form the mineral dissolution and deformation at grain contacts (Fig. 3.4) (Bjørlykke et al., 1989). The dissolved silica are transported away from the stylolite and precipitated as quartz cement which reduced porosity in sandstones. If deeply buried reservoirs are in overpressured and high porosity present due to grain coatings may compact mechanically as fluid pressure is reduced and effective stress increased during production. To stop the mechanical compaction during production phase we need to inject fluid to maintain the pore pressure and effective stress.

3.1.3 Porosity preserving mechanism

There are many factors which influence the porosity destruction during burial. These are like geothermal gradient, mineralogy and texture of the sand, pore fluid chemistry and pressure gradient (Bjørlykke et al., 1989). There are no universally valid porosity-depth function exists because some other factors like hydrocarbon emplacement, fluid overpressure and grain coatings prevent porosity loss during burial. So the porosity depth gradient is too complicated in a basin. Selley (1978) estimated porosity gradients using Galloway's data which is equal to -12.8% and -8.5% per Km for wells with geothermal gradients equal to 35^0C/km and 25^0C/km respectively (Bjørlykke et al., 1989). In sandstone the early carbonate cementation which distributed the stress over larger contact areas may prevents porosity loses (Bjørlykke et al., 1989). According to Bloch et al. (2002), there are four major causes of anomalously high porosity in sandstones in a greater depth are as follows:

a) Grain coats and grain rims (effective only in detrital-quartz-rich sandstones)
b) Early emplacement of hydrocarbons

c) Shallow development of fluid overpressure, and
d) Secondary porosity.

Grain coats are the result of authigenic processes in which clay and microcrystalline quartz coated the framework grain and prevent the outward growth, except at points of grain to grain contact (Bloch et al., 2002). The grains are coated by Chlorite, Micro-quartz, Clay Rims, Iron Oxide and Carbonate Specks. The early hydrocarbon emplacement conventionally reduces the quartz cementation rate (Barclay and Worden, 2000) and also preserves the porosity at greater depth. On the other hand, the development of fluid overpressure decreases the effective stress which also influences the porosity preservation. Because of coated grains the mechanical compaction may observe at greater depth that generates fractures and secondary porosity.

3.2 Rock Physics

Rock physics deals with the effective physical properties of the earth materials such as density, P- and S-wave velocities of the earth (Poisson's ratio can be derived from P-wave and S-wave velocity) and infer the lithology and fluid content from these parameters. The problem is in the earth model how to determine these three parameters unambiguously and how to infer lithology from these physical parameters. The earth sometime does not follow the physical processes which are the big challenges during rock physical analysis. The empirical relations among these parameters are helped to determine the relative values. Some of these empirical relations are discussed below:

3.2.1 Relationship between P- and S-wave velocities

Because of the limitation of the Biot-Gassmann model which falls down when applied to small grained clastic rocks such as mudstones, Castagna et al. (1985) derived a much simpler empirical relationship between P-wave and S-wave velocity called the mudrock line:

$$V_P = 1.16V_S + 1.36 \text{…….. (3.5)}$$

Based on laboratory ultrasonic data, Han (1986) gave another empirical relation:

$$V_S = 0.794V_p - 0.787, \text{ where velocity is in km/s …….. (3.6)}$$

Krief et al. (1990) proposed an excellent linear fit equation using square of two velocities, the equation is:

$$V_P{}^2 = aV_S{}^2 + b \text{…… (3.7)}$$

where V_p and V_s are measured in km/s and the constant a and b are determined by Krief et al. (1990) can be summarized as:

Table 3.1: The values of constant a and b in different fluid situation

Lithology	a	b
Sandstone (wet)	2.213	3.857
Sandstone (gas)	2.282	0.902
Sandstone (shaly)	2.033	4.894
Limestone	2.872	2.755

Castagna et al. (1993) gave another least square linear fit relation between P- and S-wave velocities that commonly used to estimate Vs from Vp:

$$V_S = 0.804V_p + 0.856 \text{…….. (3.8)}$$

3.2.2 Relationship between velocity and porosity

Wyllie et al. (1956) velocity and porosity relation depend on some parameters like:

- The sedimentary rocks have relatively uniform mineralogy
- They are fluid saturated
- They are at high effective pressure.

The expression is

$$\frac{1}{V_P} = \frac{\emptyset}{V_{P-fl}} + \frac{(1-\emptyset)}{V_{P-O}} \text{……. (3.9)}$$

Where V_P, $V_{P\text{-}0}$ and $V_{P\text{-}fl}$ are the P-wave velocities of the saturated rocks, of the mineral material making up the rocks and of the pore fluids respectively. The interpretation of the equation is that the total transit time is the sum of the transit time in the mineral plus the transit time in the pore fluid. Hence it is often called the time-average equation.

Raymer et al. (1980) suggested improvements to Wyllie's empirical velocity-to-travel time relations as follows:

$$V = (1-\emptyset)^2 V_O + \emptyset V_{fl}, \qquad \emptyset < 37\% \text{..... (3.10)}$$

$$\frac{1}{\rho V_P} = \frac{\emptyset}{\rho_{fl} V_{fl}^2} + \frac{(1-\emptyset)}{\rho_O V_O^2}, \qquad \emptyset > 47\% \text{..... (3.11)}$$

Where V, V_{fl} and V_0 are the velocities in the rock, the pore fluid and the minerals respectively. The term ρ, ρ_{fl} and ρ_0 are the densities of the rock, the pore fluid and the minerals respectively. Figure 3.5 compares the predictions of Raymer et al. (1980), Wyllie et al. (1956) and Gardner et al. (1974) for velocity versus porosity to data for water-saturated clay-free sandstones. None of the equations adequately models the uncemented sands.

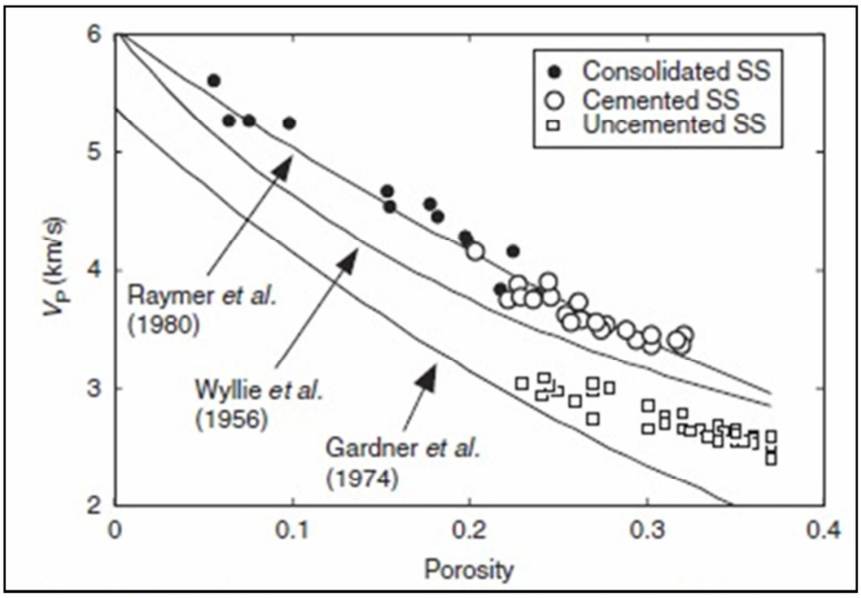

Fig. 3.5: Velocity versus porosity in water-saturated clay-free sandstones (Source: Mavko et al., 2009).

3.2.3 Relationship between velocity, porosity and clay

Han (1986) suggested a series of empirical equations by relating ultrasonic velocities to porosity and clay content. The regressions are shown in the Figure 3.6.

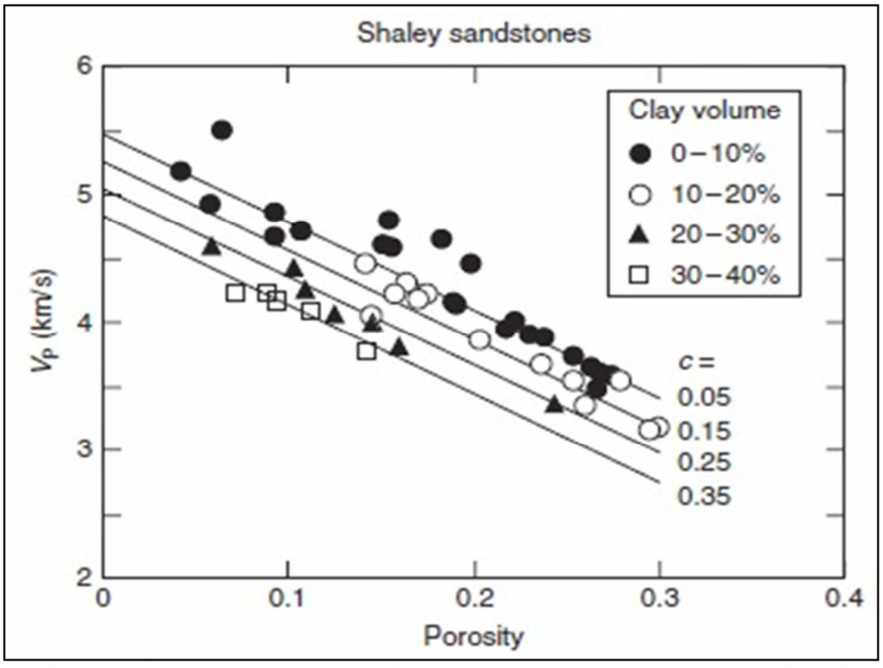

Fig. 3.6: Han's water-saturated ultrasonic velocity data at 40 MPa compared with his empirical relations evaluated at four different clay fractions (modified after Mavko et al., 2009).

3.2.4 Effective elastic media: bounds and sand models

To predict effective elastic moduli of a mixture of grains and pores theoretically we need to specify:

- The volume fractions of the various phases
- The elastic moduli of the various phases, and
- The geometric details of how the phases are arranged relative to each other

We can predict upper and lower bounds for specify the volume fractions and the constituent moduli. At any given volume fraction of constituents the effective modulus will fall between the bounds but its precise value depends on the geometric details. The stiffer shapes cause the value to be higher whereas the softer shapes cause the value to be lower.

3.2.4.1 Hashin-Shtrikman-Walpole bounds

The best bounds for an isotropic linear elastic composite given by Hashin-Shtrikman (1963) which giving the narrowest possible range without specifying anything about the geometries of the constituents. When there are only two constituents, the bounds are written as:

$$K^{HS\pm} = K_1 + \frac{f_2}{(K_2 - K_1)^{-1} + f_1\left(K_1 + \frac{4}{3}\mu_1\right)^{-1}} \quad \text{..... (3.12)}$$

$$\mu^{HS\pm} = \mu_1 + \frac{f_2}{(\mu_2 - \mu_1)^{-1} + 2f_1(K_1 + 2\mu_1) / \left[5\mu_1\left(K_1 + \frac{4}{3}\mu_1\right)\right]} \quad \text{..... (3.13)}$$

where K_1 and K_2 are the bulk moduli of individual phases; μ_1 and μ_2 are the shear moduli of individual phases; and f_1 and f_2 are the volume fractions of individual phases. When the stiffer material is termed 1 then the expressions yield the upper bound whereas the lower bound when the softer material is termed 1.

Walpole (1966) slightly modified the Hashin-Shtrikman bound which is called Hashin-Shtrikman-Walpole bounds, can be written as:

$$K^{HS\pm} = K_1 + \frac{f_2}{(K_2 - K_1)^{-1} + f_1\left(K_1 + \frac{4}{3}\mu_m\right)^{-1}} \quad \text{..... (3.14)}$$

$$\mu^{HS\pm} = \mu_1 + \frac{f_2}{(\mu_2 - \mu_1)^{-1} + f_1\left[\mu_1 + \frac{\mu_m}{6}\left(\frac{9K_m + 8\mu_m}{K_m + 2\mu_m}\right)\right]^{-1}} \quad \text{..... (3.15)}$$

Where the subscripts 1 and 2 again refer to the properties of the two components. Theses equations yield the upper bound when K_m and μ_m are the maximum bulk and shear moduli of the individual constituents and the lower bound when k_m and μ_m are the minimum bulk and shear moduli of the constituents. Figure 3.7 showing the physical interpretation of the Hashin-Shtrikman bounds for bulk modulus of a two-phase material.

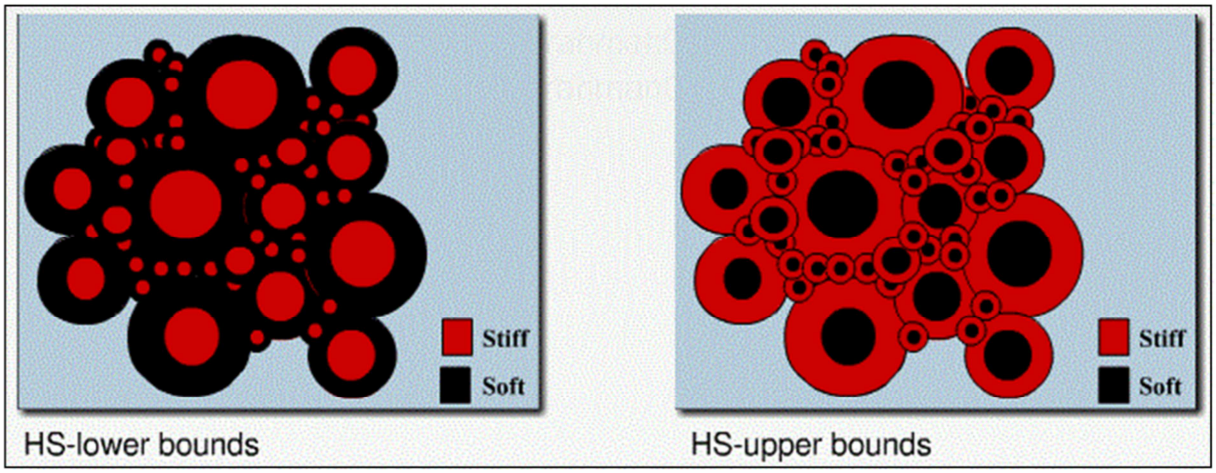

Fig. 3.7: Physical representation of Hashin-Shtrikman bound for two-phase material (modified after Gelius and Johansen, 2010).

3.2.4.2 The friable sand model

Dvorkin and Nur (1996) introduced the friable sand model or the unconsolidated line which described the velocity-porosity relation changes with sorting. This model describes how the well sorted end member modified with additional smaller grains filled the pore space.

The elastic moduli of the dry well sorted end member at critical porosity are given by Hertz-Mindlin theory (Mindlin, 1949) as follows:

$$K_{HM} = \left[\frac{n^2(1-\emptyset_c)^2\mu^2}{18\pi^2(1-\vartheta)^2}P\right]^{\frac{1}{3}} \ldots\ldots\ldots\ldots\ldots \text{(3.16)}$$

$$\mu_{HM} = \frac{5-4\vartheta}{5(2-\vartheta)}\left[\frac{3n^2(1-\emptyset_c)^2\mu^2}{2\pi^2(1-\vartheta)^2}P\right]^{\frac{1}{3}} \ldots\ldots\ldots \text{(3.17)}$$

Where K_{HM} and μ_{HM} are the dry rock bulk and shear moduli, respectively, at critical porosity Φ_C (i.e., depositional porosity); P is the effective pressure; μ and υ are the shear modulus and Poisson's ratio of the solid phase; n is the coordination number (the average number of contacts per grain). The Poisson's ratio can be expressed in terms of the bulk (K) and shear (μ) moduli as follows:

$$\vartheta = \frac{3k-2\mu}{2(3k+\mu)} \ldots\ldots\ldots\ldots\ldots\ldots\ldots \text{(3.18)}$$

Effective pressure versus depth is obtained with the following formula:

$$P = g\int_0^Z(\rho_b - \rho_{fl})dz \ldots\ldots\ldots \text{(3.19)}$$

Where, g is the gravity constant and ρ_b and ρ_{fl} are the bulk density and the fluid density, respectively at a given depth Z. The coordination number (n) depends on porosity as shown by Murphy (1982). The relationship between coordination number and porosity can be approximated by the following empirical equation:

$$n = 20 - 34\emptyset + 14\emptyset^2 \ldots\ldots\ldots\ldots\ldots \text{(3.20)}$$

Hence, for a porosity Φ = 0.4, n = 8.6. The other end point in this model is at zero porosity and has the mineral bulk and shear modulus.

3.2.4.3 The contact-cement model

The contact-cement model assumes that porosity reduces from the initial porosity of a sand pack because of the uniform deposition of cement layers on the surface of the grains (Fig. 3.8). It dramatically increases the stiffness of the sand. Dvorkin et al. (1994) gave the mathematical solutions are as follow:

$$K_{dry} = \frac{n(1-\emptyset_c)M_c S_n}{6} \quad \text{..... (3.21)}$$

$$\mu_{dry} = \frac{3K_{dry}}{5} + \frac{3n(1-\emptyset_c)\mu_c S_\tau}{20} \quad \text{..... (3.22)}$$

Where Φ_c is critical porosity; K_s and μ_s are the bulk and shear moduli of the grain material, respectively; K_c and μ_c are the bulk and shear moduli of the cement material respectively; $M_c = K_c + 4/3\ \mu_c$ is the compressional modulus of the cement; and n is the coordination number, defined as average number of contacts per grain.

3.2.4.4 The constant-cement model

Avseth et al. (2000) proposed constant-cement model where they assume that sands of varying sorting (and therefore varying porosity) all have the same amount of contact cement (Fig. 3.8). This model is a combination of contact-cement model and the expression is:

$$K_{dry} = \left[\frac{\emptyset/\emptyset_b}{K_b+(4/3)\mu_b} + \frac{1-\emptyset/\emptyset_b}{K+(4/3)\mu_b}\right]^{-1} - \frac{4}{3}\mu_b \quad \text{..... (3.23)}$$

$$\mu_{dry} = \left[\frac{\emptyset/\emptyset_b}{\mu_b+z} + \frac{1-\emptyset/\emptyset_b}{\mu+z}\right]^{-1} - z \quad \text{..... (3.24)}$$

$$z = \frac{\mu_b}{6}\left(\frac{9K_b+8\mu_b}{K_b+2\mu_b}\right) \quad \text{..... (3.25)}$$

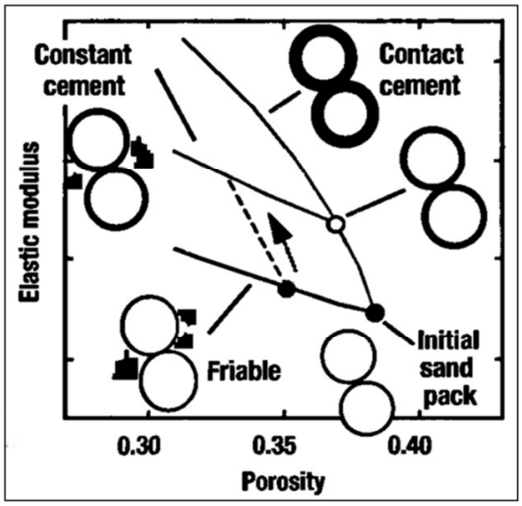

Fig. 3.8: Schematic depiction of the three-cement model (modified after Avseth et al., 2005)

3.3 Theory behind AVO

3.3.1 Gassmann fluid substitution theory

The Gassmann fluid substitution theory solves the problem related to the seismic velocities in rocks saturated with one fluid to predict those of rocks saturated with another fluid. The low frequency Gassmann-Biot (Gassmann, 1951; Biot, 1956) theory predicts the resulting increase in effective bulk modulus, K_{sat} of the saturated rock using the following equations:

$$\frac{K_{sat}}{K_0 - K_{sat}} = \frac{K_{dry}}{K_0 - K_{dry}} + \frac{K_{fl}}{\emptyset(K_0 - K_{fl})} \quad \ldots\ldots\ldots\ldots \quad (3.26)$$

$$\mu_{sat} = \mu_{dry} \quad \ldots\ldots\ldots\ldots\ldots\ldots\ldots\ldots\ldots\ldots \quad (3.27)$$

Where K_{dry} is the effective bulk modulus of dry rock, K_{sat} is the effective bulk modulus of the rock with pore fluid, K_0 is the bulk modulus of mineral material making up rock, K_{fl} is the effective bulk modulus of pore fluid, Φ is the porosity, μ_{dry} is the effective shear modulus and μ_{sat} is the effective shear modulus of rock with pore fluid.

Gassmann's equation assumes a homogeneous mineral modulus and statistical isotropy of the pore space but is free of assumptions about the pore geometry. The basic assumptions about the porous fluid-filled rock are:

- All pores are connected (i.e. open porosity)
- All grains have the same physical properties (effective mineral grains)
- The pore fluid is homogenous and fully saturates the pore volume (effective fluid)
- Valid only for low frequencies

The one most common problem during using the Gassmann's relations to predict saturated rock moduli from dry-rock moduli or vice versa is that to predict the change that result when one fluid is replaced with another. We can solve this problem simply use this equation twice like from initial to dry state and from dry state to any new fluid saturated state. We can algebraically eliminate the dry-rock moduli from the equation and relate the saturated-rock moduli Ksat1 and Ksat2 in terms of the two fluid bulk moduli K_{fl1} and K_{fl2} as follows (Mavko et al., 2009):

$$\frac{K_{sat1}}{K_0 - K_{sat1}} - \frac{K_{fl1}}{\emptyset(K_0 - K_{fl1})} = \frac{K_{sat2}}{K_0 - K_{sat2}} - \frac{K_{fl2}}{\emptyset(K_0 - K_{fl2})} \quad \ldots\ldots\ldots\ldots \quad (3.28)$$

3.3.2 Synthetic Seismogram

Synthetic seismogram is an output of a seismic forward model. We consider the earth model as an input and after processing it we get seismic traces which we called synthetic seismogram. In order to model the effective rock parameters from given petrophysical logs, a synthetic seismogram can then be generated. This synthetic seismogram can then be compare to real seismic data. The main input required to generate a synthetic seismogram are the density and sonic velocity and an assigned wavelet. A wavelet is a kind of mathematical function used to divide a given function into different frequency components and study each component with a resolution that matches its scale. The acoustic impedance (Z) of a medium is given by a product of the density (ρ) and sonic velocity (V) of that medium.

$$z = \rho V \quad \ldots\ldots\ldots\ldots\ldots\ldots\ldots\ldots\ldots\ldots \quad (3.29)$$

The impedance contrast across an interface is responsible for the wave reflection phenomena. This is called the reflection coefficient or reflectivity series (R) which is given by:

$$R = \frac{\rho_2 V_2 - \rho_1 V_1}{\rho_2 V_2 + \rho_1 V_1} = \frac{Z_2 - Z_1}{Z_2 + Z_1} \quad \ldots\ldots\ldots\ldots\ldots\ldots \quad (3.30)$$

Where:

R = reflectivity series,
ρ = density,
V = sonic velocity
Z = acoustic impedance

The magnitude of the reflection coefficient (R) depends on the contrast in acoustic impedance and the range is -1 to +1. The earth's reflectivity series can be described as a time series of spikes, each of which actually represents a zero offset plane wave reflection coefficient (Fig. 3.9). The seismic trace is simply the convolution of the earth's reflectivity with a seismic source function with the addition of a noise component. The equation is:

$$s(t) = w(t) * r(t) + n(t) \quad \ldots\ldots\ldots\ldots \quad (3.31)$$

Where, s(t) is the seismic trace, w(t) is a seismic wavelet, r(t) is the earth reflectivity and n(t) is the noise. A seismic trace is a time measurement corresponding to a given source-receiver pair. The distance between any source-receiver pair is referred to as offset.

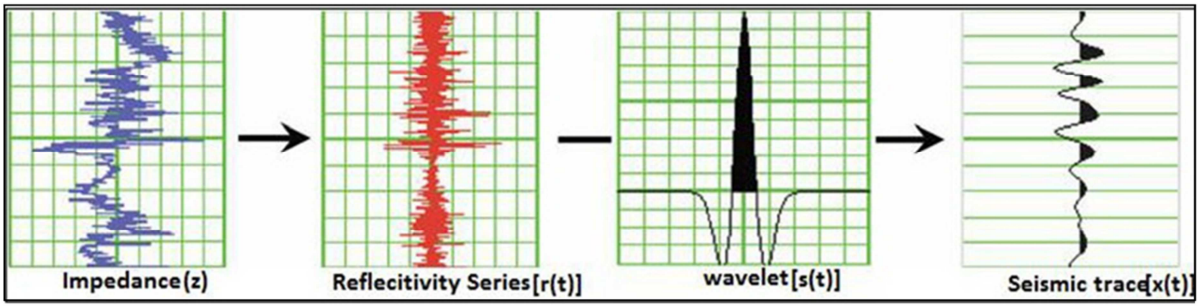

Fig. 3.9: Seismic trace is a result of convolution of a wavelet and the reflectivity series plus noise (modified after Mondol, 2010)

Some assumptions in the convolutional trace model include:

- No variation of the source pulses(t) with depth i.e stationary source pulse
- No noise contribution present
- Normal incident plane waves through a simple horizontal stratigraphically layered earth model

3.3.3 Angle dependent reflection coefficient

In a normal incidence P-wave generates only one reflected wave and one transmitted wave. But for a non-normal incidence the situation is more complicated. An incident P-wave generates reflected P- and S-waves and transmitted P- and S-waves (Fig. 3.10). The reflection

and transmission coefficients depend on the angle of incident as well as on the material properties of the two layers.
The angles of the incident, reflected and transmitted rays (Fig. 3.10) are related by Snell's law as follows:

$$p = \frac{\sin\theta_1}{V_{P1}} = \frac{\sin\theta_2}{V_{P2}} = \frac{\sin\theta_{S1}}{V_{S1}} = \frac{\sin\theta_{S2}}{V_{S2}} \quad \ldots\ldots\ldots\ldots\ldots\ldots\ldots\ldots \quad (3.32)$$

Where p is the ray parameter. θ and θ_S are the angles of P- and S-wave propagation, respectively relative to the reflector normal. Subscripts 1 and 2 indicate angles or material properties of layer 1 and 2, respectively.

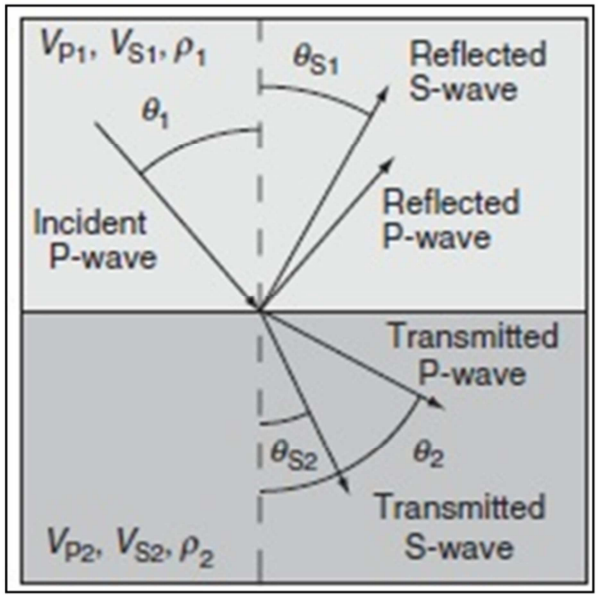

Fig. 3.10: The angles of the incident, reflected and transmitted rays of a P-wave with non-normal incidence (modified after mavko et al., 2009)

The P-P reflection coefficient is given by the Zoeppritz equations:

$$R_{pp} = \frac{\left[\left(b\frac{\cos\theta_1}{V_{p1}} - c\frac{\cos\theta_2}{V_{p2}}\right)F - \left(a + d\frac{\cos\theta_1}{V_{p1}}\frac{\cos\emptyset_2}{V_{s2}}\right)Hp^2\right]}{D} \quad \ldots\ldots \quad (3.33)$$

where

$$a = \rho_2(1 - 2V_{s2}^2p^2) - \rho_1(1 - 2V_{s1}^2p^2),$$
$$b = \rho_2(1 - 2V_{s2}^2p^2) + 2\rho_1V_{s1}^2p^2,$$
$$c = \rho_1(1 - 2V_{s1}^2p^2) + 2\rho_2V_{s2}^2p^2,$$
$$d = 2(\rho_2V_{s2}^2 - \rho_1V_{s1}^2),$$
$$D = EF + GHp^2,$$
$$E = b\frac{\cos\theta_1}{V_{p1}} + c\frac{\cos\theta_2}{V_{p2}},$$
$$F = b\frac{\cos\emptyset_1}{V_{s1}} + c\frac{\cos\emptyset_2}{V_{s2}},$$
$$G = a - d\frac{\cos\theta_1}{V_{p1}}\frac{\cos\emptyset_2}{V_{s2}},$$
$$H = a - d\frac{\cos\theta_2}{V_{p2}}\frac{\cos\emptyset_1}{V_{s1}}.$$

This is a very complicated expressions but no simple physical insight is provided by this exact formula. For AVO we need more simplified expressions of the P_P reflection coefficient which have a simple physical interpretation.

Aki and Richard's (1980) approximation is based on the first order linearized analysis. The expression is:

$$R_p = \frac{V_{p2}\rho_2 - V_{p1}\rho_1}{V_{p2}\rho_2 + V_{p1}\rho_1} \cong$$

$$\frac{(V_p + \Delta V_p/2)(\rho + \Delta\rho/2) - (V_p - \Delta V_p/2)(\rho - \Delta\rho/2)}{(V_p + \Delta V_p/2)(\rho + \Delta\rho/2) + (V_p - \Delta V_p/2)(\rho - \Delta\rho/2)} \cong$$

$$\frac{(\Delta V_p\rho + V_p\Delta\rho)}{2V_p\rho + \Delta V_p\Delta\rho/2} \cong \frac{1}{2}\left[\frac{\Delta V_p}{V_p} + \frac{\Delta\rho}{\rho}\right] \text{ …….. (3.34)}$$

Now the P-P reflection coefficient can be approximated as:

$$R_{pp}(\theta) = \frac{1}{2}\left[\frac{\Delta V_p}{V_p} + \frac{\Delta\rho}{\rho}\right] - 2\left(\frac{V_s}{V_p}\right)^2\left[2\frac{\Delta V_s}{V_s} + \frac{\Delta\rho}{\rho}\right]sin^2\theta + \frac{1}{2}\frac{\Delta V_p}{V_p}tan^2\theta \text{ ……. (3.35)}$$

Assuming small angles ($\tan\theta \approx \sin\theta$) and $V_p/V_s = 2$, this equation can be further simplified (Wiggens or Gelfand's approximation):

$$R_{pp}(\theta) = R_p + Gsin^2\theta \text{ ……..……..…….. (3.36)}$$

where

$$G = R_p + 2R_s \text{ …… (3.37)}$$

and R_p and R_s are the zero-offset reflection coefficients for P- and S-waves, respectively (linear analysis):

$$R_p = \frac{1}{2}\left[\frac{\Delta V_p}{V_p} + \frac{\Delta\rho}{\rho}\right] \text{ ……..…… (3.38)}$$

and

$$R_s = \frac{1}{2}\left[\frac{\Delta V_s}{V_s} + \frac{\Delta\rho}{\rho}\right] \text{ ……..……. (3.39)}$$

This Rp called AVO intercept and G is called AVO gradient. Poisson's ratio √ is related to the V_p/V_s ratio through the expression

$$\vartheta = \frac{\frac{1}{2}\left(\frac{V_p}{V_s}\right)^2 - 1}{\left(\frac{V_p}{V_s}\right)^2 - 1} \text{ ……..…… (3.40)}$$

Differentiation of this relationship gives

$$\Delta\vartheta = \frac{\left(\frac{V_p}{V_s}\right)^2\left(1 - 2\vartheta\left[\frac{\Delta V_p}{V_p} - \frac{\Delta V_s}{V_s}\right]\right)}{\left[\left(\frac{V_p}{V_s}\right)^2 - 1\right]} \text{ …….. (3.41)}$$

Finally, by setting Vp/Vs = 2 and consequently √ = 1/3, we obtain

$$\Delta\vartheta = \left(R_p + G\right)\frac{4}{9} \quad \text{..... (3.42), which is Shuey's (1985) approximation.}$$

Hence from an estimate of Rp and G the change in Poisson's ratio can be estimated.

Smith and Gidlow (1987) approximation based on Gardner's equation which is related to density and P-wave velocity:

$$\rho = aV_p^{1/4} \quad \text{..... (3.43)}$$

Which can be differentiated to give $\frac{\Delta\rho}{\rho} = \frac{1}{4}\frac{\Delta V_p}{V_p}$ ..... (3.44)

Finally, substituting this equation into the Aki-Richard's equation gives the final result:

$$R_{pp}(\theta) = \left[\frac{5}{8}\frac{1}{2}\left(\frac{V_s}{V_p}\right)^2 sin^2\theta + tan^2\theta\right]\frac{\Delta V_p}{V_p} - \left[4\left(\frac{V_s}{V_p}\right)^2 sin^2\theta\right]\frac{\Delta V_s}{V_s} \quad \text{..... (3.45)}$$

3.3.4 Classification of reservoir sands based on AVO

Based on impedance and AVO-characteristics Rutherford and Williams (1989), classify three different gas sands.

- Class 1: high-impedance sands
- Class 2: near-zero impedance contrast sands, and
- Class 3: low-impedance sands

Based on the amplitude variation class 3 sand has another classification called class 4 (Fig. 3.11).

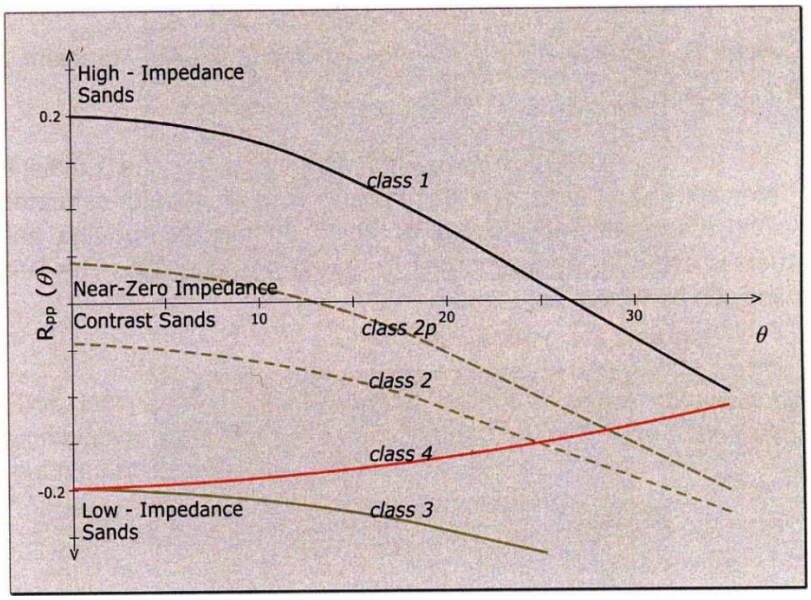

Fig. 3.11: Rutherford and Williams (1989) classification of gas sand (modified after Gelius and Johansen, 2010).

Class 1: high-impedance sand

- Impedance higher than in the surrounding medium (shale)
- Zero-offset reflection coefficient is large and positive for the interface between shale and sand
- Normally associated with areas onshore
- Mature sand that has undergone moderate to high compaction
- Reflection coefficient decreases with offset

The reflection coefficient of high-impedance sand is positive at zero offset and initially decreases in magnitude with offset. The rate of the change of magnitude is higher in class1 sand than class 2 and 3 sand (Rutherford and Williams, 1989). It also changes the polarity if adequate angle/offset is available.

Class 2: near-zero impedance contrast sand

- Impedance of sand is almost identical to that of the surrounding material
- Associated with areas both offshore and onshore
- Normally moderate consolidated and moderate degree of compaction
- Large chage in reflectivity with offset
- Polarity change can exits if the reflection coefficient at zero offset is positive

The small offset/angle reflectivity of class 2 sand is close to zero and is often undetectable in the presence of noise. A polarity change occurs if reflectivity is positive but it is usually not detectable because the signal is below the noise level (Rutherford and Williams, 1989).

Class 3 and 4: low impedance sand

- Impedance of sand is lower than in the surrounding medium
- Associated with a marine environment
- The sand is unconsolidated
- Amplitude anomalies (bright spots) occur on stacked data
- The reflectivity is large for all offsets
- Relative amplitude change not so large
- No polarity change
- Class 3: amplitude increases with offset
- Class 4: amplitude decreases with offset

No polarity change occurs in class 3 sand because both reflection coefficient and gradient are negative. The class 4 sand is the only sand that's AVO-gradient is positive.

3.4 Inversion Methodology

Geophysical inversion involves mapping of the physical structure and properties of the subsurface of the earth using measurements made on the surface of the earth. It is a technique for creating a model of the earth using the seismic data as input. There are several types of seismic inversion methods are currently used in the industry. The following Figure 3.12 shows the different types of inversion techniques commonly used. This study utilizes four inversion techniques that briefly describe here.

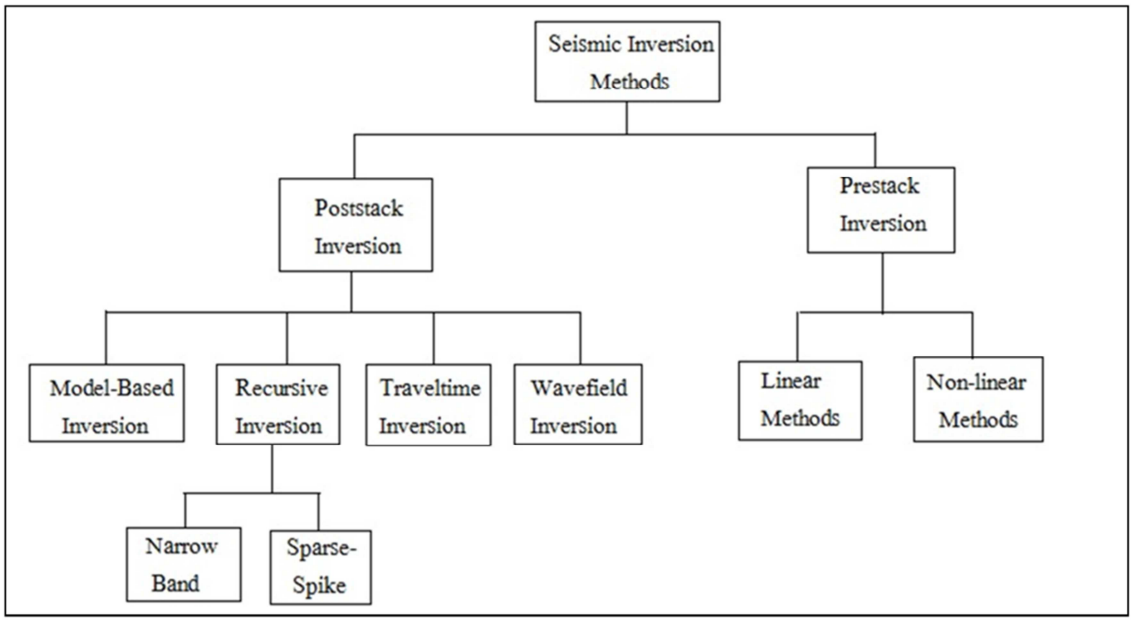

Fig. 3.12: Summary of current inversion techniques (modified after Russell, 1988).

3.4.1 Recursive Inversion

The reflectivity was defied in terms of acoustic impedance changes. The formula was:

$$r_i = \frac{\rho_{i+1}V_{i+1} - \rho_i V_i}{\rho_{i+1}V_{i+1} + \rho_i V_i} = \frac{Z_{i+1} - Z_i}{Z_{i+1} + Z_i} \quad \text{..... (3.46)}$$

Where, r=reflection coefficient, ρ=density, V=compressional velocity, Z=acoustic impedance of layer i overlies layer i+1.

If we have available true reflectivity, it is possible to recover the acoustic impedance by inverting the above formula.

$$1 + r_i = \frac{Z_{i+1} + Z_i}{Z_{i+1} + Z_i} + \frac{Z_{i+1} - Z_i}{Z_{i+1} + Z_i} = \frac{2Z_{i+1}}{Z_{i+1} + Z_i} \quad \text{..... (3.47)}$$

Also

$$1 - r_i = \frac{Z_{i+1} + Z_i}{Z_{i+1} + Z_i} - \frac{Z_{i+1} - Z_i}{Z_{i+1} + Z_i} = \frac{2Z_{i+1}}{Z_{i+1} + Z_i} \quad \text{..... (3.48)}$$

Therefore

$$\frac{Z_{i+1}}{Z_i} = \frac{1 + r_i}{1 - r_i} \quad \text{..... (3.49)}$$

$$Z_{i+1} = Z_i \left[\frac{1 + r_i}{1 - r_i}\right] \quad \text{..... (3.50)}$$

This is called the discrete recursive inversion formula and is the basis of many current inversion techniques. If we know the acoustic impedance of a particular layer and the reflection coefficient at the base of that layer, we may recover the acoustic impedance of the next layer. We need an estimation of the first layer impedance. Two serious problems have been encounter during applying in real data. These are:

- Frequency band limiting
- Noise

3.4.2 Sparse-Spike Inversion

Sparse-spike methods are more recent deconvolution techniques which assume a certain model of the reflectivity and making a wavelet estimate based on this assumption. These techniques include:

- Maximum-likelihood deconvolution and inversion.
- L1 norm deconvolution and inversion.
- Minimum entropy deconvolution (MED)

From the seismic inversion point of view, sparse-spike methods have an advantage over classical methods of deconvolution because the sparse-spike estimate with extra constraints can be used as a full bandwidth estimate of the reflectivity. Figure 3.13 shows the flow chart of sparse-spike inversion.

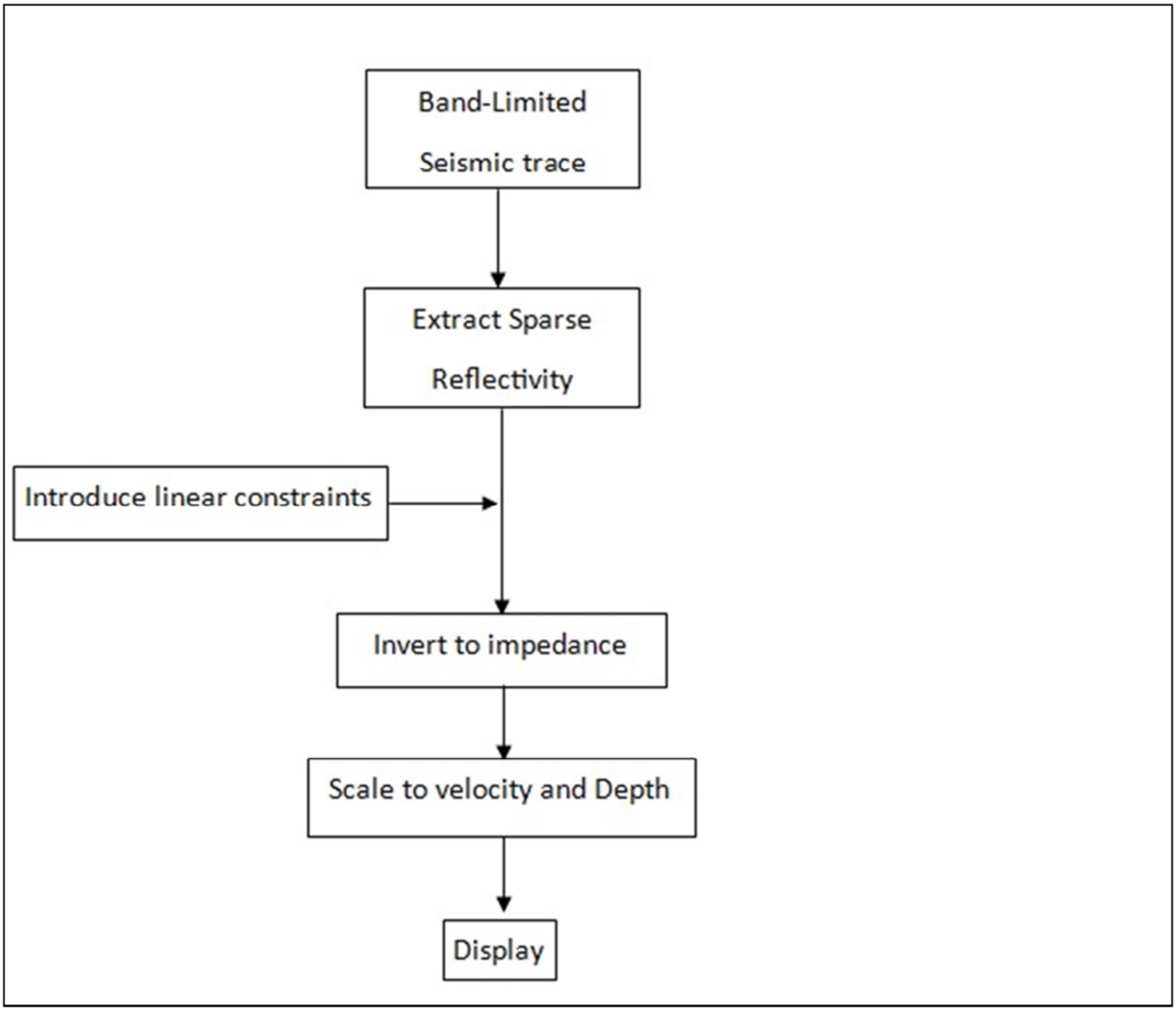

Fig. 3.13: Flow chart of sparse-spike inversion

3.4.3 Model Based Inversion

In case of model based inversion we build a geological model first and comparing the model to our seismic data. We shall than use the results of this comparison between real and modeled data to iteratively update the model in such a way as to better match the seismic data. The basic idea of this approach is shown in the Figure 3.14.

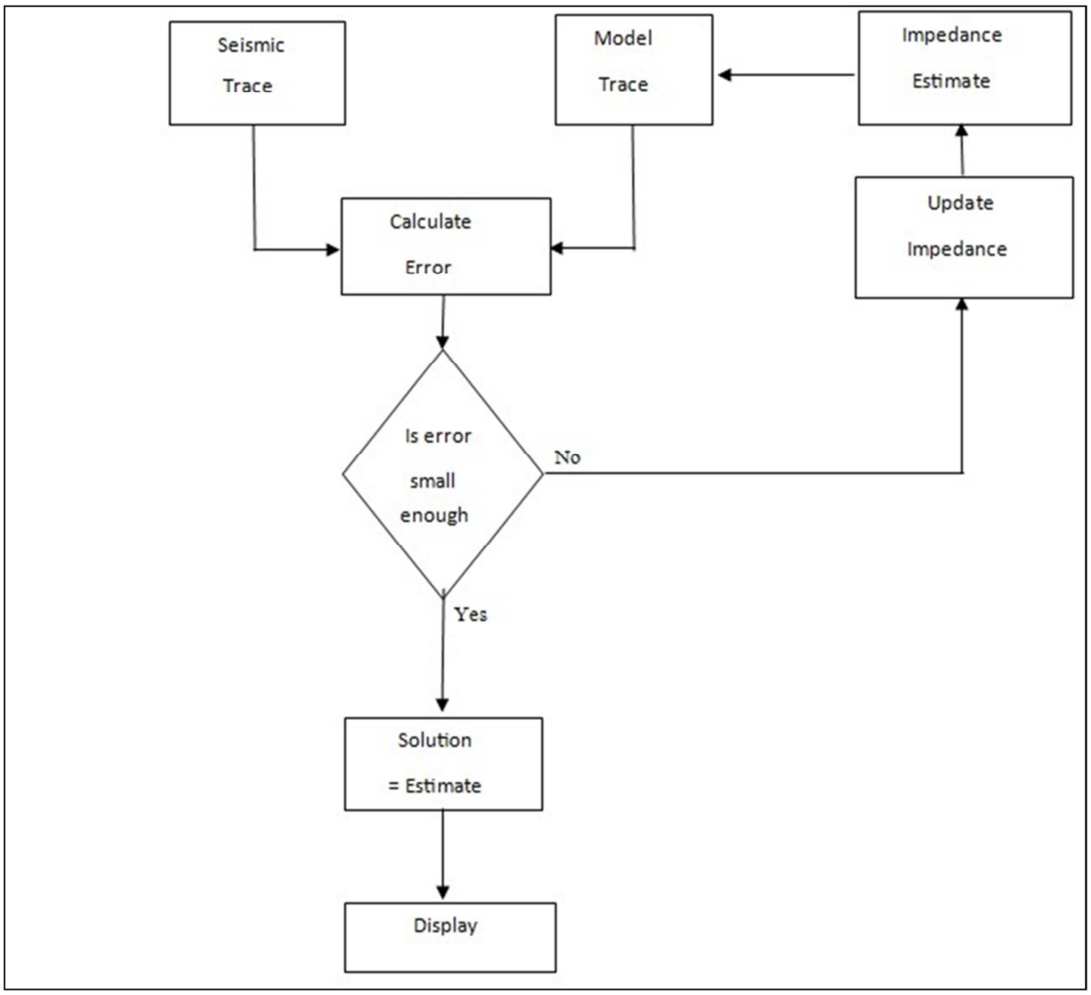

Fig. 3.14: Flowchart for the model based inversion technique.

3.4.4 Neural Network Inversion

Neural Network is a mathematical algorithm which encodes a relationship between two data sets. That relationship may be non-linear and in fact, it is not necessary to know what the relationship is to use the Neural Network. Neural Network consists of two steps. The first step is to train the network. In this step, the network is presented examples of the two types of data for which want to find a relationship. The second step is to apply the trained Neural Network to a larger volume of data on which we wish to use the relationship. During the training, the network is shown these two sets of data:

- A single composite trace at each well location, calculated by averaging along the borehole trajectory.
- The known acoustic impedance from the well at that location.

Chapter 4: Materials and Methods

UNIVERSITY OF OSLO

FACULTY OF MATHEMATICS AND NATURAL SCIENCES

Chapter 4: Materials and Methods

This research is an integrated approach of combining seismic and well logs data from Snøhvit area. Well logs are used for petrophysical analysis to identify the compaction behavior, uplift, reservoir and source rock characterization. Real and synthetic seismics are used for AVO modeling and inversion to investigate the reservoir properties of the Snøhvit field. The Table 4.1 shows the six wells included in this study with their fluid contents.

Table 4.1: Six wells with purpose, fluid contents and year of drilled.

Well Name	Year	Purpose	Content
7120/5-1	1985	Wildcat	Shows
7120/6-1	1985	Appraisal	Oil/Gas
7120/6-2S	2007	Appraisal	Oil/Gas
7121/4-1	1984	Wildcat	Oil/Gas
7121/4-2	1985	Wildcat	Gas/Condensate
7121/5-1	1985	Appraisal	Oil/Gas

All wells are wildcat and appraisal wells within which 7120/5-1 is dry well. All other wells contain hydrocarbons both oil and gas. Moreover, three 2D seismic lines have been used for seismic inversion modeling in this project. The 2D lines are: ST8817-116, ST8817-343 and ST8624-410. The seismic line with corresponding wells is shown in Table 4.2.

Table 4.2: 2D seismic line with well-tie.

Well Name	2D seismic line
7120/6-1	ST8817-343
7121/5-1	ST8817-116
7120/5-1	ST8624-410

Data interpretation and analysis has been carried out using different softwares like Petrel, Interactive Petrophysics (IP) Hampsson Russell (HR), Surfer and Microsoft Office Excel. Petrophysical analyses is carried out using Petrel, IP, surfer and Microsoft Office Excel softwares. Petrel is used for well correlations and seismic horizon interpretation whereas IP and Excel are used mostly for identifying the transition zone from mechanical to chemical compaction, exhumation study and analysis of mixed lithology (sand-shale mixtures). Surfer is used for contouring.

Most of the AVO and seismic inversion works carried out by using Hampson Russell software packages Geoview, Elog, AVO and Strata. Geoview is used for data loading and quality checking whereas new log calculation and fluid substitution models are running in Elog module. Synthetic seismic is generated and modeled in AVO module. This module is also use for single well AVO modeling and AVO analysis case study. Strata module is used in this research for seismic inversion. In addition,, few laboratory data have been used for compaction and exhumation studies.

4.1 Compaction and exhumation studies

Sediments in a sedimentary basin experienced several kinds of compactions. Upto a certain depth the compaction dominated by stress and below this level temperature take over this processes. Another trend called depositional trend is very important in compaction and rock properties evaluation study. Depositional trend is depends on the geology of the local basins and influenced the diagenetic trend. Because of changing local geology from basin to basin or formation to formation or different depositional environment within same formation, the diagenetic responses are different. Different tectonic settings also give different diagenetic trends. Overconsolidated or underconsolidated terms came from exhumation point of view due to different tectonic movement which is given different diagenetic response compare to normal consolidated rocks. The reservoir rock quality depends on diagenetic history and the source rock maturation depends on the temperature history of the basin those are the output of diagenetic trend and exhumation estimation processes.

To investigate the diagenetic trend and to estimate exhumation in the Hammerfest basin, six wells have been used in this study from the Snøhvit area. The wells are 7120/5-1, 7120/6-1, 7120/6-2S, 7121/4-1, 7121/4-2 and 7121/5-1. As we know Hammerfest basin is a clastic sedimentary basin and shales are more common than sandstones, I used mostly shale rock properties for diagenetic and exhumation studies. Therefore, the calculation of shale volume is critical for further analyses.

4.1.1 Shale volume (V_{sh}) calculations

Gamma ray has been used to calculate shale volume (V_{sh}). The first step is to calculate gamma ray index (I_{GR}) by using the following equation:

$$I_{GR} = \frac{GR_{log} - GR_{min}}{GR_{max} - GR_{min}} \quad \text{..... (4.1)}$$

Where, I_{GR} is the gamma ray index, GR_{log} is the gamma ray reading of formation, GR_{min} is the minimum gamma ray (clean sand or carbonate) and GR_{max} is the maximum gamma ray (shale) (Asquith and Krygowski, 2004). The linear relation of I_{GR} with volume of shale (V_{sh}) is the first order estimation of shale volume. The two equations (Larionov, 1969) were used in this study to calculate Vsh:

For unconsolidated rocks,

$$V_{sh} = 0.083(2^{3.7.I_{GR}} - 1) \quad \text{.....(4.2)} \quad \text{and}$$

For consolidated rocks:

$$V_{sh} = 0.33(2^{2.I_{GR}} - 1) \quad \text{..... (4.3)}$$

4.1.2 Temperature gradients

Temperature is very important in case of chemical compaction because the mineral transformation is depended on it. The temperature used in this study, calculated from bottom hole temperature (BHT). The equation for temperature gradient is:

$$m = \frac{y-c}{x} \quad \ldots\ldots\ldots\ldots\ldots\ldots\ldots\ldots\ldots\ldots\ldots\ldots \quad (4.4)$$

Where, m is the geothermal gradient, y is the bottom hole temperature (BHT), c is the mean annual surface temperature and x is the total depth. I used 4^0C as a mean annual surface temperature and get the geothermal gradients showing below in Table 4.3:

Table 4.3: Geothermal gradients of studied wells

Well Name	Total depth (m) RKB	Oldest unit	Bottom Hole Temperature (BHT)	Geothermal Gradients (^{0}C/Km)
7120/5-1	2699	Fruholmen Fm.	66	23
7120/6-1	2820	Tubåen Fm.	104	35.46
7120/6-2S	3035	Snadd Fm.	111	35.25
7121/4-1	2609	Fruholmen Fm.	88	32
7121/4-2	2799	Fruholmen Fm.	95	32.5
7121/5-1	3197	Snadd Fm.	115	34.68

4.1.3 Calculation of shear modulus (μ)

Out of six wells used in this study, only one well (7120/6-2S) has direct shear wave measurement only in reservoir zone which is below the transition zone of mechanical to chemical compaction. As we know the shear wave velocity (Vs) as well as shear modulus (μ) is very sensitive to cement, we need Vs to identify the transition zone. Using the measured Vp-Vs data from the well 7120/6-2S, I calculated a 2nd derivative equation that was used to calculate Vs for other wells (Fig. 4.1). The equation is:

$$V_s = 0.47 + 0.06V_p + 0.1V_p^2 \quad \ldots\ldots\ldots\ldots\ldots\ldots\ldots\ldots\ldots\ldots \quad (4.5)$$

Where Vp and Vs are in km/s and R^2 = 0.91. This calculated Vs values were used then to calculate μ for other wells. The following equation is used to calculate μ:

$$\mu = \rho V_s^2 \quad \ldots\ldots\ldots\ldots\ldots\ldots\ldots\ldots\ldots\ldots\ldots\ldots \quad (4.6)$$

Where μ is in GPa, ρ is kg/m^3 and V_s is m/s. These shear moduli are used to find the transition zone from mechanical to chemical compaction.

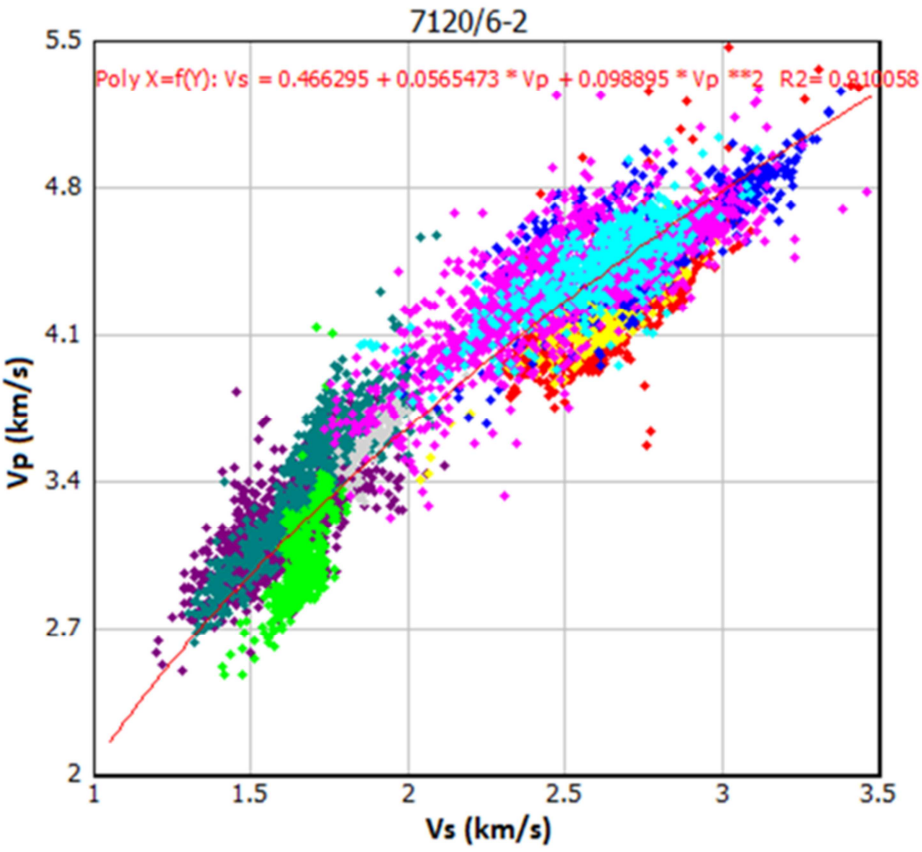

Fig. 4.1: Vp-Vs plot of all data points in the well 7120/6-2S showing the empirical equation as well as R^2 values.

4.1.4 Exhumation correction

The Barents Sea experienced several stages of uplift and erosion (Exhumation) which makes the whole area geologically complex. A correction needed for understanding the rock properties, the maximum burial depth or the maximum temperature experienced by reservoir and source rocks. These are very important in exploration perspective. A simple method used in this study to estimate the maximum burial depths. Exhumation was estimated by comparing the compaction trend observed in well logs and a well define laboratory experimental compaction curve. The experimental compaction curve is from a well characterized kaolinite-silt (50:50) mixture suggested by Mondol et al. (2009). Few simplistic approaches are employed to estimate the exhumation:

- The transition zone from mechanical to chemical compaction at present day burial depth is deciphered using rock physics crossplots.
- Volumetric shale fraction (V_{sh}) correspond to the mechanical compaction at present day burial depth is calculated across the entire area and cross-plotted as a function of depth with published kaolinite-silt (50:50) compaction trends.
- The difference along the depth (m) axis gives an estimate of the magnitude of exhumation which natural samples may have undergone in that area.

These corrected exhumations are later used to explain the diagenetic effects on rocks around Snøhvit fields.

4.2 Rock physics analysis

Rock physics makes relations between geological rock properties (e.g., porosity, mineralogy, grain configuration and different fluids) with seismic properties (e.g., elastic moduli, interval velocities, P-wave impedance and Vp/Vs ratio) (Storvoll and Brevik, 2008). Out of six wells only one well is dry and rest of wells contain hydrocarbon. Also the mineralogy and sorting of grains in studied wells vary from east to west as well as north to south because of geological setting of the Hammerfest basin (Fig. 4.2). To compare the fluid and mineralogical effect on rock physics analysis I used all six wells (marked cyan color circle in Fig. 4.2) to find out the rock physics relations.

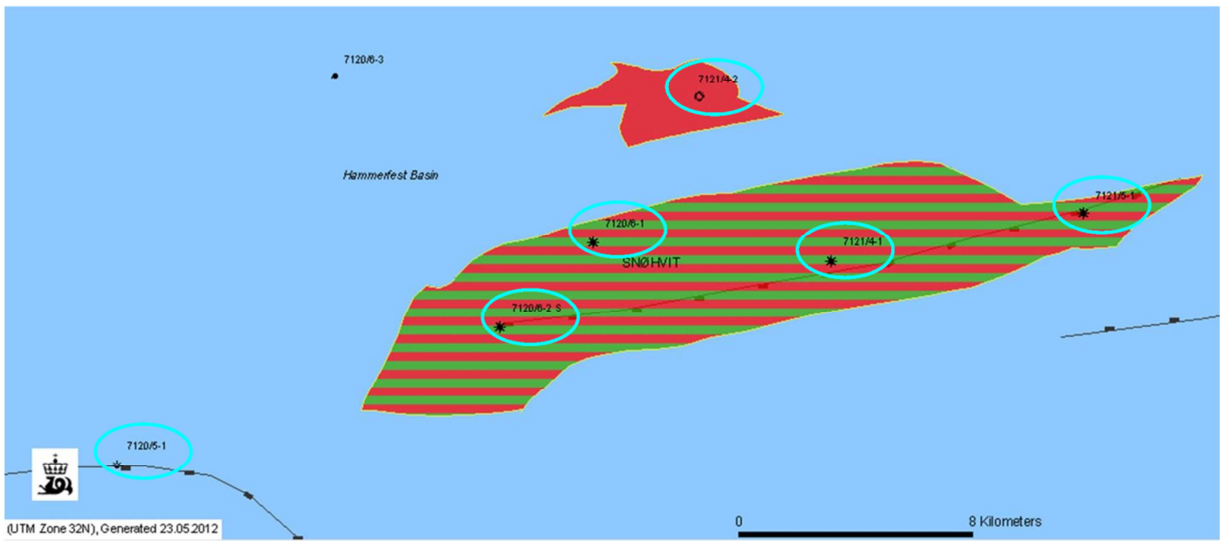

Fig. 4.2: Location of studying wells in rock physics analysis (modified after NPD).

The data from Stø formation in the well 7120/6-2S is used for rock physics analysis in the first part of the study due to availability of shear wave velocity data. Based on lithologic variations that clearly observed in the Gamma Ray Log, the Stø formation can be subdivided into three distinct litho-facies (Fig. 4.3). The top of the Stø formation is encountered at a depth 2373.807 m (TVD-RKB) which is the started depth of facies 1 till 2414.974 m (TVD-RKB) whereas depth of the facies 2 and 3 are 2415.119-2456.913 and 2457.058-2478.724 m (TVD RKB) respectively. Facies 1 has several small scale transgression-regression events which consist of shaly sandstones. On the other hand Facies 2 and 3 are more or less clean sandstones where the facies 2 is the cleanest. Within the facies 2 the velocity (both Vp and Vs) plots show two high velocity events. These two event also showed high density and low neutron porosity.

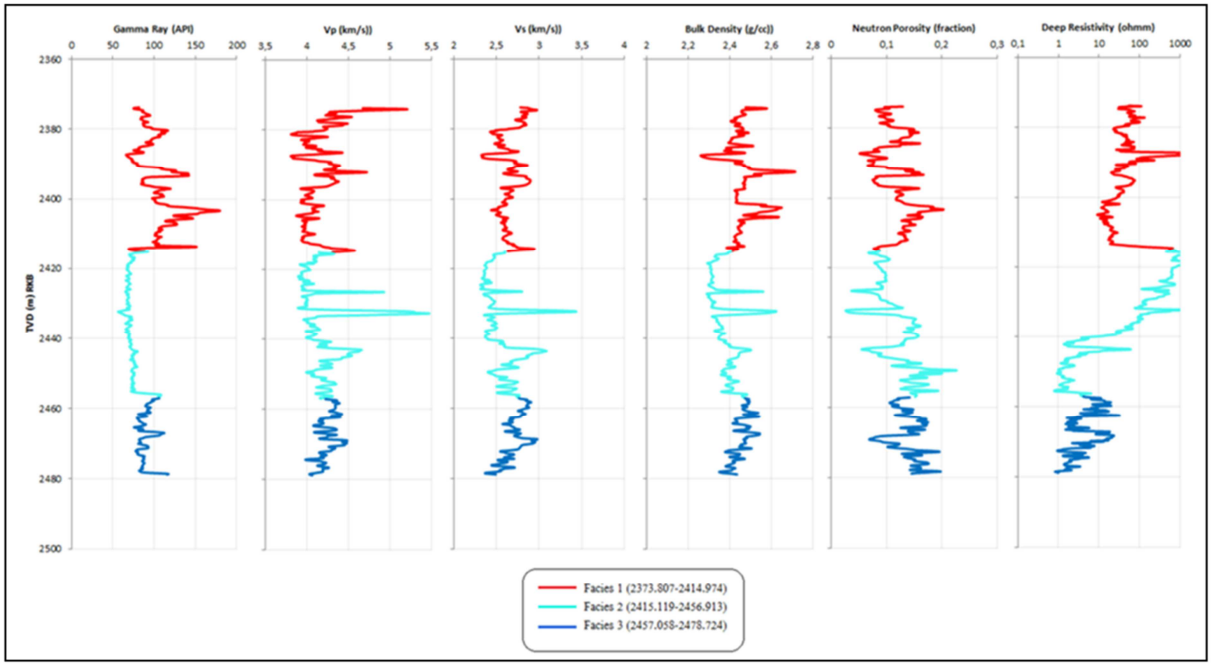

Fig. 4.3: Different logs of Stø formation in the well 7120/6-2S with three define facies using gamma ray log.

4.2.1 Porosity and density calculations

The Gardner equation (Gardner et al., 1974) is used to calculate density from Vp where density logs are missing:

$$\rho_b = 1.741 V_p^{0.25} \quad \text{..... (4.7)}$$

Where Vp is in km/s and ρ_b is in g/cc. The measured Vp in this well of Stø formation has been used for calculating density. The Wyllie time average equation has been used for comparing the measured porosity and calculated porosity. The time average equation is:

$$\frac{1}{V_p} = \frac{\emptyset}{V_{p-fl}} + \frac{1-\emptyset}{V_{p-0}} \quad \text{..... (4.8)}$$

If assumed fully water saturated quartz formation, then using Carmichael (1989) pure quartz $V_{p\text{-}0}$ (6.05 km/s) and water velocity (1.484 km/s) the relation between Vp and porosity is as follow:

$$\emptyset = \frac{1.966}{V_p} - 0.325 \quad \text{..... (4.9)}$$

The measured Vp used in this equation to calculate porosity which is later compare with measured density porosity. The density porosity is calculated from bulk density log. The equation used for this is:

$$\emptyset_{Density} = \frac{\rho_{matrix} - \rho_{bulk(\log)}}{\rho_{matrix} - \rho_{fluid}} \quad \text{..... (4.10)}$$

The matrix and fluid density is assumed as quartz and brine of densities which are 2.65 and 1.1 g/cc respectively.

4.2.1.1 Porosity correction

The neutron tool is measured mainly the amount of hydrogen atoms in the formation which is called neutron log. The main use of this log is to determine porosity of a formation. Since it is depends on hydrogen atoms, it has a relation with Hydrogen Index (HI). A relative scale of porosity and HI is if the neutron tool is in 100% water (a large tank of water), the HI is 1.00 and this is equivalent to a rock of 100% porosity saturated with water. So it has given a fixed point that when HI is 1, it represents ∅ is also 1. Also the limestone rocks with zero porosity has been 0 HI represents 0 porosity (Glover, 2005). Since HI is different in gas reservoirs compared to water, the neutron log gives a lower value than the original porosity which needs correction using the following equation:

$$\emptyset_N = \emptyset\left[1 \times S_{XO} + HI_{gas} \times (1 - S_{XO})\right] \ldots\ldots\ldots\ldots\ldots\ldots \text{(4.11)}$$

Where $\emptyset_N$ is the netron porosity, $\emptyset$ is the original porosity, S_{XO} is the saturation of mud filtrate and HI_{gas} is the hydrogen index of the gas of this formation. The S_{XO} value of gas at 15-20% porosity is 0.85 (Asquith and Krygowski, 2004), which give an equation for porosity correction is

$$\emptyset = 1.11\emptyset_N \ldots\ldots\ldots\ldots\ldots\ldots\ldots\ldots\ldots\ldots\ldots\ldots \text{(4.12)}$$

The gas corrected porosity is showing in the Figure 4.4 with the measured values of the Sn. Because of the lacking of thin section and uncertainties of density and neutron porosity for a gas reservoir, an average porosity is calculated using the following equation:

$$\emptyset_{Avg} = \sqrt{\frac{\emptyset^2_{density} + \emptyset^2_{neutron}}{2}} \ldots\ldots\ldots\ldots\ldots\ldots\ldots\ldots \text{(4.13)}$$

The Vp of Stø formation is plotted for quality checking of different porosities with Voigt upper and Reuss lower bounds (Fig. 4.5). Some data points in density plot are plotted outside the Reuss lower bound. It is not possible in physical point of view whereas the gradient of increasing Vp with decreasing porosity is more convenient in average porosity plot compare to neutron porosity plot. However average porosity showed better control than other porosity values though it has limitations. The calculated average porosity is used for rock physics analysis chapter.

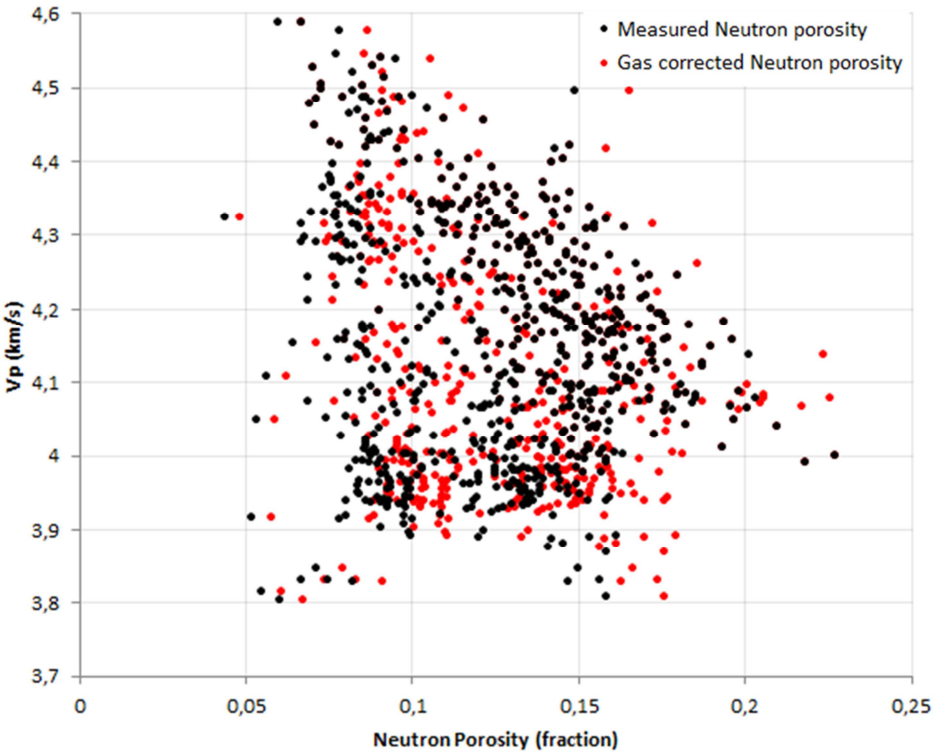

Fig. 4.4: The velocity versus neutron porosity plot showing the porosity increasing after gas effect correction in the Stø formation of the well 7120/6-2S.

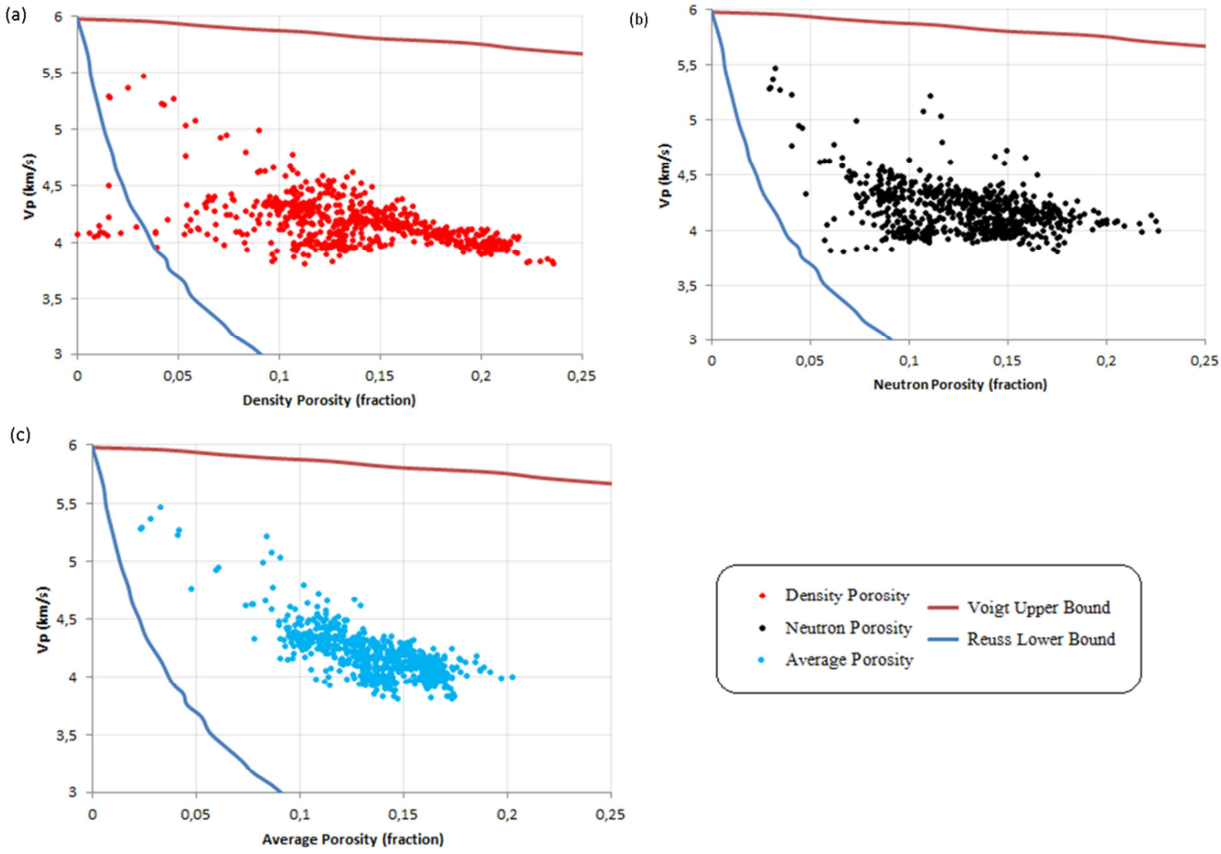

Fig. 4.5: velocity of Stø formation in the well 7120/6-2S against porosities (a) density porosity, (b) neutron porosity and (c) average porosity with Voigt and Reuss Upper and Lower bound.

4.2.2 The cement model

The following steps are used to build a friable sand model for the Hammerfest basin around the Snøhvit field:

- Estimate dry bulk and shear moduli at initial porosity (φ_c = 0.40), applying Hertz-Mindlin theory which is related with effective pressure.
- Estimate another end point as the mineral points in zero porosity, here I used the quartz bulk and shear modulus as a mineral point.
- Interpolate between the two-end members using modified Hashin-Shtrikman lower bound for different porosities moduli.
- Analyze different cross-plots to emphasize cementation effect on reservoirs: porosity versus Vp, Vs, shear modulus, bulk modulus, Poisson's ratio, acoustic impedance etc.

For mineral points Carmichael (1989) pure quartz grain velocity and modulus have been used for this model. The constant and contact cement lines have been digitized from Avseth et al. (2010) and interpolate it upto mineral points (φ_c = 0) using quartz bulk and shear modulus.

4.3 Rock Physics templates

Rock physics templates (RPTs) are charts and graphs of rock physics models which constrained by local geology, used for prediction of lithology and hydrocarbons from well logs and seismic data. These templates are basin specific and depend on local geological factors like lithology, mineralogy, burial depth, diagenesis, pressure and temperature that must be considered during generating RPTs for a given basin (Avseth et al., 2005). The most common and useful RPT is crossplot of acoustic impedance (AI) versus Vp/Vs ratio, as combination of these two elastic properties is a good lithology and fluid indicator (Avseth et al., 2005; Chi and Han, 2009) (Fig. 4.6). Other forms of RPT include the combination of shear impedance (SI) and AI, elastic impedance (EI) and AI, Lame's parameter and shear modulus (μ), etc. (Avseth et al., 2005; Boruah and Chatterjee, 2010).

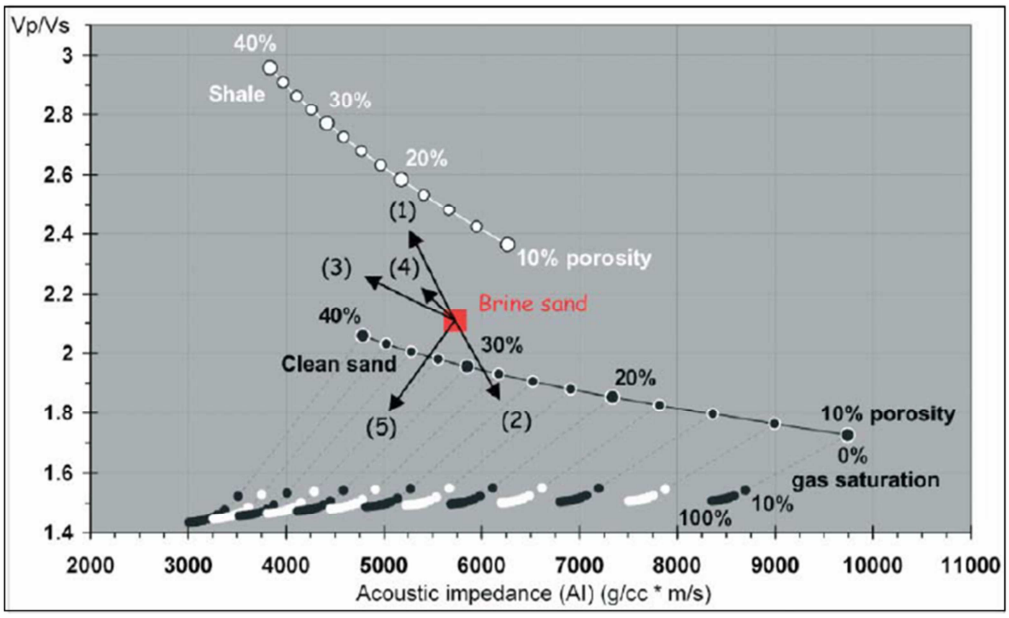

Fig. 4.6: Rock physics template in Vp/Vs versus AI cross plot (modified after Odegaard and Avseth, 2004).

Figure 4.6 includes a background shale-trend line, a brine-sand-trend line, and curves for increasing gas saturation as a function of porosity on a rock physics template in Vp/Vs versus AI cross-plot domain. The black arrows shows (conceptually) the effects of various geologic trends: 1) increasing shaliness, 2) increasing cement volume, 3) increasing porosity, 4) decreasing effective pressure, 5) increasing gas saturation. The ambiguity of interpretation is noticeable. For example, increase in shale content can be misinterpreted with decreasing in effective pressure or nature do not follow the increasing or decreasing trend exactly like these trend lines etc. The initial step in creating a template is determining the appropriate rock physics model. Theoretical rock physics models are calibrated and validated using the local rock parameters considering local geology and well log data. Well log data are analyzed to define the reservoir and source rock and evaluate reservoir properties. Then the lithology and fluid content of the rock is diagnosed by superimposing theoretical rock physics curve. It is important to map the data to a common fluid during creating templates, otherwise the effect of pore fluid and rock frame become mixed (Milovac, 2009).

The following steps are used to build a template for the Snøhvit field (Fig. 4.7):

- Estimate dry bulk and shear moduli at the initial porosity (φ_c = 40%), applying Hertz-Mindlin theory.
- Used Carmichael (1989) quartz bulk and shear modulus as a zero porosity mineral point.
- Interpolate between the two-end members using modified Hashin-Shtrikman upper bound at different porosities.
- Perform Gassmann fluid substitution to calculate effective moduli at different fluid saturations.
- From calculated moduli and density at different saturations and porosities, determine Vp and Vs which later use for analyze in different cross-plots to emphasize fluid and lithology component.

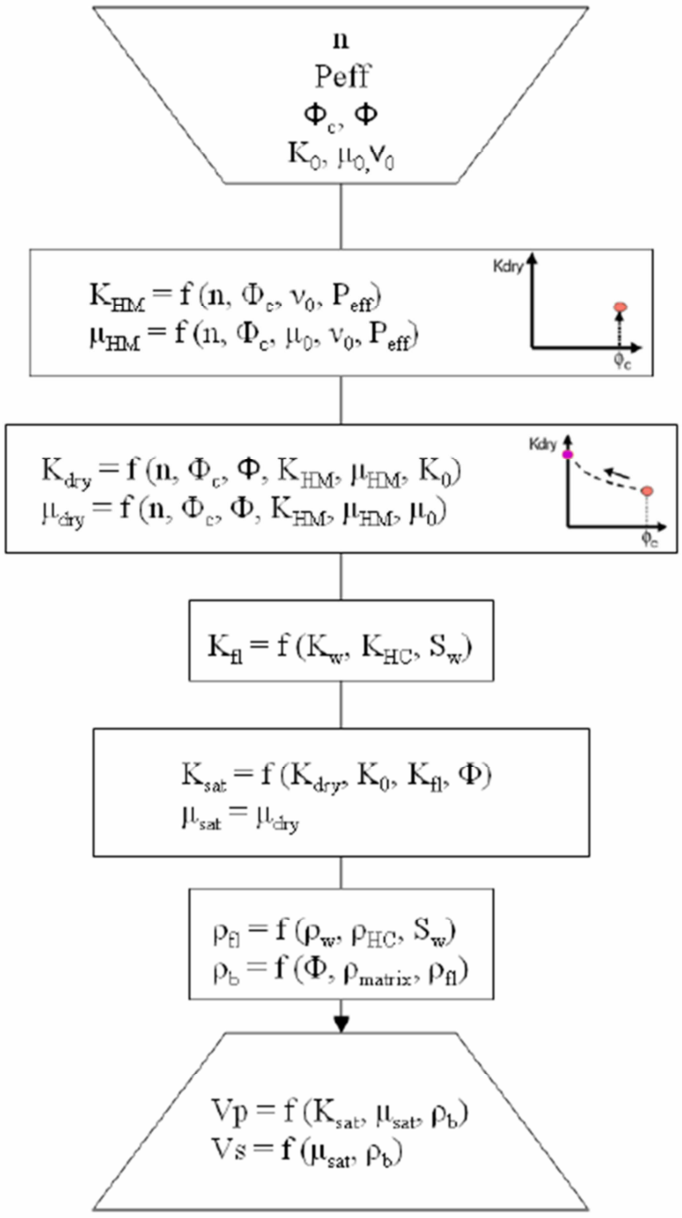

Fig. 4.7: Rock physics template used for this study (Source: Milovac, 2009).

4.3.1 Mineral and fluid properties

The mineral used for this template is assume a single mineralogical condition which is quartz and the elastic properties used for this is taken from Carmichael (1989) quartz grain elastic properties mention in the Table 4.4:

Table 4.4: Elastic properties of quartz by Carmichael (1989) (Source: Mavko et al., 2009).

Mineral	Bulk Modulus (Gpa)	Shear Modulus (Gpa)	Density (gm/cc)	Vp (km/s)	Vs (km/s)
Quartz	37	44	2.65	6.05	4.09

Pore fluids strongly influence the rocks effective elastic properties as well as seismic properties. Their properties varied because of composition, pressure or temperature that influences the effective properties. The Hampson-Russell fluid calculator has been used for calculating bulk modulus and density using different parameters mentioned in the NPD Factpages for the well 7120/6-1 (Fig. 4.8).

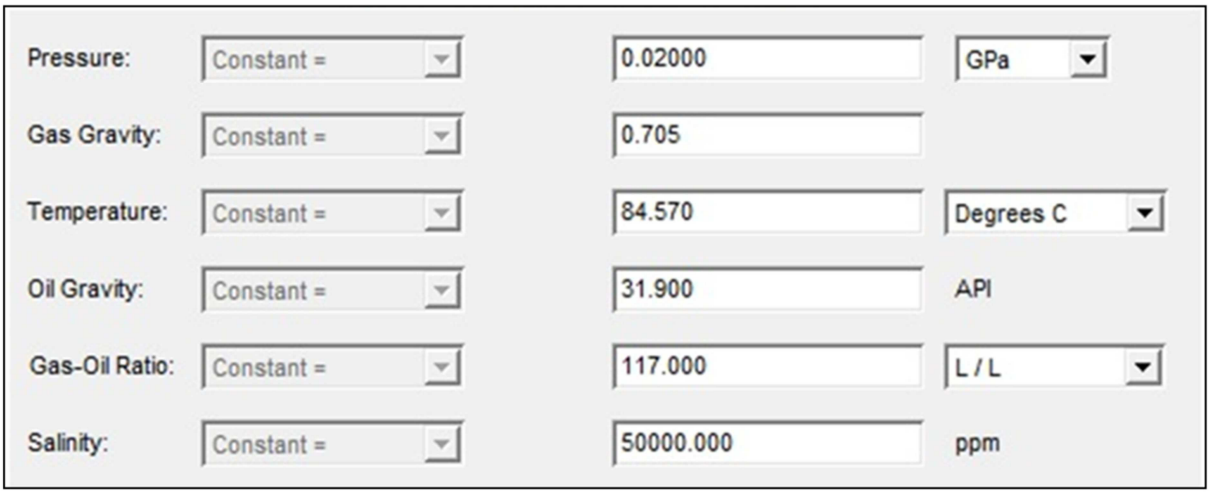

Fig. 4.8: Values prevail in the reservoir conditions in the well 7120/6-1.

The Figure 4.9 Showing the fluids density and modulus calculated on the fluid calculator in Hampson-Russell elog module which is later considered for making different fluid trends in the RPT.

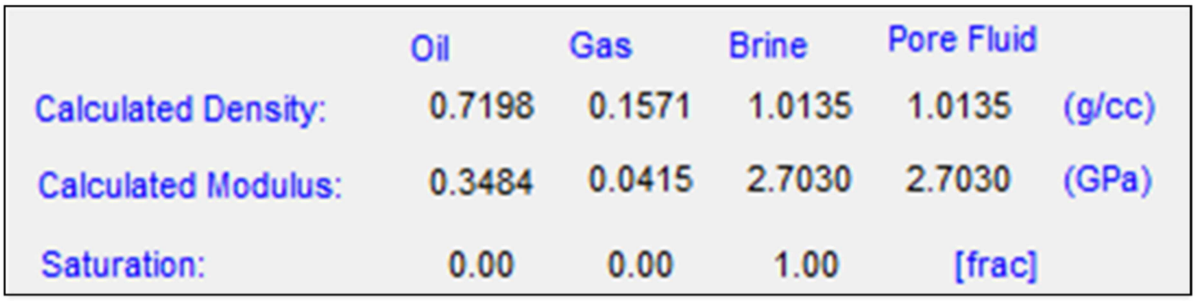

Fig. 4.9: The density and bulk modulus of different fluids using similar reservoir condition mentioned earlier.

4.4 AVO modeling

The AVO modeling and/or analysis carried out by Hampson Russell (HR) software. The Geoview, elog and AVO modules in HR used for different perspectives. Geoview module is use for data loading and quality checking whereas new log calculation and fluid substitution models are carried out in elog module. Synthetic seismics are generated and modeled in the AVO module. This module is also use for single well AVO modeling and in AVO analysis.

Like compaction and rock physics, a suite of six wells have been used for AVO analysis. Because of the lacking of seismic data, AVO analysis only carried out in the synthetic seismic generated by using different well logs. AVO modeling and analysis has been carried out for the main reservoir of Snøhvit field Stø formation. The Fuglen formation has been used as a cap rock which is a thin shale unit in the studied area.

4.4.1 Calculation of shear wave velocity (Vs)

The main input logs used in AVO modeling are Vp, Vs and density logs. Direct measurements of Vs is only present in one well (7120/6-2S) and another five wells have no Vs measurement. The Vp log was then used to create a Vs log using linear log transforms in HR. The comparison of Vs of Stø formation in the well 7120/6-2S show Krief gas equation is closer to the measured value than others (Fig. 4.10). Therefore, This equation is used for whole AVO chapter. The equation is:

$$V_s = 0.438 \times V_p^2 - 0.395 \quad \ldots\ldots\ldots\ldots\ldots\ldots \quad (4.14)$$

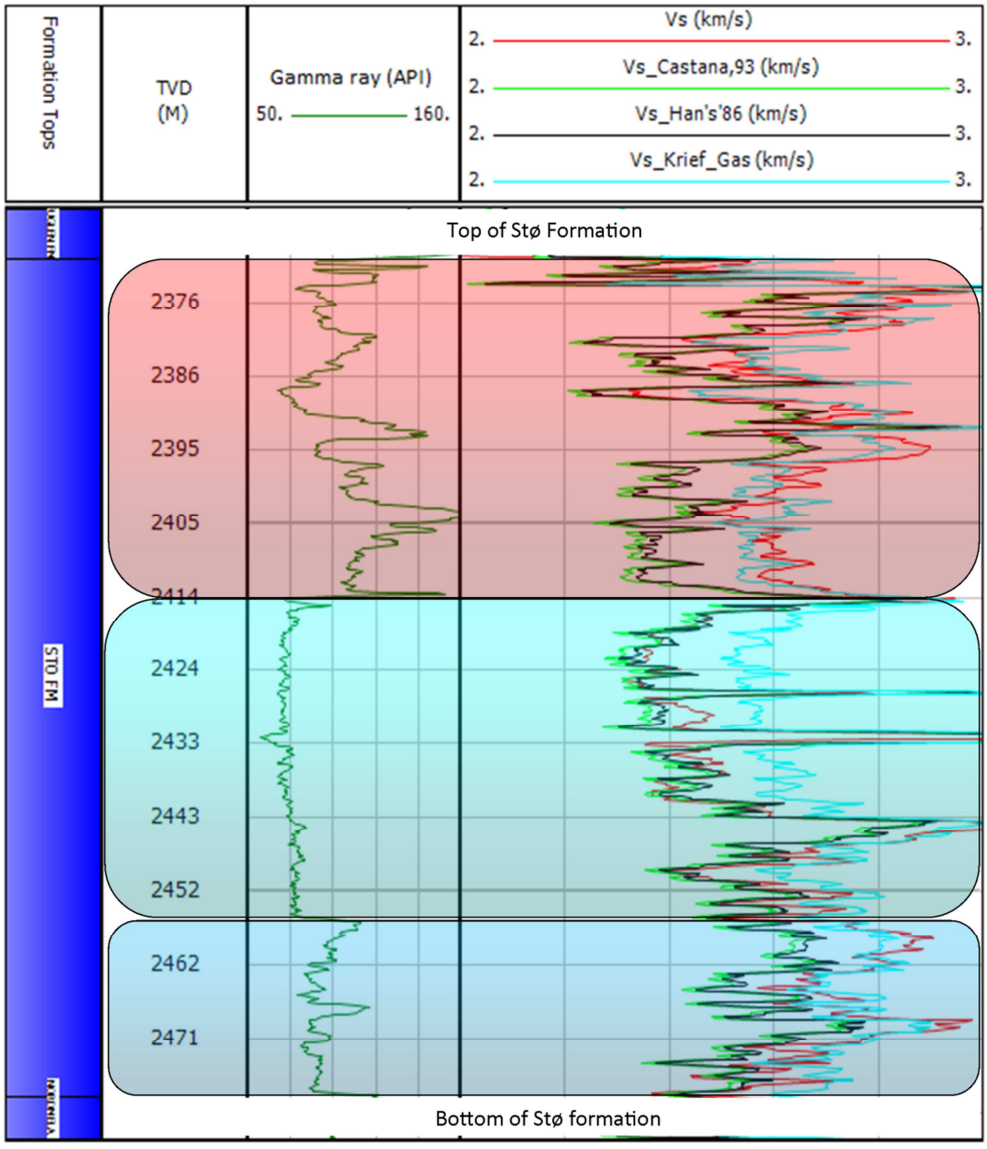

Fig. 4.10: Comparison of Vs of Stø formation in the well 7120/6-2S.

4.4.2 Wavelets

One important parameter is seismic wavelet which needed to generate a synthetic seismogram. The default Ricker linear wavelet was used in this study which is shown in the Figure 4.11. The dominant frequency of this wavelet is 45 Hz. The Ricker linear wavelet used

has a wavelength of 200ms and employs a sample rate of 2ms. The average phase of this wavelet is a zero phase. There are no side lobes in this wavelet, leading to an ideal signal-to-noise ratio. This gives an exaggerated vertical resolution than can be normally achieved in a seismic exploration survey.

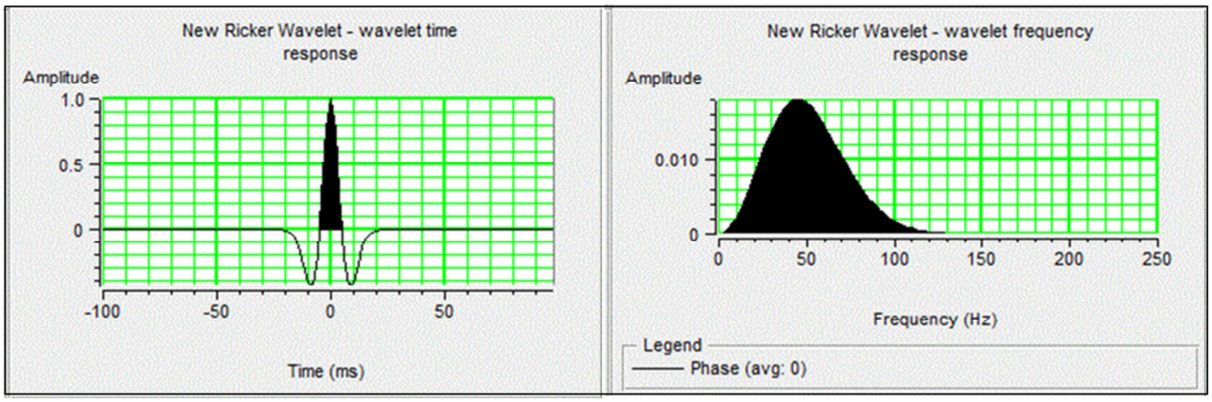

Fig. 4.11: Time and frequency domain Ricker linear wavelet.

4.4.3 Comparison of synthetic output

In order to generate an offset/angle dependent synthetic seismogram, automated ray tracing was used to calculate the angle of incidence. The amplitudes were then calculated using the full Zoeppritz equation and then analyzed using the simplified Aki-Richard equation. The angle range used in generating the synthetic seismogram ranged from 0-45 degree, with an output sample rate of 2ms. No effects of geometrical spreading or transmission losses were considered in the model. The synthetic seismic outputs used in this study are NMO corrected CMP gathers. Output reflectivity was chosen over output amplitude in HR, as this generates a synthetic seismic with better vertical resolution (Fig. 4.12).

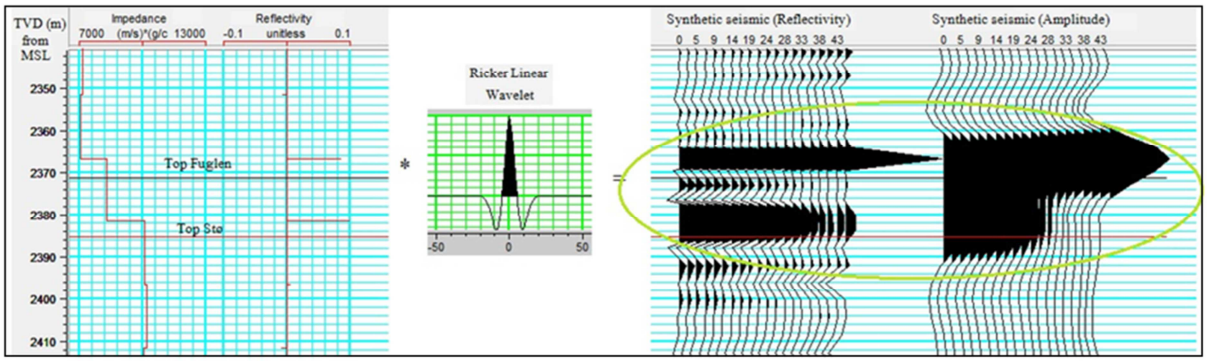

Fig. 4.12: Resolution differences between reflectivity and amplitude output in the synthetic seismic generation window for top Fuglen and top Stø in well 7120/6-2S.

4.4.4 Matrix and fluid properties

The Biot-Gassmann method is applied using Fluid Replacement Modeling (FRM) in HR to investigate ‘what if’ scenarios for different fluid types and saturations. Because of 0.8 net to gross ratio both quartz (80%) and clay (20%) used for matrix minerals. For comparison, one model with 100% quartz matrix minerals also calculated. The effective matrix properties calculated using Hashin-Shtrikman average in HR. The matrix properties used in this chapter

is shown in Table 4.5. Pressure effects are not modeled in this study. As a consequence of this, the input porosity is set to be equal to output fluid substituted model.

Table 4.5: Matrix properties used in FRM

Matrix type	ρ (g/cc)	K (Gpa)	μ (Gpa)
Quartz	2.65	36.60	45.00
Clay	2.58	20.90	6.90
Effective	2.636	32.63	30.20

Table 4.6: Fluid properties used in FRM

Fluid type	ρ (g/cc)	K (Gpa)
Brine	1.0135	2.7030
Oil	0.7198	0.3484
Gas	0.1571	0.0415

The fluid properties presented in Table 4.6 represent the default values in the HR software based on Batzle and Wang (1992). For simplification, homogeneous saturation method has been used for calculating fluid properties in the HR software. These properties were set as constant and used for the different fluid saturations in this study. The assumed matrix and fluid properties, used for different reservoir sections is an over simplification of the actual properties. Despite these simplifications, the Biot-Gassmann approach is yet robust enough to give consistent results.

4.5 Seismic Inversions

Geoview, Elog and Strata modules in HR software are used for seismic inversion modeling. Only post-stack seismics are available for this project. Therefore, three post-stack 2D seismic lines have been used for post-stack inversion modeling (Table 4.2). Geoview mainly used for uploading well logs data. The Elog program is used to perform manipulations on the logs such as editing, smoothing and log correlation. Strata module is a program in HR software, can be used to perform post-stack inversion of seismic data.

4.5.1 Well correlation

The well log correlation is a process which examines the correlation between events on the synthetic traces and the events on the seismic data. The well log is correlated with real seismic via synthetic seismogram. The well log has been calculated in depth where seismic is in time. Therefore, well logs need to be transformed from depth into time for tie with seismic. This is achieved by using checkshot information at each well (Fig. 4.13). The comparison between real and synthetic seismic of the well 7121/5-1 show in Figure 4.14. Before well correlation the similar reflector in synthetic seismic mismatched with real seismic (zone indicated by yellow color). But after well correlation the synthetic seismic looks better matched with real seismic.

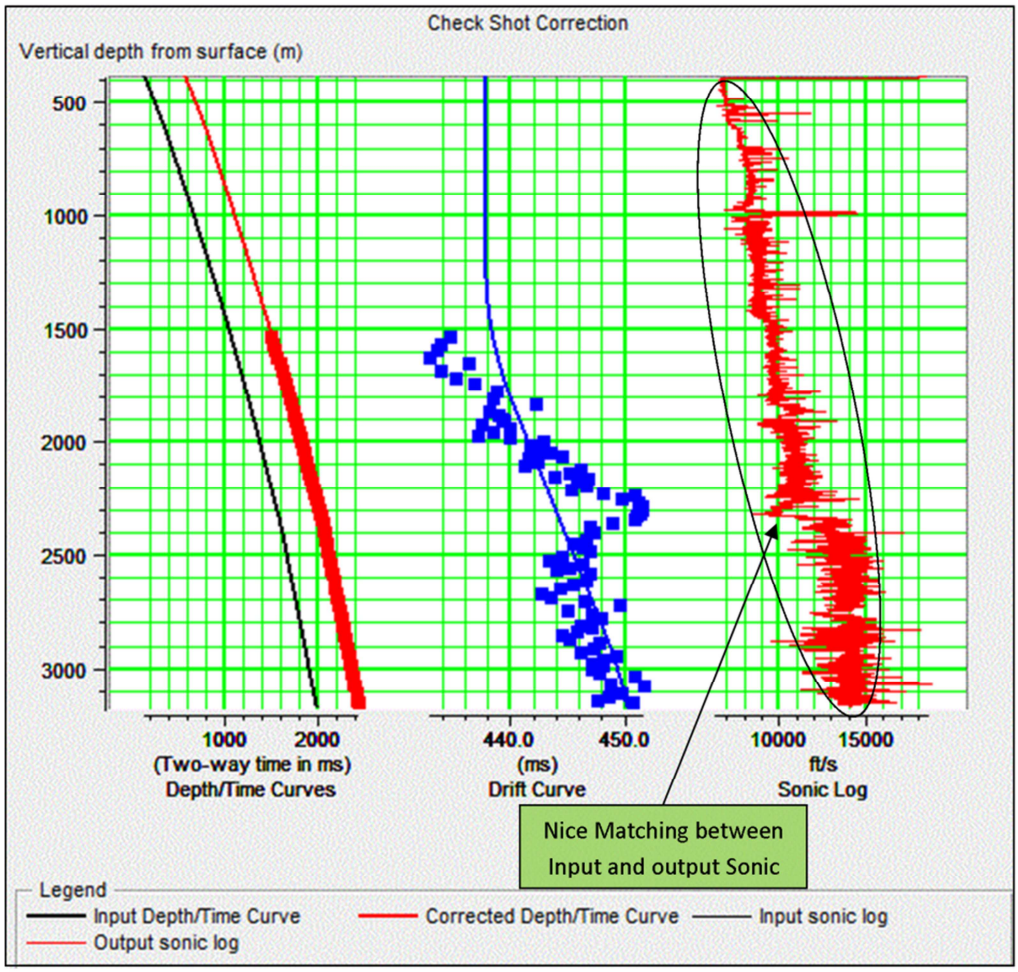

Fig. 4.13: Check shot correction during log correlation between well 7121/5-1 and seismic

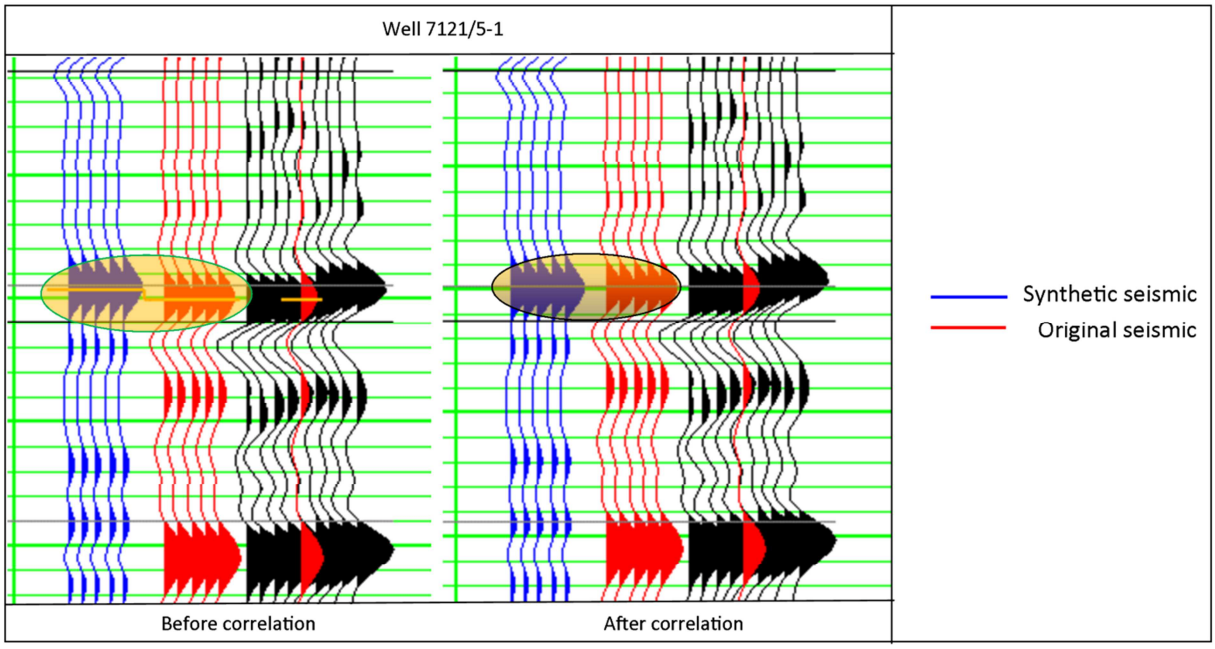

Fig. 4.14: Comparison between synthetic and real seismic in the well 7121/5-1. The blue trace is the synthetic seismic constructed by a convolution between a wavelet and a reflectivity series. Red trace is from real seismic data. Before correlation of the well the synthetic trace is not matched properly with the real seismic trace but after correlation it looks much better matched.

Chapter 5: Compaction and Rock property evaluation

UNIVERSITY OF OSLO

FACULTY OF MATHEMATICS AND NATURAL SCIENCES

Chapter 5: Compaction and Rock property evaluation

Compaction is a process which changes the rock properties throughout its life span after deposition. Based on different factors acting on rock bodies, we divided compaction into two different types: mechanical and chemical which is dependent on stress and temperature respectively. The effective rock properties depend on compaction. In a normal subsidence basin the rock properties change linearly with depth but in an exhumed basin like Hammerfest Basin, it is difficult to predict the changes of rock properties. The main challenge in this research is to explore the rock properties using different compaction methods.

The following sections describe the general description of all logs, transition zone identification, time temperature effect on compaction and uplift estimation on Snøhvit field area.

5.1 Results

5.1.1 The Petrophysical analysis in the study area

The petrophysical analysis of well logs reveals two distinct compaction trends across the entire study area, mechanical compaction (MC) and chemical compaction (CC) (Storvoll et al., 2005; Marcussen et al., 2009; Marcussen et al., 2010; Thyberg et al., 2010). There is an inherent independent relationship that exists between different logs as a function of depth due to the combined effects of MC and CC. Different logs like Vp, bulk density, gamma ray and porosity show a general trend against depth for a given uniform lithology and fluid saturation condition. In general, Vp and bulk density increase with depth whereas porosity decreases as a consequent effect of compaction.

Figure 5.1 shows the plots of Vp, bulk density, gamma ray, neutron porosity and deep resistivity against depth in all six wells used in this study. The depth used in this chapter is referenced from Bottom Sea Floor (BSF). The water depth is excluded from the compaction depth because the sediments compensate the water pressure during deposition. The effect of MC is only because of overburden sediment stress. The stress from water depth does not affect compaction.

The Vp-depth curves display a general trend in all six wells (increases with depth). The source rock (Hekkingen Formation) shows abnormal from the normal trend. It shows velocity inversion (lower reading than lower and upper Formations). A transition zone (MC to CC) is identified in Vp-depth plot, based on the abrupt change in velocity. This zone is located within Knurr Formation. Above this transition zone (TZ) is the MC regime which is stress dependent. On the other hand, the CC regime is located below this TZ which is temperature dependent. Velocity gradients of these two zones are also different. The depths of the TZ are different between wells but are still within the same formation (Knurr formation) across the area. The Kviting Formation is a thin unit in the studied area and conformably deposited above the Kolmule Formation. The Formation is located in a shallow depth (above 1000m, BSF). This formation shows exceptionally high Vp in the well 7121/5-1 and 7121/4-1, though the depth of the formation is relatively shallow. Moreover, it shows high density and high deep resistivity log values which is expected in a high Vp zone. The gamma ray and neutron porosity logs of these wells also show low readings.

Usually, bulk density increases with depth in normal conditions. The density log plots also show similar increasing trend with depth except some areas. Some zones have lower density readings compared to other zones. The main reason for density inversion is overpressure which reduces the effective pressure. Density has a linear relation with velocity and porosity. Velocity increases with increasing density whereas porosity decreases with increasing density.

The gamma ray log is the response of radioactive elements in the rocks. This log is mostly used for lithology identification. The gamma ray logs in the studied wells show two distinct zones. Shale dominated upper zone and sand dominated lower zone. The boundary between these two zones is between the Fuglen and Stø Formations. The source rock (Hekkingen Formation) shows high gamma ray all over the area. The sand dominated zone, locally in the well 7120/6-2S shows higher gamma ray readings compared to other wells.

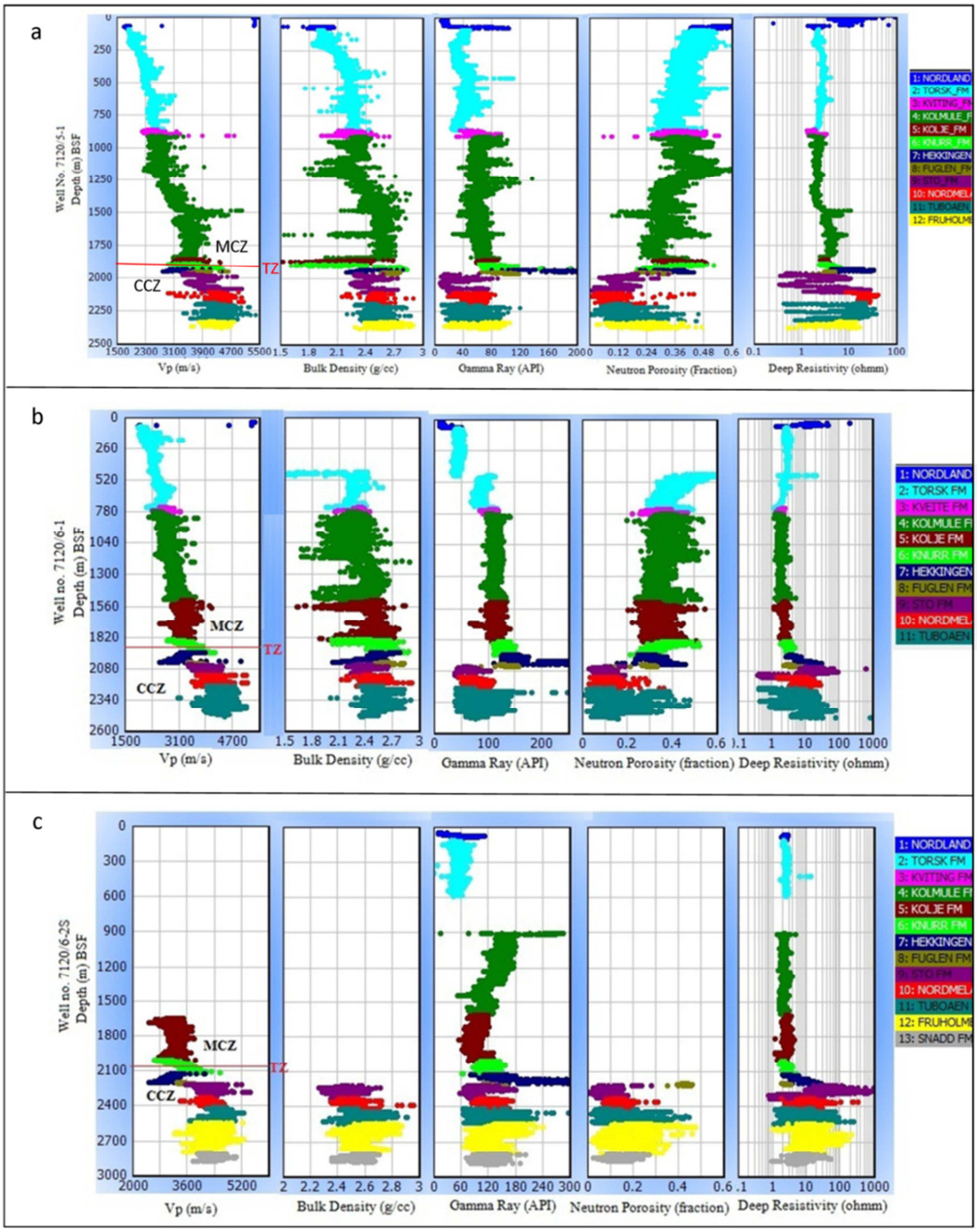

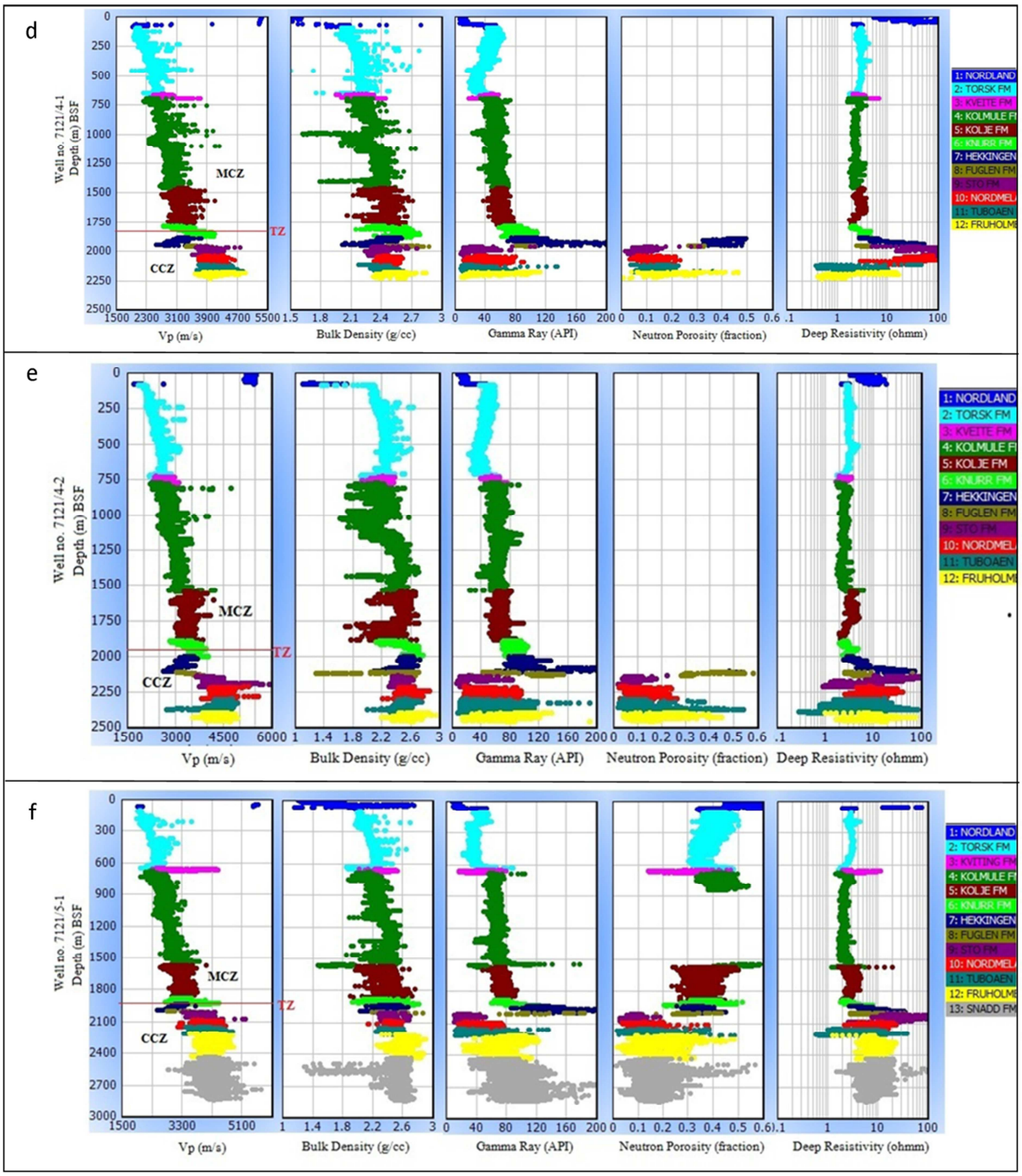

Fig. 5.1: Compaction trends of logs observed in wells (a) 7120/5-1, (b) 7120/6-1, (c) 7120/6-2S, (d) 7121/4-1, (e) 7121/4-2 and (f) 7121/5-1.

The velocity gradient is dependent on many factors. Based on velocity gradient, six different zones can be inferred in Vp-depth plot. Vp data of all six wells have been used for this plot where green represents source rock (Hekkingen Formation) and all other formations are in blue (Fig. 5.2). Zone 1 consists of the Nordmela Group and the upper part of the Torsk Formation. This unit is dominated by grey to greenish-grey, non-calcareous claystones and follows the normal velocity gradient trend. Zone 2 is dominated by shales and claystones with tuffaceous and glauconitic components. The lower part of the Torsk and Kveite Formations consist this zone. This zone shows a sparse distribution of Vp. Some data points show very high Vp where some others show lower gradient than normal trend.

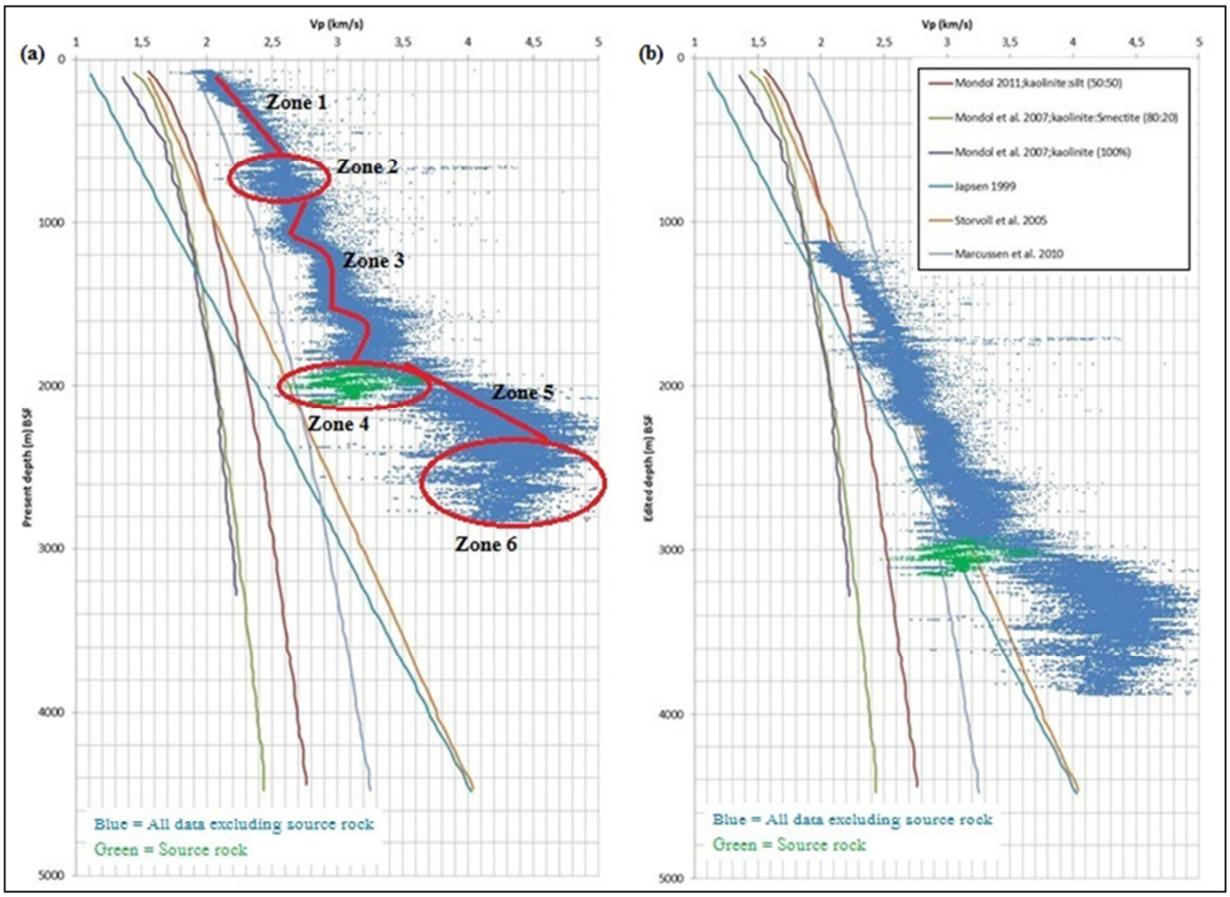

Fig. 5.2: Sonic velocity-depth plot of all data with green color source rock and different zones (a) before exhumation (b) after exhumation.

Zone 3 entailed three formations; Kolmule, Kolje and upper part of Knurr. This zone is consisting of mainly shale and claystones with minor interbeds of siltstones, sandstones, limestone and dolomite stringers. Different lithologies have different compaction rates which give a zig-zag pattern of velocity gradient. Hekkingen formation which is the source rock of this area is Zone 4. This zone shows velocity inversion (lower velocity than upper and lower units). Zone 5 is mainly consisting of sandstones which are the main reservoir rocks of this area. These units show a general increasing of velocity with increasing depth. The gradient is higher than any other gradients. Only two wells out of six are penetrating in to the Triassic Snadd Formation. This formation belongs to Zone 6 which shows lower Vp than Zone 5 though the overburden is higher.

5.1.2 Transition from mechanical to chemical compaction

Transition from MC to CC is very important because these two compaction domains change the rock properties in different ways. To evaluate the rock properties, it is important to know the exact compaction domain of rocks. The MC is stress dependent whereas CC is temperature dependent. Therefore, the MC range is in the first few kilometers (Km) (depends on temperature gradient), then CC takes over the compaction domain. In a certain temperature range, CC changes the rock stiffness by quartz precipitate. The Vp values increased dramatically with this stiffness change. The rate of quartz cementation is very slow in the transition zone but it is enough for changing velocity. Good indicator to identify a transition zone is when Vp changes from MC to CC. Porosity and density data also changes in this

transition zone but the influences are not prominent like Vp. Therefore, Vp is used to identify transition zones.

The Vp and density logs from six wells are plotted against depth (Fig. 5.3). Both Vp and density plots, Mondol (2009) kaolinite-silt (50:50) laboratory experimental curve is used as a reference. Like reference curve, only shale data points ($\geq$0.75 V_{sh}) have been used for this analysis. The depth used for this part is also referenced from BSF. All wells used in this project have Vp log available both in MC and CC domains. In the well 7120/6-2S the density logs only exits within CC zone. Other five wells have full coverage of the density logs. The Vp-depth plots of all wells show clear velocity changes within the Knurr Formation. The Knurr Formation is a shaly unit in the Adventdalen Group. On the other hand, the only well 7120/5-1 and 7121/4-1 show good TZ in the density data plots. These two wells show similar TZ values both in density and Vp plots.

Since Vp-depth plots display nice transition zones in all wells, the Knurr formation has been focused to check the TZ more carefully. The gamma ray logs are also investigated to check lithological variation. Gamma ray logs representing the lithology in the TZ could be applicable to investigate velocity difference because of cement dependent or lithology dependent (Fig. 5.4).

The gamma ray log in the Knurr Formation shows more or less similar readings in all wells but the velocity changes within this formation are dramatic. The MC regime of the Knurr Formation follows similar gradients started from the top. The gradients changed dramatically when crossing the TZ. The velocity increases are different between wells. The average velocity change from MC to CC is around 400 m/s (Fig. 5.4). Based on the change in Vp from MC to CC, one fixed transition point has been identified. The present day transition depth is shown in Table 5.1. The depth is measured from BSF is different between the wells. The lowest depth is 1827 (m, BSF) in well 7121/4-1 whereas the highest depth is 1944 (m, BSF) in well 7121/4-2. Since CC is dependent on temperature, the present day temperature at the transition points are also measured which is shown in Table 5.1.

Table 5.1: The transition depth and the temperature in six wells

Well No.	Transition depth (m) BSF	Temperature at Transition point (^{0}C)
7120/5-1	1907	43.85
7120/6-1	1888	66.95
7120/6-2S	1860	65.56
7121/4-1	1827	58.81
7121/4-2	1944	69.01
7121/5-1	1922	66.67

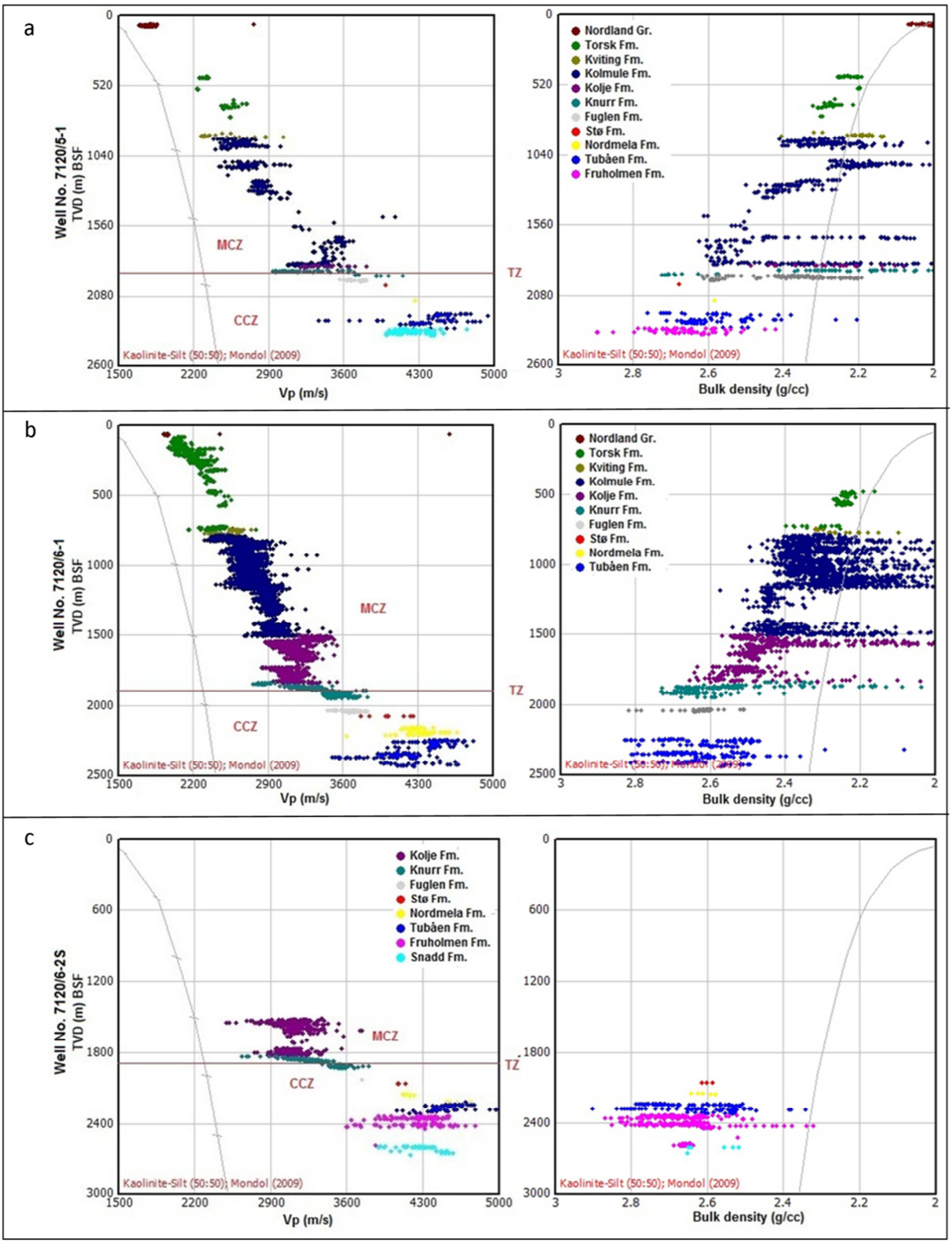
a
Well No. 7120/5-1
TVD (m) BSF
MCZ
CCZ
TZ
Kaolinite-Silt (50:50); Mondol (2009)
Vp (m/s)
Bulk density (g/cc)
Nordland Gr.
Torsk Fm.
Kviting Fm.
Kolmule Fm.
Kolje Fm.
Knurr Fm.
Fuglen Fm.
Stø Fm.
Nordmela Fm.
Tubåen Fm.
Fruholmen Fm.
b
Well No. 7120/6-1
TVD (m) BSF
MCZ
CCZ
TZ
Kaolinite-Silt (50:50); Mondol (2009)
Vp (m/s)
Bulk density (g/cc)
Nordland Gr.
Torsk Fm.
Kviting Fm.
Kolmule Fm.
Kolje Fm.
Knurr Fm.
Fuglen Fm.
Stø Fm.
Nordmela Fm.
Tubåen Fm.
c
Well No. 7120/6-2S
TVD (m) BSF
MCZ
CCZ
TZ
Kaolinite-Silt (50:50); Mondol (2009)
Vp (m/s)
Bulk density (g/cc)
Kolje Fm.
Knurr Fm.
Fuglen Fm.
Stø Fm.
Nordmela Fm.
Tubåen Fm.
Fruholmen Fm.
Snadd Fm.

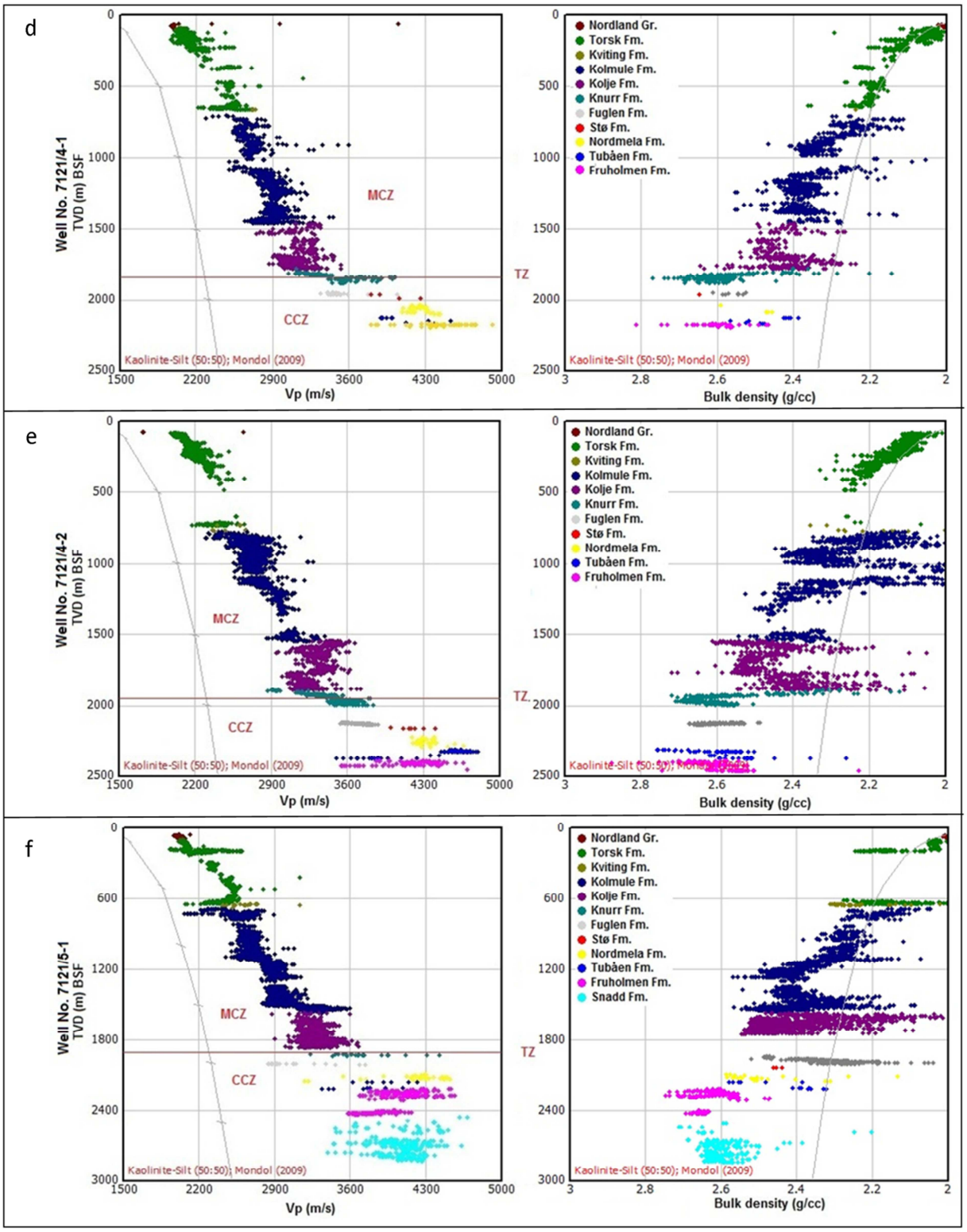

Fig. 5.3: Depth versus Vp and bulk density plots of shale data points with kaolinite-silt (50:50) experimental curve in the wells (a) 7120/5-1, (b) 7120/6-1, (c) 7120/6-2S, (d) 7121/4-1, (e) 7121/4-2 and (f) 7121/5-1.

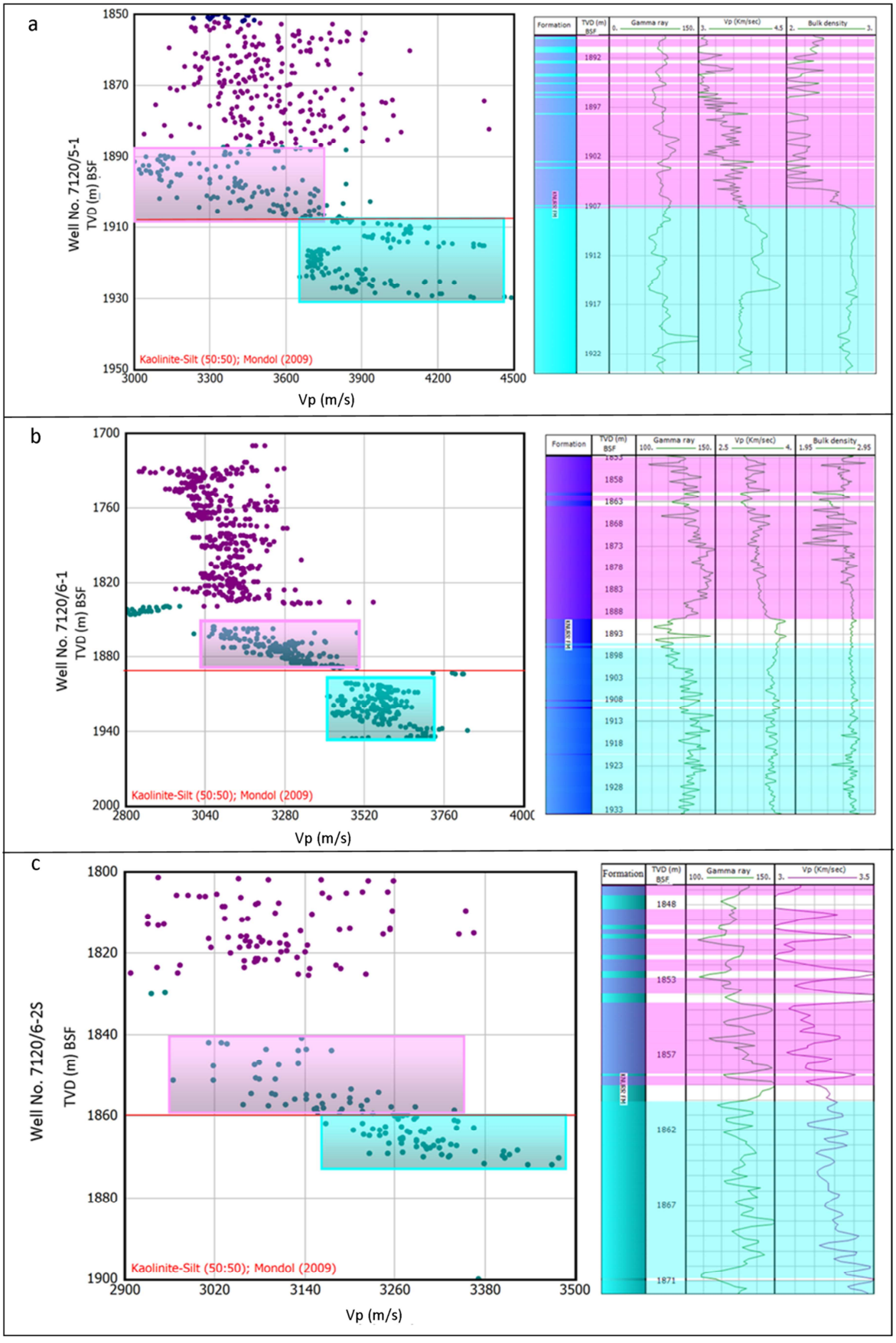
a
Well No. 7120/5-1
TVD (m) BSF
Vp (m/s)
Kaolinite-Silt (50:50); Mondol (2009)
Formation
TVD (m) BSF
Gamma ray
Vp (Km/sec)
Bulk density
b
Well No. 7120/6-1
TVD (m) BSF
Vp (m/s)
Kaolinite-Silt (50:50); Mondol (2009)
Formation
TVD (m) BSF
Gamma ray
Vp (Km/sec)
Bulk density
c
Well No. 7120/6-2S
TVD (m) BSF
Vp (m/s)
Kaolinite-Silt (50:50); Mondol (2009)
Formation
TVD (m) BSF
Gamma ray
Vp (Km/sec)

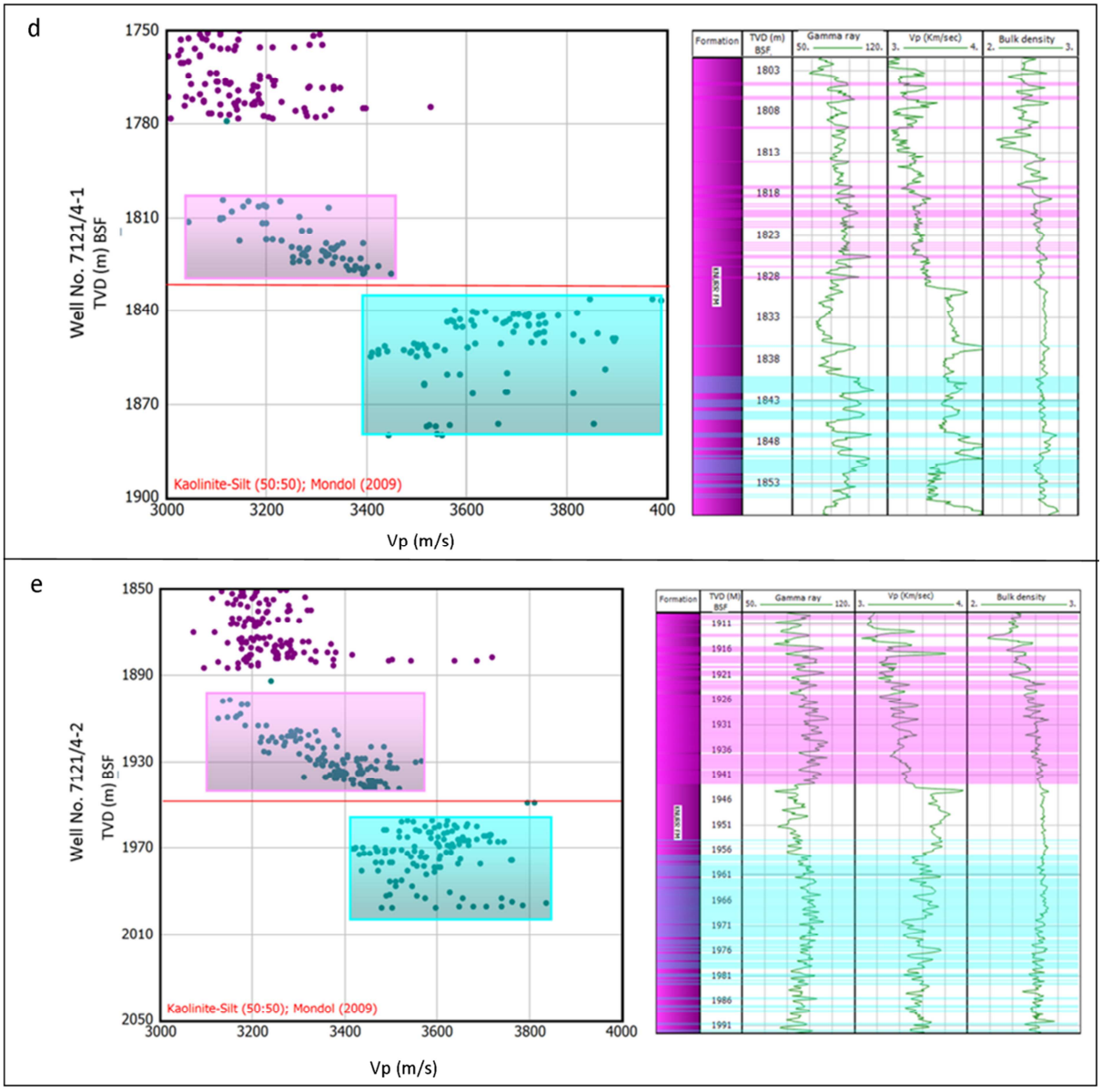

Fig. 5.4: The TZ of wells within Knurr formation with gamma ray, Vp and density logs.

Both velocity and density increase when the compaction domain changes from MC to CC. Therefore, the cross plot of velocity and density is a good indicator for identifying TZ (MC to CC). For this purpose, the Vp and bulk density data have been plotted against each other. These plots are shown in Figure 5.5. Different colors represent different formations. Five out of six wells have been used for these plots because the density data above Stø Formation does not exist for the well 7120/6-2S. The cross plots show two clusters of data distribution zones. The first zone consists of the formations of MC whereas other zone consists of CC formations. The first zone has lower Vp and density than that of the second zone. Moreover, the transition between these two zones is within the Knurr Formation expected.

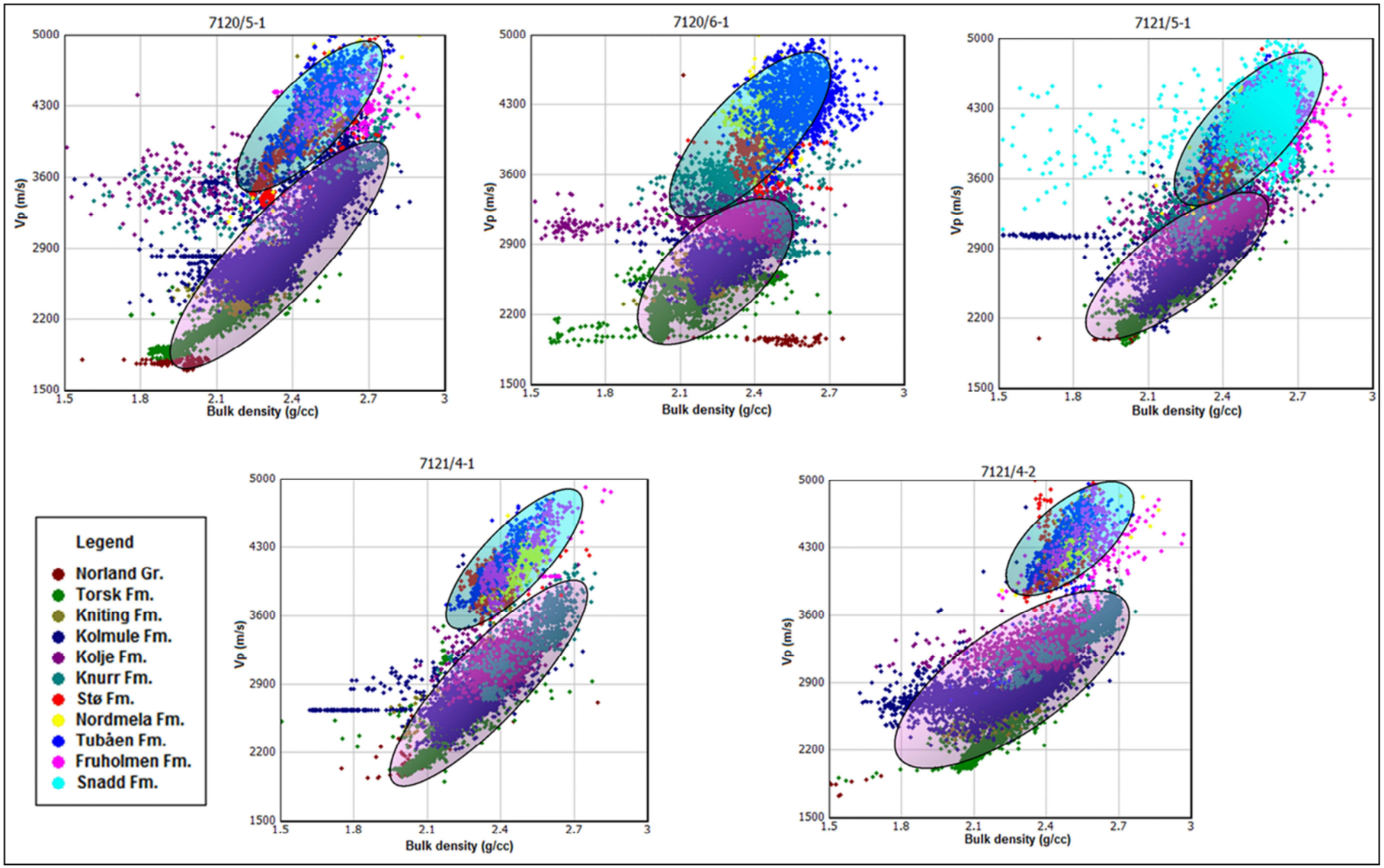

Fig. 5.5: Vp versus bulk density plot of all wells showing two different clusters of the data sets color coded by formation.

5.1.3 Time-Temperature effects on compaction

Time and temperature are very important parameters in the compaction in which the transition between MC and CC depends on time-temperature integral (Storvoll and Brevik, 2008). The CC is temperature dependent and starts with the precipitation of quartz cement. Time is also involved because the chemical reaction needs time to precipitate quartz cement. These two parameters change the rock properties within CC domain. Therefore, time temperature integral (TTI) is very important in case of CC.

Time and temperature are also important in transition (MC to CC). The transition depends on temperature when MC domain changes to CC domain. The present day temperature at transition points are shown in Table 5.1. In a normal subsidence basin the TZ (from MC to CC) normally starts at 70-80^{0}C (Storvoll and Brevik, 2008). In the studied area, the present day temperature in the transition points range from 44 to 69^{0}C which lower than normal transition temperature. Moreover, well 7120/5-1 shows only 44^{0}C present day transition depth temperature which is too low but the transition depth is more or less similar with other wells. This is an indication of local different paleo-temperature.

Like Vp, shear modulus is also very sensitive to cementation. A small amount of cement can change the shear modulus significantly which helps to identify the transition zone (MC to CC). The shear modulus versus density cross plots also show two clusters of data distribution in the Figure 5.6. The color code is used to show the temperature distribution within the wells. All wells show knee points where the shear modulus increases significantly but the density tends to be similar. The points
The knee points (start of increase shear modulus) indicate TZ (MC to CC). The color of the data in the knee points gives an idea about the temperature in the transition depth. The temperature found from these plots is shown in the Table 5.2. The temperatures range given by the modulus-density plots are more or less similar to the temperature calculated earlier.

Table 5.2:Temperature range in the transition points given by the shear modulus-density plots.

Well No.	Temperature range (°C)
7120/5-1	40-50
7120/6-1	60-70
7121/4-1	50-60
7121/4-2	60-70
7121/5-1	60-70

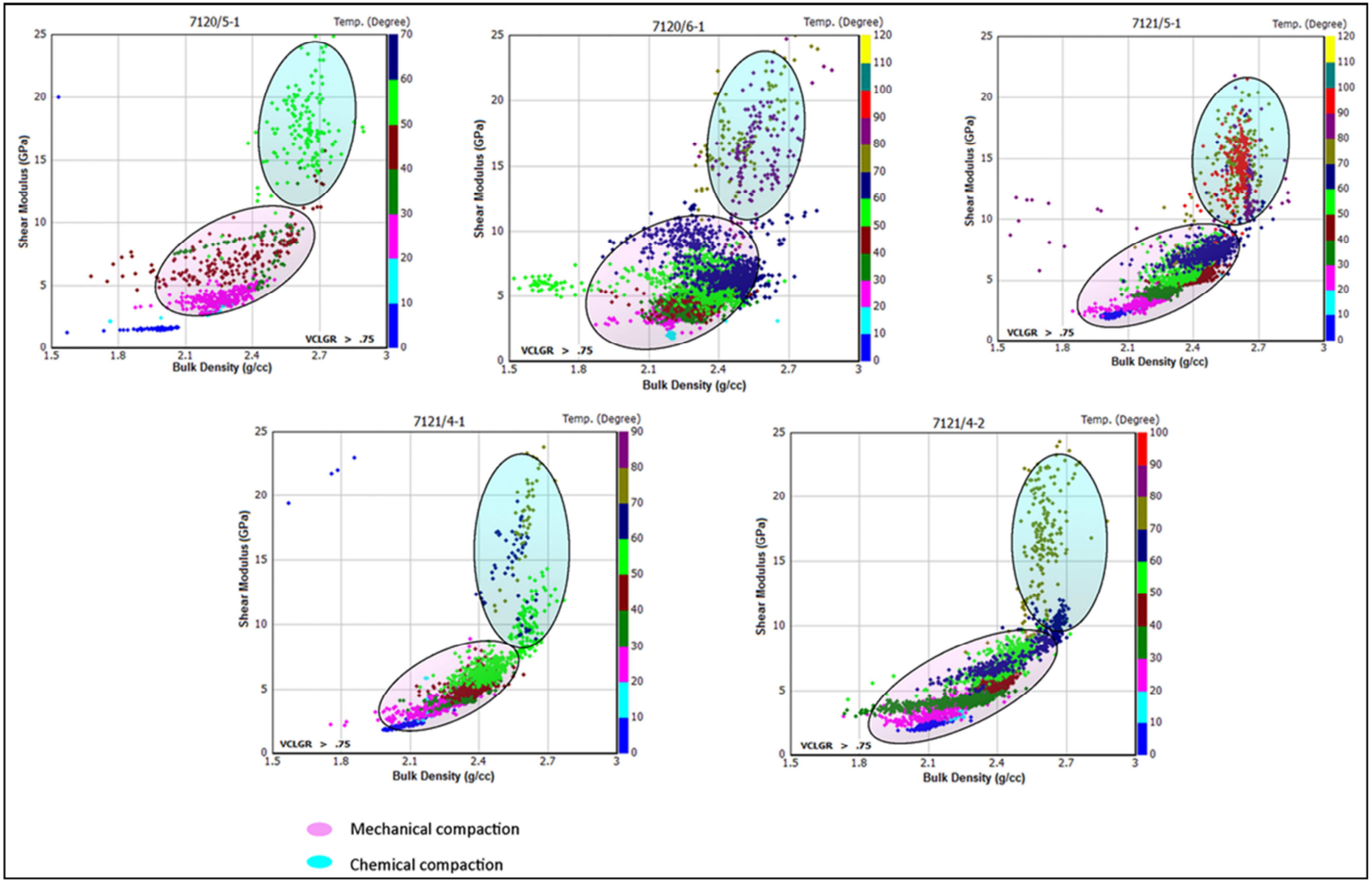

Fig. 5.6: The bulk density-shear modulus plots (only shales) color coded by temperature showing the transition from mechanical to chemical compaction with temperature ranges.

Vp versus density plot of well 7120/5-1 has been used for detailed study of temperature influence on rock properties. Figure 5.7 shows the Vp-density cross plot of Knurr Formation in well 7120/5-1. The blue represents temperature 44 ºC whereas cyan represents 45 ºC. These two different temperature ranges show two sets of data. The data color coded in blue (44 ºC) showed more or less similar velocity range (2900 to 3700 m/s). The density of this zone shows a long range (1.6 to 2.4 g/cc). On the other hand, the data color coded in cyan (45 ºC) suddenly increases in velocity upto 4500 m/s. The gamma ray reading in similar depth level does not show any dramatic changes. The lithology looks to be similar in that depth level. The dramatic increase of velocity due to one degree temperature change is indicating this point as the transition points (MC to CC). The gamma ray reading has proven that an increase in Vp is not because of lithology changes but the precipitation of quartz cement.

Since temperature is closely related to the TZ (MC to CC) in which the TZ has a standard temperature range, any mismatch between the present day temperature at transition points and standard temperature will be the indication for exhumation (uplift and/or erosion). In this well the transition zone temperature shows 44ºC which is too low when compared to the standard transition zone temperature (about 60-70º C).

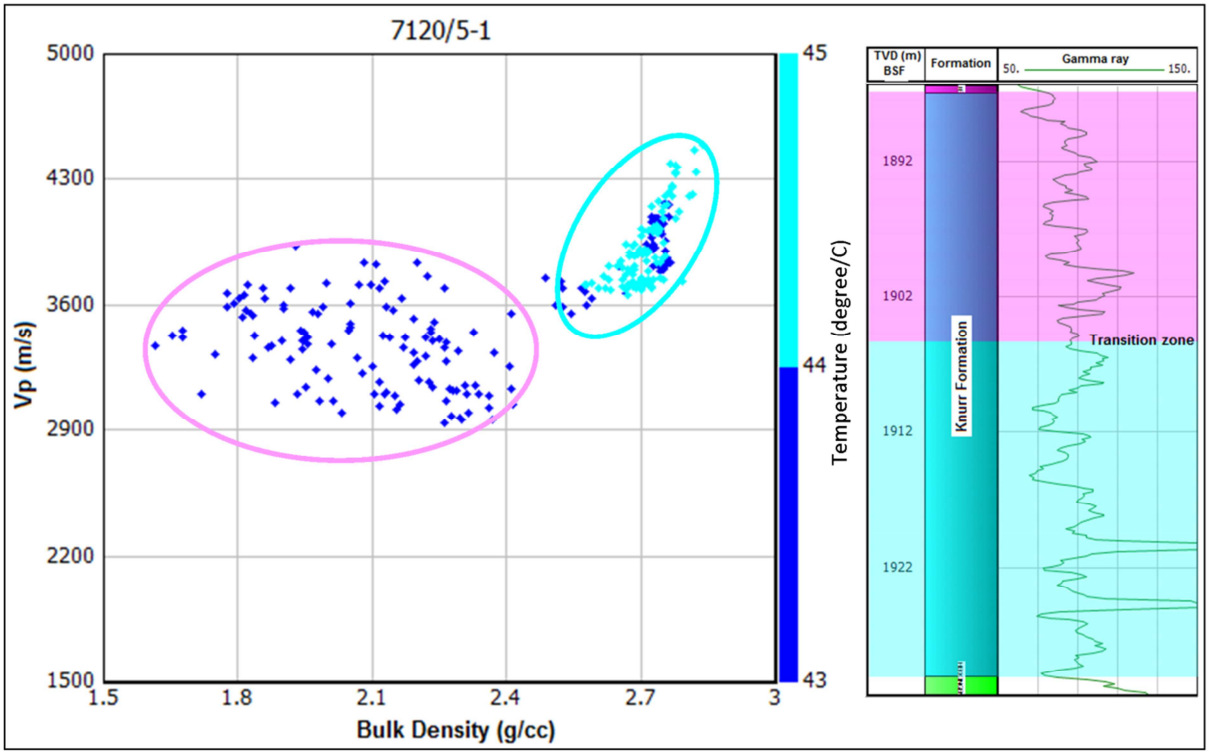

Fig. 5.7: Vp-bulk density plot of Knurr formation shales data points in the well 7120/5-1 showing the different Vp-density values with changing only one degree temperature.

5.1.4 Sand and shale compaction trends

Compaction depends on lithological composition of the rocks. The studied area is a clastic sedimentary basin. Hence, sandstone and shale compaction trends are identified using the data from well 7121/4-1. The Vp data points of well 7121/4-1 are plotted against depth. Figure 5.8 shows the Vp-depth plots (a) all data point, (b) only sandstone data points and (c) only shale data points. Clean sandstones (V_{sh}≤35%) and shales (V_{sh}≥75%) have been sorted out using V_{sh} which is calculated from gamma ray log. Two different gradients have been identified

both in sandstone and shale plots. The yellow represents MC gradient whereas cyan represents CC gradient. The MC gradient of sandstones is higher than shales. The Vp increases more in sandstones compare to shales. On the other hand, the Vp increases in higher rate in shales than sandstones in the CC zone.

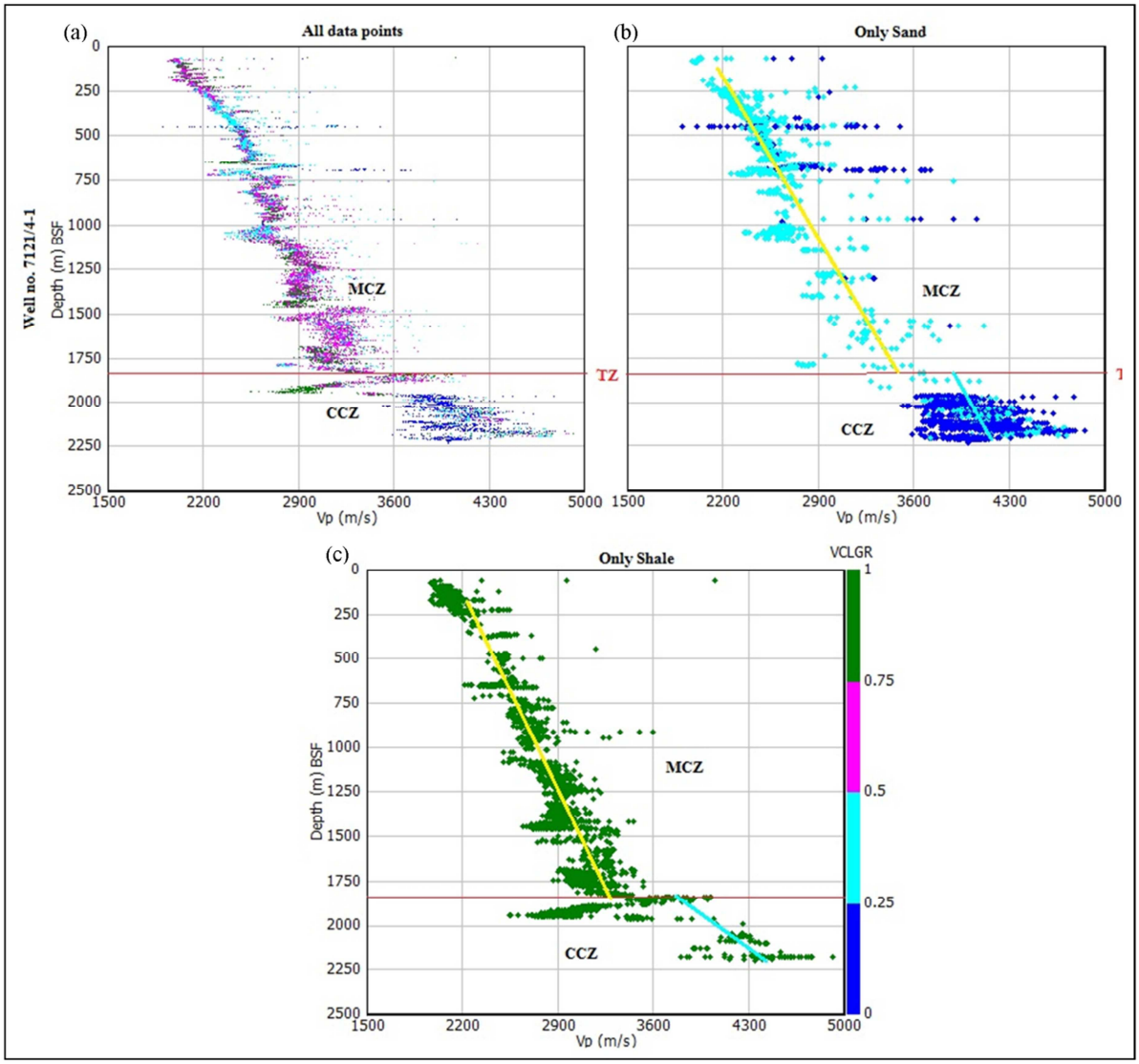

Fig. 5.8: The compaction trends of sand and shale in the well 7121/4-1

5.1.5 Uplift estimation

The present day temperature at TZ (MC to CC) is showing mismatch with standard temperature which represents the Hammerfest basin is an uplifted basin. Hence, in this section total exhumation (how much uplifted or eroded) will be estimated. Exhumation means the displacement of rocks with respect to the surface (England and Molnar, 1990). Figure 5.9 (a) shows Vp versus depth data points of all wells used in this research. Few established velocity curves also presented in this plot. A significant mismatch is observed between established curves with velocity data points in the MC zone. The deviation becomes greater in the chemical compaction zone. The mismatch between velocity data in this area and the established velocity curves also reveal this basin may be experienced uplift. After exhumation the velocity data matched with established curves (Fig. 5.9b). This deviation could be seen

due to overconsolidation at higher depths and the subsequent upliftment. It is important to quantify this exhumation as it has consequences on the petroleum system in the area. Both reservoir rock quality and source rock maturation depend on time-temperature relationship which is influenced by exhumation.

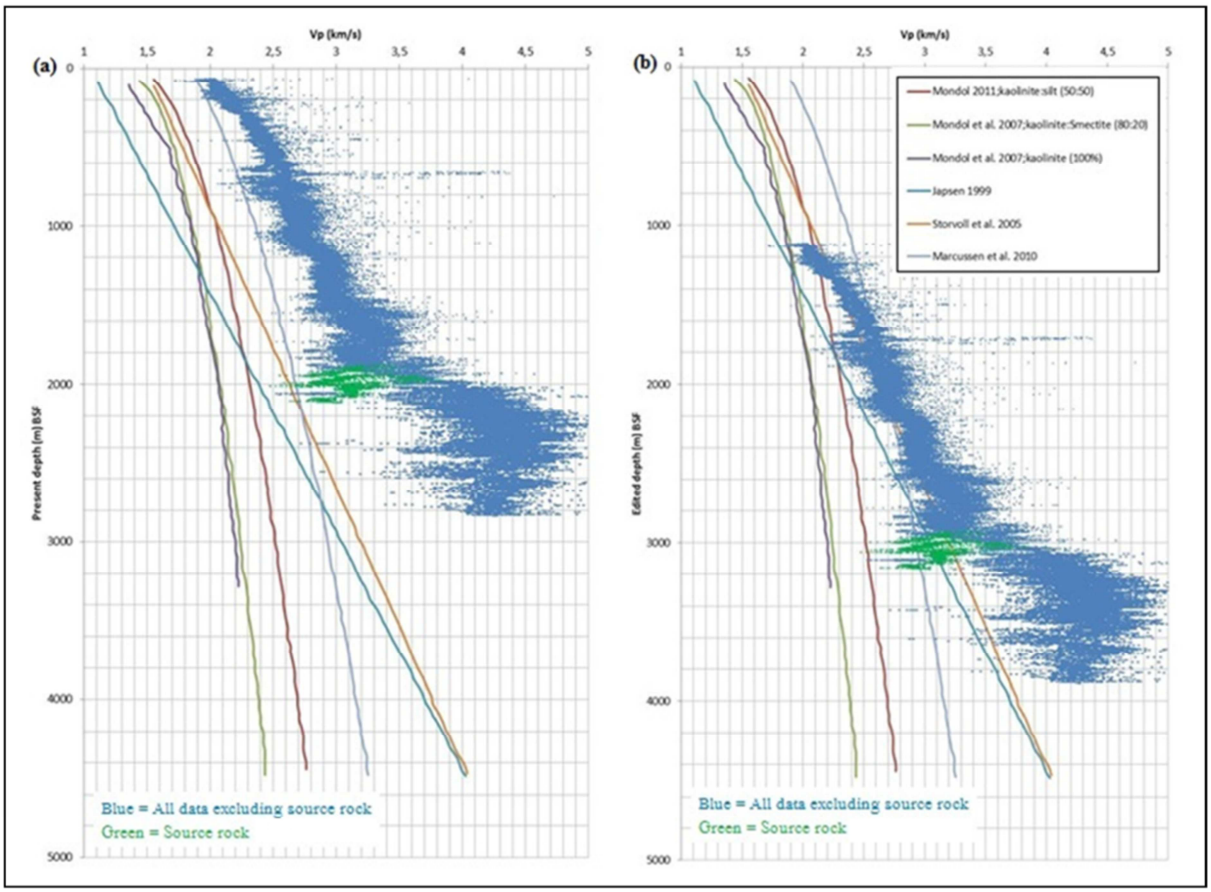

Fig. 5.9: Sonic velocity measurements from all wells (a) before exhumation and (b) after exhumation.

Because the compaction depends on mineralogy, it is important to choose the standard established curve for exhumation as showed in Figure 5.10. Only shale data points (V_{sh}≥75%) from the well 7120/6-1 are used in these plots. Because of the lack of mineralogical data, three different mineralogical experimental curves have been used for comparison. The red curve representing Kaolinite-Silt (50:50) (Mondol, 2009) mineralogical condition indicates 700m exhumation. The kaolinite-Smectite (80:20) (Mondol et al., 2007) (green) curve shows 1200m exhumation and 100% kaolinite (Mondol et al., 2007) curve gives 1400 m total exhumation (Fig. 5.10). Because of the lithological variations, different experimental curves show variation in different exhumation at same data point. Therefore, it is very important to choose standard reference curve used for estimating the exhumation.

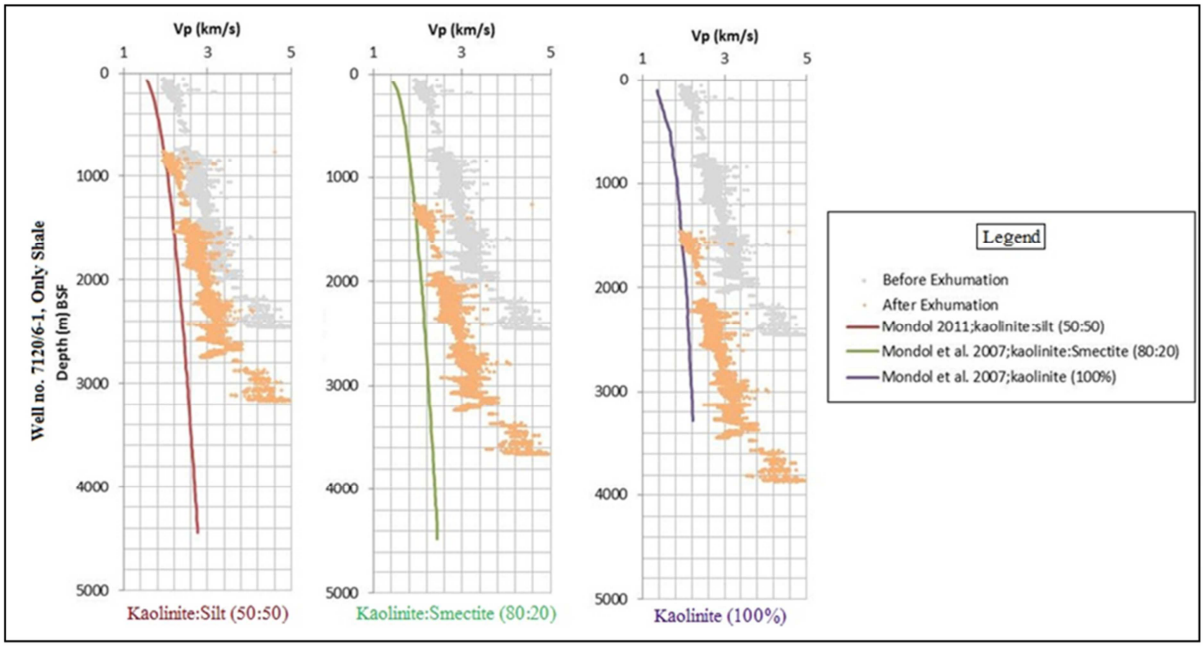

Fig. 5.10: Exhumation estimation using clay-silt, kaolinite-smectite and kaolinite curves of shales in 7120/6-1 well.

The kaolinite:silt (50:50) experimental curve has been used to identify the total exhumation of the studied area (Fig. 5.11). Table 5.3 shows the total uplift in different wells. The easternmost well 7121/5-1 (760 m) shows the highest exhumation compared to the westernmost well 7120/5-1 (300 m). The exhumation increased from west to east.

Table 5.3: Total uplift calculated using kaolinite-silt (50:50) experimental curve.

Well No.	Total exhumation
7120/5-1	300
7120/6-1	700
7121/4-1	680
7121/4-2	720
7121/5-1	760

Three important properties; Vp, density and porosity are linked and vary with depth as a function of burial diagenesis. The velocity and density increase with depth while porosity decreases with increasing velocity and density. All three parameters are plotted and compared with kaolinite-silt (50:50) (Mondol, 2009) experimental curve. Only shaly part ($V_{sh} \geq 0.75$) from the well 7120/6-1 is considered for these plots. These parameters are plotted against both present day depth and exhumed depth (Fig. 5.12). By comparing the data with experimental curve, present day depth plots show deviation. This is due to the exhumation as demonstrated earlier and the log plots can partially be fit to Mondol curve using 700m uplift exhumation correction.

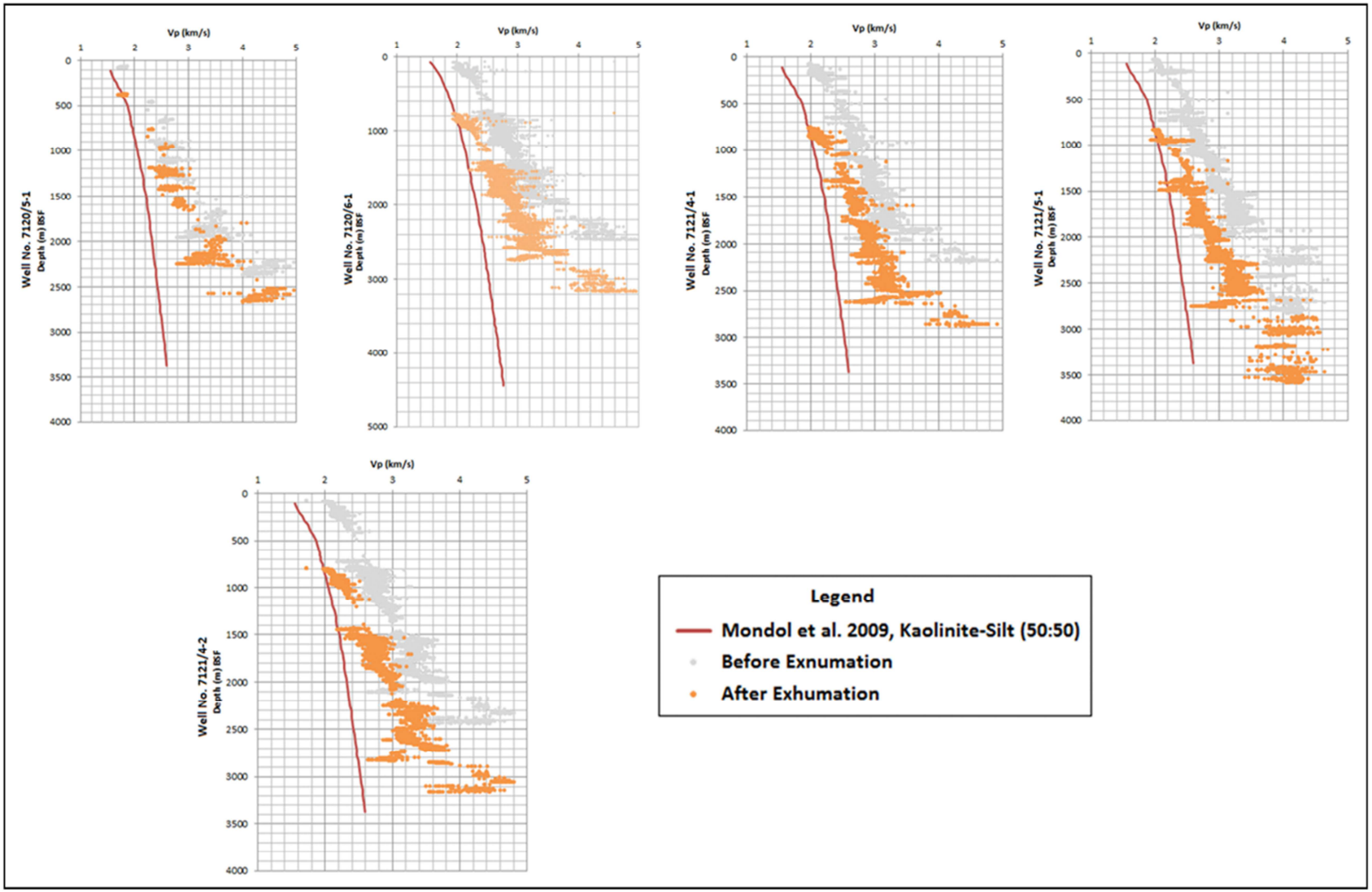

Fig. 5.11: Vp against depth plots of shales with kaolinite-silt (50:50) experimental curve of five wells showing the total exhumation of each well.

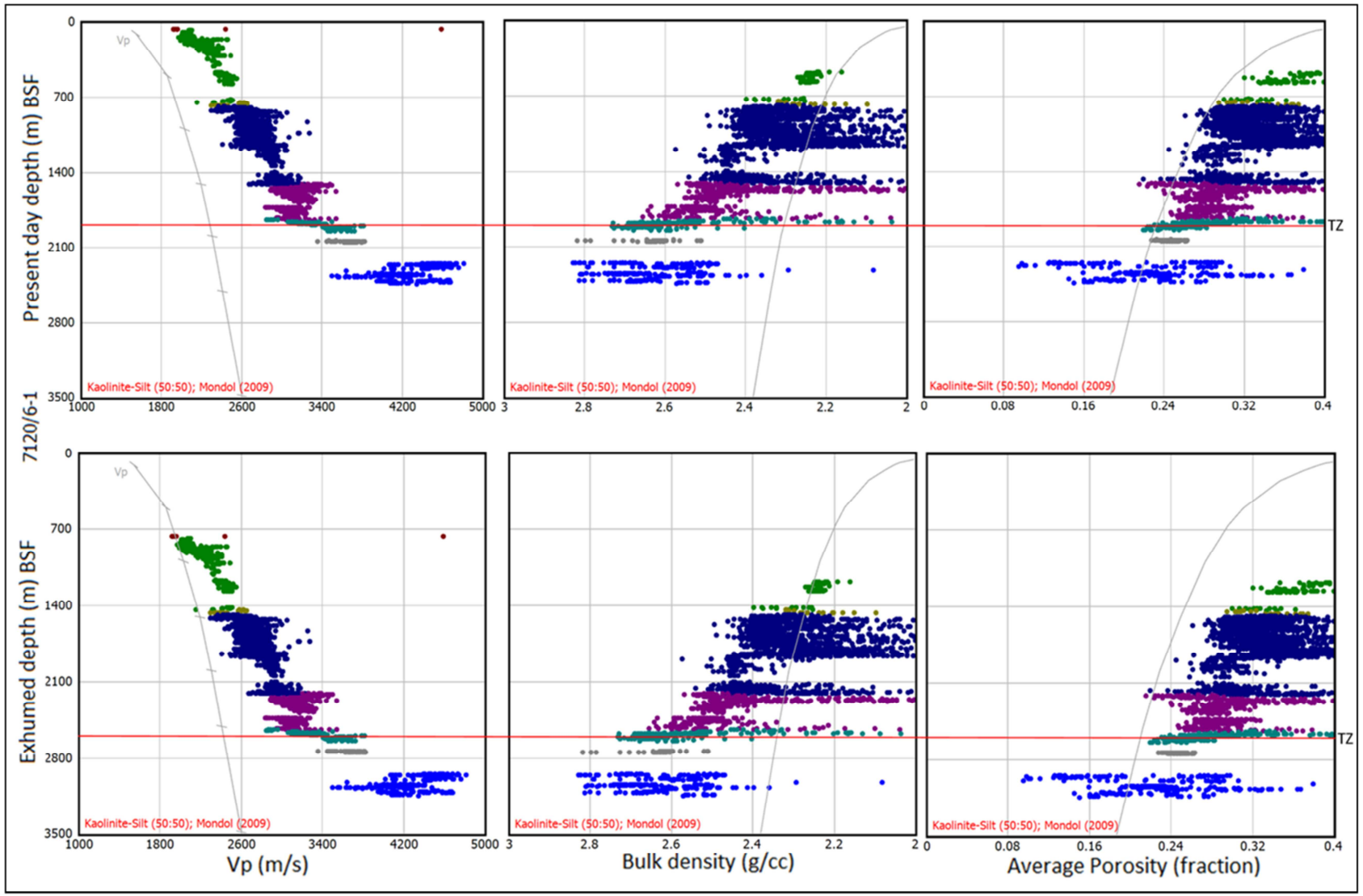

Fig. 5.12: Vp/bulk density/porosity-depth trend of Shale in the.

5.2 Discussions

5.2.1 Petrophysical analysis in the studied area

Petrophysical properties of the studied area are more or less similar. The Vp-depth plots of all six wells (Fig. 5.1) show a general trend in both MC and CC zones. This indicates that the effective stress acted in MC zone is equivalent over the studied area. Moreover, the temperature distribution in the CC zone around the studied area is also similar. The Kviting Formation in two wells shows high Vp in a shallow depth. Three possible reasons for higher velocity in the shallow depth in a clastic composition are (Bjørlykke and Jahren, 2010):

- Meteoric water leaching and precipitation of Kaolinite.
- Presence of biogenic carbonate and silica.
- Precipitation of authigenic minerals on the seafloor.

Meteoric water is rainwater and the flow of meteoric water needed for mineral dissolution and precipitation in the shallow depth. Both of the wells which have high velocity in shallow depth are located in the eastern side of the basin. The paleo coast line is in the east as well (Ch.2 Fig. 2.6). The meteoric water flow is higher in the eastern side which influences more shallow water precipitation in the east than in the west (Fig. 5.13).

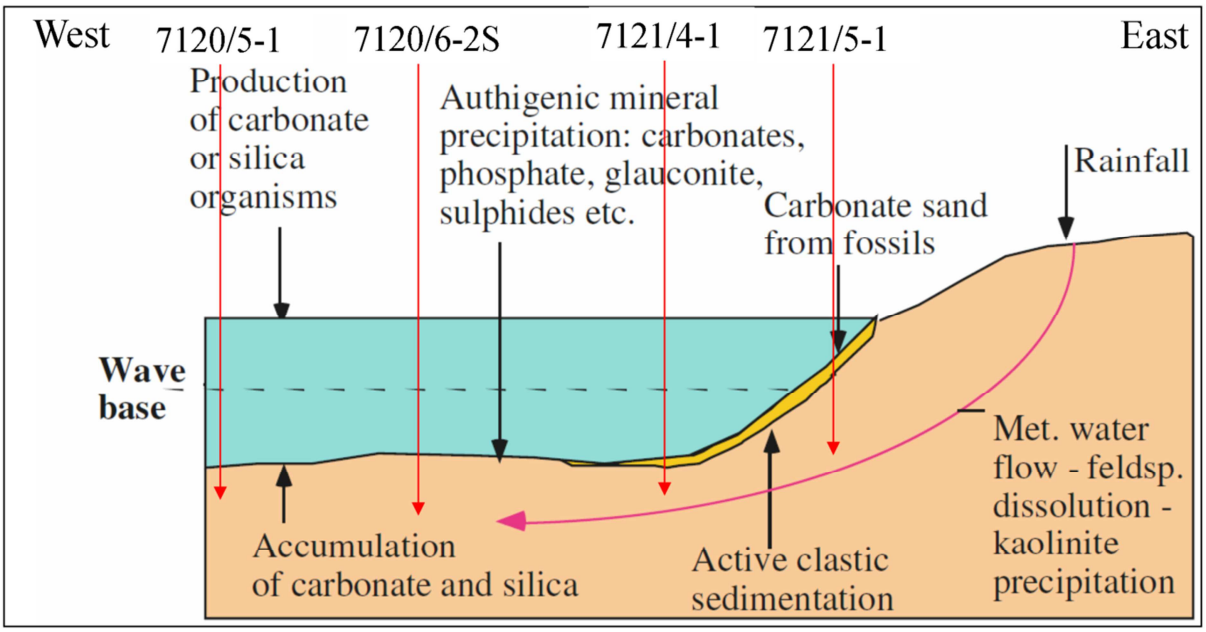

Fig 5.13: Diagenetic processes in shallow marine environments with the schematic distribution of the wells (modified after Bjørlykke and Jahren, 2010).

The gamma ray log of the studied area gives two distinct lithological units (sandstone and shale). These two units separate from each other along the Fuglen-Stø formation boundary. The gamma ray readings are different from well to well though the trends similar. The location of the wells in paleo-depositional environments is another reason for different gamma ray readings within same formation.

The thickness of the main reservoir rock (Stø Formation) is increases from east to west whereas the source rock (Hekkingen Formation) thickness is decreases from west to east (Fig.

5.14). The depositional setting is responsible for that. The Stø formation is deposited in delta to shoreface environment. The provenance of that time is located in the south-east direction which has carried a lot of sediments from the south-east. On the other hand, Hekkingen formation is deposited in deep sea depositional condition which does not allow more sediment to go further west. Moreover, the Kolje and Knurr Formations have been thinned out in the western well 7120/5-1 which is similar depositional environment like Hekkingen.

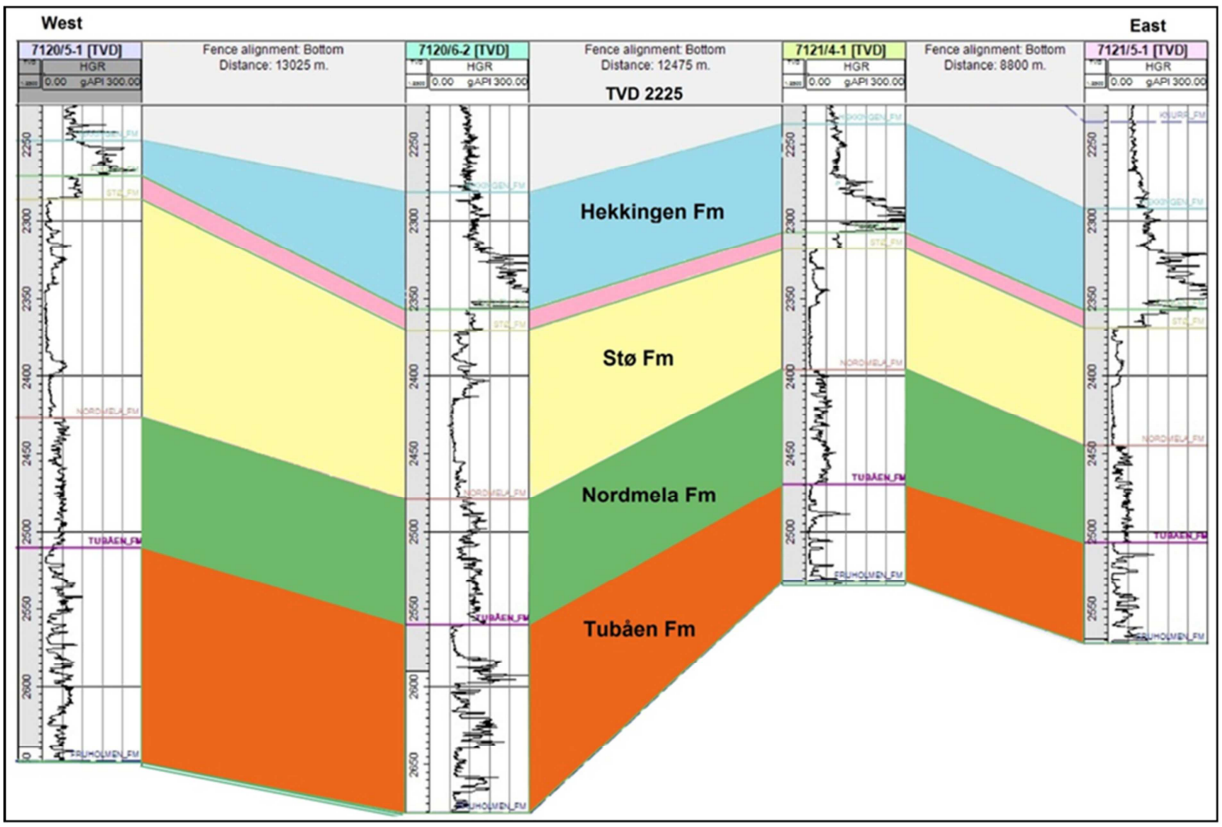

Fig. 5.14: Formation correlation of different wells using gamma ray log from west to east.

5.2.2 Transition from mechanical to chemical compaction

The overall present day transition (MC to CC) depth is shown in Figure 5.15. The transition depth is decreased from north to south. The present day structural setup of this basin is very complex which explains variations in the transition depth. The transition depth is very much dependent on temperature which is the key factor to change the compaction process of sediments from mechanical to chemical. The present day temperature gradient is very low in westernmost well 7120/5-1, though the present day transition zone is almost similar in other wells (Fig. 5.16). The temperature gradient of this well shows 23^0C/km whereas the other wells mostly show between 32 and 35^0C/km. This is a big difference within very small area. The present day transition depth comparing with present day temperature gradient gives an idea about the paleo temperature gradient in this area. The transition depth of well 7120/5-1 indicates that the paleo temperature is more or less similar with other wells, but present day temperature is too low when compared with other wells.

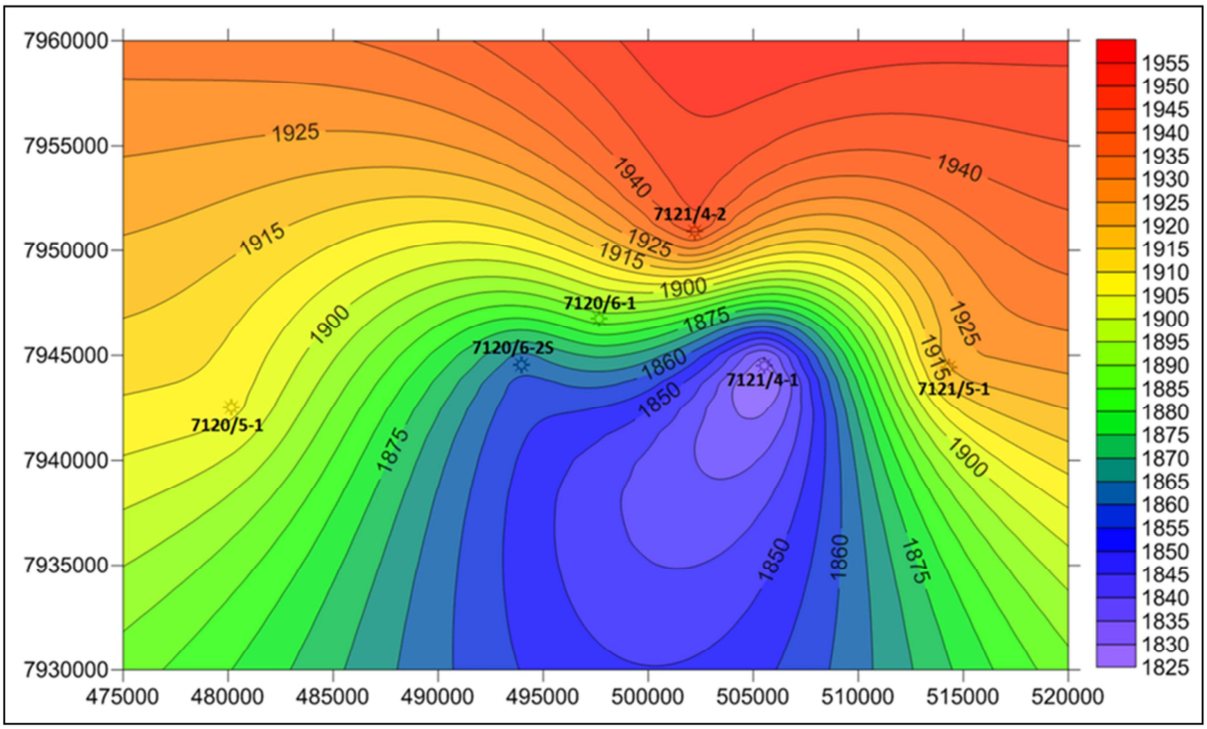

Fig. 5.15: Present day transition depth contour map with studied wells.

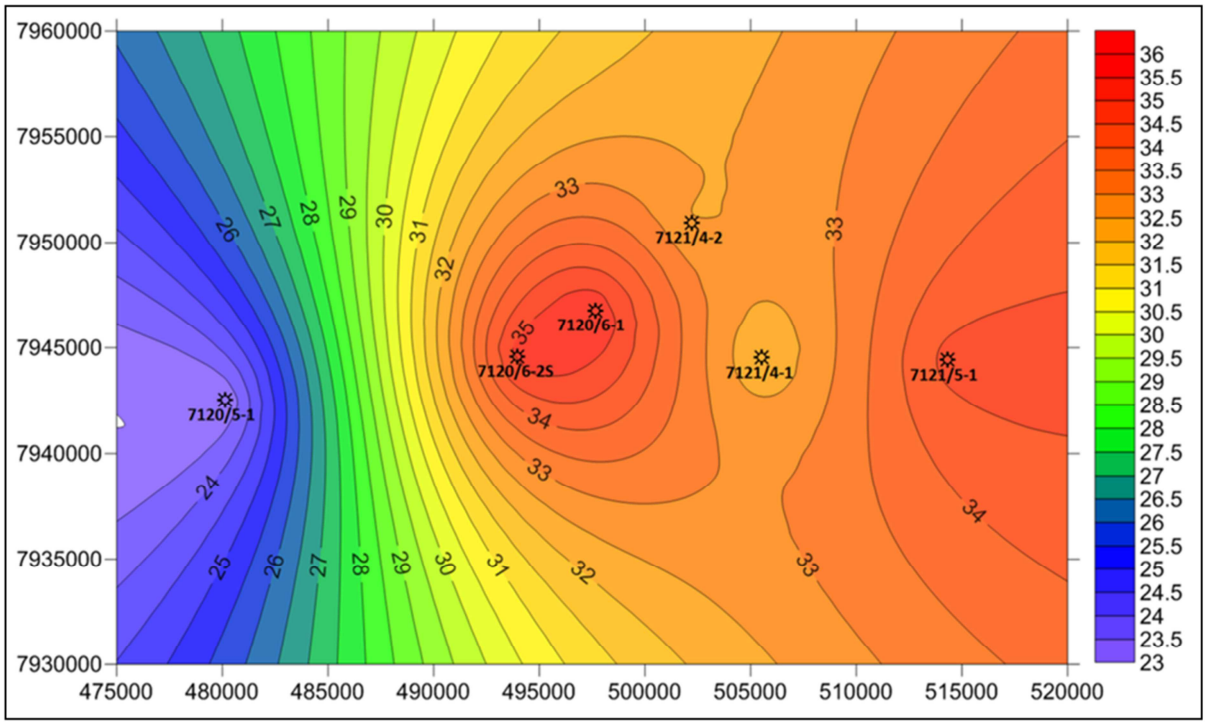

Fig. 5.16: Present day temperature gradient of the studied area.

The TZ has been identified within the Knurr Formation. This formation is a mudstone unit in studied area. Even all formation above the Knurr Formation is shale units. Hence, all MC zones comprised with mudstone units. The compaction of mudstones is mainly controlled by mineralogy and micro-fabric (Fawad et al., 2011) which mainly depends on temperature. In the well 7120/5-1 1^0C temperature changed in the transition (MC to CC) point is responsible for the density shifting from 2.1 to 2.7 g/cc. On the other hand, Vp has shifted from 3400 to

3800 m/s (Fig. 5.7). Moreover, almost all wells have increased velocity around 400-500 m/s in the transition point (Fig. 5.4). This sharp increase in velocity and density is not due to a sudden change in lithology but rather a chemically induced change controlled by thermodynamics.

Present day temperature in the transition depth is not a sufficient parameter to infer thermal and chemical aspects of the transition zone. It is lower than the standard temperature which indicates uplift and erosion. After adding exhumation depth to the present day transition depth the temperature is more reliable except for the well 7120/5-1. This well shows low temperature because of the effect of low present day temperature gradient as discussed earlier (Fig. 5.17).

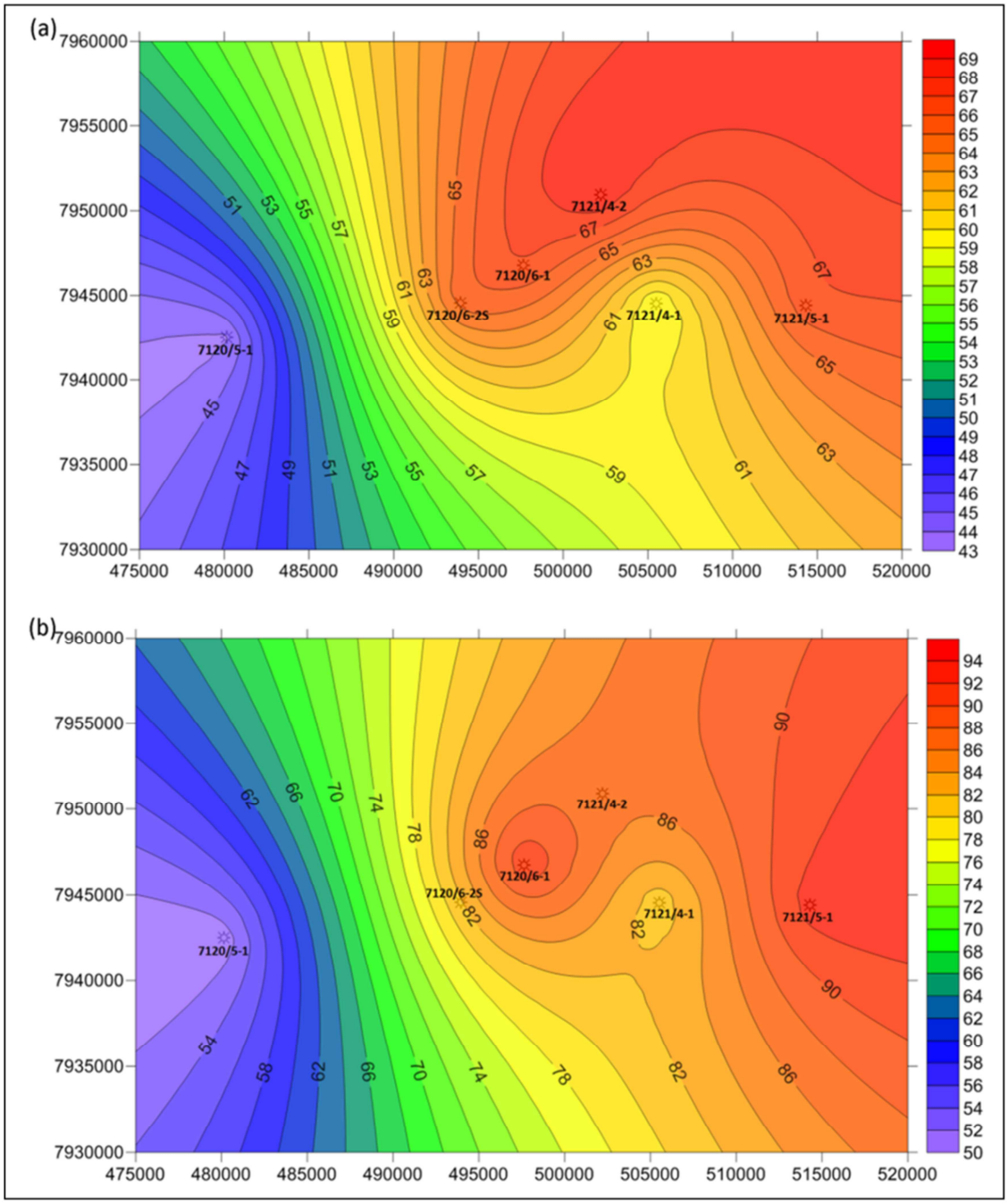

Fig. 5.17: The contour map of transition depth temperature (a) present depth, (b) before exhumation.

From the above discussion, it is clear that no unique burial depth curve exits in the nature, it changes from well to well, from basin to basin. For instance, as observed in this study, the transition depth is different from well to well. The temperature is also different (Table 5.4) and can be misleading if a unique burial history is used. It is very important to know local structural history and paleo temperature gradient to identify the actual rock properties in different wells.

Table 5.4: The transition depth temperature at before and after exhumation

Well No.	Transition depth at present day (m)	TZ Temperature at present day (^{0}C)	Transition depth before exhumation (m)	TZ Temperature before exhumation (^{0}C)
7120/5-1	1907	43.85	2207	50.76
7120/6-1	1888	66.95	2588	91.77
7120/6-2S	1860	65.56		
7121/4-1	1827	58.81	2507	80.70
7121/4-2	1944	69.01	2664	86.58
7121/5-1	1922	66.67	2682	93.04

5.2.3 Uplift estimation

The total exhumation calculation is very important for exploration in an uplifted basin. It gives the actual temperature history of the reservoir and source rocks. Temperature is the major controlling factor of compaction (both mechanical and chemical), diagenesis, source rock maturation, cap rock integrity and hydrocarbon migration. Compaction based on well data reveals that, in the mechanical compaction zone the natural shales were compacted more than experimental kaolinite-silt mixtures at the equivalent effective stress level (Fig. 5.11). This high velocity in natural compacted shales could be because of higher stress experienced by the sediments before exhumation. This signature is still present though it is uplifted several hundred meters.

The mineralogy and textural compositions of shales are very important during compaction such that velocity-depth trends vary greatly in different types of shales (Storvoll et al., 2005). The mineralogy of shales used in this uplift estimation is not analyzed due to the lacking of thin sections. However, different experimental curve data in the well 7120/6-1 give different exhumation results (Fig. 5.10) showing the importance of mineralogy and textural composition during exhumation estimations. The fixed mineralogy of experimental curve is different from the composition of natural compacted shales. Hence, composition variation between the data and experimental curves influenced uplift estimation. Due to this effect when the first data point touches the experimental curve during exhumation estimation, the rest of the mechanical compaction parts do not exactly follow the laboratory experimental curve.

There are some uncertainties such as calculation of volume of shales, overlapping of natural compacted data with experimental curve are influenced the exhumation estimation. However,

the estimated exhumation values in the studied area have been followed the curve published by Ohm et al. (2008) using vitrinite reflectance data (Fig. 5.18). The estimated uplift has a general increase in the magnitude from west to east.

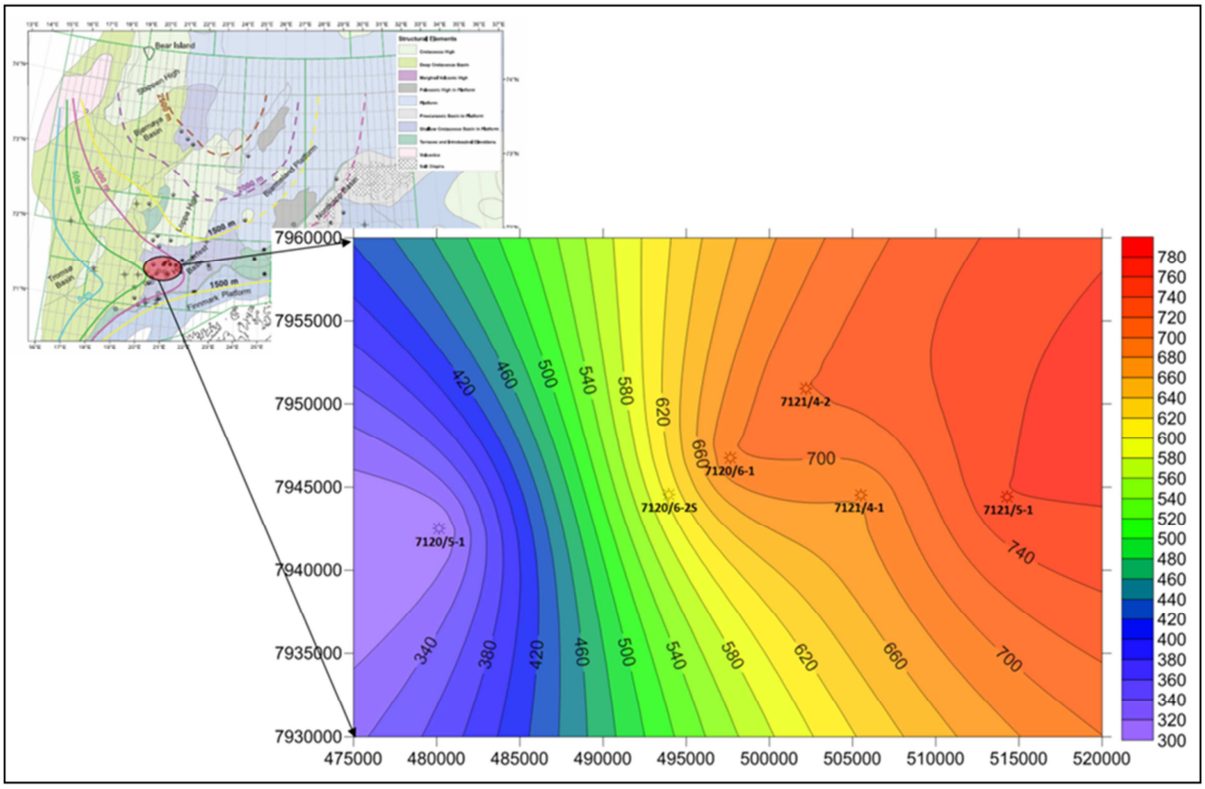

Fig. 5.18: The contour map showing the uplift based on the experimental curve of the study area (inset Figure) uplift map based on vitrinite data (modified after Ohm et al., 2008).

Present day temperature of well 7120/5-1 pay attention because of its low temperature gradient. Present day temperature within main source rock (Hekkingen Formation) is around 52^0C which is not enough to generate hydrocarbon (HC) (oil window start at 70-80^0C). On the other hand, the main reservoir rock (Stø Formation) has temperature around 53^0C. Hence, cementation ended up in present day temperature situation. However, it is very important to know the time interval of present day temperature condition in well 7120/5-1. This time interval helps to evaluate the reservoir rock properties as well as source rock maturation.

Chapter 6: Rock physics analysis

UNIVERSITY OF OSLO

FACULTY OF MATHEMATICS AND NATURAL SCIENCES

Chapter 6: Rock physics analysis

Rock physics studies are used to improve the understanding of rock properties. These rock properties show an uncertainty estimation of amplitude and corresponding elastic responses. Rock physics study reduces these uncertainties of rocks. To date, most of the published trends are derived from grain-supported, pure quartz sandstones (Polyaeva et al., 2011). Hence, rock physics analysis of mineralogically and diagenetically complex reservoirs such as the reservoirs of Hammerfest Basin are poorly understood. These complexities exhibit a wide range of elastic properties that depart from the results of the published trends.

The main challenge in this project is to overcome these complexities and find a better understanding of reservoir lithologies and fluids. To do this, the following topics are described briefly: the basic rock physics analysis of Stø formation and rock physics diagnostics using Rock physics templates (RPT) for all formations belongs to Kapp-Toscana Group. The direct measurement of Vs data is only available in well 7120/6-2S. Hence, this well is used in almost every section.

6.1 Results

6.1.1 P-wave Velocity – Density – Porosity effect

Density measured by logging tools is the simple volumetric average of the rock constituent densities. The density is closely related to porosity. Velocity is often not very well related to porosity. In a very tight sandstone (porosity near to zero), cracks and grain boundaries can be substantially decreases the velocity but the porosity change might be negligible (Mavko et al., 2009). This complex relation of velocity and porosity makes the relationship between velocity and density more complicated. Ignoring theses complexities Gardner et al. (1974) suggested a useful empirical relation between Vp and density. This equation is used for calculating density from velocity where there is no density logs exist.

The Gardner density calculated from Vp is plotted with measured density of Stø formation in well 7120/6-2S (Fig. 6.1). The Stø Formation is divided into 3 units based on their lithological compositions. Facies 1 (red) represents shaly sandstones whereas facies 2 (cyan) represents clean sandstones. Facies 3 (blue) combines the lithologies both in facies 1 and 2. Depth-density (Fig. 6.1a) and Vp-density (Fig. 6.1b) plots show that, the direct measured density in facies 2 and 3 are matched well with Gardner equation derived density but not in facies 2. The Gardner density has been calculated from Vp. This Vp log is influenced by mineralogy and fluid content of the rock bodies. So, this velocity changes with different parameters (mineralogy and fluid) make it non-satisfactory for expressing the real density as observed in the facies 2. Another important parameter is effective pressure which influences the velocity-density relationship. The pressure distribution in an uplifted basin is very complicated. Hence, the pressure affected velocity and density in the Hammerfest basin are also complicated. Even though, there are many limitations in Gardner equation regarding the uplift affected rock properties, it is still very useful for many rock types. Finally, one has to be careful when using this relation in complicated fluid saturation or effective pressure conditions.

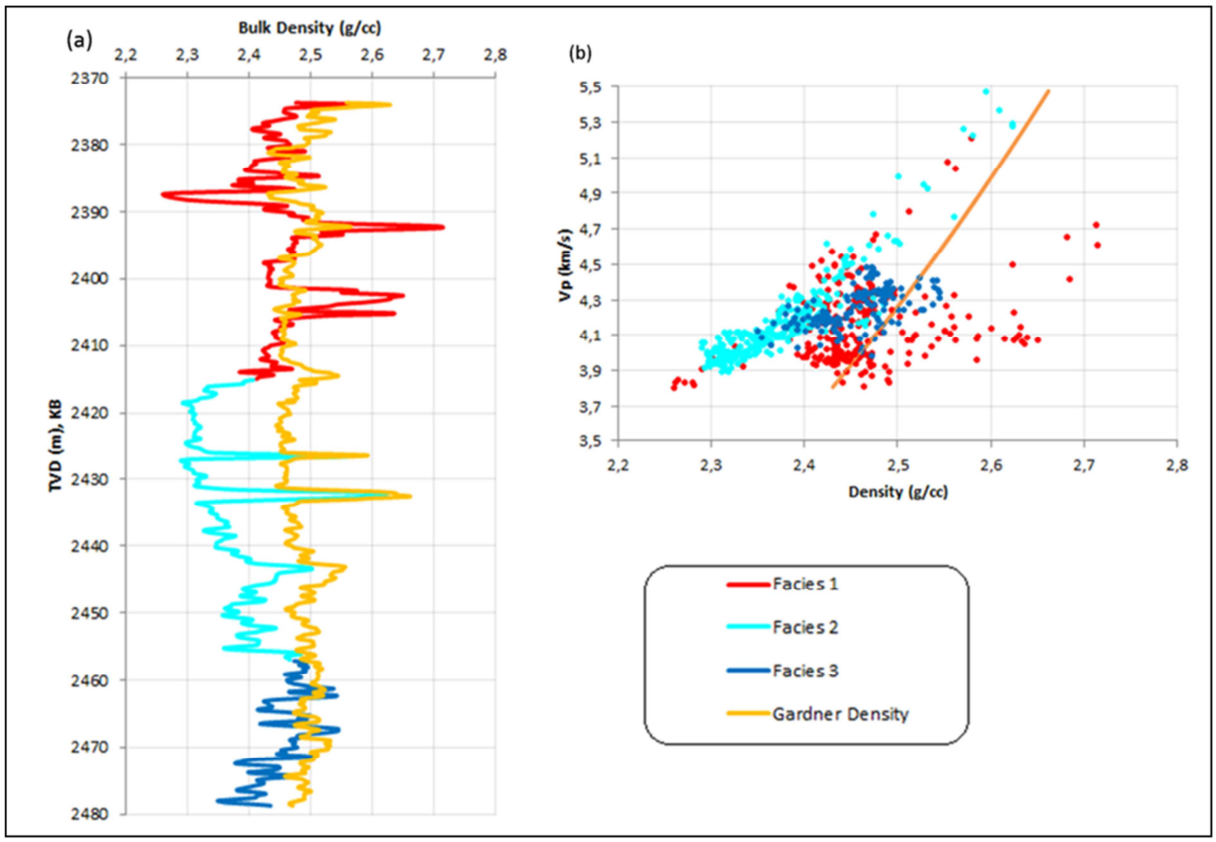

Fig. 6.1: Comparison of measured and Gardner density with three distinct facies (a) density versus depth and (b) density versus Vp plots of Stø formation in the well 7120/6-2S.

The density porosity of clean sandstones (facies 2) has been plotted against Vp shown in Figure 6.2. The data points have been divided into two units based on saturation. The red represents hydrocarbon saturated sandstones whereas black represents brine saturated. Three established reference curves were also plotted; Wyllie et al. (1956) (redish), Gardner et al. (1974) (green) and Raymer et al. (1980) (blue). Most of the data points fall between Raymer and Wyllie reference curves except few. The water saturated data points are closer to the Wyllie curve, whereas hydrocarbon saturated data points are closer to Raymer curve. The Wyllie curve underestimates the data points, whereas Raymer equation overestimates. Gardner reference curve under-predicts all of the measured values.

The facies 2 (clean sandstones) data points plotted herein are not clay free sandstones which are the pre-requisite for all three curves. Isotropic rock medium and consideration of the same velocity for all the constituent minerals are the limiting assumptions for these three relations. In nature, rock is not isotropic and rock constituent minerals have different velocity ranges. Hence, the data points are shifted from reference curves. Moreover, the uncertainties of density porosity make the data distribution ambiguous to some extent.

The porosity calculating using Wyllie porosity equation has been plotted with density porosity both against depth (Fig. 6.3a) and Vp (Fig. 6.3b). The variation is more sever in the hydrocarbon saturated part compared to brine saturated part. The Vp-density trend of Wyllie equation does not follow the real data trend. A great mismatch is found between these two trends. Therefore, it is important to consider these errors when the equation is applied.

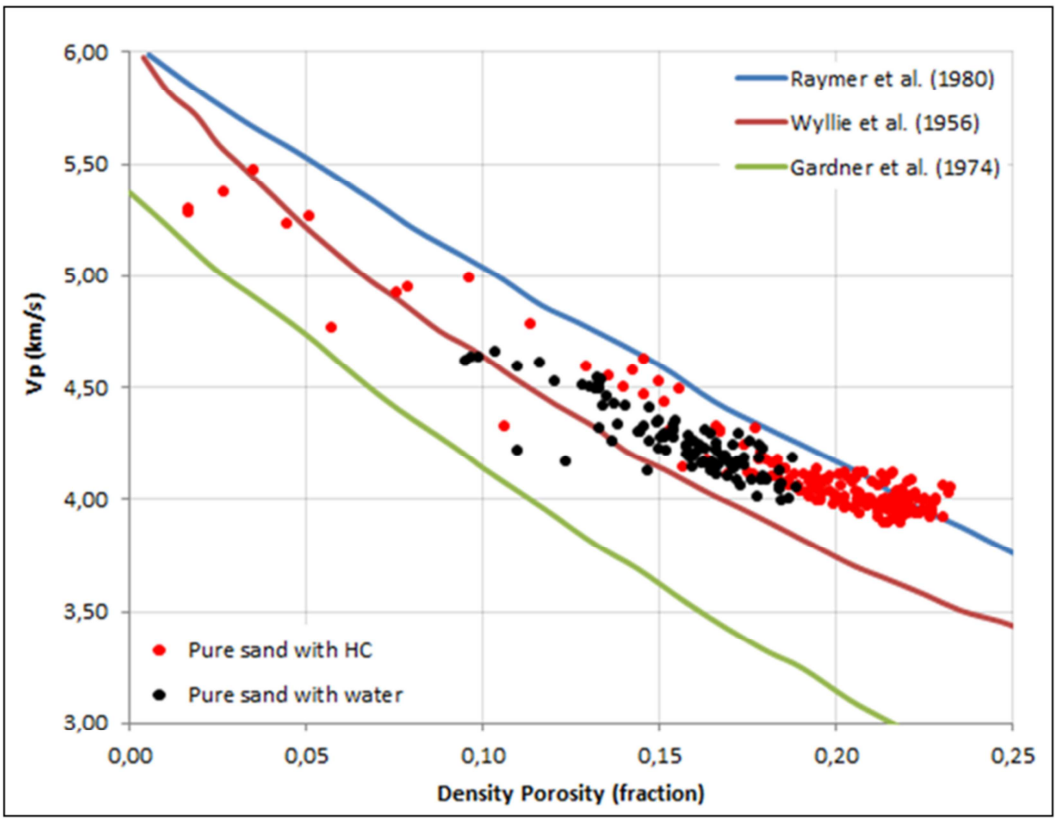

Fig. 6.2: Density porosity versus Vp cross-plot of hydrocarbon and water saturated rocks in the facies 2 of Stø formation in well 7120/6-2S with Raymer et al. (1980), Wyllie et al. (1956), and Gardner et al. (1974) established curves.

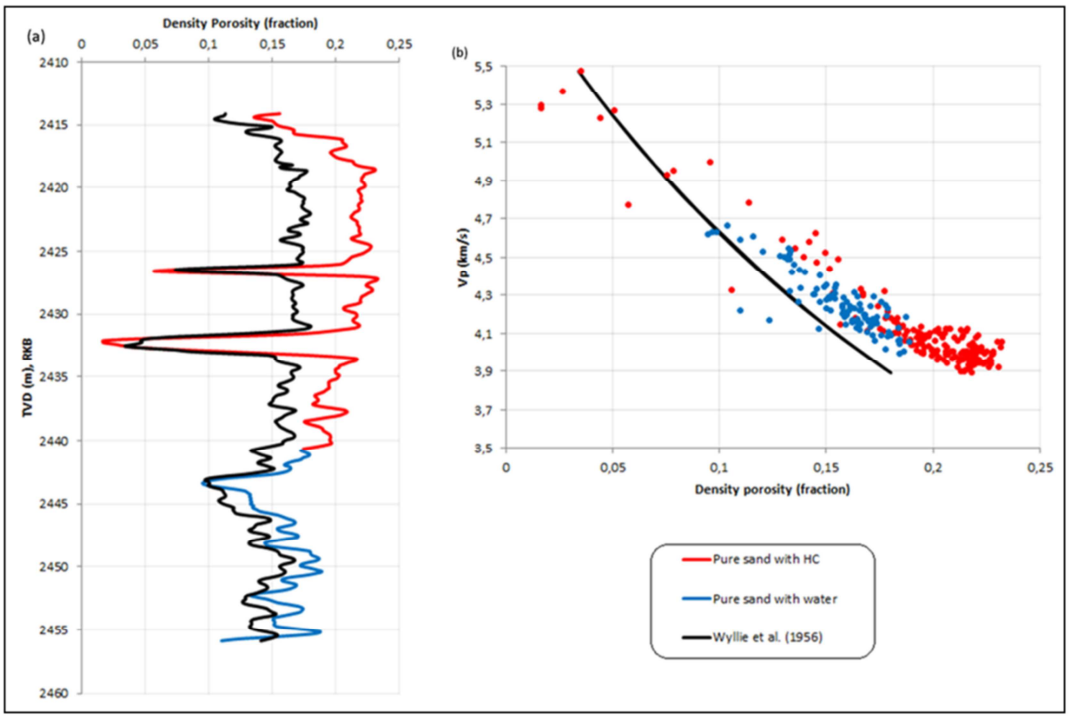

Fig. 6.3: Comparison of measured and Wyllie porosity in different fluid saturated sandstones (a) density porosity versus depth and (b) density porosity versus Vp plots of Stø formation in the well 7120/6-2S.

6.1.2 P-wave velocity – Porosity – Clay volume effect

Wyllie et al. (1956), Gardner et al. (1974) and Raymer et al. (1980) equations have been used for pure quartz sandstones. These equations did not consider clay content within sandstones. However, clay particles simultaneously deposited with sandstones in a sedimentary basin which subsequently affect the velocity-porosity relationship. Han (1986) specified an empirical relation combined with velocity-porosity and clay contents.

The Vp-porosity data points in the Stø Formation from well 7120/6-2S are plotted with Han's different clay volume fraction curves which are calculated at 40 MPa effective pressures condition (Fig. 6.4). The data points were divided into four different units based on clay volume fractions. The data shows a nice trend illustrating a decrease in Vp and porosity with increasing clay contents. The data points with 0-10% clay content fall between 5-25% Han's line, whereas data points with 10-20% clay content follow 25% line. The rest of the data follows 35% Han's line.

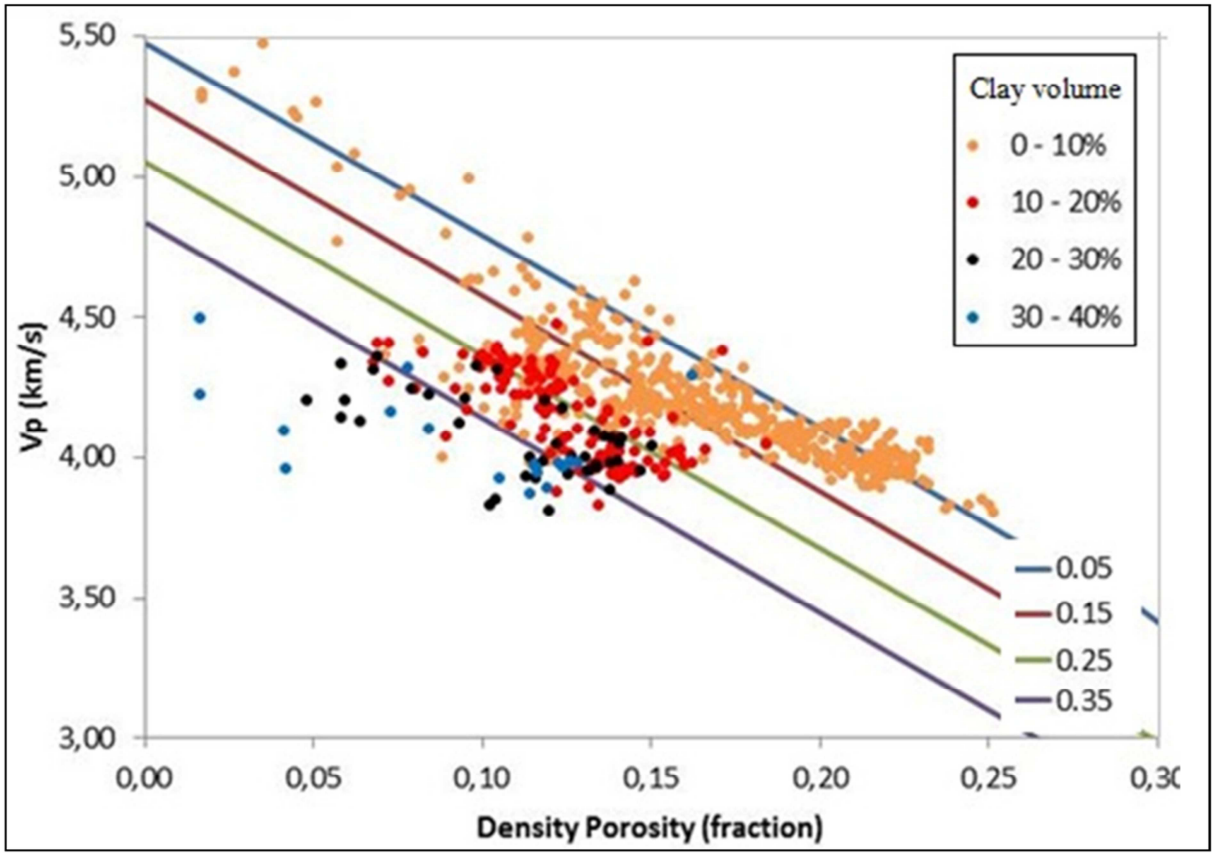

Fig. 6.4: Density porosity versus Vp of the Stø formation in the well 7120/6-2S compared to Han's empirical relation at four different clay fractions at 40 MPa effective stress.

One important observation in an uplifted basin is the effective stress. The rock stiffness and present day effective stress do not follow each other. The rock is stiffer than expected considering the present effective stress. It represents higher velocity than ones at similar depths located in normally subsided sedimentary basins. All the equations assume effective stress to be mainly interconnected with stiffness of the rock. So it is very important to know the actual depth of burial to identify the rock stiffness which is needed when using these equations. Another parameter is clay volume calculation which influences the result of the

calculation. Gamma ray log is used to calculate clay volume. The density porosity is also not the actual porosity because of mineral and fluid density variations. These two important parameters deviate the data points from Han's empirical lines.

6.1.3 Rock physics analysis of litho-facies

The porosity of three facies in the Stø Formation in the well 7120/6-2S has been plotted against (a) bulk modulus, (b) shear modulus, (c) Vs and (d) Vp/Vs (Fig. 6.5). An unconsolidated or friable sand model (green line) was also displayed. Facies 1 consists of shaly sand with gas fill. On the other hand, Facies 2 is the cleanest sand with gas, oil and water saturation respectively and Facies 3 is water saturated cleaner sandstones (Ch. 4, Fig. 4.3). The log response in different plots against friable sand model is different. Distribution of different facies within plots is different. In bulk modulus plot, facies 1 shows lower modulus compared to other facies. Clean sandstone (Facies 2) has higher porosity as expected but bulk modulus is higher in shaly sandstone (Facies 1). On the other hand, shear modulus and Vs values of clean sandstone is lower than that of shaly sandstone. However, because of fluid effect in bulk modulus, clean sandstone has higher modulus than shaly sandstone. While Vs and shear modulus do not have any fluid sensitivity, give high porosity low modulus in clean sandstone compare to shaly sandstone. The bulk modulus data distributed sparsely, whereas there is a trend in shear modulus and Vs plots. Because of higher Vp and lower Vs in clean sandstone (facies 2), Vp/Vs ratio is higher which shows in Vp/Vs plot. However, higher Vp/Vs ratios expected in shales than sands (Avseth et al., 2005) which do not follow these facies (clean sands have higher Vp/Vs ratio).

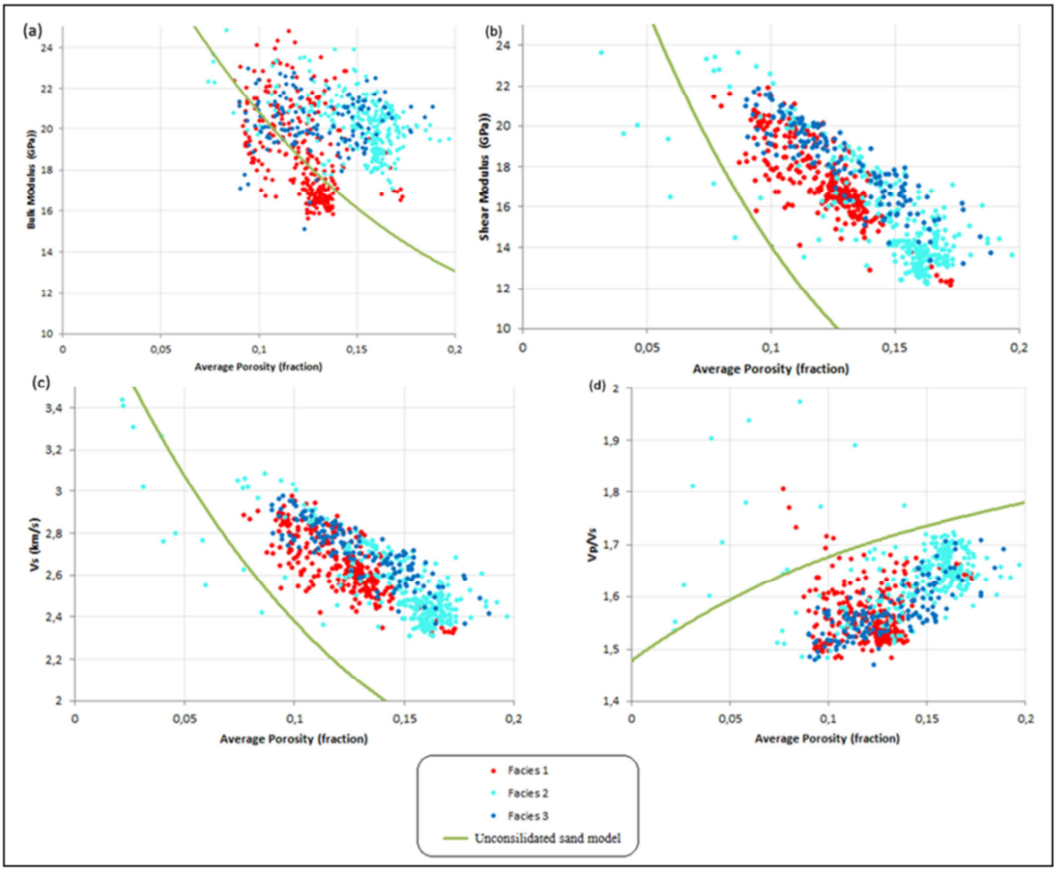

Fig. 6.5: Different facies in Stø formation from the well 7120/6-2S in the (a) Bulk modulus- porosity, (b) shear modulus-porosity, (c) Vs-porosity and (d) Vp/Vs-porosity cross-plots.

The shaly sandstones have higher Acoustic Impedance (AI) values than those of the clean sandstones. Both density and Vp is higher in shaly sandstones which comprises a higher value of AI (Fig. 6.6a). Poisson's ratio (PR) depends on Vp/Vs ratio. The cross-plot of PR versus porosity exactly follows the similar trend to Vp/Vs versus porosity cross-plot (Fig. 6.6b). The PR versus AI cross-plot shows good lithology separation (Fig. 6.6c). Clean sandstones have low AI and high PR compared to shaly sandstones. This cross-plots show a good lithology indicator.

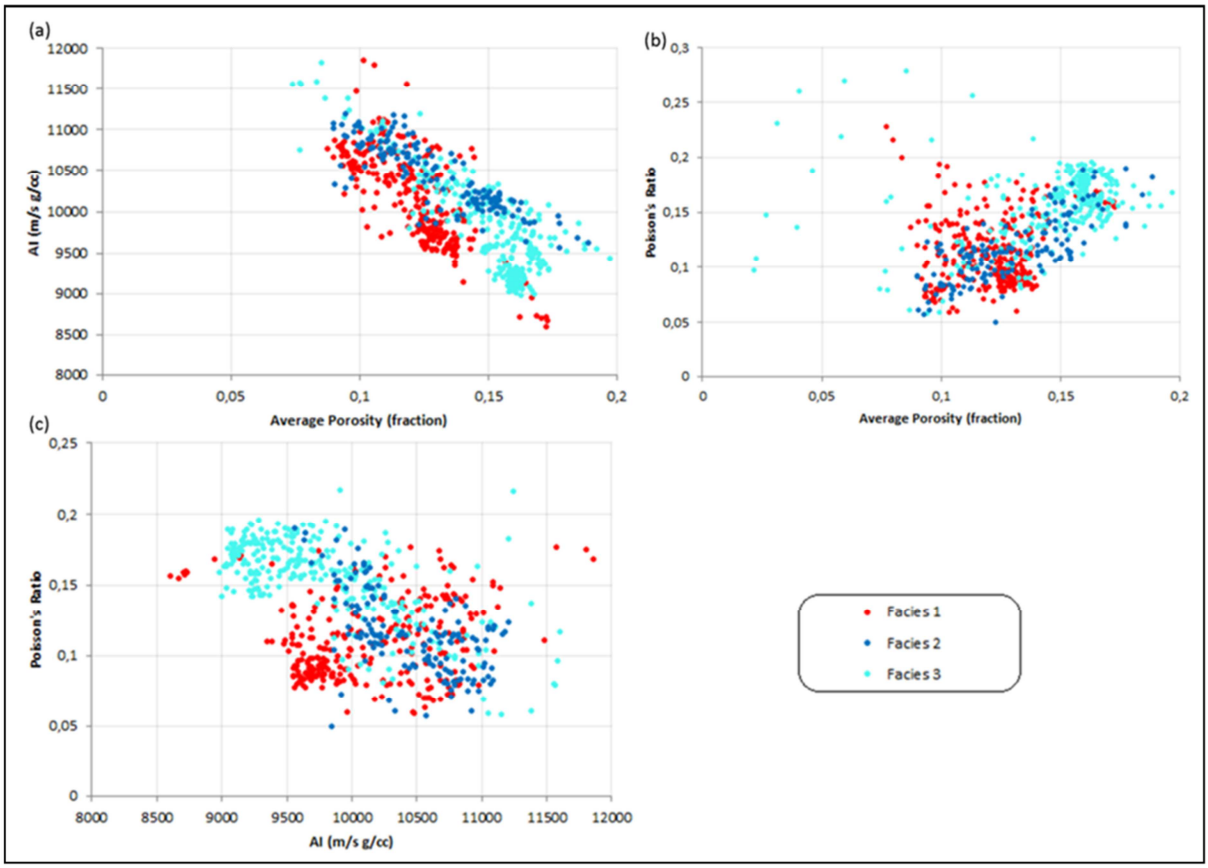

Fig. 6.6: Different facies in Stø formation from the well 7120/6-2S in the (a) AI- porosity, (b) Poisson's ratio-porosity and (c) Poisson's ratio – AI cross-plots.

6.1.4 Shaly sand model

The data taken from the Fruholmen Formation in the well 7120/6-2S in a depth range 2710 to 2734 m (TVD RKB) (Fig. 6.7) were used for shaly sand model. Based on gamma ray response, the whole section has been divided into 3 distinct facies. Facies 1 represents shale (light purple) whereas facies 3 represents sandstone (green). Facies 2 (cyan) shows the data from shaly sand to sandy shales. This data set has been used for validating the shaly sand model in rock physics analysis.

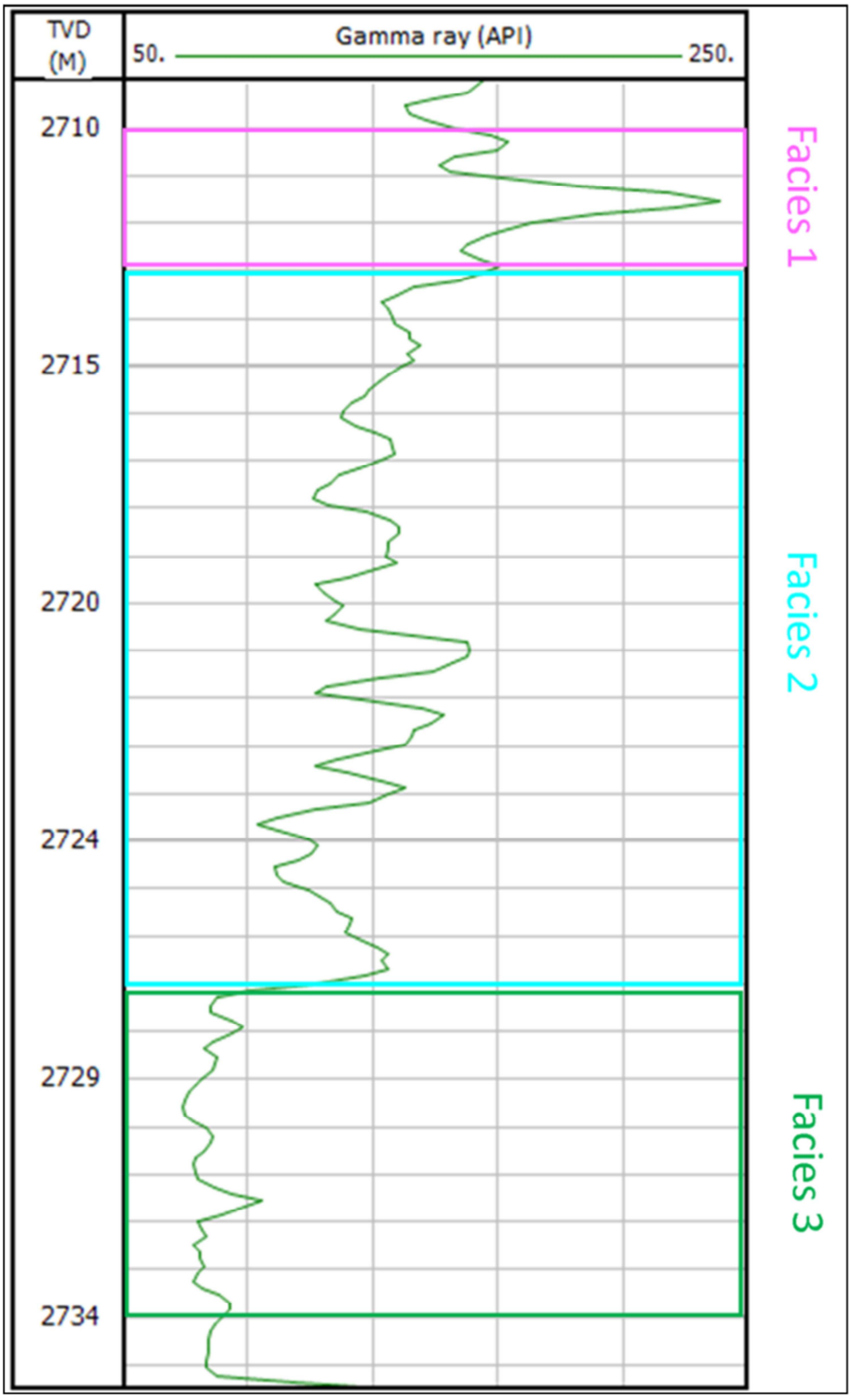

Fig. 6.7: The gamma ray log of Fruholmen formation in the well 7120/6-2S showing three different facies where facies 1 is shale, facies 2 is sandy shale to shaly sand and facies 3 is sand.

For shaly sands, it can be assumed that porosity will decrease linearly with increasing clay content. But Marion (1990) first introduced the V-shape (in case of porosity-clay content) or inverted V-shape (in case of velocity-clay content) behaviors of sand-shale mixture instead of linear relationship. According to Marion et al. (1992), porosity decreases and velocity

increases with increasing clay content up to a critical clay point. This point is the transition point between shaly sand to sandy shale. Above this point porosity increases and velocity decreases with increasing clay content.

This three facies from the Fruholmen Formation are plotted in Vp versus volume of shale (V_{sh}) (calculated from gamma ray) plot which shows the inverted V shape behavior (Fig. 6.8). The velocity starts to increase from sandstones to shaly sandstones because pore space is filled with fine grain particles. The velocity continues to increase up to 4.95 km/s at 40% clay content. When it cross 40% clay content, the velocity starts to decrease. This is the critical clay point where the velocity decreases with increasing clay content. This point is also the transition point from shaly sand to sandy shale. The velocity continues to decrease till 100% shale. This transition point (shaly sand to sandy shale) is different in different grain size distributions (Mondol et al. 2007).

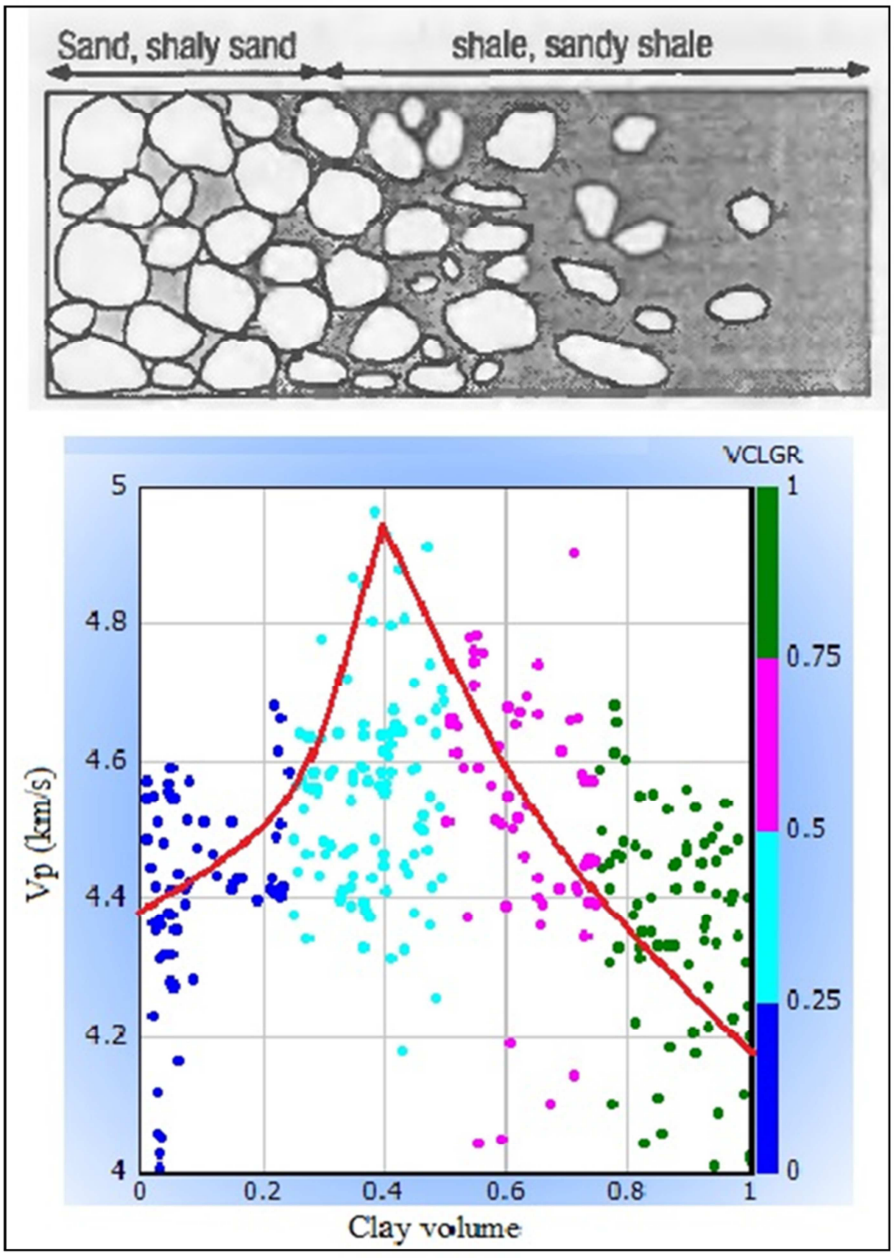

Fig. 6.8: The clay volume versus Vp plot showing the inverted V shape behavior explained by Marion et al. (1992).

6.1.5 The cement model

The important quartz cement models are introduced by different authors. These are:

- The contact cement model by Dvorkin et al. (1994).
- The friable or unconsolidated sand model by Dvorkin and Nur (1996).
- The constant cement model by Avseth et al. (2000).

Figure 6.9 shows all three cement models. The friable cement model is calculated using data from Snøhvit field, while contact and constant cement models are adapted from Avseth et al. (2005). The constant cement line consists of 2% constant cement fraction. This model has been used for further analysis in this research.

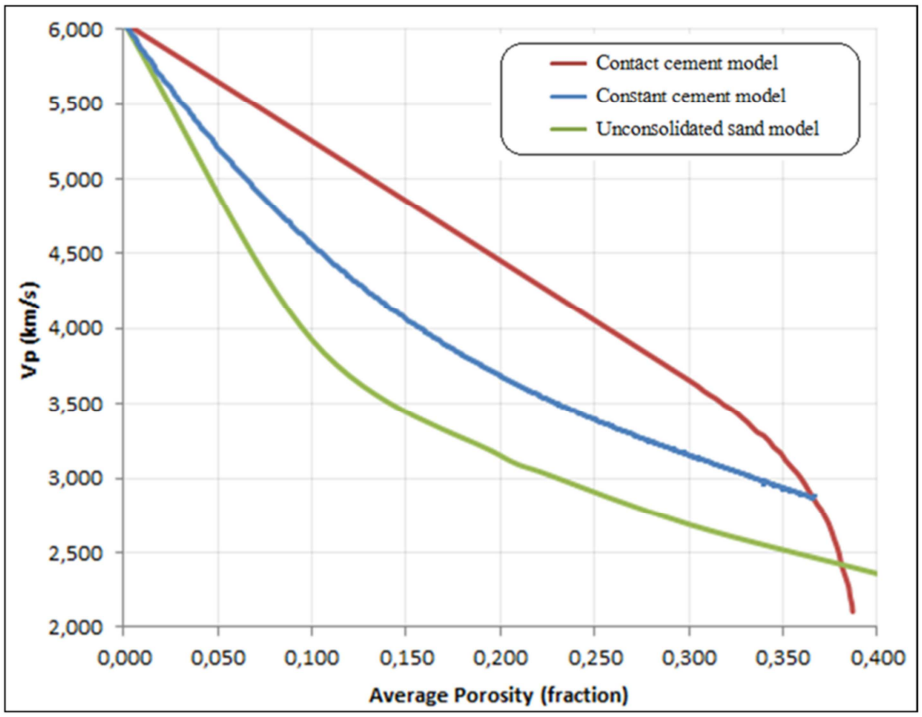

Fig. 6.9: Cement models of pure quartz in water saturated conditions. The constant cement fraction is 2% in the constant cement model.

The Vp of Stø Formation from six wells used is plotted against porosity (Fig. 6.10). It shows different cement distribution within wells. The western well 7120/5-1 has thick Stø Formation which is shown as long cluster of data distribution from constant cement model to friable model. On the other hand, eastern well 7121/5-1 follows more or less friable sand model. The porosity of well 7120/5-1 ranges between 7 to 24% whereas, in well 7121/5-1 shows 18-10% porosity. Moreover, velocity increases from 3.2 to 4.6 km/s in the westernmost well and from 3.2 to 4.1 km/s in the easternmost well. The southern well 7121/4-2 which has maximum overburden above Stø formation (maximum present day effective stress) follows constant cement line. The porosity is low (17-8%), but velocity is higher (3.7 to above 5 km/s).

The well 7120/5-1 located in the western part of the study area is a dry well. Therefore, the western most hydrocarbon filled well 7120/6-2S is used for comparison with easternmost hydrocarbon saturated well 7121/5-1. The well 7120/6-2S shows similar porosity range to well 7121/5-1, but velocity is higher.

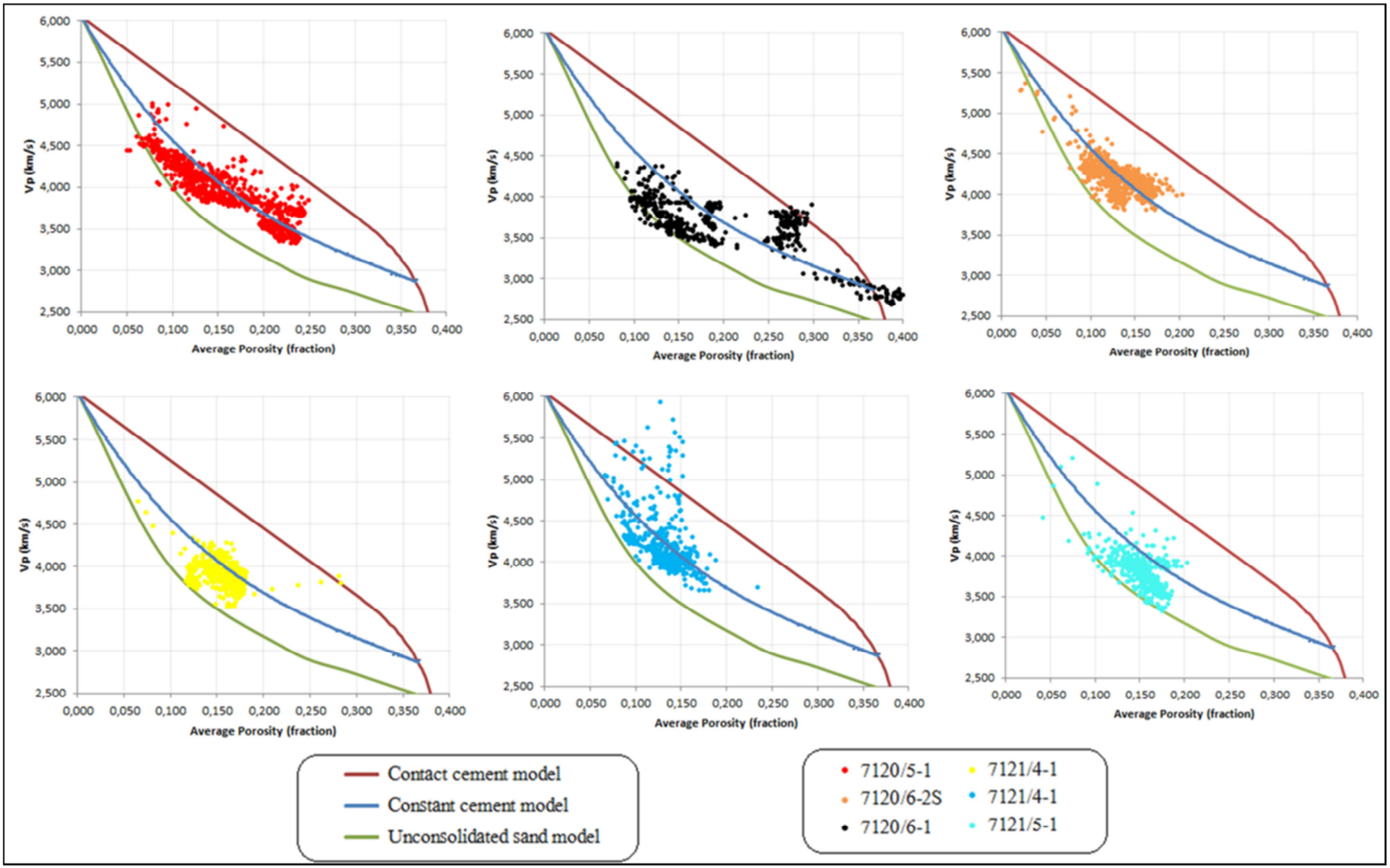

Fig. 6.10: Vp versus porosity cross-plots of Stø formation of six wells with three cement models.

The top of the Stø Formation is in similar depth in both wells (7120/6-2S and 7121/5-1) which is around 2370 m (TVD RKB). Both wells are situated in the same major fault block (Ch. 2, Fig. 2.12) indicating similar overburden stress. The present day temperature gradients of these two wells are very similar (around 66° C/Km) (Ch. 5, Table 5.1). The Vp values of these wells are different though it is as expected in similar compaction conditions (both mechanical and chemical). On the other hand, the gamma ray logs are also showing a big difference in both wells (Fig. 6.11). The gamma ray readings of well 7121/5-1 are low compared to well 7120/6-2S. The pattern of the logs is similar, but different in values. The Vp ranges from 3.5 to 4 km/s in well 7121/5-1, whereas from 3.9 to 4.4 km/s in well 7120/6-2S. Moreover, the gamma ray values ranges from 13 to 50 (API) and 60 to 175 (API) respectively. These lithological variations as well as different velocity affect the cement models. Well 7121/5-1 is closer to friable sand model than well 7120/6-2S. The velocity of well 7121/5-1 is lower than well 7120/6-2S but have similarity in porosity ranges (Fig. 6.11).

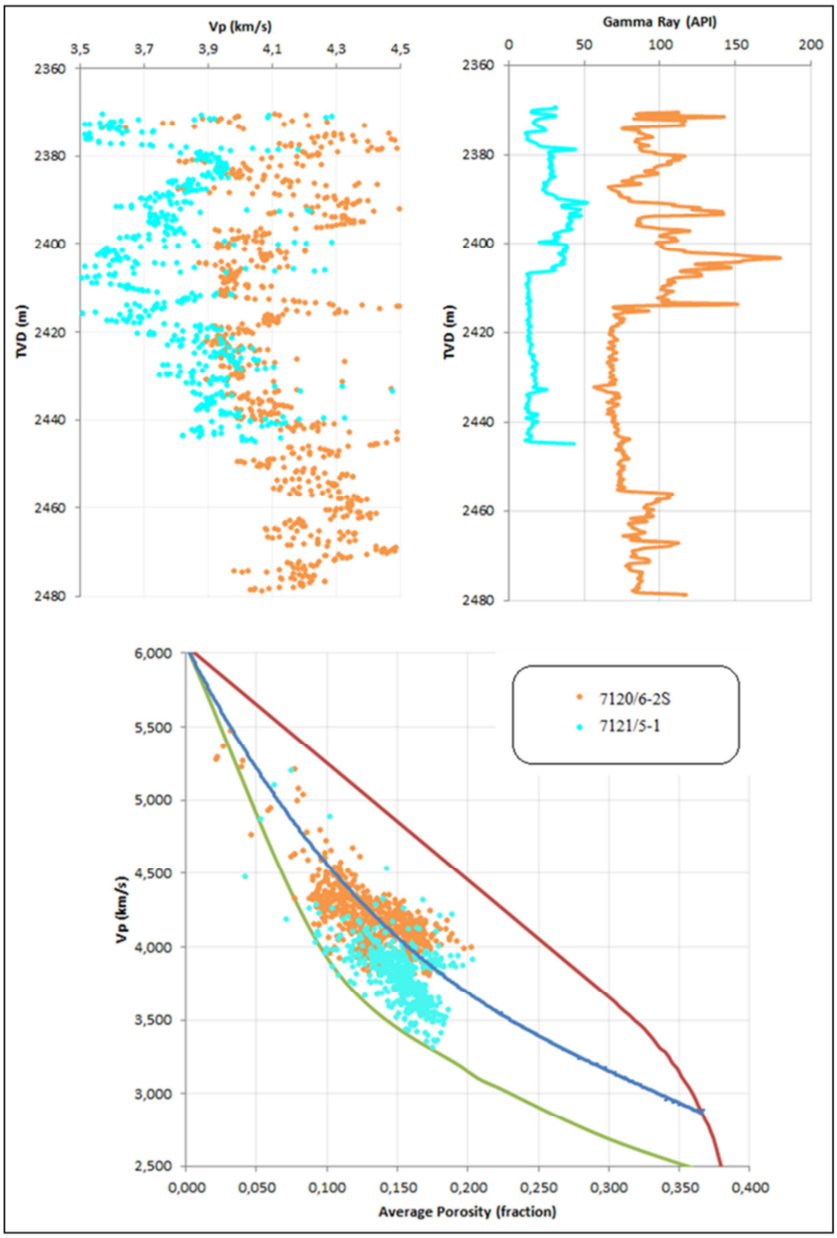

Fig. 6.11: The Stø formation of the wells 7120/6-2S and 7121/5-1 showing the different velocity, gamma ray and cement models.

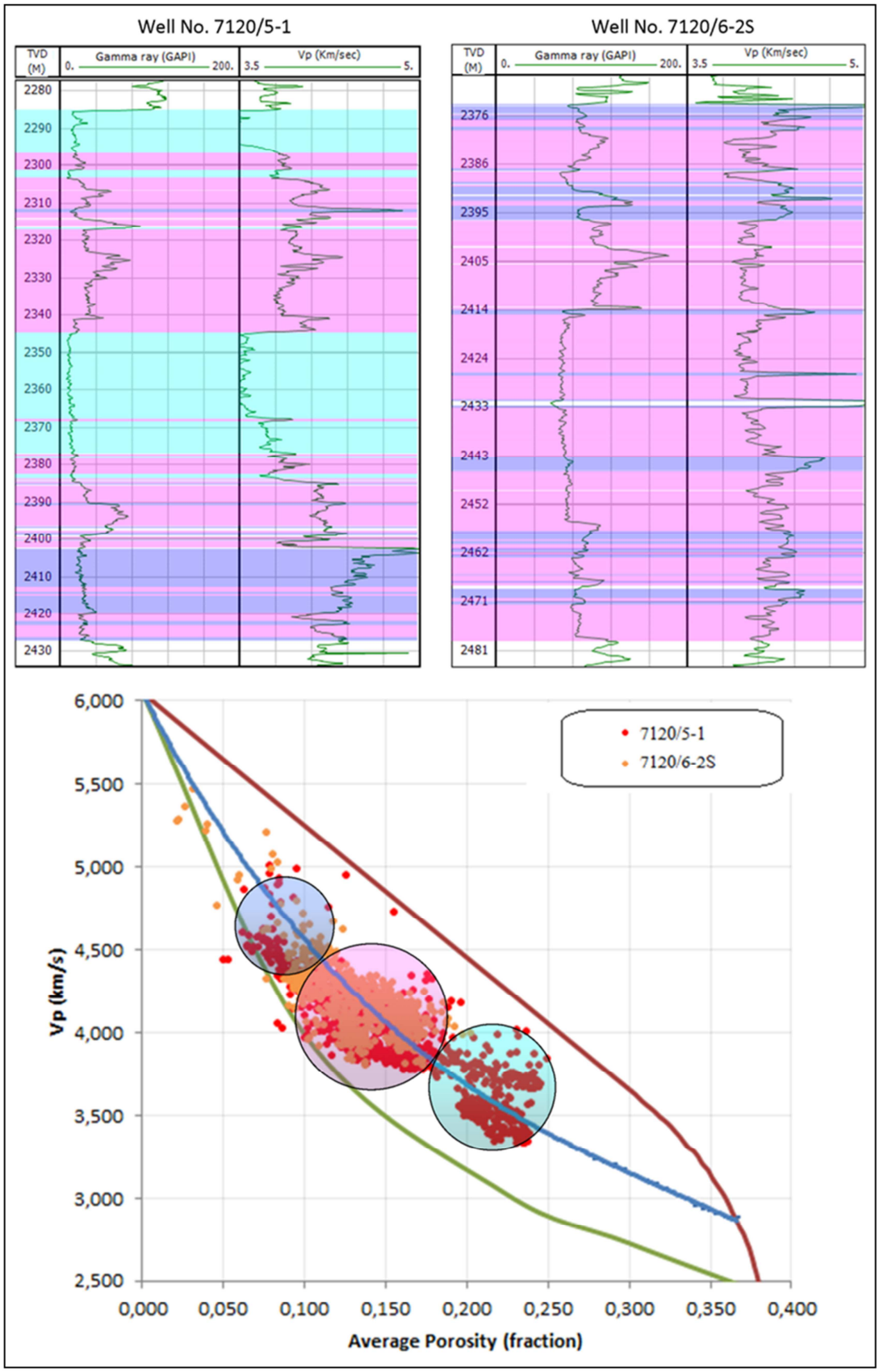

Fig. 6.12: The cross-plots of depth versus gamma ray, Vp and porosity versus Vp with cement lines of Stø formation in the well 7120/5-1 and 7120/6-2 showing the different porosity velocity trends.

Dry well 7120/5-1 is compared to well 7120/6-2S which is gas saturated. These two wells are located in different fault block. The gamma ray reading in well 7120/5-1 ranges from 13 to 90 API which is very low compared to 7120/6-2S (Fig. 6.12). The overall gamma ray log is increasing from east to west in the studied area. Well 7120/5-1 is showing low gamma ray readings. On the other hand, the trend of Vp against depth is also different in comparison with well 7120/6-2S. The facies 2 (cleanest sandstone) and upper part of the facies 1 (shaly sandstone) in well 7120/5-1 show low Vp readings and high porosity (Green) in Vp-depth plot. On the other hand, very little velocity variation is observed within well 7120/6-2S (red) of all zones. The lower part of facies 3 shows very high Vp in well 7120/5-1. The top of the Stø formation starts around 2370 m (TVD RKB) in well 7120/6-2S, whereas it begins around 2285 m (TVD RKB) in well 7120/5-1. These give an idea about present day overburden stress. The well 7120/5-1 has lower present day overburden stress compared to well 7120/6-2S.

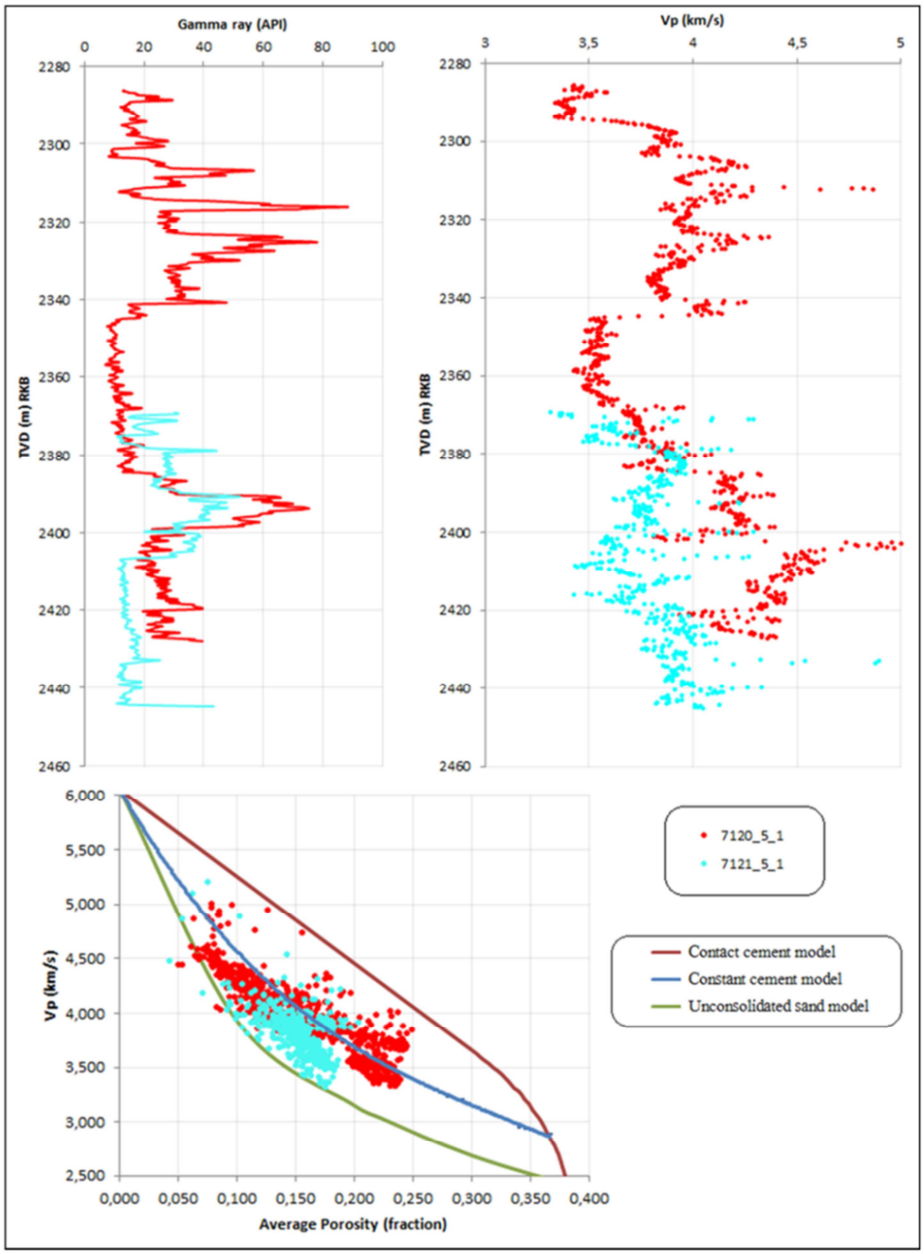

Fig. 6.13: The plots show different cement model trends of Stø formation in the well 7120/5-1 and 7121/5-1 though their gamma ray value shows similar lithology.

The westernmost dry well 7120/5-1 has similar gamma ray response to easternmost well 7121/5-1. The thickness of the Stø formation is increasing from east to west. Hence, the thickness is thicker in well 7120/5-1 than in well 7121/5-1. Both eastern and western wells have more or less similar gamma ray trend. The gamma ray log readings vary between facies to facies. Facies 2 (clean sandstone) has similar gamma ray values whereas in facies 1 in well 7120/5-1 has higher readings compared to well 7121/5-1. The depth of top of the Stø Formation starts at 2285 m (TVD RKB) in well 7120/5-1 and at 2370 m (TVD RKB) in well 7121/5-1. These values (depth of top Stø) indicate that, the present day overburden stress implying on these wells are different. The present day effective pressure are also similar (if similar pore pressure is assumed) in both wells. The velocity of facies 2 is similar in both wells. The facies 1 has higher velocity in well 7120/5-1 compared to well 7121/5-1 (Fig. 6.13). The cement model of these two wells also show different trend. Well 7120/5-1 follows constant cement model, whereas well 7121/5-1 follows the friable sand model.

Three wells from eastern part of the studied area are plotted in the cement model. The wells are 7121/4-1, 7121/4-2 and 7121/5-1. Well 7121/4-2 is located in south-western part of this area. Presently it is also located in a separate fault block compared to well 7121/4-1 and 7121/5-1. However, well 7121/4-1 shows higher Vp values compared to well 7121/5-1 though both wells have more or less similar gamma ray readings (Fig. 6.14). But the present day overburden stress is higher in well 7121/5-1 (based on overburden thickness). On the other hand, cement model has higher cement concentration in well 7121/4-1 compared to well 7121/5-1.

The present day overburden thickness is higher in well 7121/4-2. This thicker unit represents higher effective stress (assume similar pore pressure) than other two wells. Vp value also response with this higher stress. This well shows higher Vp with higher cementation compared to well 7121/4-1 and 7121/5-1. But gamma ray readings of all three wells show similar readings (Fig. 6.14). After exhumation, the overburden thickness ratio between these three wells is almost similar compared to before exhumed thickness.

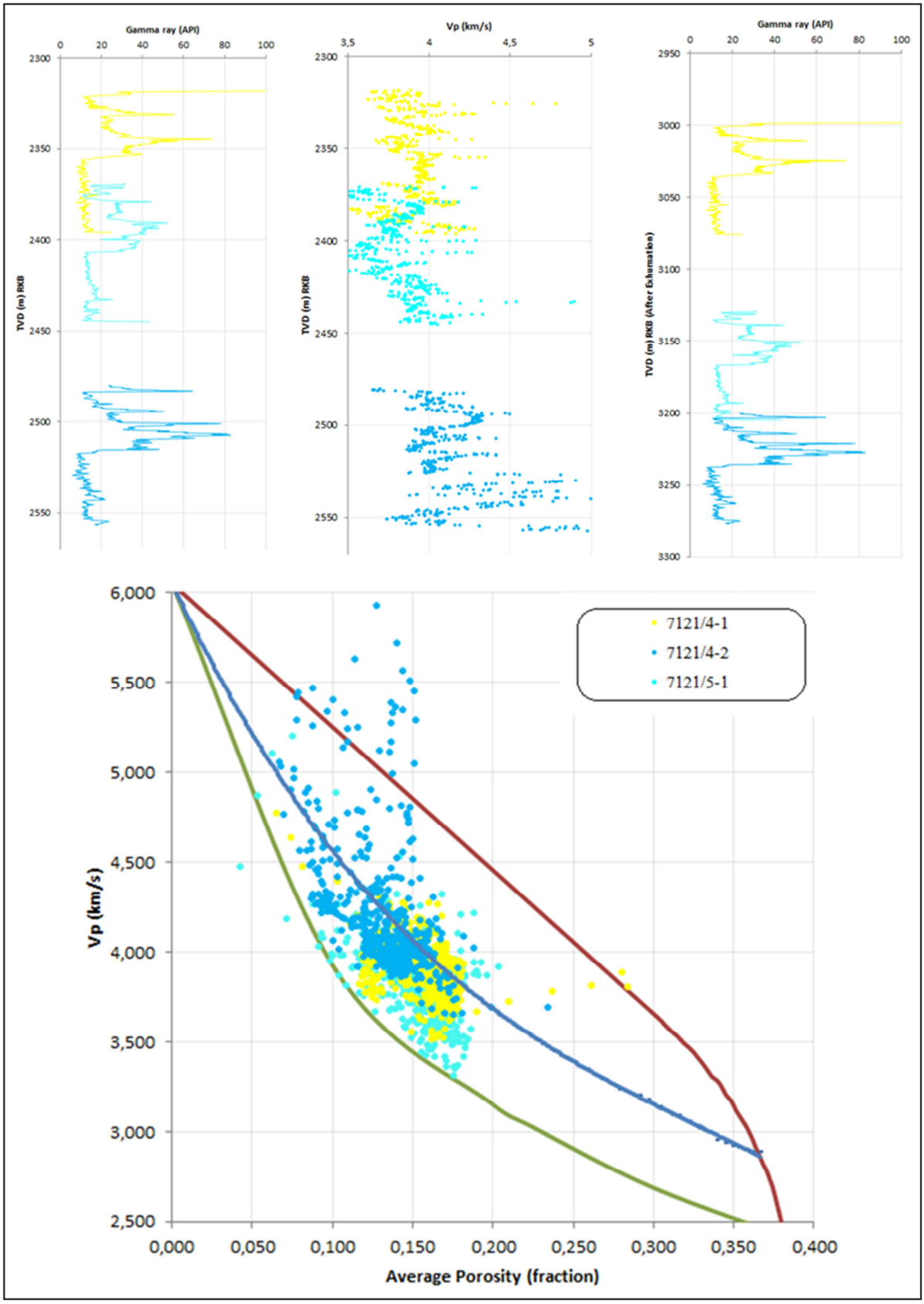

Fig. 6.14: The Vp-porosity plot with cement model of Stø formation in the well 7121/4-1, 7121/4-2 and 7121/5-1 showing the cement model with gamma ray and Vp values.

6.1.6 Rock physics diagnostics of facies 2

Facies 2 in the Stø Formation is the cleanest compared to the other two facies (facies 1 and 3). Thickness of this unit remains unchanged (38 to 45 m) in all wells, though the thickness of the Stø formation is increasing from east to west (Fig. 6.15). However, gamma ray logs trend of facies 2 is similar in all wells. Each well shows very low range of gamma ray reading for facies 2 compared to other facies but the reading is different between wells. The easternmost well 7121/5-1 and westernmost well 7120/5-1 have similar gamma ray readings and for facies 2. While well 7120/6-1 showed higher and well 7120/6-2S showed the highest gamma ray readings (Fig. 6.16).

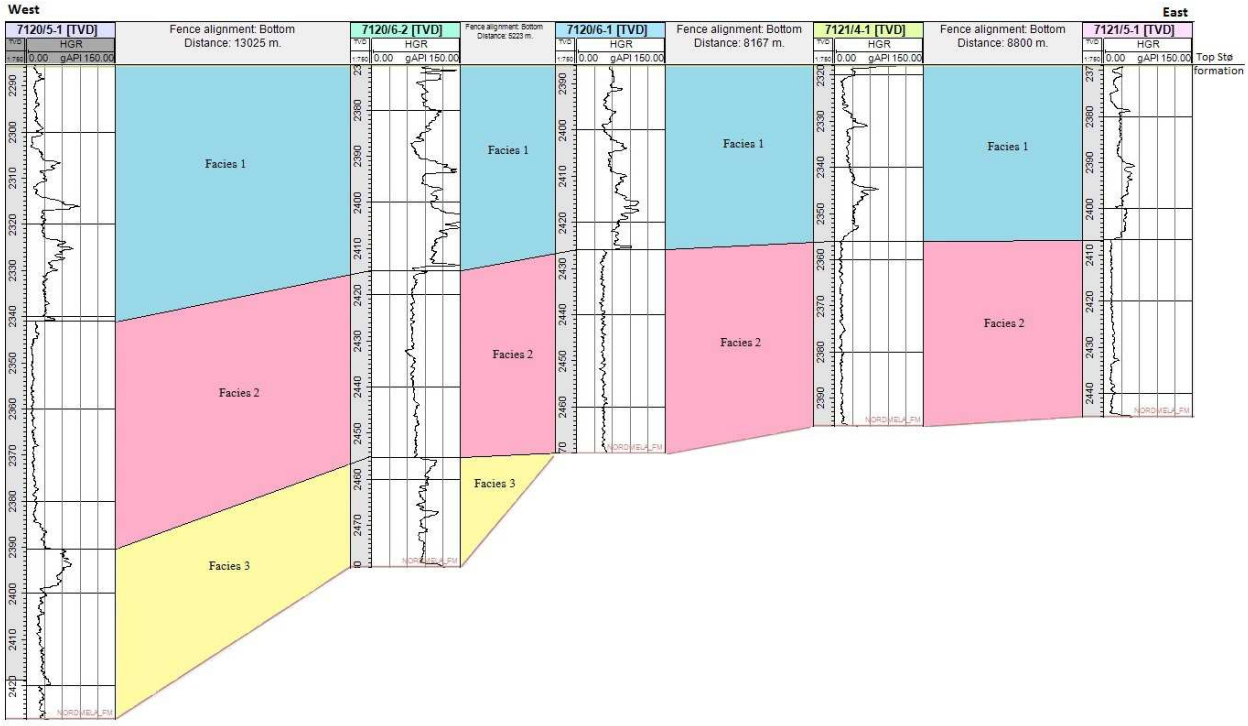

Fig. 6.15: The correlation of three facies of Stø formation from west to east direction.

The Vp and gamma ray versus depth of facies 2 are shown in Figure 6.16. The present day overburden stress is lower in well 7120/5-1 compared to other wells. These wells (7120/6-1, 7120/6-2S and 7121/5-1) have more or less similar present day overburden thickness. The Vp values also show different between wells. Well 7120/6-2S depicts higher Vp reading than other wells. The value ranges from 3.5 to 4 km/s. Though the Vp values are more or less similar, the cement line has shown different trend between wells. The well 7120/6-1 data points follow friable sand line, whereas well 7121/5-1 coincides 1% constant cement line. On the other hand, both wells 7120/6-2S and 7120/5-1 follow 2% constant cement line. The porosity is higher in well 7120/5-1 compared to other wells (Fig. 6.16).

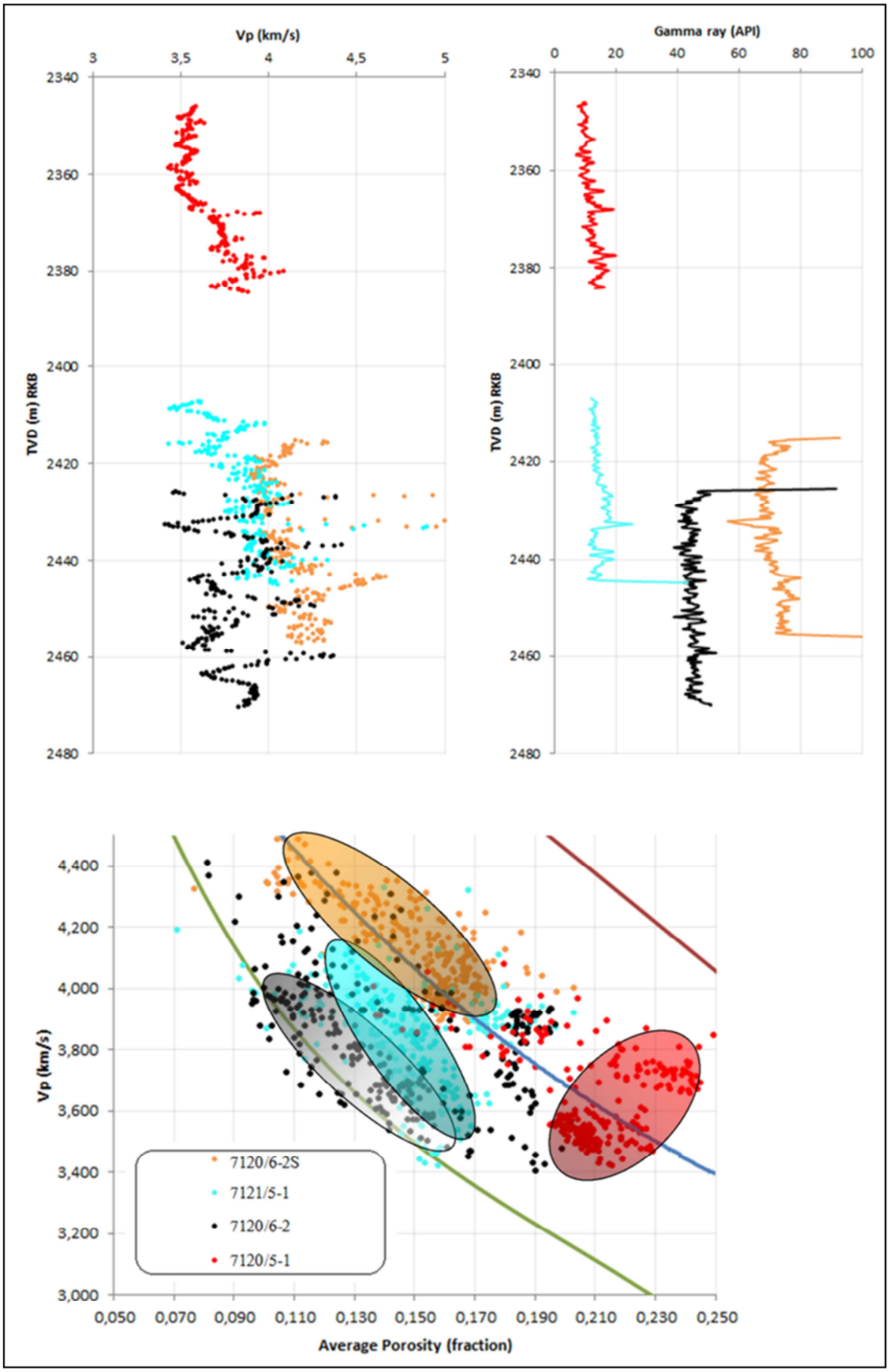

Fig. 6.16: The facies 2 data from four wells plotted in the Vp-porosity plot with three cement models where the depth versus VP and gamma ray showing different values for different wells

6.1.7 Fluid effect on rock physics diagnostic

The Stø formation has been sub-divided into four different sub zones based on their fluid content (NPD) to identify the effect of fluid on rock properties (Fig. 6.17). The data of the Stø Formation from the well 7120/6-2S has been chosen for this analysis because of the availability of shear wave velocity (Vs). Two rock physics templates have been used for analyzed these data. The first template is the Vp versus porosity cross plot with three cement models (friable, constant and contact). Second template is Vp/Vs ratio versus acoustic impedance (AI) cross plot with water, oil and gas sand models. The Vp/Vs ratio versus AI crossplot can be used both for lithology and fluid identification. Figure 6.17 shows different logs of this formation color coded by fluid saturations. The higher deep resistivity log reading within hydrocarbon zones confirm the presence of hydrocarbon which exactly follow the depth taken from the NPD.

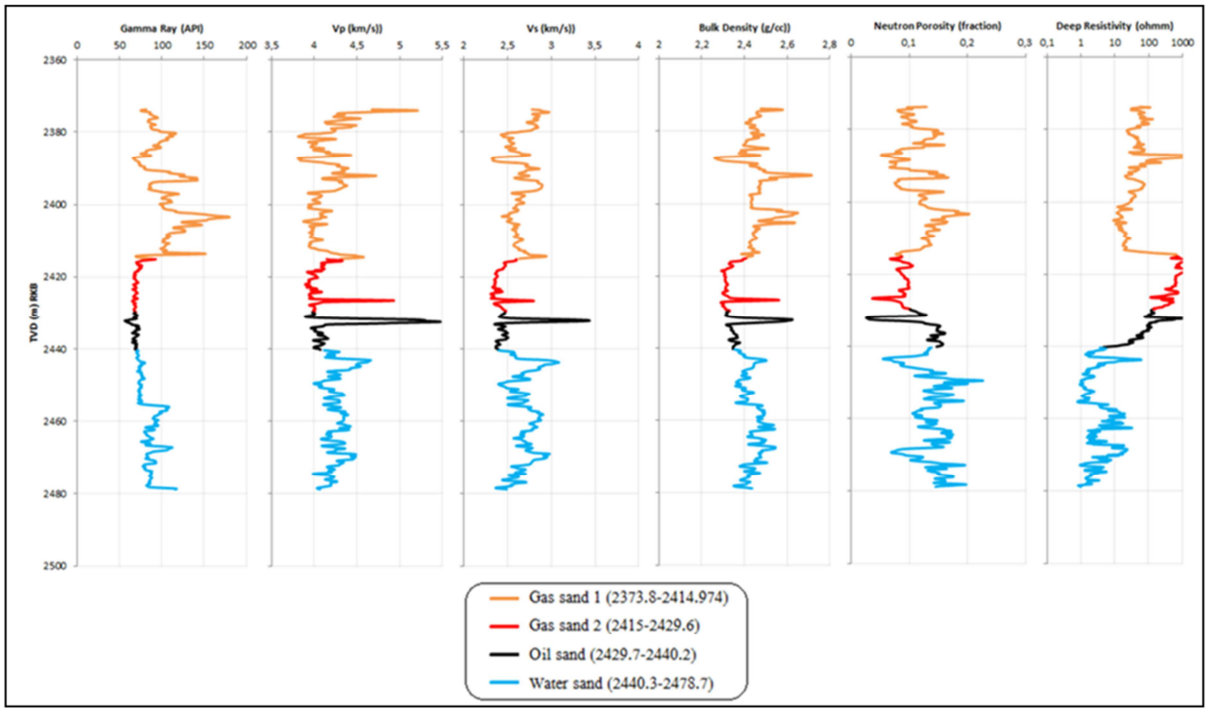

Fig. 6.17: The logs of Stø formation in the well 7120/6-2S showing different fluid zones

In the cement model gas sand 1 (brown) and some of data points from brine sand (blue) follow the line below 2% constant cement line. On the other hand, rest of the brine sand, gas sand 2 (red) and oil sand (black) fall above 2% constant cement line (Fig. 6.18a). All four units follow the constant cement model though their value is different.

Three saturation models have been added with Vp/Vs versus AI cross plot. The blue represents 100% brine saturated model, red represents 100% oil saturated model and green represents 100% gas saturated model (Fig. 6.18b). Most of gas sand 1 data points fall near to 100% gas sand line. Gas saturation of this unit gradually decreases (some data points fall close to brine line). The gas sand 2 and oil sand data plotted in the upper western part which is far from the standard gas sand model even some data points have been crossed 100% water saturated line which is unusual. The major problem shows in brine saturated sandstones. It follows gas saturated line instead of brine saturated line. Even some data points fall on the 100% gas saturated line. The porosity range shows in this plot is 5 to 12%.

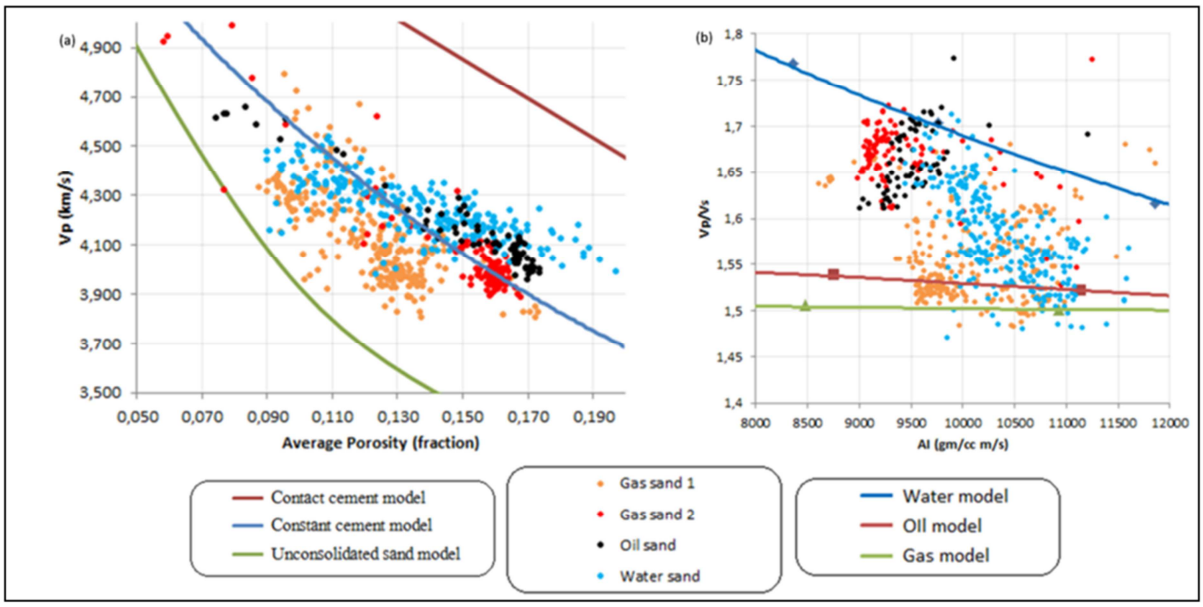

Fig. 6.18: The Stø formation of the well 7120/6-2S showing the different cement model and saturation of different fluid zones in the (a) Vp-porosity plot with cement models and (b) Vp/Vs-AI cross-plot with saturation models.

6.1.8 Rock physics diagnostics of Kapp-Toscana Group

The Kapp Toscana Group has five formations among which the Stø Formation is the best reservoir quality. Other formations also have good quality reservoir sandstone. In the basin periphery many of these lower reservoirs have hydrocarbon discoveries. The Fruholmen and Snadd Formations have good source rock quality as well. The Kapp-Toscana Group of well 7120/6-2S has been analyzed using RPTs. The same RPTs used previous sections have been used in this section as well.

Figure 6.19 shows the Vp-porosity plots of all five formations with three cement models (friable, constant and contact). The whole Kapp-Toscana Group data points used as a background presented in lighter orange. Only sand data points ($V_{sh} \leq 25\%$) from all five formations are plotted in these cross plots. All formations follow the constant cement model but the cement percentages are different for different formations. Many data points of the Stø Formation have been fallen below constant cement (2%) line. The Tubåen formation also follows the similar trend but higher compaction (lower porosity) than the Stø Formation. On the other hand, the Fruholmen Formation data points have been fallen above this 2% cement line. The porosity is lower in Tubåen formation compared to other formations. The Snadd Formation has very few sand data points and show low cementation and high porosity compared to the other formations. The porosity range is similar in the Fruholmen and Snadd Formations, but the cementation is larger in the Fruholmen Formation (Fig. 6.19).

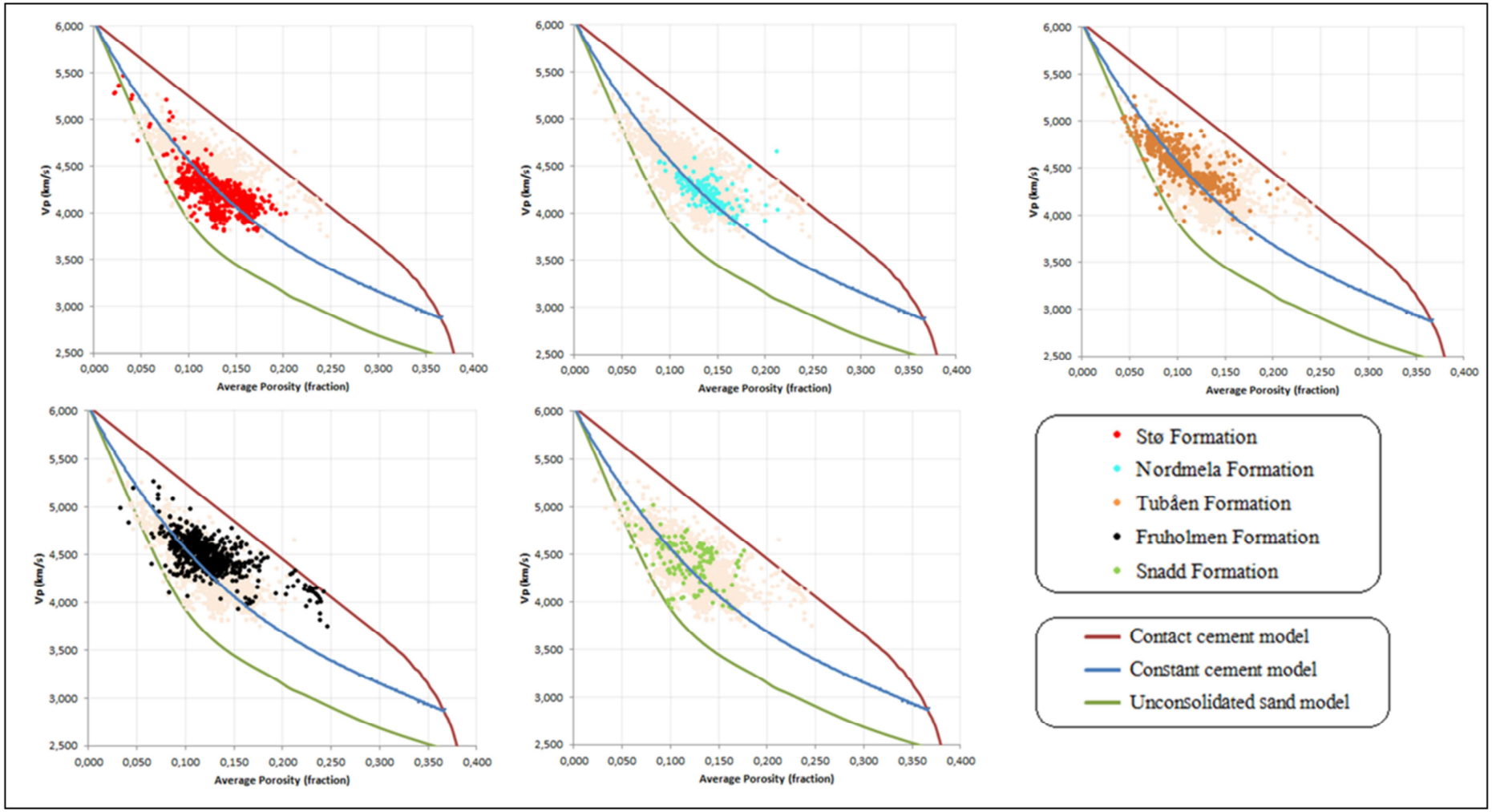

Fig. 6.19: The sandstone of different formation in Kapp-Toscana group showing all formations are followed the constant cement line in the Vp-porosity plots where the back ground trend is all Kapp Toscana formations

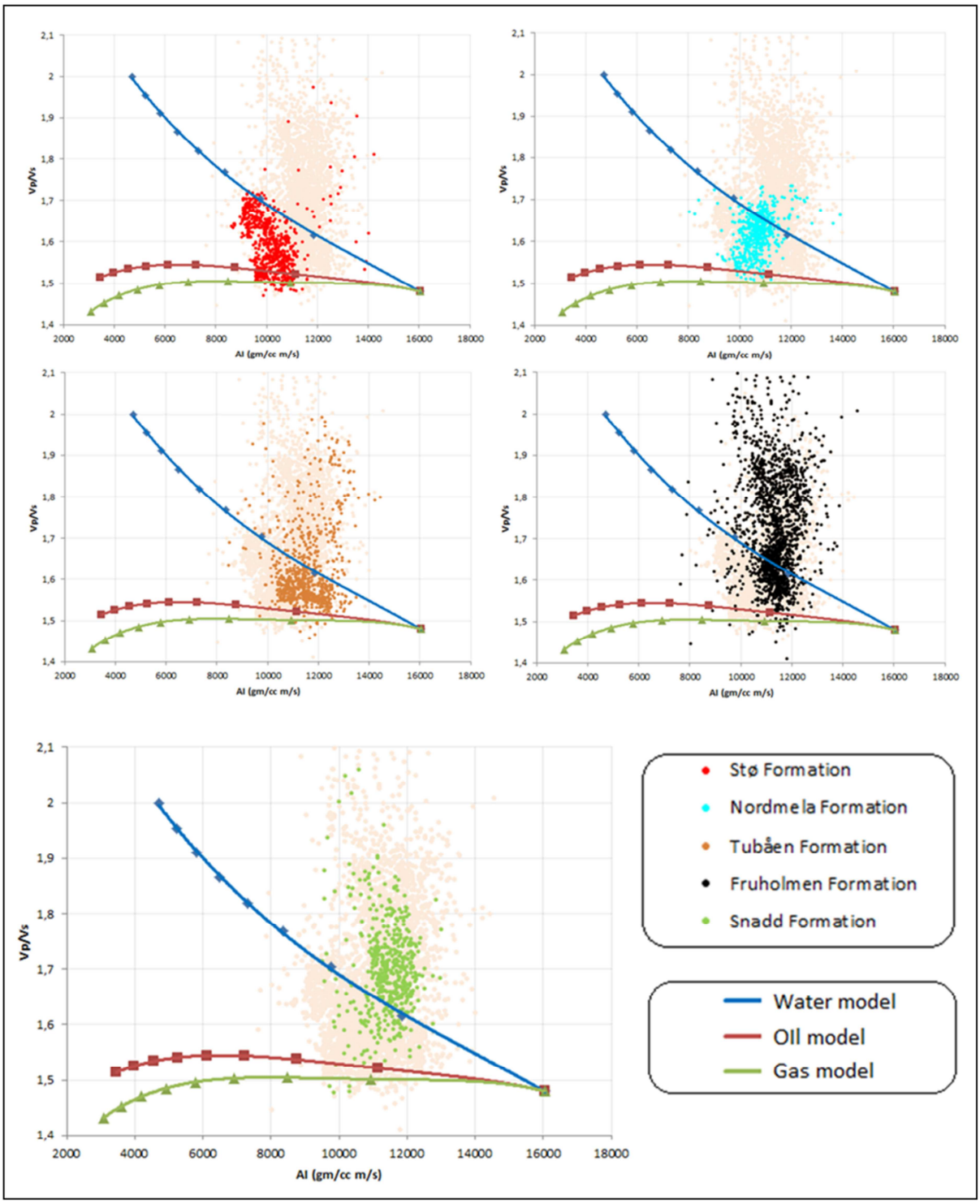

Fig. 6.20: The Vp/Vs versus AI cross-plots of five formations in the Kapp Toscana group.

The Vp/Vs versus AI cross-plots of all five formations of Kapp-Toscana Group from the well 7120/6-2S is shown in Figure 6.20. Three saturation models also added to this cross-plot, brine model (blue line), oil model (red line) and gas model (green line). The lighter orange data points represent the whole Kapp-Toscana Group.

The Stø formation is already explained in previous section which shows some abnormality of gas sand 2 and oil sand data as well as some brine saturated sand data points. The data points

of the Nordmela Formation falls on the brine saturated line but some points are falling on the oil saturated line. The Tubåen, Fruholmen and Snadd Formations data points are distributed around the brine line model. Most of the data points of the Tubåen Formation fall below water sand line, whereas above the line is covered by the Fruholmen and Snadd Formations data points.

6.2 Discussions

6.2.1 Rock physics diagnostic of the Stø formation

The well location related to depositional environment is very important in rock physics diagnostics. Same depositional environment have different sorting and grain size distribution which later influence the compaction history and changes the rock physical properties. One specific formation is deposited in similar time interval within same depositional environment. Also another important factor is provenance. The location of wells as a function of provenance is also important factors in rock properties evaluation. The sediment distribution within any basin is also depends on the direction of sediments supply (Provenance). In addition, the number of sediment sources with respect to textural variation in wells is also important parameter. Several sediment sources influenced the rock particles as well as changes the rock properties compared to single source. Different agents such as wind, water etc. carry different sizes of the grains because of their energy level variation. This is also influenced in depositional system. Different agents have been deposited different size and sorted sediments. If within same formation different sub-environment exits, it leads to deposited different sediments within same formation. Hence, depositional history of different formation is very important during rock properties evaluation. Moreover, to know the rock properties is the key of reservoir characterization.

Gamma ray reading is dependent on many factors, but for the sake of simplicity, the grain size has been regarded as the main affecting parameter. The gamma ray values gradually increase from east to west until it reaches well 7120/6-2S. But, the westernmost well in the studied area 7120/5-1 has more or less similar gamma response like easternmost well 7121/5-1. However, within the Stø Formation, the trends of every facies (facies 1, 2 and 3) in every well are similar. This similar trend is indicated the similar paleo-depositional environment all over the studied area. Gradual increase in gamma (from east to west) follows the proximal and distal settings of paleo-environment. In the proximal zone, the energy of the agent is higher hence coarser sediments (less fine grains) have been deposited. On the other hand, in distal zone, more fine grain sediments are deposited because of low energy level. Moreover, in proximal areas well sorted sediments have been deposited compared to distal areas. From proximal to distal, the finer grains increased gradually resulting in increasing gamma ray values.

In the study area, the easternmost well 7121/5-1 is most probably located in the proximal zone which is close to the shoreface, whereas well 7120/6-2S is located in more distal part(Lower shoreface or below it). The other three wells are located in between these two wells. Moreover, well 7120/5-1 is located further west. Though the well 7120/5-1 is the westernmost well, the sediments are as clean as eastern well 7121/5-1 probably because of another source from south explained by Berglund et al. (1986) (Fig. 6.21). But, the sorting and grain size is different due to different source and sub-environment. Low energy level and S-E direction provenance leads to increase the thickness of Stø Formation from east to west (Fig. 6.15).

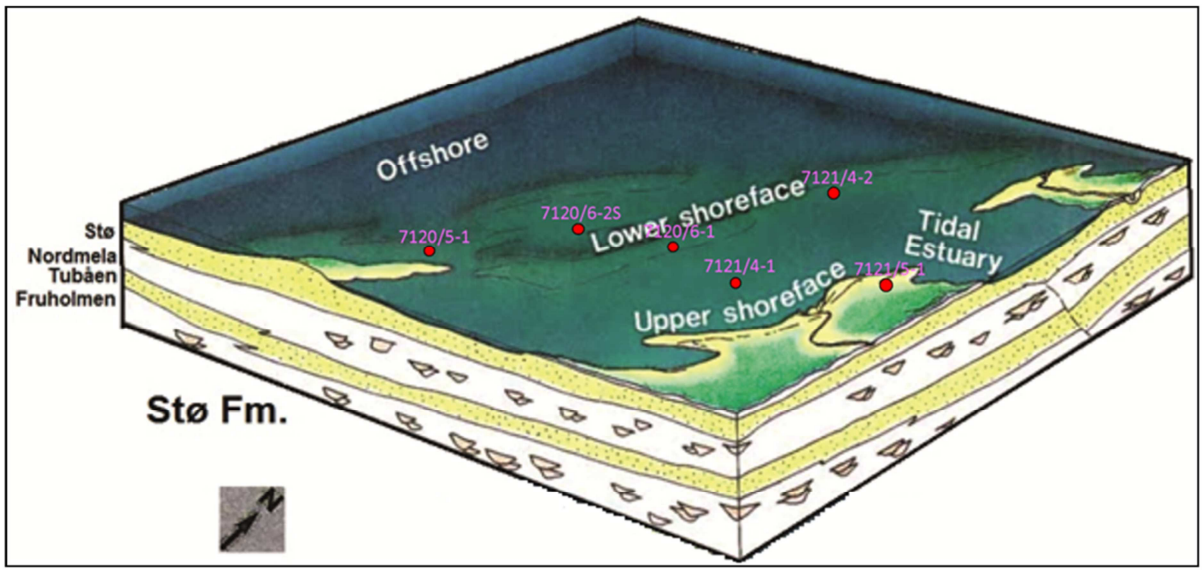

Fig. 6.21: The possible location of studying wells based on gamma ray logs response onto the depositional environment of Stø formation at Hammerfest basin explained by Berglund et al. (1986).

Clean sandstone has lower velocity compared to shaly sandstone (Marion et al., 1992) which can explain the depositional environmental influence on Vp. The thickness of the overburden sediments is another important factor. Overburden thickness has been determined the total effective stress which is the main controlling parameter in MC. On the other hand, the total depth of the reservoir unit is giving the temperature history which acting on this unit is the factor influenced kinetic reactions causing cementation (CC). Compaction changes the stiffness of the rock which is the main cause to increase velocity. The uplift and erosion with modified structural pattern make theses relations more complicated. Hence, the rock properties do not follow the normal subsidence basin trends.

In CC zone, the quartz cementation depends on the dissolution of quartz grains at stylolites and available specific surface area for quartz cement precipitation. These stylolites are the only internal source of quartz cement within a clay-free unit which evolved from clay-rich and rarely micaceous or organic matter rich laminae (Walderhaug and Bjørkum, 2003). Some other factors like stylolite spacing, distance from stylolites also control the volume of quartz precipitation. Adjacent to the stylolites (< 1cm), quartz cement volume shows 10-20% (green color box). Volume decreases to around 5% (red color box) as distance from nearest stylolite increases to 25 cm, and then remains quite constant as distance to nearest stylolite increases to almost 2 m (Fig. 6.22). Moreover, quartz cementation is strongly influenced by the specific surface area available for formation of quartz overgrowths, but within clean sandstone (facies 2 in the Stø Formation), quartz precipitation is more influenced by the distance from nearest stylolite than specific surface area (Walderhaug and Bjørkum, 2003).

To explain the effect of stylolites in porosity, the gamma ray data points of the Stø Formation from well 7120/5-1 has been plotted against neutron porosity data points (Fig. 6.23). Because of fluid sensitivity of neutron porosity, this dry well selected to be investigated among six wells available in this project. Three clusters of data set found in this plot; high porosity low gamma ray zone (cyan), slightly high gamma but low porosity zone (red) and high gamma with intermediate porosity (green) zone. The high porosity zone belongs to clean sandstones (facies 2 and upper part of facies 1) in the Stø Formation. Low porosity zone consists of shaly sandstones belonging to facies 1 and 3 and intermediate porosities are associated with the shaly units within the Stø formation (Fig. 6.23). The slightly higher gamma ray reading

indicates existence of more clay content into the sandstone. In the greater depth this clay layer influences to generate more stylolites which provide dissolved quartz in the system. Later this dissolved quartz from stylolites accelerates the growth of quartz cementation and decreasing porosity more than clean sand (few stylolites) (Ramm, 1991). The facies 1 (shaly sandstones) which has more clay content within sandstones is induced more stylolites compared to facies 2 (clean sandstones) (Walderhaug and Bjørkum, 2003). On the other hand, clay layers in between sandstone layers are inhibits quartz precipitation and preserves porosity which follows the intermediate porosity zone in this well. The shaly units in the facies 1 and 3 probably hindered quartz cementation due to intergranular clays which preserved porosity (Ramm, 1991).

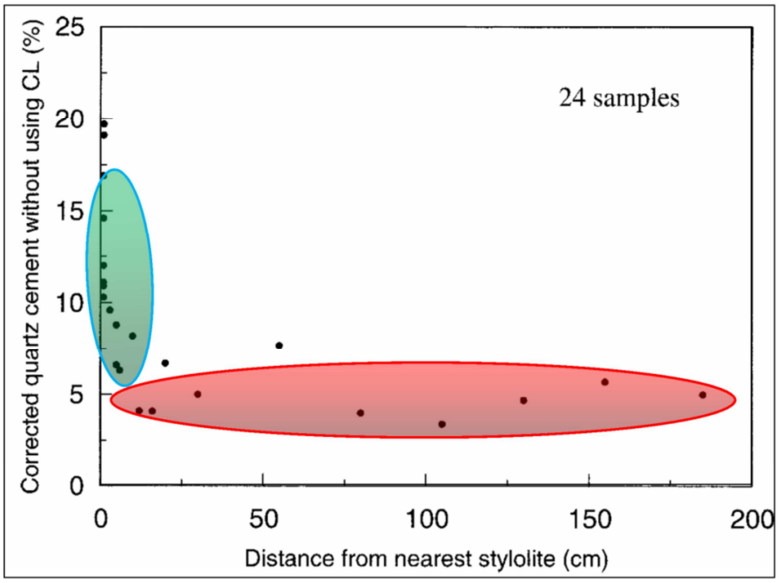

Fig. 6.22: Quartz cement volume as a function of distance from the nearest stylolite (modified after Walderhaug and Bjørkum, 2003).

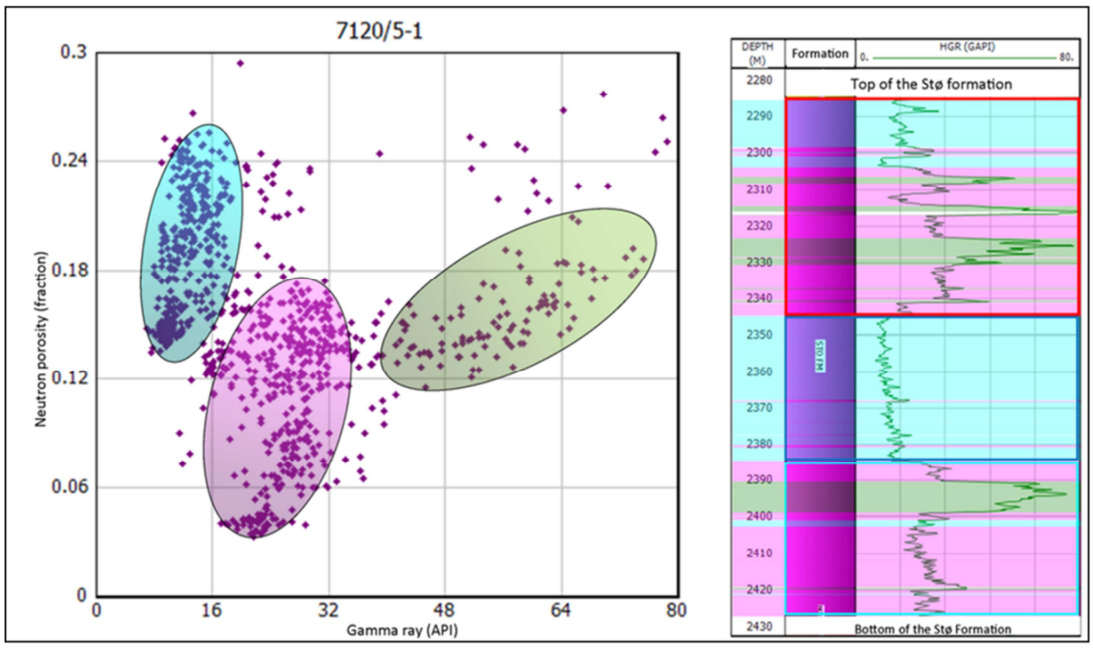

Fig. 6.23: The gamma ray versus neutron porosity plot of Stø formation in the well 7120/5-1. Three different clusters indicating facies control on the rate of porosity reduction by chemical compaction. The depth intervals of different clusters have been showing with different facies intervals.

The present day depth of the Stø Formation is almost similar in wells 7120/6-2S and 7121/5-1. This indicates almost similar overburden pressure or similar effective pressure (assuming similar pore pressure) condition. The sediments of easternmost well 7121/5-1 is well sorted, coarse grained compared with well 7120/6-2S which consists poorly sorted, fine grained sediments. In MC zones, poorly sorted sandstones are compacted more than well sorted sandstone in similar pressure condition (Marion et al., 1992). Poorly sorted Stø formation of well 7120/6-2S mechanically compacted more than well 7121/5-1 which is one possible reason for higher Vp in well 7120/6-2S. The poorly sorted sediments in well 7120/6-2S have more stylolite and more dissolved quartz than well 7121/5-1. Furthermore, the coarse grain sandstone in well 7121/5-1 has low specific surface area available for quartz precipitation compared to well 7120/6-2S. These leads to precipitate more quartz cement. Hence, the sandstone (Stø Formation) in well 7120/6-2S is stiffer than well 7121/5-1. Stiffer rocks have higher Vp than soft rocks is another possible reason for higher Vp in well 7120/6-2S. Moreover, the cementation is increasing from east to west which follows the similar gamma ray increasing trend.

The westernmost well 7120/5-1 has different cement model trend compared with eastern well 7121/5-1 though the gamma ray reading of these two wells is similar. One important point is that, presently these two wells have been located into two different fault blocks. Different fault blocks have different TTI and exhumed history. The present day temperature gradients of these two wells are different which indicate different TTI values throughout their depositional history. Moreover, present day overburden thickness of these two wells is showing different which indicate different effective stress level (assuming same fluid pressure) within these two wells as well. The stress dependent MC effect is different between these two wells. Also the effect of multiple sources (two provenance) (Fig. 6.21) in well 7120/5-1 show different rock properties than well 7121/5-1. The grain size and sorting are different in both wells because of different paleo sub-environment conditions acting up on them. These are the possible reasons for different degree of cementation and porosity distribution within these wells. Thickness of the formation is another factor which changes the rock properties in different grade. The thicker unit has more intra-mechanical compaction in MC domain. Also, in CC domain, the stylolite spacing and distance from each stylolite is influenced by thickness variations. The thickness of the westernmost well 7120/5-1 is doubled than easternmost well 7121/5-1. These reasons are the responsible for different cement model trend within these wells, though gamma ray reading are similar.

The southern well 7121/4-2 is located in another fault block compared to other wells. The present day overburden thickness of this well represent higher effective stress compared to other wells used in this study. Moreover, the temperature of the Stø Formation is higher in this well because of higher overburden thickness (temperature gradient is similar). The higher effective stress compacted more in MC domain which influenced the Vp reading of this well. Vp value is higher in this well than others which is expected. On the other hand, because of higher present day temperature followed higher quartz dissolution and precipitation in CC domain (Fig. 6.24). This higher cementation is also increase Vp.

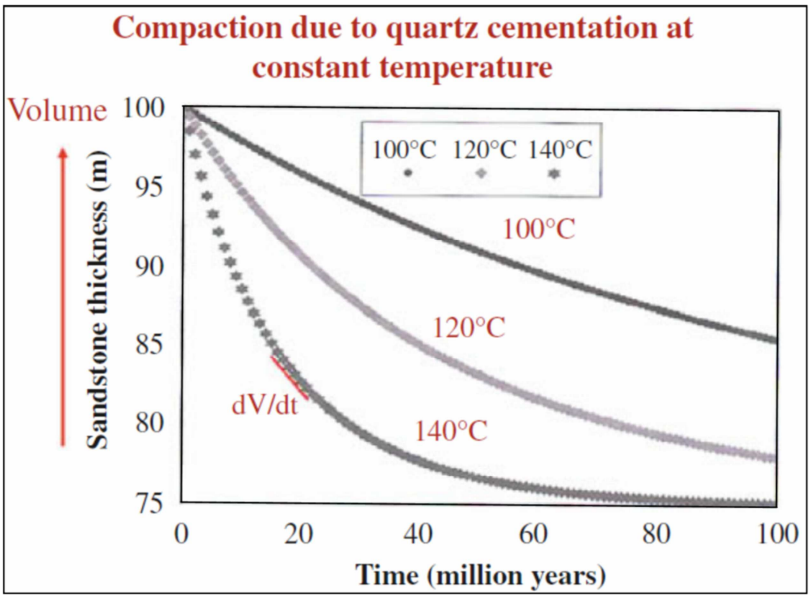

Fig. 6.24: Modeling of quartz cementation and chemical compaction due to quartz dissolution and cementation as a function of time and temperature (modified after Bjørlykke and Jahren, 2010).

Now, these depositional effects on reservoir are considered for only facies 2 (the cleanest sandstone unit) in Stø formation. Cementation of this unit is depends on the distance from stylolites than quartz specific surface area (Walderhaug and Bjørkum, 2003). Well 7120/5-1 shows low Vp and high porosity values compared to other wells. Facies 2 of this well experienced lower overburden stress in MC domain is a possible reason for lower Vp readings. The number of stylolites are higher (higher gamma reading) in well 7120/6-2S is responsible for higher cementation and lower porosity (Fig. 6.16). Well 7120/6-2S and 7120/5-1 follow the constant cement model (2% cement) though the Vp and porosity readings are different. It indicates that, cementation of these wells is more or less similar but the compaction is different.

It is clear that, the depositional environment is an important factor to change the rock properties within same formation. The paleo depositional environment or lithology within a formation seems roughly to be similar. Reservoir characterization of this research has been proved that, rock properties are different in well to well within same reservoir units. The TTI of studied area become more complex due to several stage of exhumation. Moreover, the structural setup which generates different fault blocks show different temperature distribution and different effective stress upon the reservoir rock. These factors changed the rock properties laterally as well as vertically. Finally these diagenetic effects with depositional trend make the whole area very complex and evaluate rock properties are very difficult.

6.2.2 Fluid effect on rock physics diagnostic

The shaly sandstones (facies 1 and 3) which consists gas sand 1 have low quartz cementation. This unit has higher dispersed clay within sand grains is the main reason for lower cement precipitation (Ramm, 1991). On the other hand, the clean sandstones (facies 2) which consists gas sand 2, oil sand and few brine sand show quartz cementation higher than shaly sandstones.

Gas sand 1 followed the rule number (5) given by Ødegeerd and Avseth (2004) which states that, increasing gas saturation will decrease Vp/Vs ratio and AI (Ch. 4, Fig. 4.6). Shaly

sandstones of gas sand 1 have different gas saturation because of lithological variation. Hence, it falls from gas saturated line to brine saturated line. On the other hand, the clean sandstones which is saturated with oil and gas (gas sand 2) show higher Vp/Vs ratio than gas sand 1 and brine sand violating the rules suggested by Ødegeerd and Avseth (2004). The decreasing effective pressure or increasing porosity might be a possible reason for increasing Vp/Vs and decreasing AI values. This unit shows higher porosity compared to other units. Another possibility is shaliness which we already know the facies 2 is the cleanest compared to other facies. Moreover, well 7120/6-2S the facies 2 has very high gamma ray compared to other wells which make a significant effect on Vp which might be another reason for high Vp/Vs in gas sand 2 and oil sand.

The more complicated scenario is in the water saturated sandstones. This data set falls within gas saturated zone even on 100% gas saturation line. The increased cement volume is the main reason for shifting these data points towards gas line. The porosity range of this data is about 5-8% which shows these sandstones as compacted sandstones and these sandstones have very narrow ranges of Vp/Vs and AI values. These brine saturated sandstones violating the robust results in rock physics based exploration strategy. This is a limitation of rock physics based exploration in overconsolidated reservoirs.

6.2.3 Rock physics diagnostics of Kapp-Toscana Group

One important parameter for quartz cementation is the surface area which depends on both depositional environment (sorting, size, mineralogy etc.) and diagenetic alteration (coatings, temperature, time etc.) which discussed earlier in this chapter. The temperature is increasing with a constant rate based on temperature gradient while the rate of cement precipitation dependent on temperature. Increasing of temperature accelerates rate of cementation in similar lithologic condition. Coarser grains have lower specific surface area compared to finer grains for quartz precipitation which helps to precipitate lower quartz cementation in CC zone. But higher porosity loses in the MC zone is reported due to grain crushing and rearrangement (Bjørlykke and Jahren, 2010). Cementation process needs dissolve quartz for precipitate quartz cement. Source of this dissolved quartz is stylolites. One expects more quartz cementation within sandstones which containing more clay particles because clay particles within sandstones generate more stylolites. Hence, more dissolved quartz and more cement precipitation.

The gradual increase of contact cement in Kapp-Toscana sandstones is the effect of temperature. Temperature increases with depth which increases the rate of quartz precipitation (Fig. 6.24). The low porosity of the Tubåen Formation is the consequence of poorly sorted sandstone compared to the Stø Formation which shown in Figure 6.25a. High clay content in the Snadd Formation reduces the cementation though it is in higher temperature range than the Fruholmen Formation. This effect decreases the velocity as well (Fig. 6.25b).

The Stø Formation data points plotted in Vp/Vs versus AI template fall in between brine and gas saturated line (Fig. 6.23). Some data points of Nordmela formation have gas saturated which fall closer to gas saturated line, whereas other brine saturated data points in the Nordmela Formation fall on the brine saturated line (Fig. 6.26). The Tubåen Formation which is more cemented with high velocity and low porosity falling on the lower porosity region with high AI and low Vp/Vs ratio. Increased cement volume moved this water saturated sand downward into the gas saturation zone.

Moreover, the data of more shaly brine saturated Fruholmen and Snadd Formation fall on brine saturated line. Shale units within these formations fall above brine saturated line (Fig. 6.27).

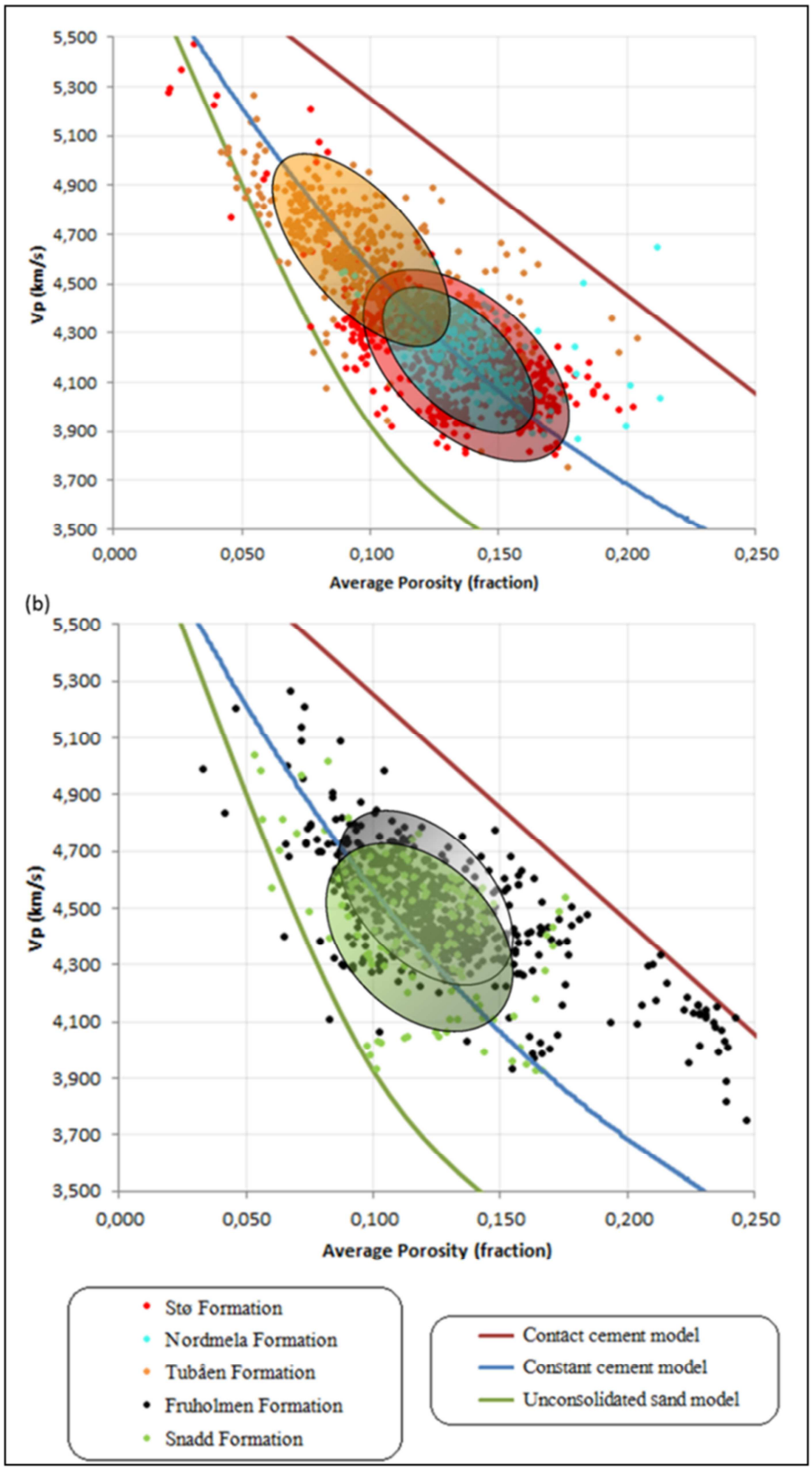

Fig. 6.25: The different formations cement trends (a) Stø, Nordmela and Tubåen and (b) Fruholmen and Snadd formation.

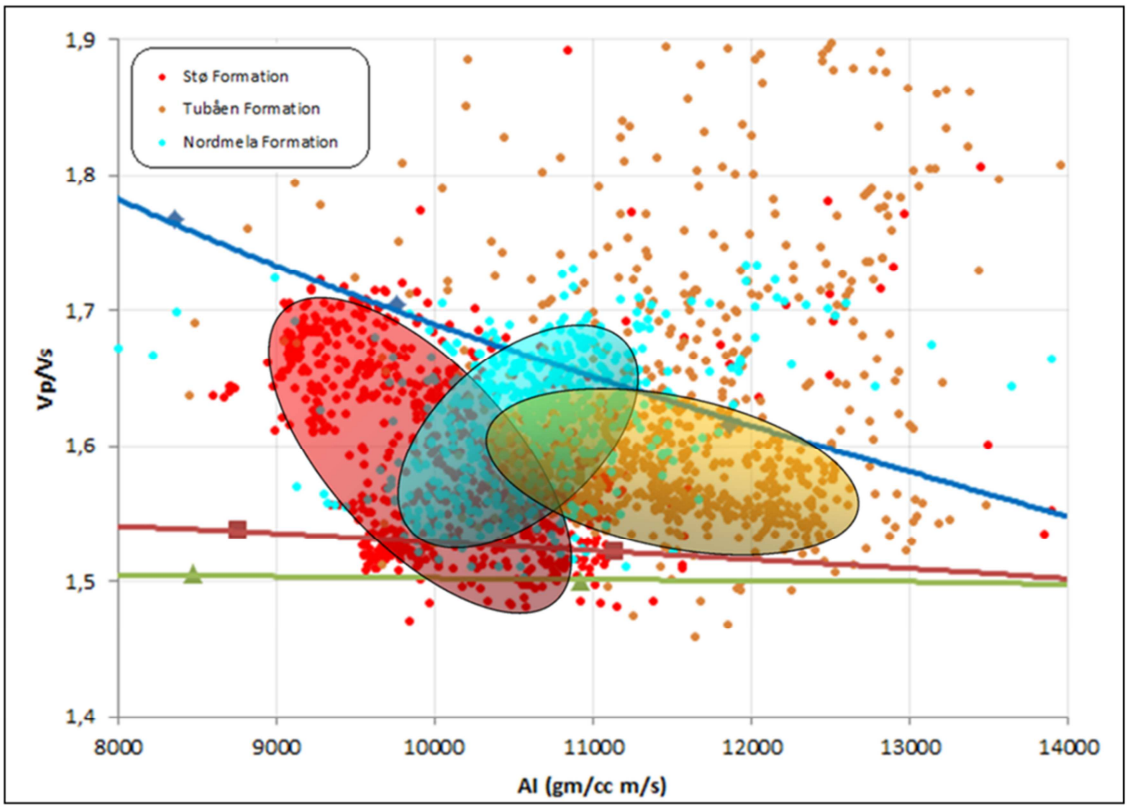

Fig. 6.26: The Stø, Nordmela and Tubåen formations of maximum data spreading position in the Vp/Vs-AI cross-plot due to different factors.

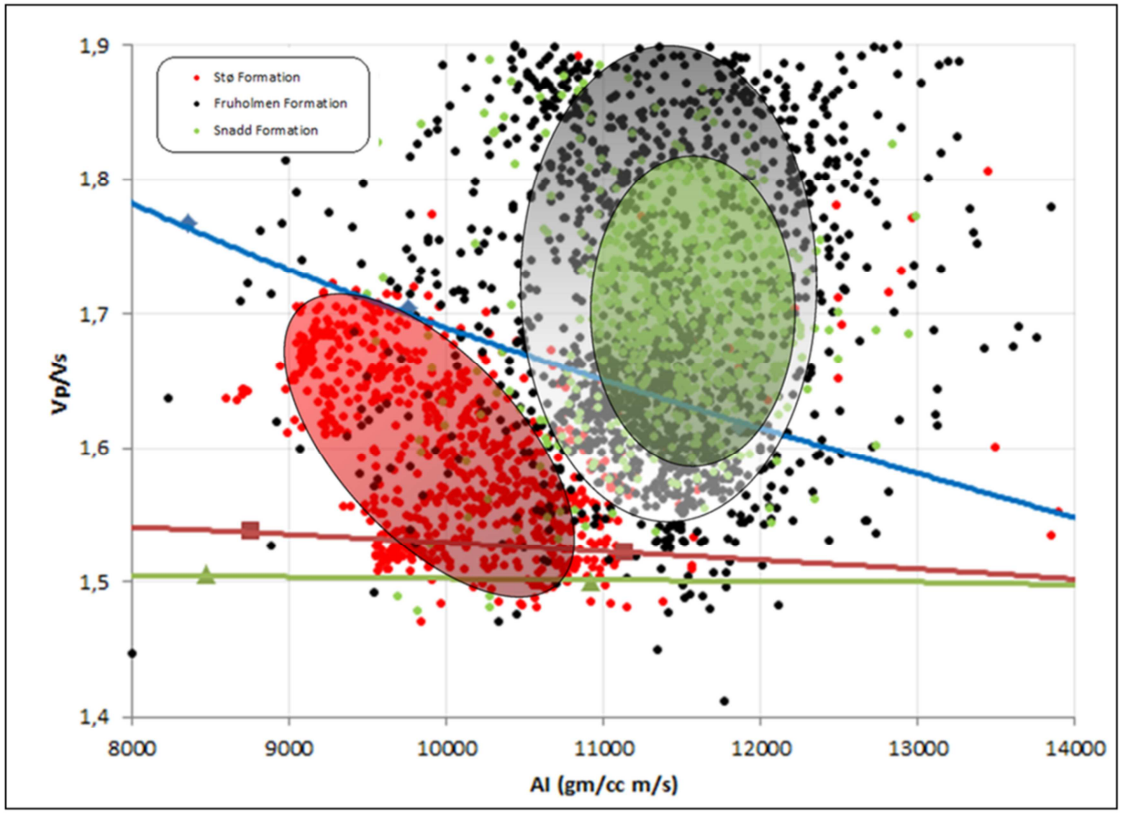

Fig. 6.27: The Stø, Fruholmen and Snadd formations of maximum data spreading position in the Vp/Vs-AI cross-plot due to different factors.

Chapter 7: AVO modeling

UNIVERSITY OF OSLO

FACULTY OF MATHEMATICS AND NATURAL SCIENCES

Chapter 7: AVO modeling

AVO (Amplitude Versus Offset) is the variation in reflection amplitudes with changing distance between shot point and receiver for a given target reflector. In the recent year, the AVO technique became very popular in the oil industry because the physical explanation of the seismic amplitude in terms of rock properties (Avseth et al., 2005). The measured shear wave velocity and proper geological understanding is the key for success of AVO analyses. This chapter focuses AVO modeling of all six wells included in this study. The Stø and Hekkingen formations (the main seal-reservoir pair in the study area) are considered for the AVO modeling.

7.1 Results

7.1.1 Effect of block size

Blocking of well log to upscale it to seismic scale is essential for AVO analysis and appropriate blocking may influence of AVO analysis. Here I investigated the importance of blocking in AVO analysis. Figure 7.1 shows the synthetic seismics by using different block sizes (eg. 10, 25 and 50 m) in the well 7120/6-1. These synthetic NMO corrected CDP gathers were generated by using a Ricker, linear wavelet. The synthetic seismograms are generated based on averaged Vp, Vs and density logs of three block sizes 10, 25 and 50 m respectively. The interest here is the top of Stø formation which shows significant differences for three different seismics generated by three block sizes.

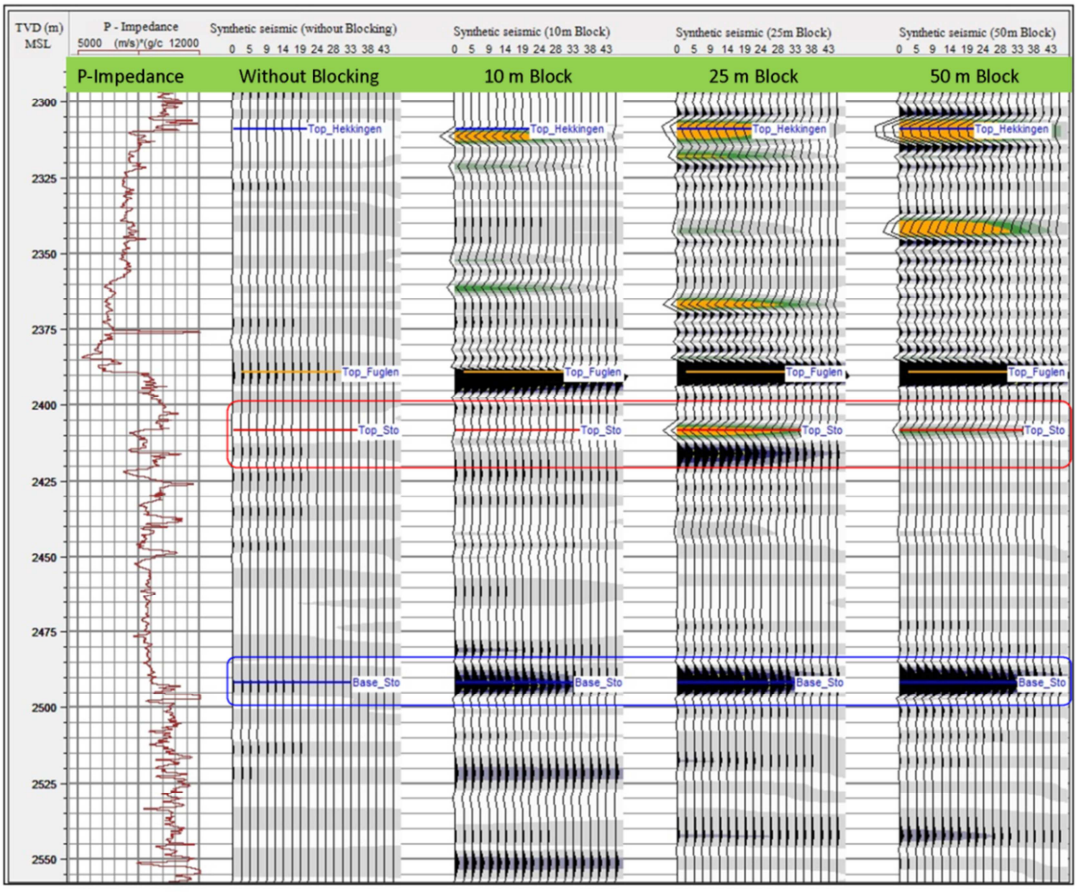

Fig. 7.1: Synthetic seismics using different block using logs from the well 7120/6-1.

As we expect the original logs (without block) has very low resolution in seismic scale, even 10 m blocking does not improve resolution (Fig. 7.25). The strongest top Stø reflector has been generated by the 25 m blocking. On the other hand, the base Stø reflector is strongest with increasing block size. The reflectors occur at different depths depending on the averaging block size used here also influence the AVO response at the target reflectors. The top Stø reservoir AVO classifications for different block sizes have shown in the Table 7.1 and Figure 7.2. The zero offset reflectivity is negative for all cases where 25m block size shows strong reflectivity (Fig. 7.3). A positive gradient for all three cases has given a class IV reservoir sands.

Table 7.1: AVO classification of Stø reservoir in 10, 25 and 50 m block size.

Well No. 7120/6-1			
Block Size	Pore Fluid	Sand Class	Zero offset Rp
10 m	In-situ Gas	Weak IV	-0.01754
25 m	In-situ Gas	Strong IV	-0.05216
50 m	In-situ Gas	Weak IV	-0.02088

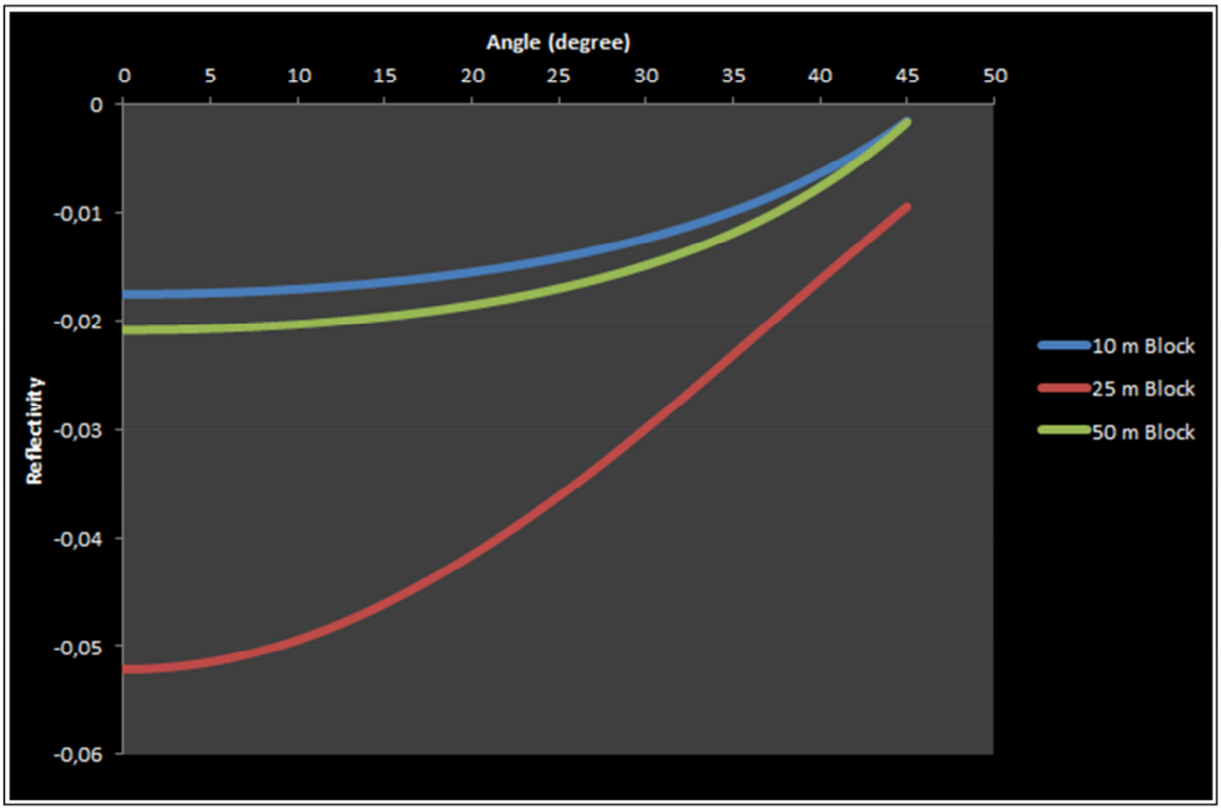

Fig. 7.2: Angle dependent reflectivity for Stø reservoir in different block size in the well 7120/6-1.

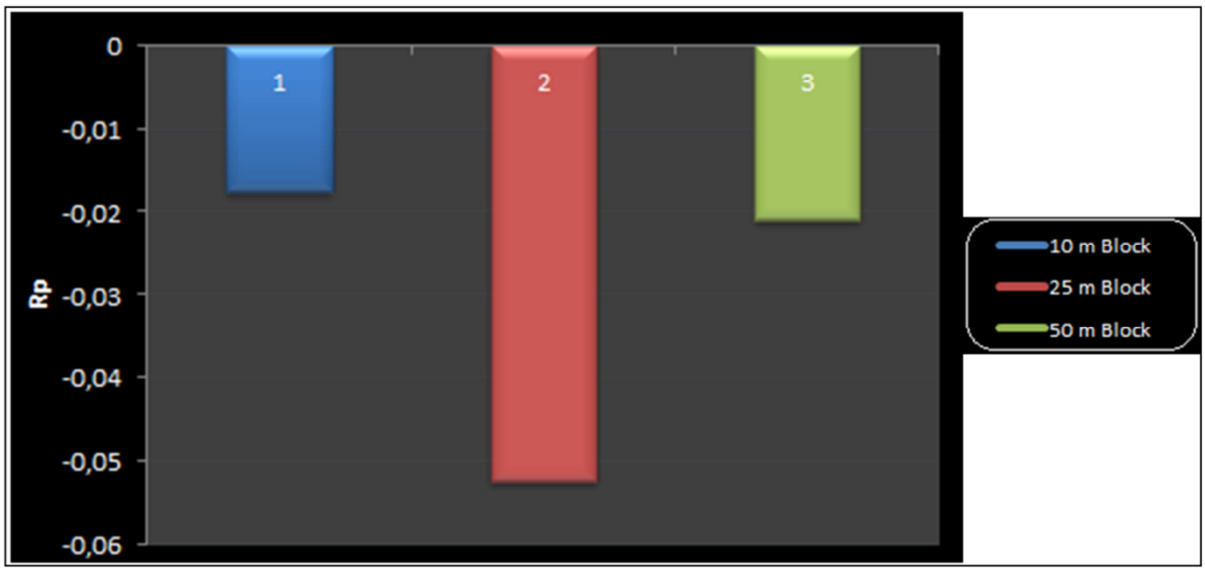

Fig. 7.3: Changes in Rp for 10, 25 and 50 m block size edited logs.

The intercept and gradient cross-plots in all three cases also showing class IV AVO sand (Fig. 7.4). The intercept values are negative whereas gradient are positive. The Table 7.2 shows the position of the data points with AVO classes.

Table 7.2: AVO sand classification based on A and B

Block Size	Pore Fluid	Class	Quadrant	A	B
10 m	In-situ Gas	IV	II	-	+
25 m	In-situ Gas	IV	II	-	+
50 m	In-situ Gas	IV	II	-	+

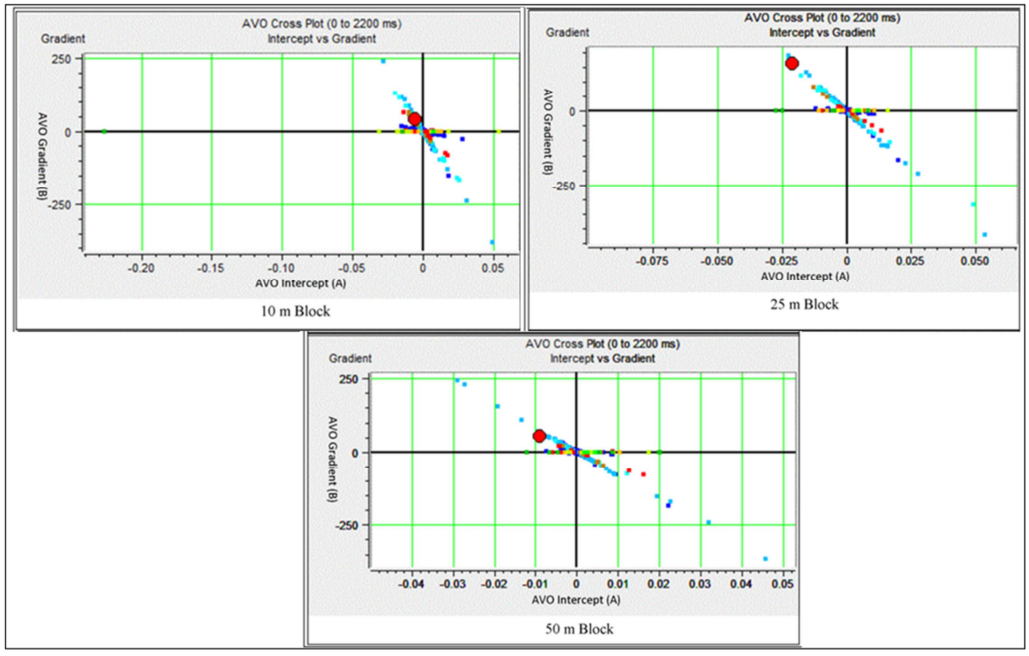

Fig. 7.4: The intercept gradient cross-plots of 10, 25 and 50 m block size logs.

7.1.2 Sensitivity analysis (gas well)

The sensitivity analysis is carried out by using the well 7120/6-2S as this is thewell where we have measured shear wave data. The four important rock properties (Vp, Vs, density and Poisson's ratio) are taken into account to see sensitivity of rock properties due to variations of pore fluids and their saturation, mineralogy and estimated versus measured Vs.

7.1.2.1 Fluid and saturation effect

The variations of fluid saturation have influenced the rock properties and so influence the AVO response. The Table 7.1 shows the variations of rock properties by gas saturation of 0. 10, 50 and 90 percentage, respectively) in a rock contains pure quartz.

The change in rock properties are only depended on the change of fluid saturation in this case. The change of fluid saturation (in this case, S_w = 90% instead of S_w = 100) has reduced the Vp dramatically. The Vp has changed from 4108 m/s to 3884.24 m/s. The effects is less pronounced in S_w = 50% compared to S_w = 10% though we have higher gas saturation (Table 7.3). In principle, Vs has no influence on fluid but the value is increased from 2296 m/s (in brine case) to 2334 m/s with 90% gas saturation. The density and Poisson's ratio are decreased with increasing gas saturation (Fig. 7.5). Vs increases because of decreasing density.

Table 7.3: Rock properties in different fluid saturation in the well 7120/6-2S

Parameters	100% Water	10%Gas	50%Gas	90% Gas
Vp (m/s)	4108.82	3884.24	3875.12	3898.96
Vs (m/s)	2296.44	2300.59	2317.45	2334.67
P (g/cc)	2.476	2.46706	2.43131	2.39556
PR	0.272861	0.229813	0.221618	0.220511

The rock properties change in different gas saturations compared to water saturated condition is shown in percentage in the Table 7.4. After introducing 10% gas in the brine-saturated quartz sands, there is a significant drop of Poisson's ratio and Vp of about 16 and 5% respectively (Fig. 7.6). For the similar saturation, there is a relatively insignificant drop in the density, meanwhile Vs shows a rather slight increase as expected. The Vp increases with 50% gas saturation but the increase is less pronounced with further increase in gas saturation (S_w = 10% in this case). Poisson's ratio is more or less constant with saturation difference from S_w = 50% to S_w = 10%.

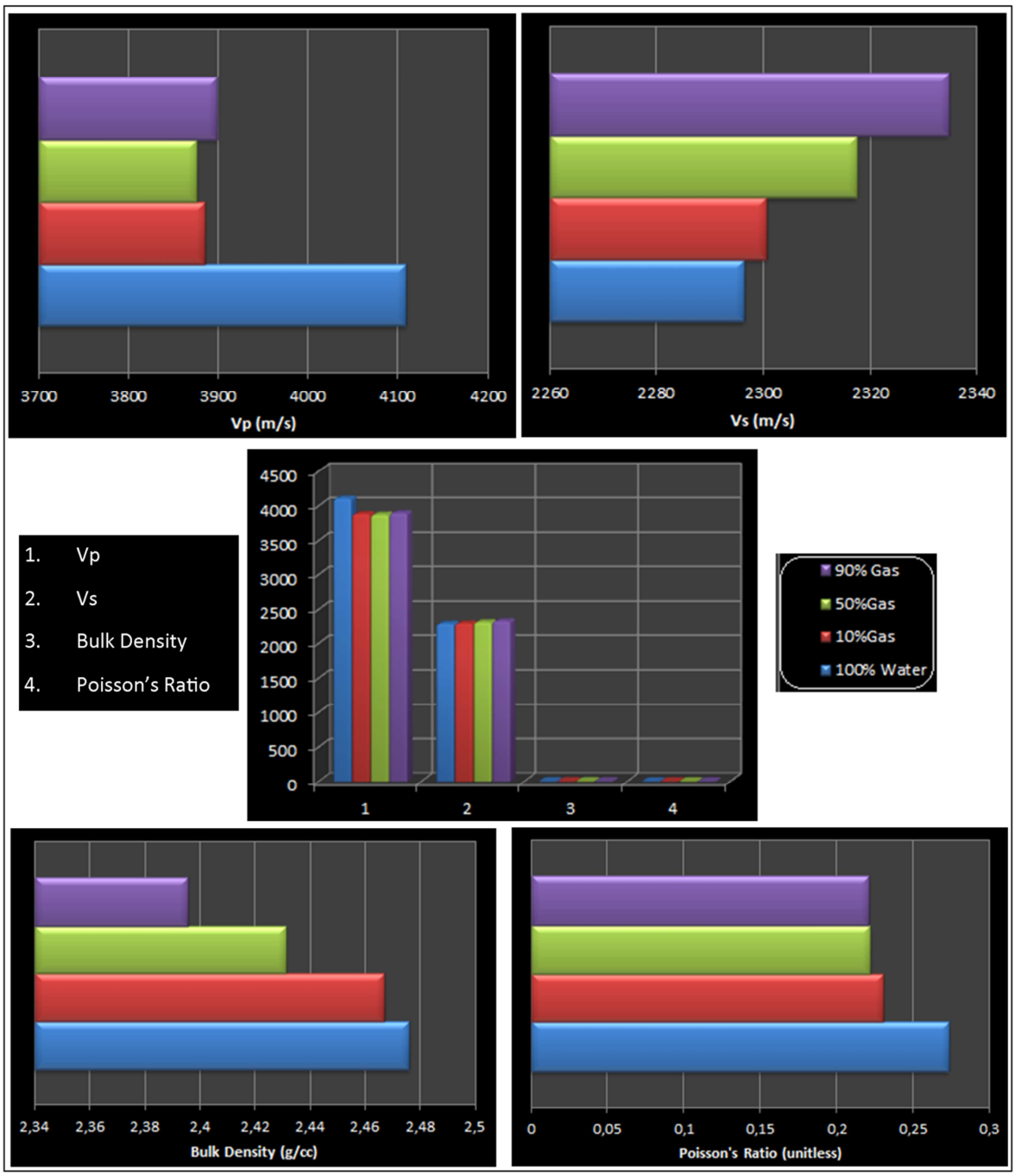

Fig. 7.5: The influence of gas saturation on Vp, Vs, bulk density and Poisson's ratio for well 7120/6-2S considered 100% quartz.

Table 7.4: Effect of gas saturation on Vp, Vs, bulk density and Poisson's ratio

Gas (%)	ΔVp (%)	ΔVs (%)	Δρ (%)	Δ√ (%)
10	-5.465802834	0.180714497	-0.361066236	-15.77653091
50	-5.68776437	0.914894358	-1.804927302	-18.77989159
90	-5.107549126	1.664750658	-3.248788368	-19.18559266

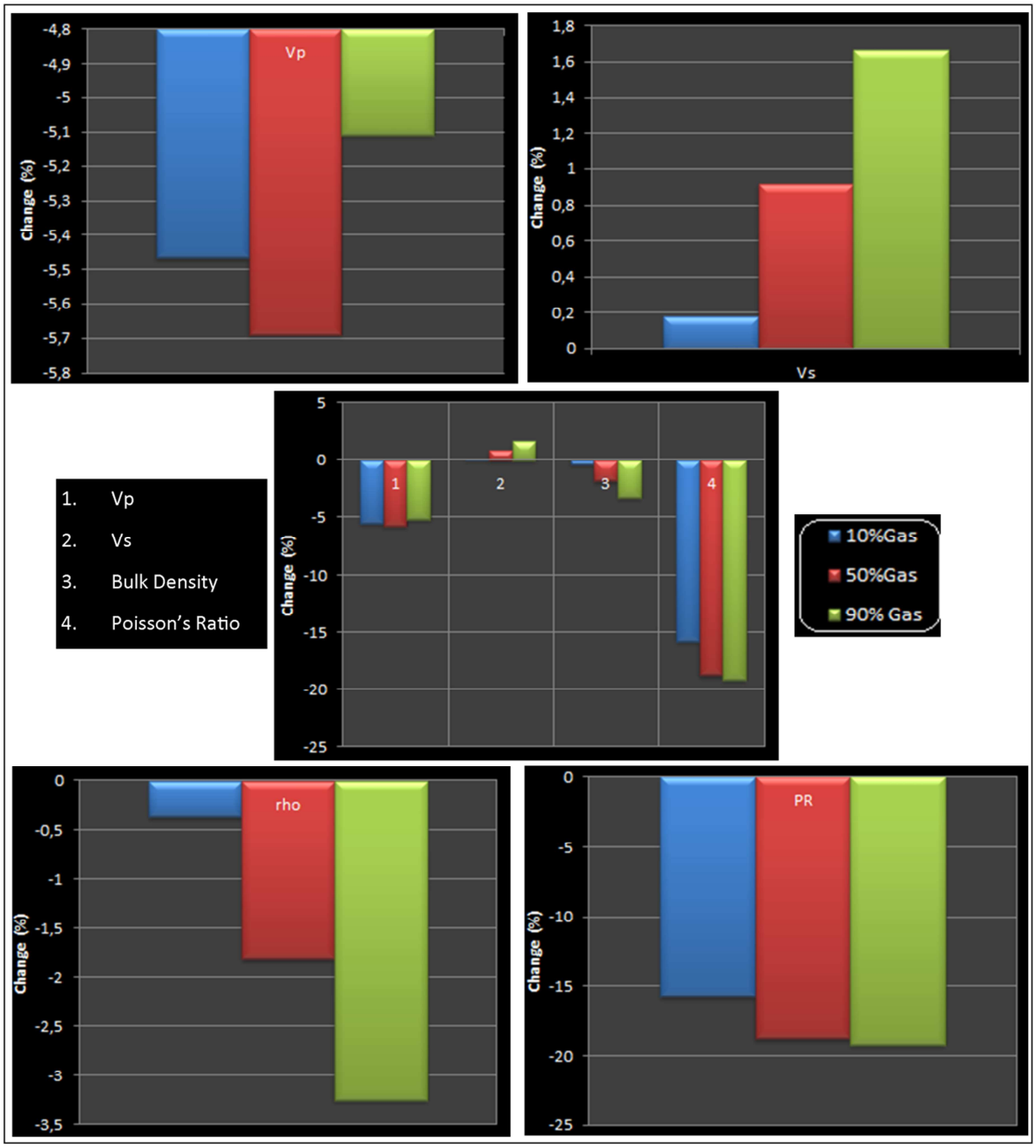

Fig. 7.6: Effect of gas saturation on Vp, Vs, bulk density and Poisson's ratio.

7.1.2.2 Comparison between clean and shaly sandstone reservoirs

The net to-gross-ratio of Stø formation is about 0.8 which give an overall idea about rock composition but not details about mineralogy (Selnes et al., 2004). Here I compare those four rock properties in two net-to-gross scenario; one is 100% quartz sand reservoir and another one is 80% quartz sand and 20% clay. By adding 20% clay in pure quartz sand reservoir, the effective modulus of the rock has changed significantly as so changed the rock properties. Because of 20% clay in the reservoir rocks instead of pure quartz reservoir, the Vp, Vs, density and PR changed significantly (Fig. 7.7). Though there are big differences of changing Vp and PR in case of two mineralogical condition but the changing trend is more or less similar (Fig. 7.8).

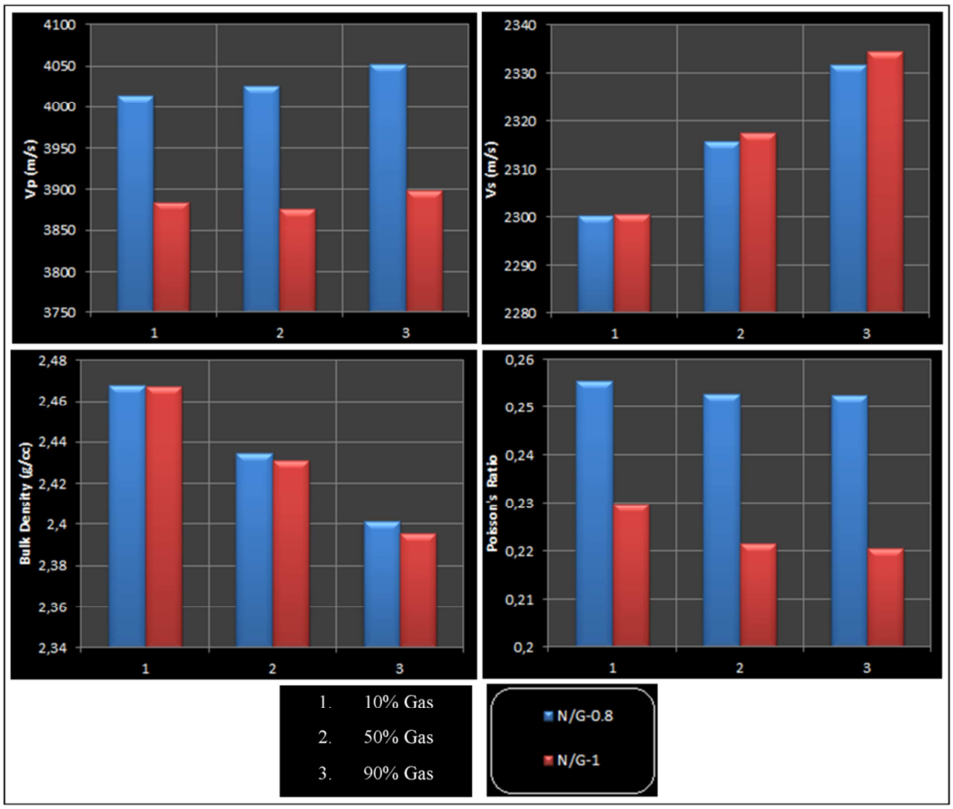

Fig. 7.7: The Vp, Vs, bulk density and Poisson's ratio values of two net-to-gross conditions in the well 7120/6-2S in different saturation.

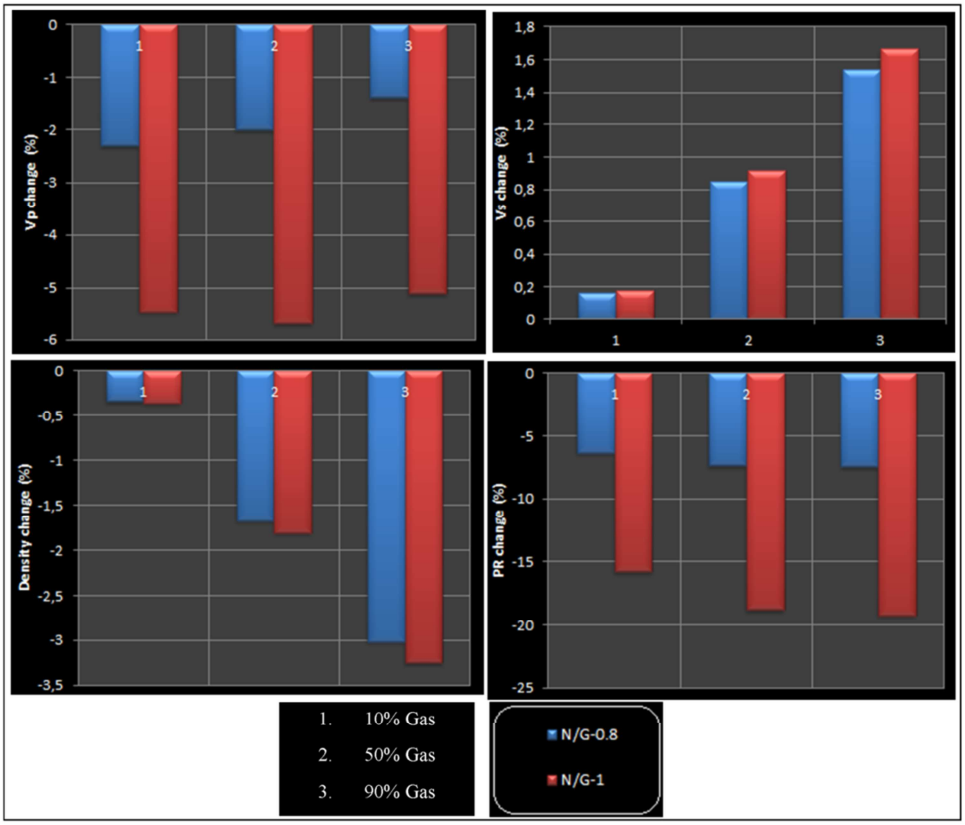

Fig. 7.8: Effect of net-to-gross ratio on Vp, Vs, bulk density and Poisson's ratio in different gas saturations.

7.1.2.3 Comparison between measured and calculated Vs

Because of lack of Vs in 5 other wells, I used Krief (1990) equation to calculate Vs. This is an empirical equation and may not be given absolute Vs compared to direct measurement. A comparison of rock properties of measured and calculated (Krief) Vs in the well 7120/6-2S is investigated. In three fluid replacement cases (FRM) (eg. 100% water, 10% gas and 100% gas), the Vp and Vs show higher in case of using measured Vs compare to calculated one. The density shows opposite behavior as the calculated one gives higher density compare to measured one. While all three rock properties are consistent in three saturation cases, the PR shows different trend in saturation difference. In case of 100% water saturated reservoir the calculated PR value is higher whereas gas models have lower PR (Fig. 7.9).

Except density, the Vp, Vs and PR are relatively higher in case of calculated Vs in both 10 and 100% gas cases respectively. The increase or decrease trends in the Vs, density and PR in case of both saturations are similar for both measured and calculated case but significant change in Vp from 10% to 100% gas saturation is observed. In case of calculated Vs, the Vp increases whereas it decreases in the measured case (Fig. 7.10).

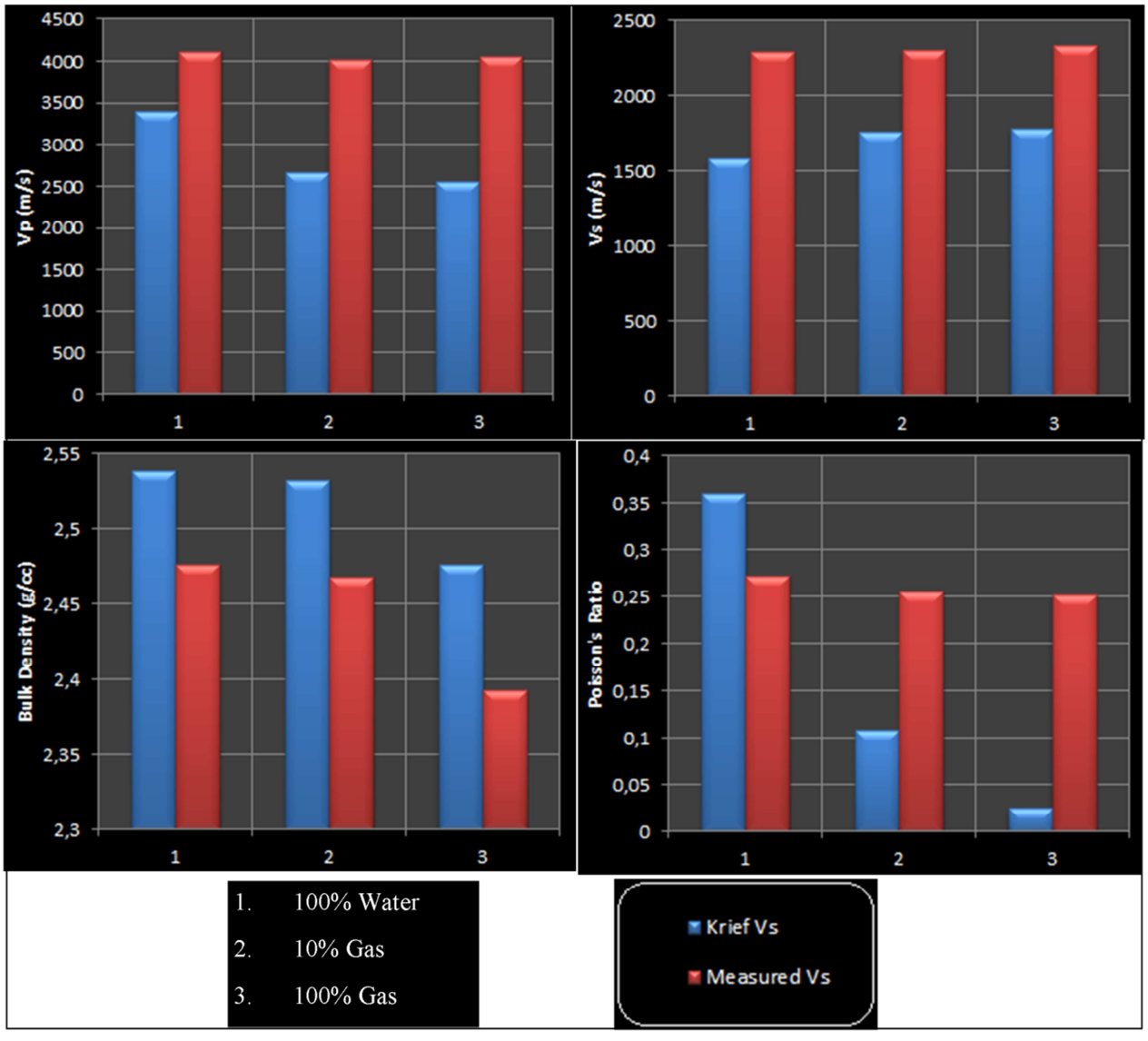

Fig. 7.9: Different rock properties using measured and calculated Vs in the well 7120/6-2S.

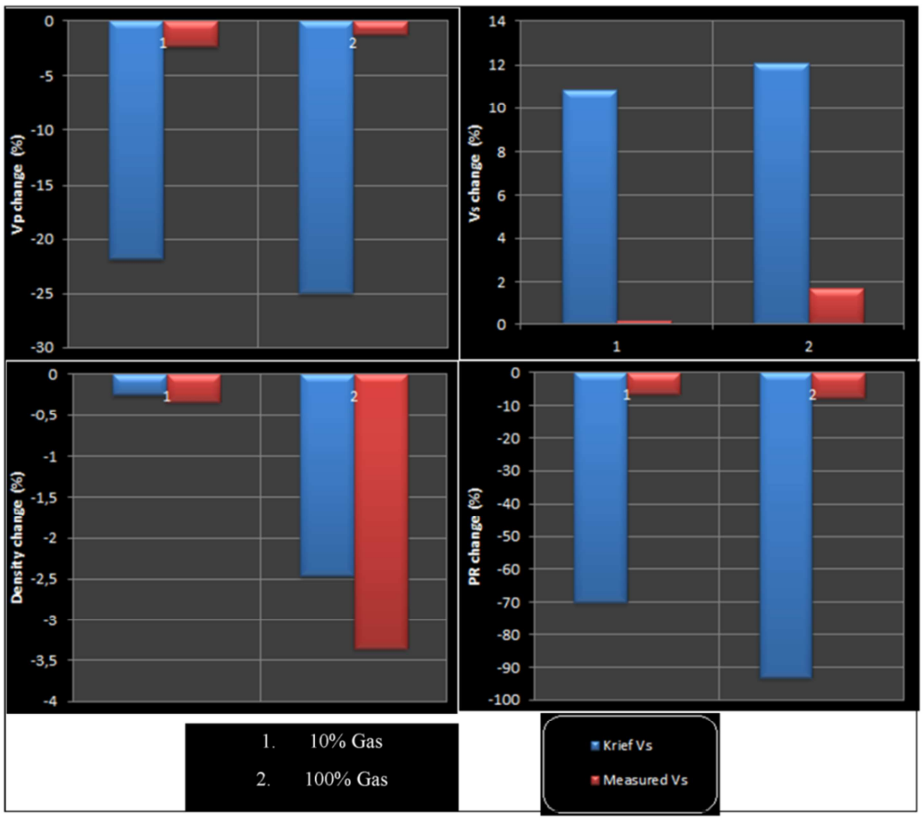

Fig. 7.10: changes of Vp, Vs, density and PR for measured and calculated Vs.

Figure 7.11 shows the angle dependent reflectivity of measured and calculated Vs cases. In both cases the zero offset reflectivity are similar and it is about 0.0046 whereas the gradient are different and the difference is increased with increasing angle (Offset). The gradient of calculated Vs case is higher compare to measured case.

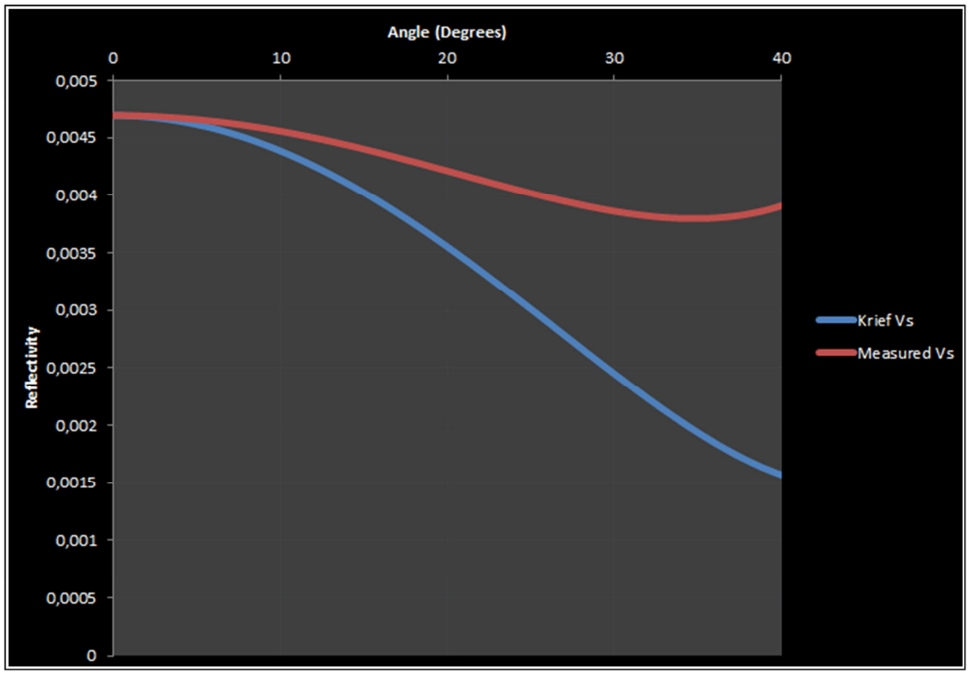

Fig. 7.11: The reflectivity of the top of Stø formation using measured and calculated (Krief) Vs in the well 7120/6-2S.

7.1.3 Sensitivity analysis (dry well)

The previous well 7120/6-2S is a gas well. Because of lacking information of gas saturation it was questionable to run actual fluid replacement modeling at field condition. To investigate the above problem and to compare it with earlier modeling I performed similar FRM. The dry well 7120/5-1 is used for sensitivity study.

The Figures 7.12 to 7.14 show the values of different rock properties and their increased or decreased in terms of percentages respectively. As we expected, when adding only 10% gas in water the Vp value dramatically changed from 3727.83 m/s to 2929.25 m/s (almost 21% decrease). Whereas from 10% to 100% gas saturation the Vp decreases only 100 m/s which is just 3%. The Vs and density are vice versa, Vs is increased with increasing gas saturation whereas density is decreased. In 100% gas saturated condition the PR shows negative values.

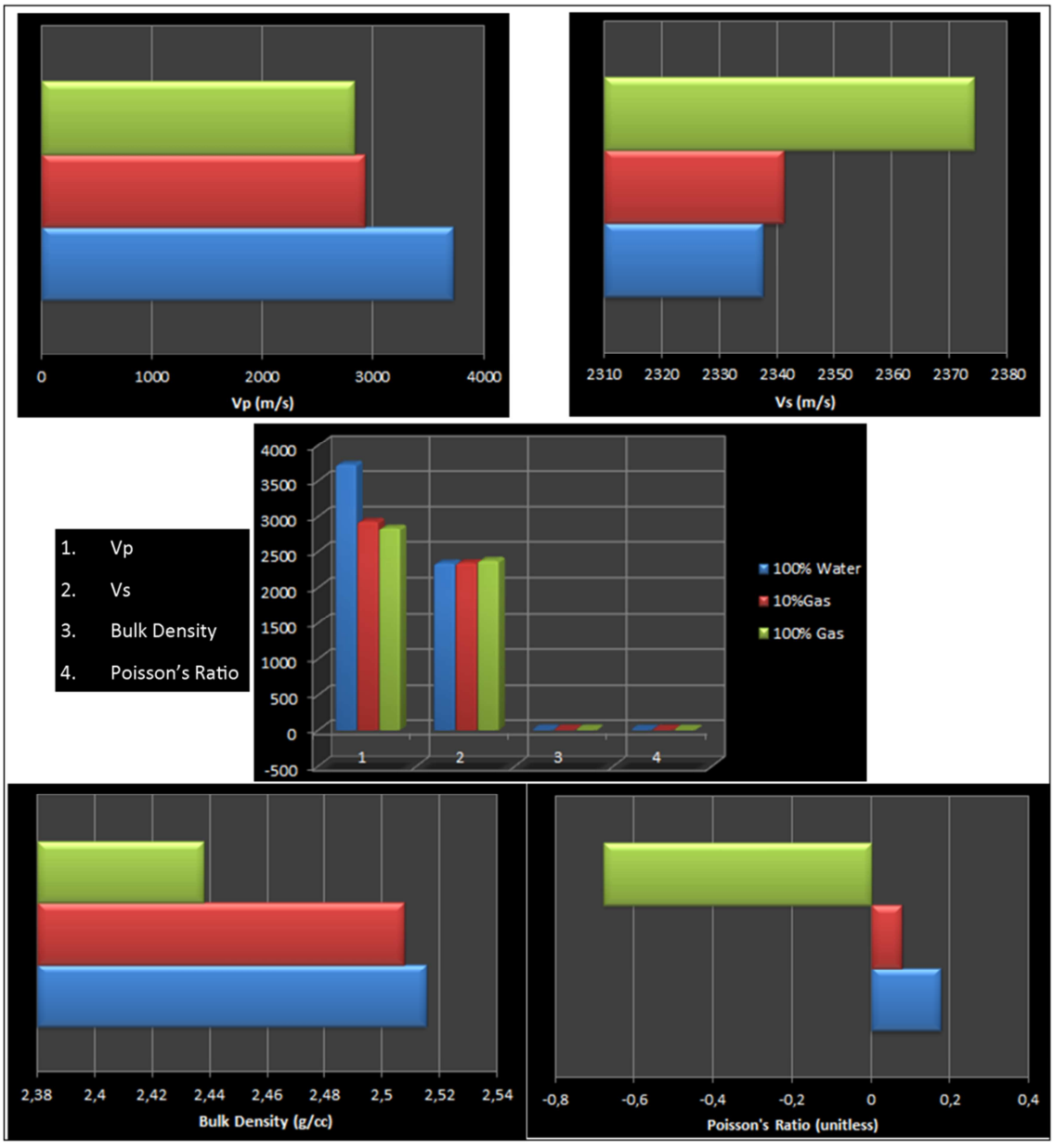

Fig. 7.12: The Vp, Vs, bulk density and Poisson's ratio values of different fluid saturation in the well 7120/5-1.

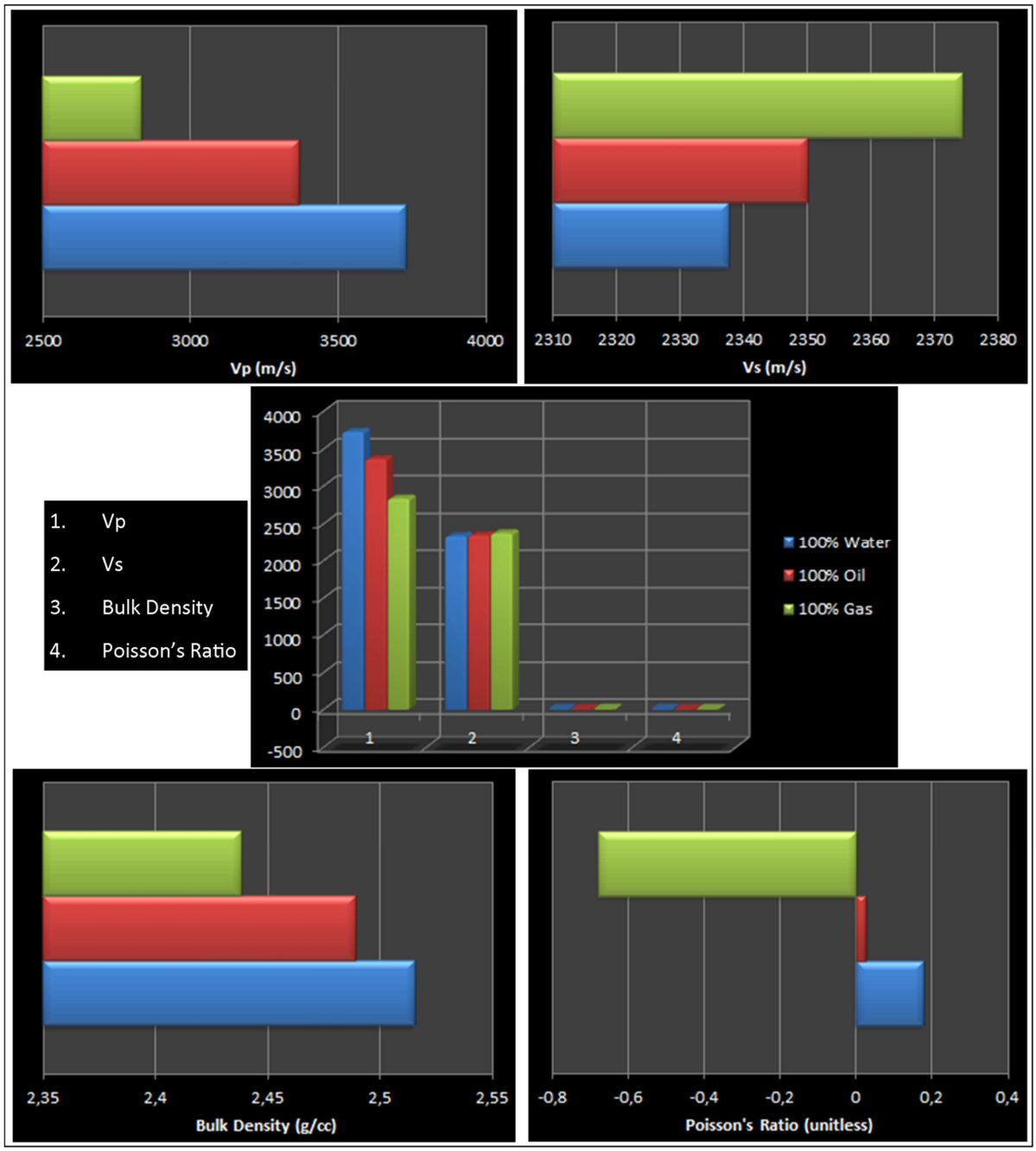

Fig. 7.13: The Vp, Vs, bulk density and Poisson's ratio values of water, oil and gas saturated sandstone in the well 7120/5-1.

The comparison of Vp, Vs, density and PR in water, oil and gas saturated conditions are shown in the Figures 7.13 to 7.15. The Vp decreases gradually whereas the Vs increases from water to gas. The bulk density is decreased but oil and water saturated conditions are more close compared to gas saturated cases. The negative value of PR in 100% gas saturation is ambiguous and may reflect the limitation of AVO modeling.

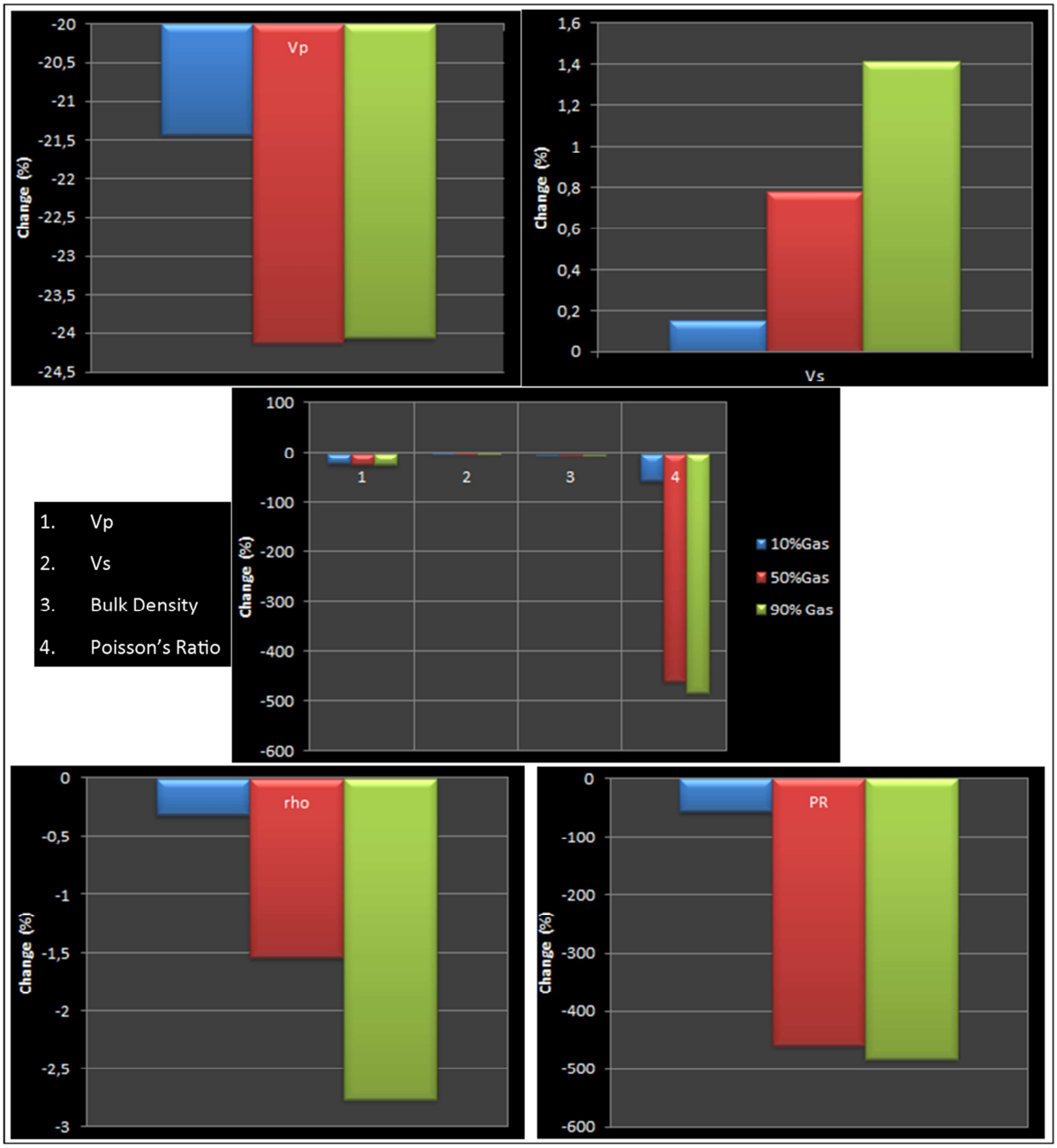

Fig. 7.14: Effect of fluid saturation on Vp, Vs, bulk density and Poisson's ratio in well 7120/5-1.

The effect of saturation changes is more evident in the angle dependent amplitude with offset (Fig. 7.16). The magnitude of the zero offset AVO intercept increases i.e. becomes more positive with increasing gas saturation compared to in-situ water saturation whereas oil reservoir is in between. All four scenarios have a positive AVO intercept and a negative gradient. The percentage changes in the AVO intercept is greater in 10% gas saturation whereas the value is smaller in case of 100% oil and gas saturation respectively.

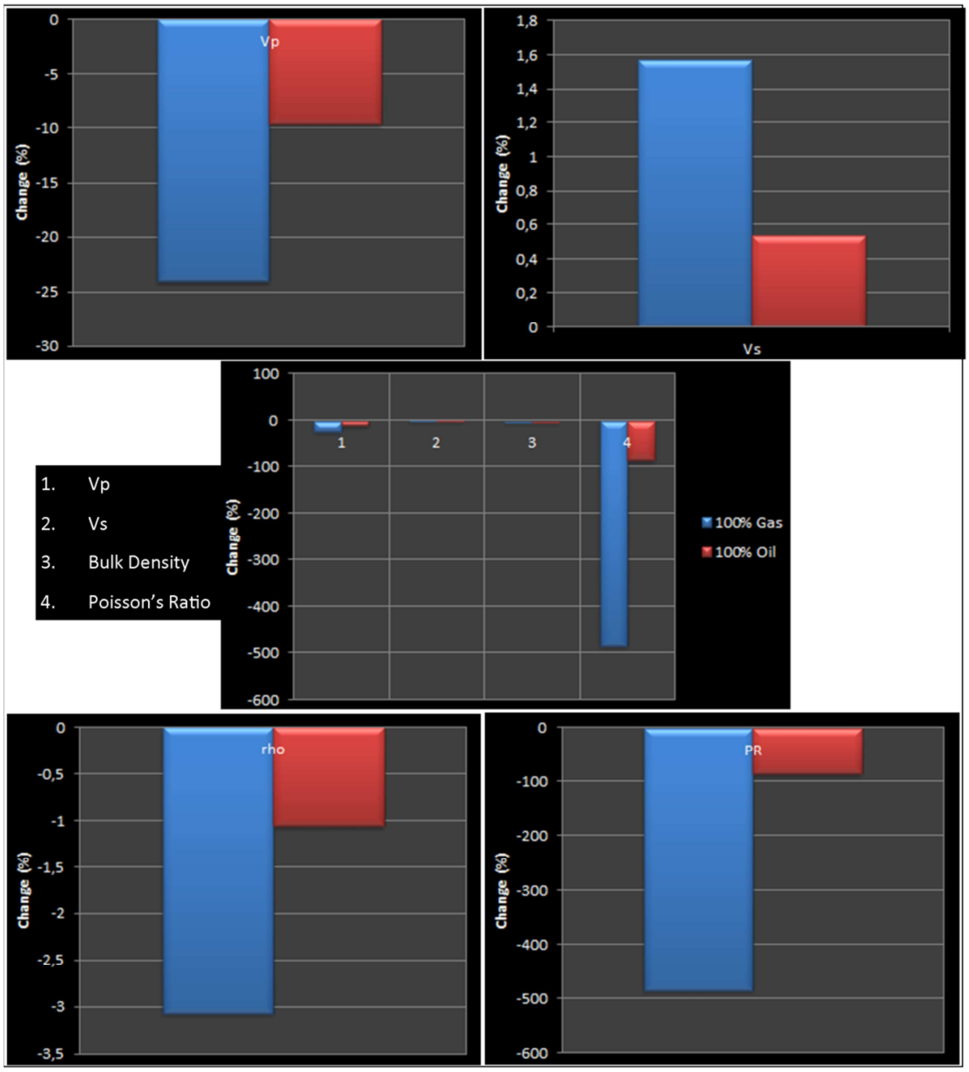

Fig. 7.15: Effect of changing fluid on Vp, Vs, bulk density and Poisson's ratio in well 7120/5-1.

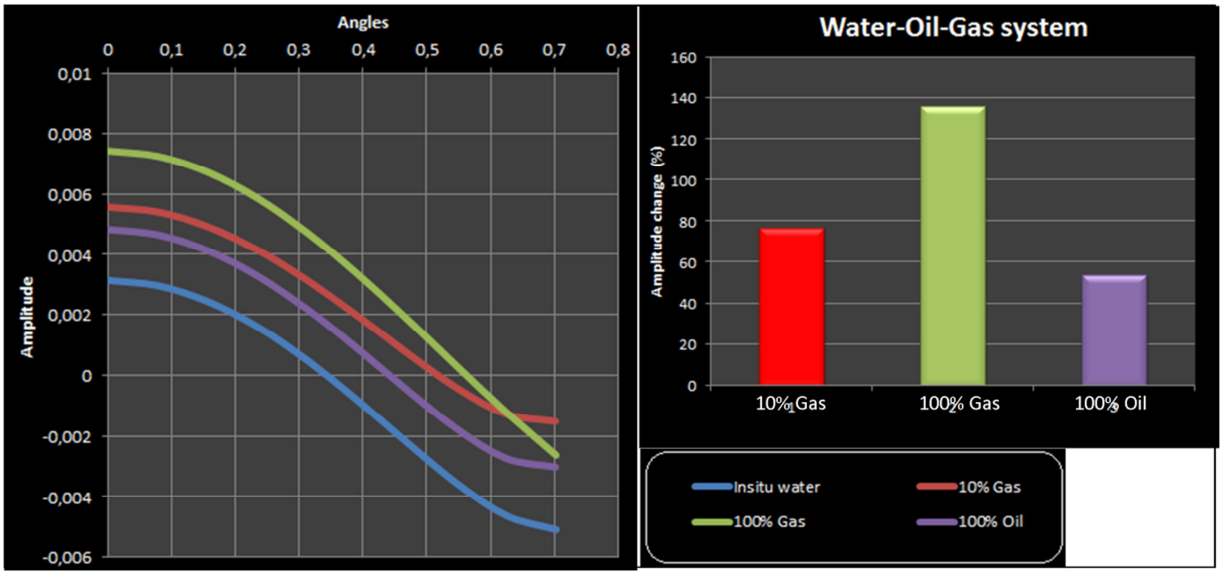

Fig. 7.16: Effect of gas saturations on reflection amplitude of in-situ, 100% oil, 100% gas and 10% gas cases in well 7120/5-1.

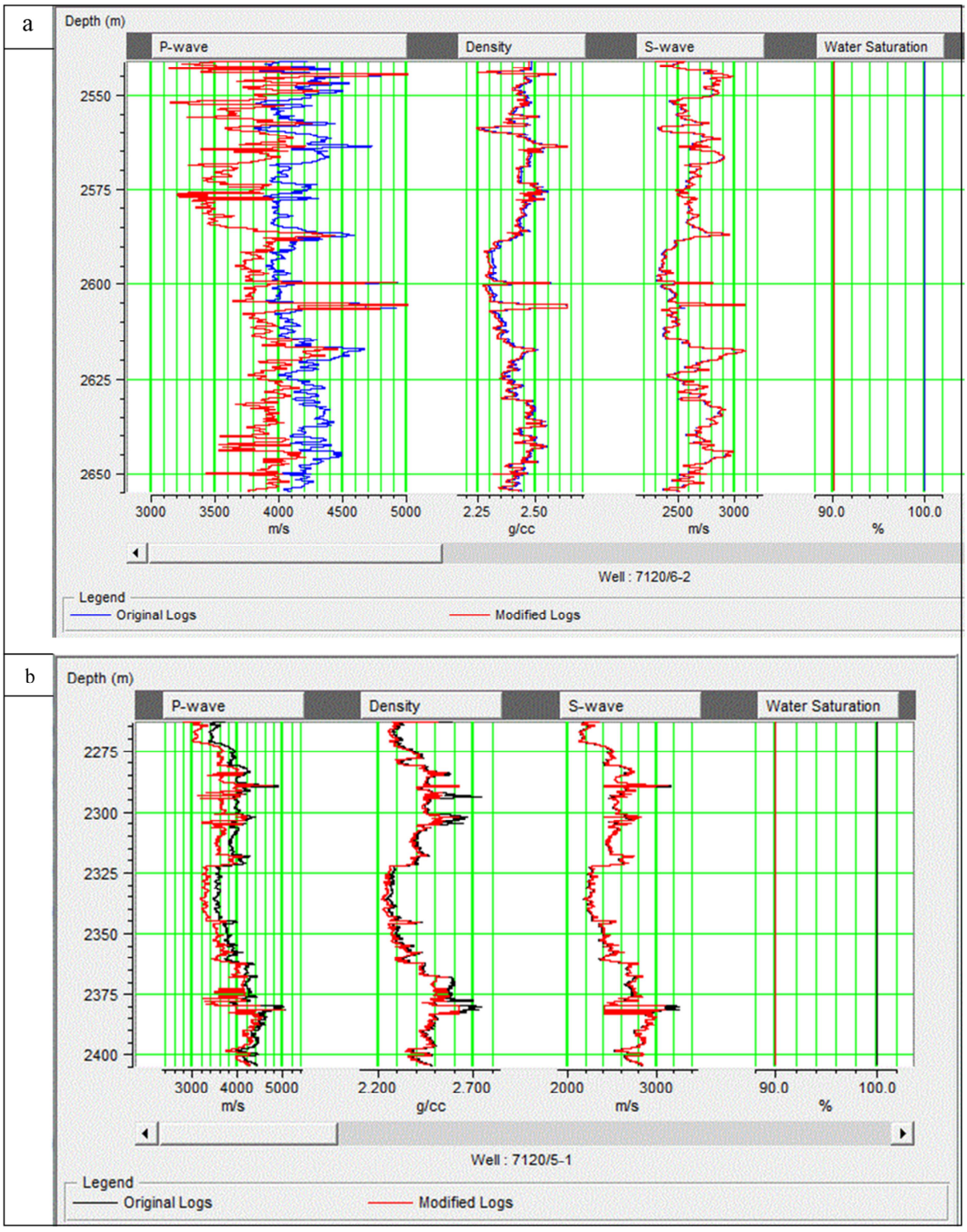

Fig. 7.17: Comparison of Vp, density and Vs logs by adding 10% gas in a water saturated Stø formation in the wells (a) 7120/6-2S and (b) 7120/5-1.

The Figure 7.17 showed the comparison between the logs Vp, Vs and density during adding 10% gas in the water saturated Stø reservoir in both wells 7120/6-2S (Fig. 7.17a) and 7120/5-1 (Fig. 7.17b). The decrease of Vp is more consistent in the well 7120/5-1 compare to 7120/6-2S whereas density and Vs are more or less similar response. The trend of increasing and decreasing of Vp, Vs or density are similar in different fluid saturation condition. But in case

of 100% gas saturation in the well 7120/5-1 showed negative whereas the other well showed positive value (Fig. 7.18 & 7.19).

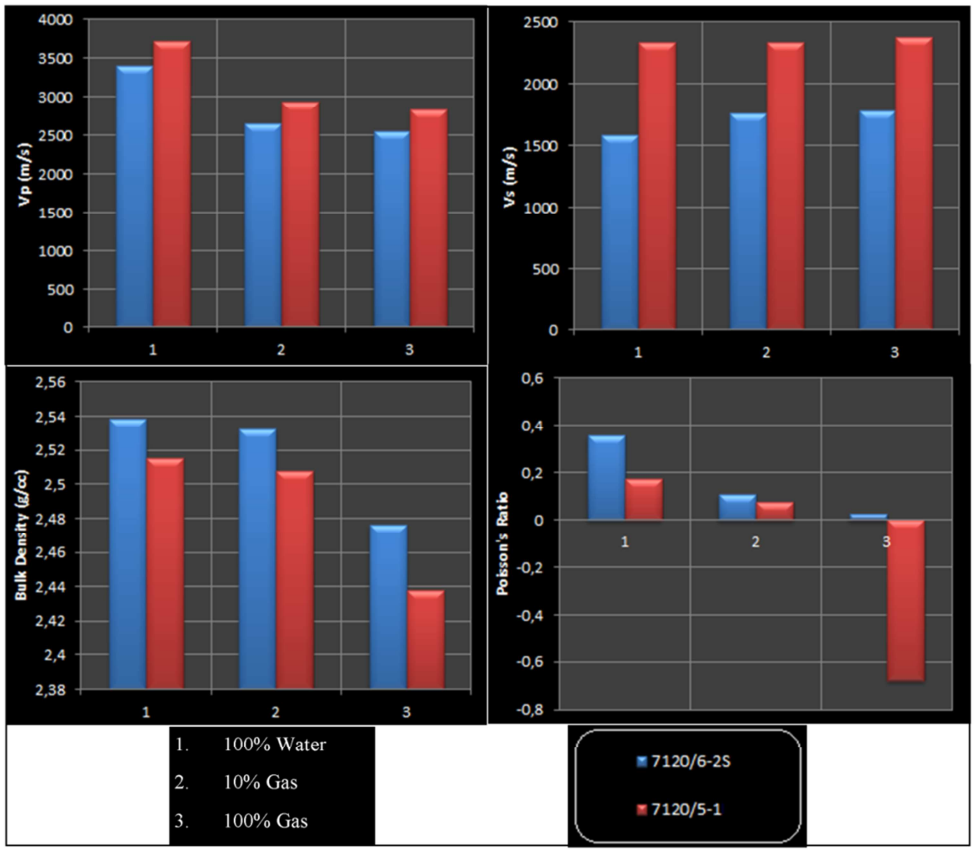

Fig. 7.18: Comparison between two wells of rock properties in different fluid saturation conditions.

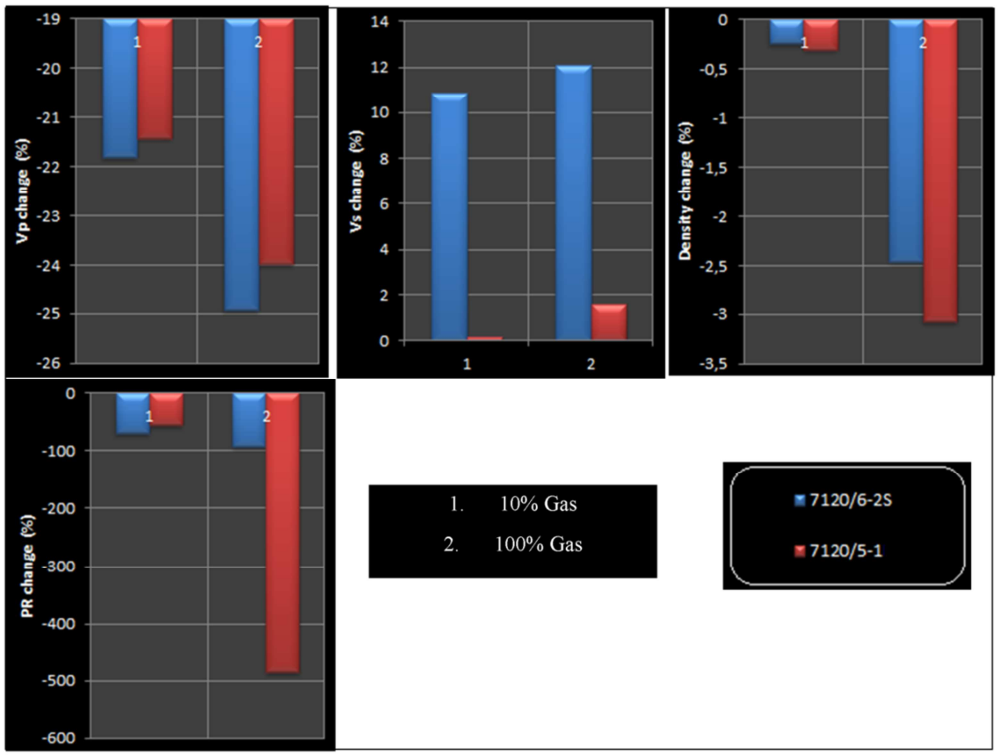

Fig. 7.19: Effect of changing gas saturation on Vp, Vs, density and PR in both wells.

The synthetic seismograms of different saturation scenarios have been generated using a Ricker Linear wavelet and applying the Zoeppritz equation for a total angle range of 45 degree for both wells 7120/6-2S (Fig. 7.20a) and 7120/5-1 (Fig. 7.20b). All logs used for these synthetic seismics are 15m blocked. The data has been displayed using the normal polarity convention. The corresponding synthetic seismic for the different saturations show a slight change just for the initial 10% gas saturation. The seismic for higher gas saturation is more or less similar whereas oil saturated seismic response is in between. In the gas bearing 7120/6-2S well, there is a strong reflection because of OWC whereas it is missing in the dry well 7120/5-1. The main observation is the relative changes in the petrophysical parameters due to 10% gas into the water saturated reservoir.

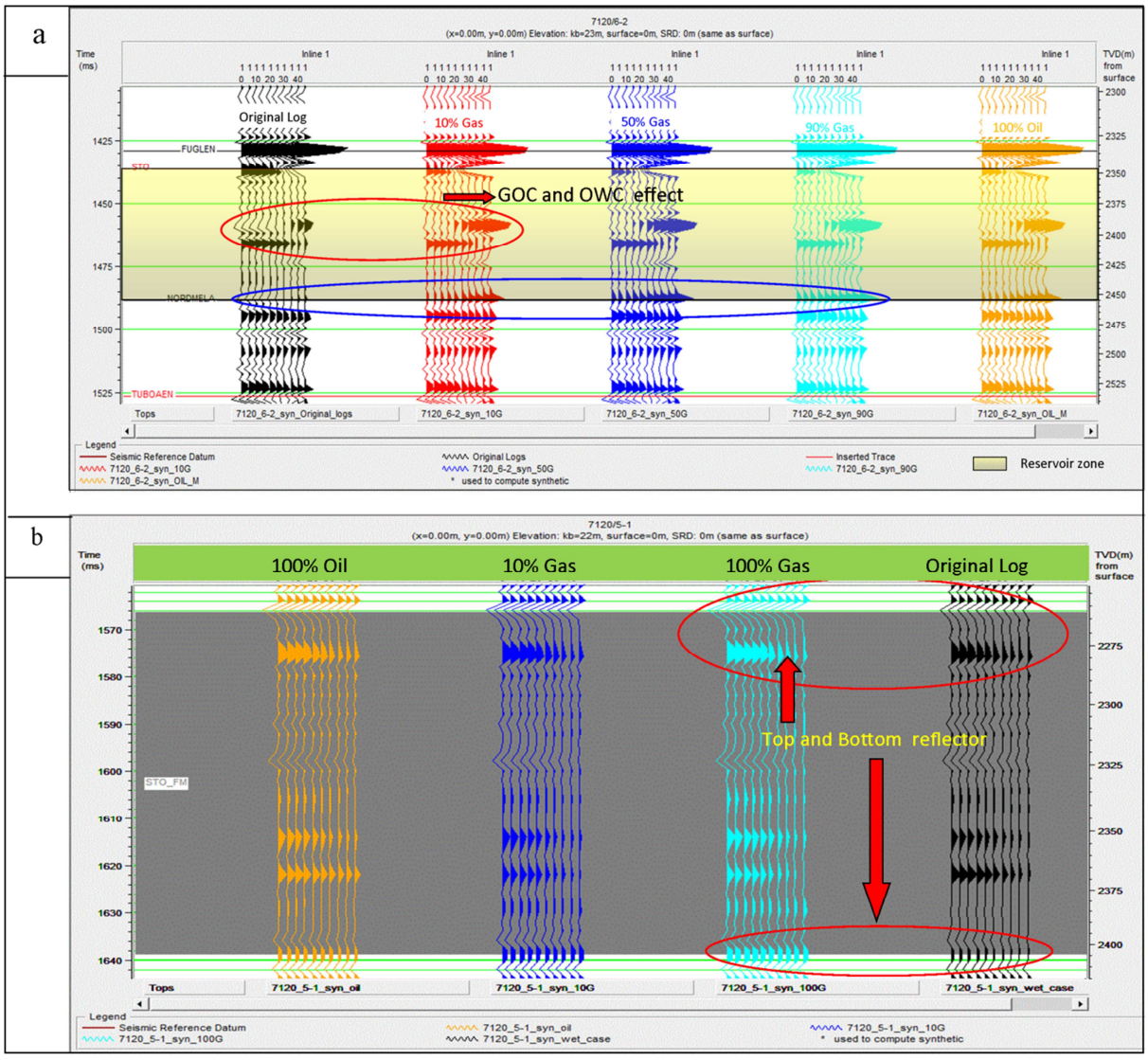

Fig. 7.20: The synthetic seismograms well (a) 7120/6-2S and (b) 7120/5-1 in different fluid saturation scenario.

7.1.4 Classification of reservoir sands

The model described here represents simple two layer models with a single interface. Only the top target reflector in Stø reservoir has been used in this study without considering the base of the reservoir horizon of interest. The wells used in this part are gas bearing except the well

7120/5-1 which is day. In the modeling part, I changed in-situ gas saturation to water and in-situ dry case to gas by using the FRM method in the HR elog module.

The Table 7.5 shows the AVO sand classification of different wells in both cases. The maximum positive and negative zero offset reflectivity is given by the same wells in both in-situ and modeled condition (Fig. 7.21). The well 7121/5-1 shows strong positive reflectivity with negative gradient (Class I) in both in-situ and modeled conditions, though in modeled condition the reflectivity is smaller (from 0.06 to 0.04) compared to the in-situ gas condition (Fig. 7.22). The strongest negative reflectivity of well 7120/5-1 is increases in case of modeled situation (-0.063 to -0.069) with a positive gradient in both cases (Class IV).

Table 7.5: AVO classification based on the angle dependent reflectivity in the Stø reservoir

Wells	Pore Fluid	Class	Zero offset Rp
7121/4-1	In-situ Gas	IIa	0.016768
	Water model	IIb	-0.02759
7121/4-2	In-situ Gas	IIb	-0.00346
	Water model	IIb	-0.02388
7121/5-1	In-situ Gas	I	0.067131
	Water model	I	0.044491
7120/6-1	In-situ Gas	IV	-0.01754
	Water model	III	-0.03822
7120/5-1	In-situ Water	IV	-0.06331
	Gas model	IV	-0.06903

The wells 7121/4-1 and 7121/4-2 are consistent of Class II sand in both cases though the reflectivity of the well 7121/4-1 has changed from positive to negative due to change in-situ gas to water. Both gas and water cases in the well 7120/6-1 give a negative zero reflectivity but the gradient is positive in case of gas (weak IV) whereas negative in water case (Class III). Except the well 7121/5-1, all other wells show the zero offset reflectivity negative or close to zero.

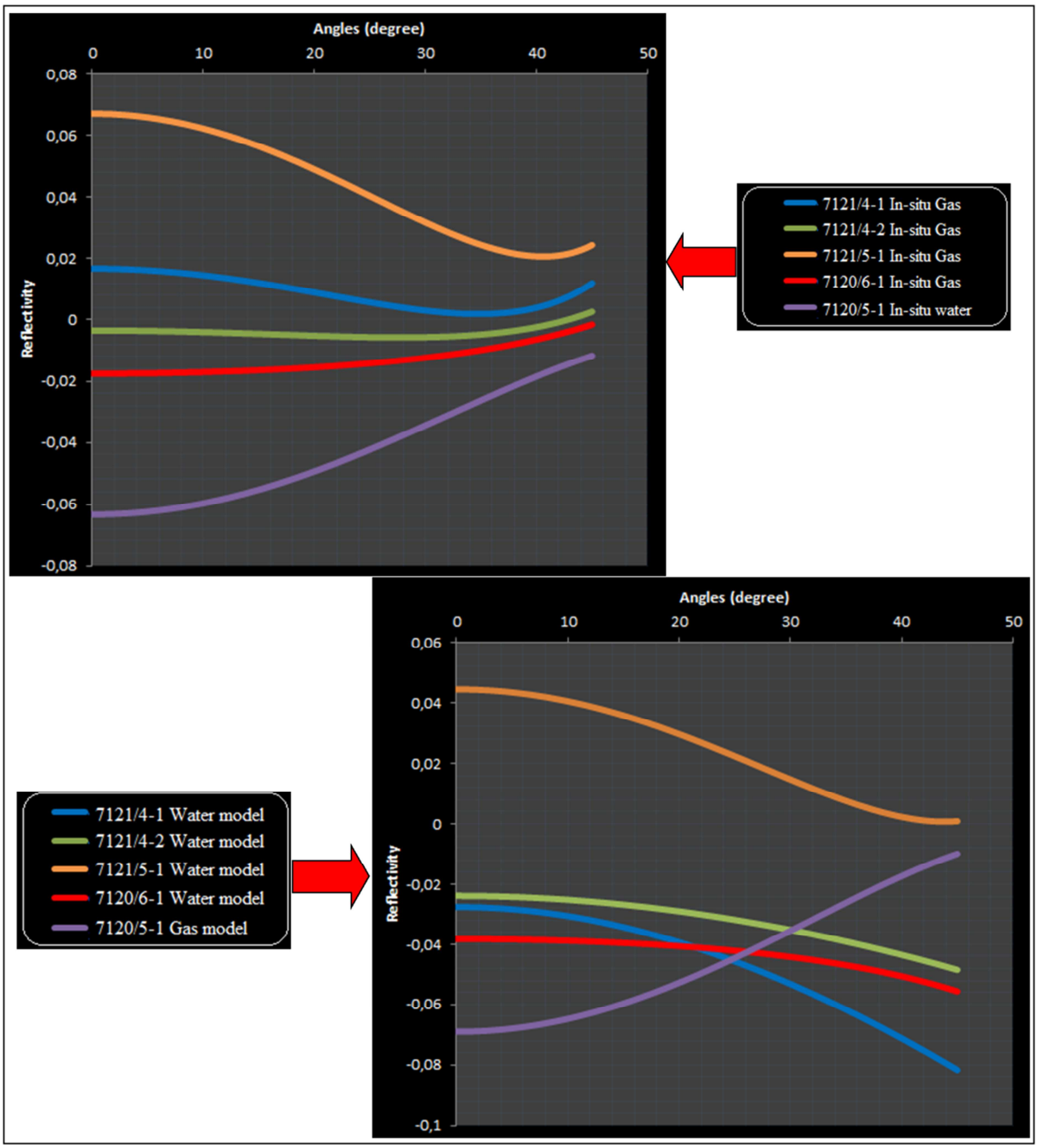

Fig. 7.21: Angle dependent reflectivity of Stø formation in gas-water system.

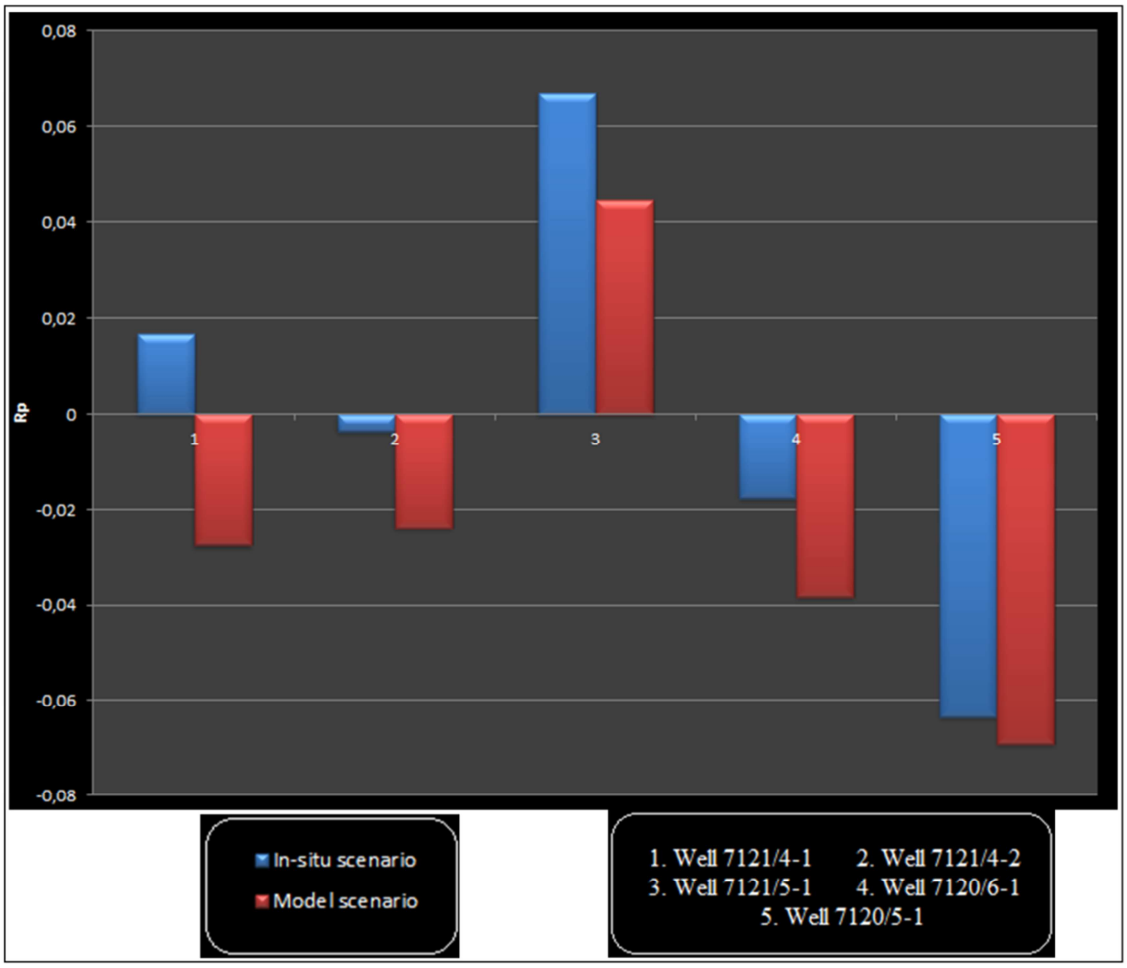

Fig. 7.22: Quantitative changes in Rp for the Stø reservoir after fluid replacement modeling.

7.1.5 Intercept and gradient analysis

The AVO analysis is carried out of all six wells with in-situ fluid conditions. All Vp, Vs and density logs have been blocked by using a 15 m block. To determine the AVO sand classes both gradient and reflectivity analyses have been carried out. The intercept gradient cross-plots for all well are shown in the Figure 7.23. These gradient analyses are carried out using A/B two term Aki-Richards analysis type with robust stabilizing method. The values of AVO intercept (A) and AVO gradient (B) are showed in the Table 7.6.

Table 7.6: AVO intercept (A) and Gradient (B) values of all six wells with robust correction.

Wells	AVO Intercept (A)	AVO Gradient (B)	Robust Correction
7121/4-1	0.00936908	-78.8467	0.876098
7121/4-2	0.00609572	11.4915	0.993976
7121/5-1	0.0280185	-222.722	0.940777
7120/6-1	-0.0107023	65.7816	0.993516
7120/6-2S	0.0213409	-167.758	0.902423
7120/5-1	-0.0290264	180.751	0.973172

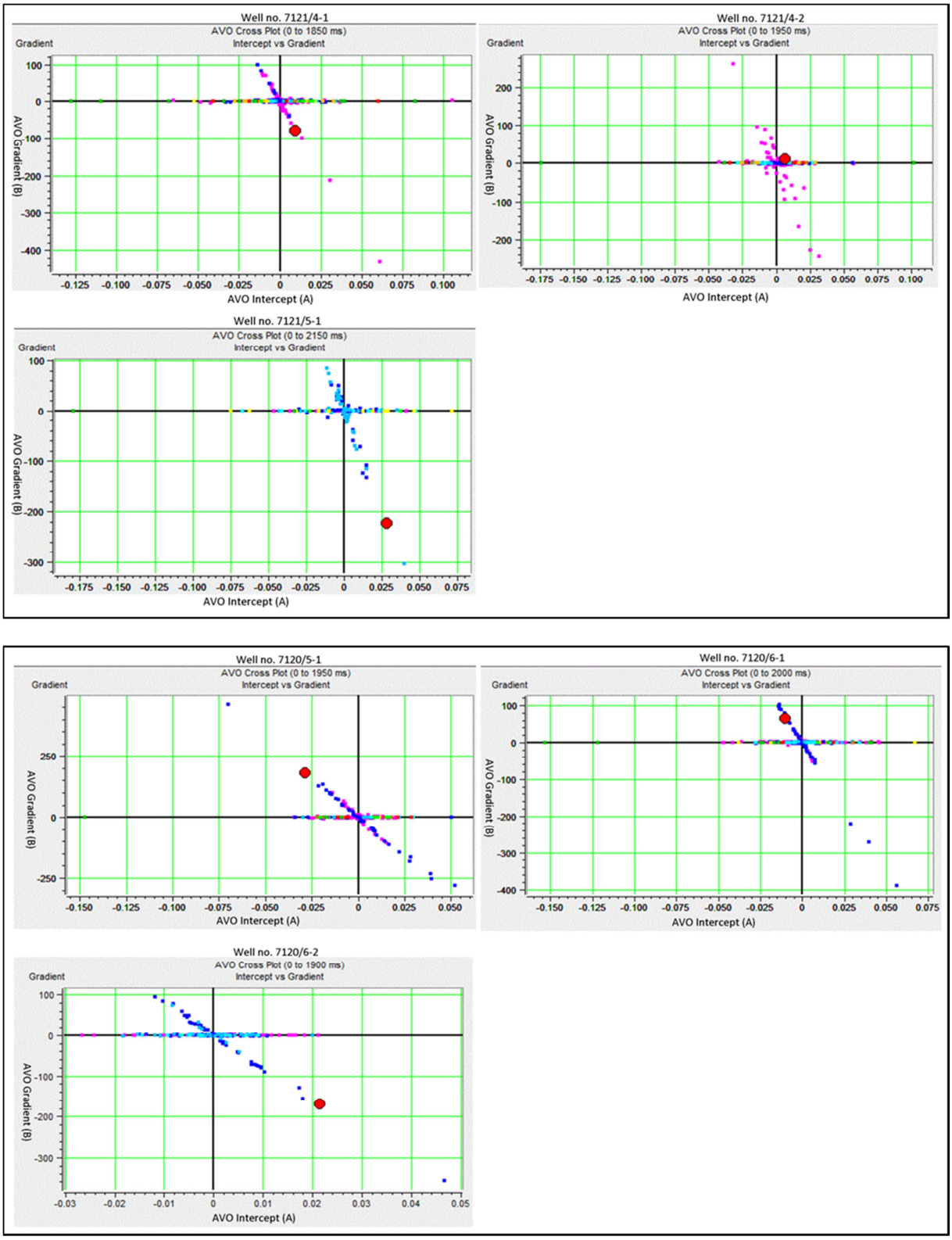

Fig. 7.23: The intercept gradient cross-plots of six wells used in this study.

Four wells (give names) out of six have shown positive intercept whereas five wells (give names) have decreased their gradient with increasing angles (Fig. 7.24). The gradient of 7121/4-2 has been increased with increasing angles. The maximum positive amplitude is given by the well 7121/5-1 which is a gas well whereas maximum negative amplitude is given by the well 7120/5-1 which is a dry well.

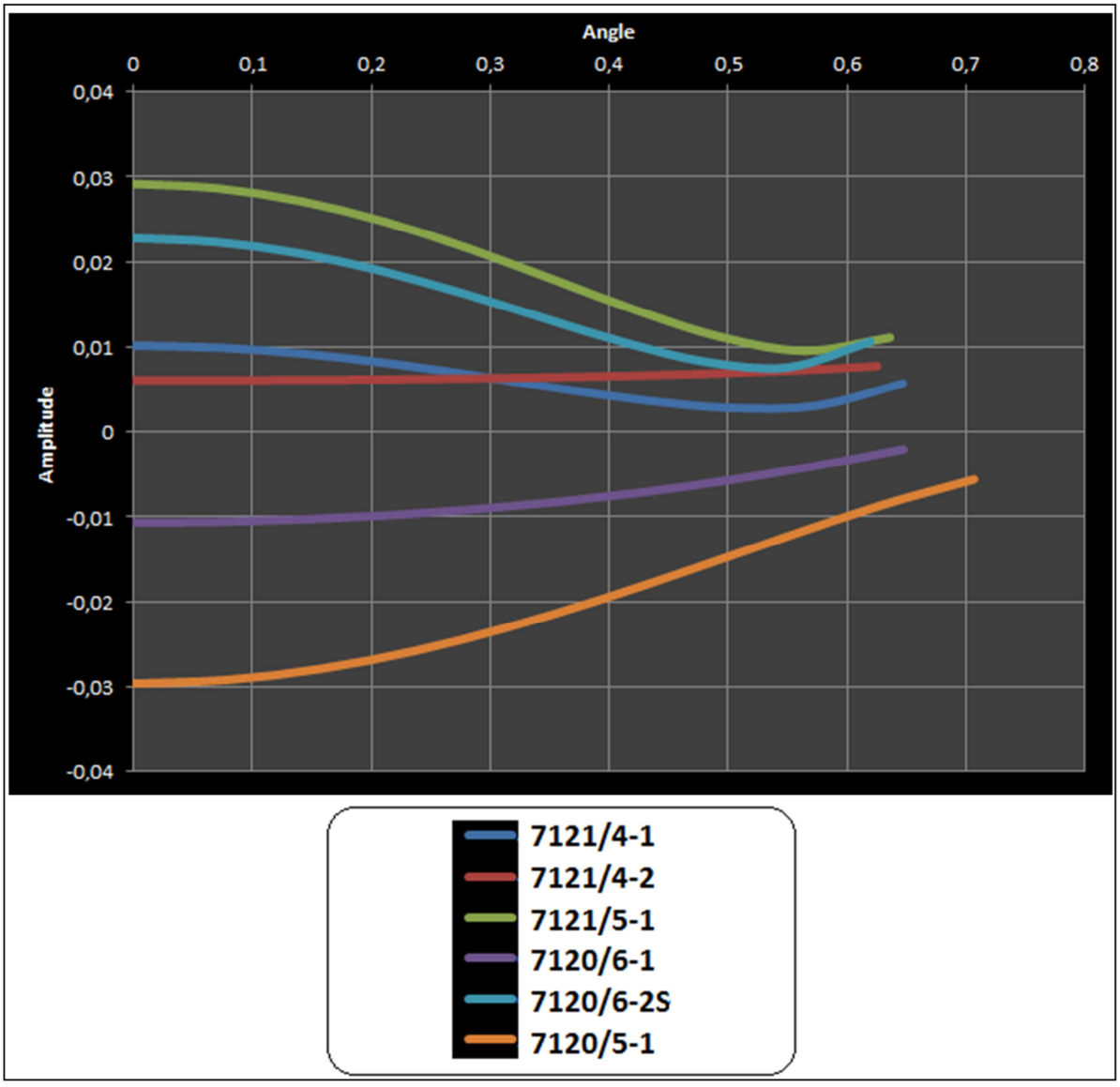

Fig. 7.24: The amplitude of the synthetic seismic of six wells.

The Table 7.7 shows the difference of AVO sand classes of the Stø Formation based on the values of A and B. The wells 7121/4-1, 7121/4-2 and 7120/6-1 showed class II sand whereas 7121/5-1 and 7120/6-2S have given class I sand. The dry well 7120/5-1 has shown the class IV sand.

The maximum positive and negative reflectivities are also given by the wells 7121/5-1 and 7120/5-1 respectively (Fig. 7.25). The Table 7.8 shows the difference of sand classes based on their angle dependent reflectivity in their in-situ fluid conditions of the Stø sandstone. The wells 7121/4-1 and 7120/6-2S have given the IIa AVO sand Class whereas 7121/4-2 and 71206-1 have given IIb sand. The well 7121/5-1 has strong positive reflectivity and has given class I AVO sand.The dry well has given class IV AVO response.

Table 7.7: AVO sand class of Stø sandstone based on A and B.

Wells	Pore Fluid	Class	Quadrant	A	B
7121/4-1	In-situ Gas	II	IV	+	-
7121/4-2	In-situ Gas	II	I	+	+
7121/5-1	In-situ Gas	I	IV	+	-
7120/6-1	In-situ Gas	II	II	-	+
7120/6-2S	In-situ Gas	I	IV	+	-
7120/5-1	In-situ Water	IV	II	-	+

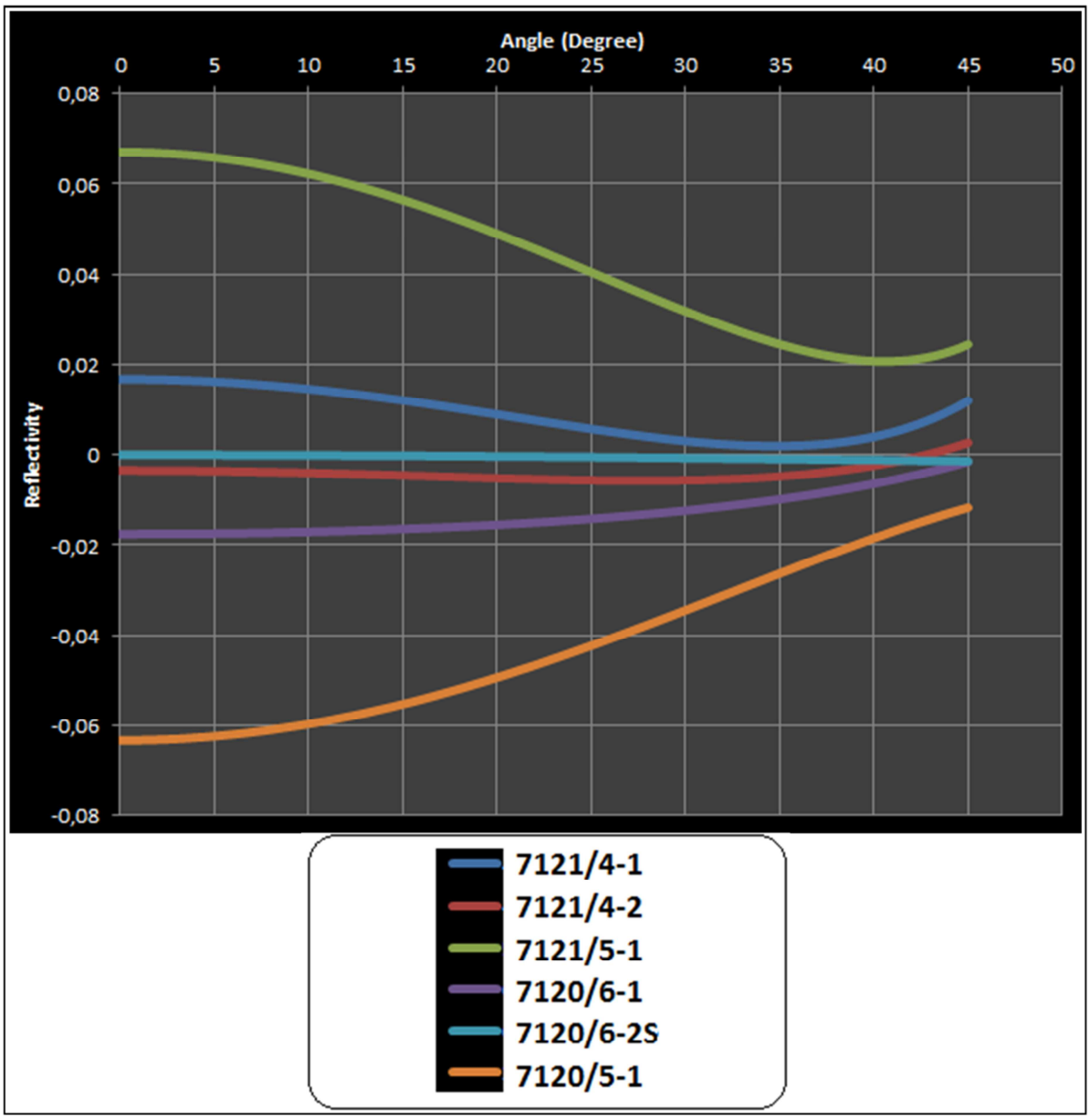

Fig. 7.25: The angle dependent reflectivity of Stø sandstone of all six wells.

Table 7.8: AVO classification based on the reflectivity of Stø sandstone

Wells	Pore Fluid	Class	Zero offset Reflectivity
7121/4-1	In-situ Gas	IIa	0.018
7121/4-2	In-situ Gas	IIb	-0.003
7121/5-1	In-situ Gas	I	0.068
7120/6-1	In-situ Gas	IIb	-0.018
7120/6-2S	In-situ Gas	IIa	0
7120/5-1	In-situ Water	IV	-0.063

7.1.6 Effect of diagenesis on AVO response

One important factor in diagenesis is temperature which is dependent on depth of the formation (greater depth, higher temperature). To avoid the fluid effect I used dry well 7120/5-1 to investigate the diagenetic effect. Three potential reservoir sandstones (, top Stø, top Nordmela and top Tubeån formation) are incorporated for the analysis. The gamma ray log is used to describe lithological variation within the target formations. The other logs such as Vp, Vs, density, deep resistivity, calculated P-impedance and calculated reflectivity are shown in the Figure 7.26 with a block size of 15 m.

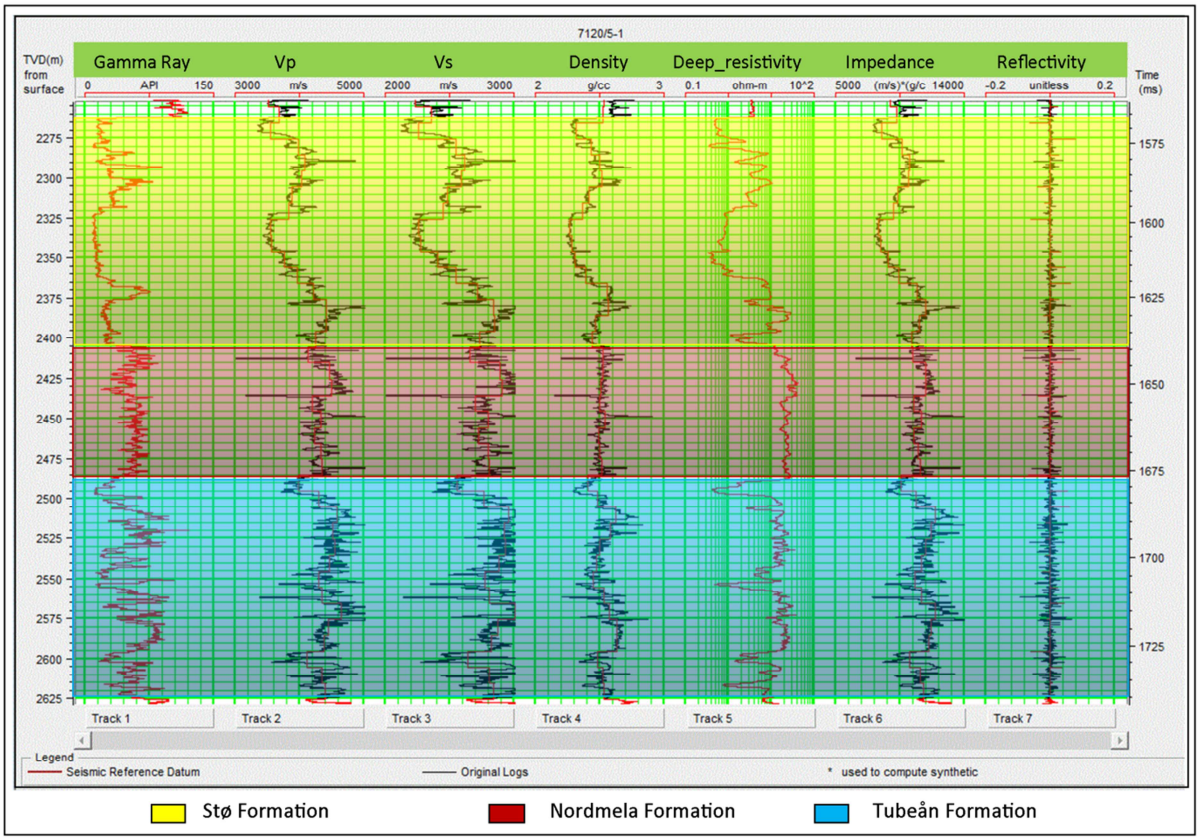

Fig. 7.26: Showing different log responses with the three in the well 7120/5-1.

The Table 7.9 shows the AVO classes of three reservoir sandstones in in-situ conditions. The Nordmela formation shows the class I sand whereas other two show the class IV AVO response. The formation tops of Stø and Tubeån show negative zero-offset reflectivity with values -0.06331 and -0.06623 respectively whereas the Nordmela formation shows the positive reflectivity (0.03905) (Figs. 7.27 and 7.28). The gradients of all three formations are positive and increasing with increasing angles (Offset).

Table 7.9: AVO classification of top Stø, top Nordmela and top Tubeån formation

Well 7120/5-1			
Formation Tops	Pore Fluid	Class	Zero offset Rp
Top Stø	In-situ Water	IV	-0.06331
Top Nordmela	In-situ Water	I	0.03905
Top Tubeån	In-situ Water	IV	-0.06623

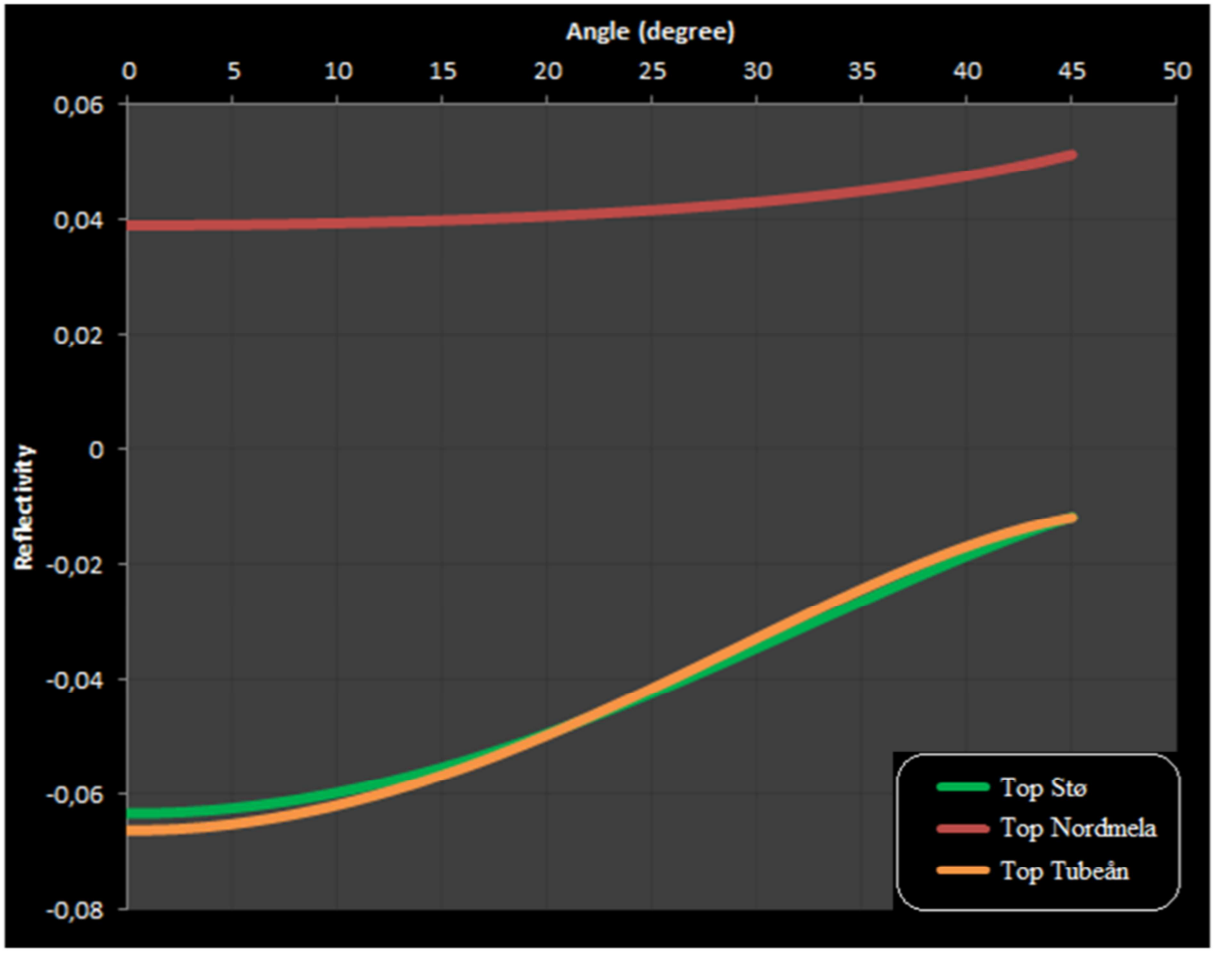

Fig. 7.27: Angle dependent reflectivity of three formation tops in the well 7120/5-1.

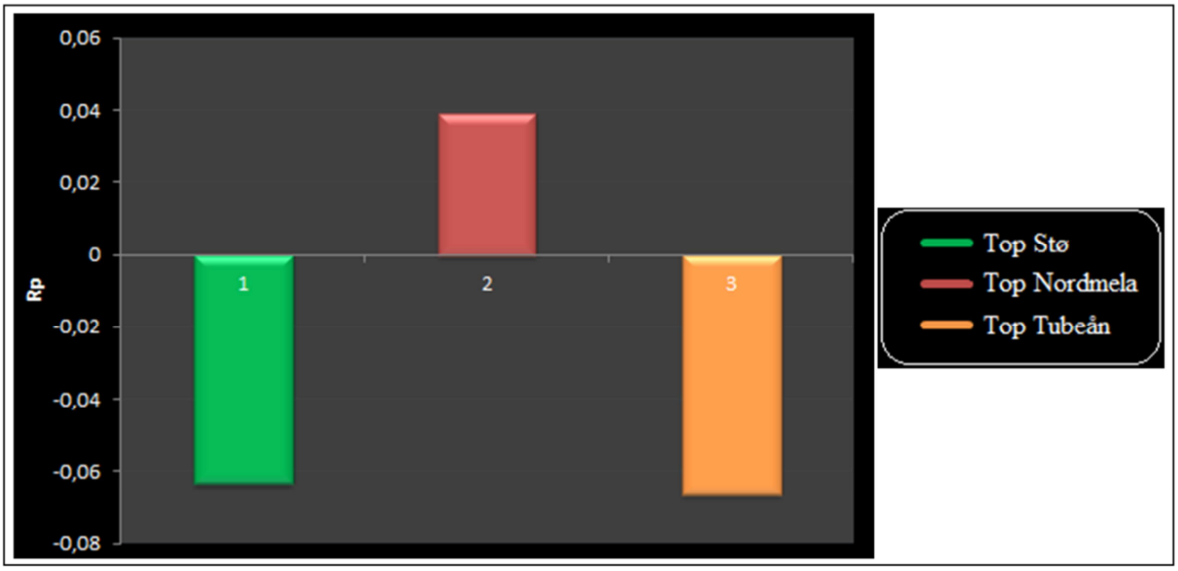

Fig. 7.28: Changes in Rp for different tops.

7.2 Discussions

7.2.1 Influence of block size

It is clear from modeling that the block size is very important for AVO analysis. The location of the target reflector is shifted because of different block sizes that we observed in our modeling (Fig. 7.5). The top Stø reflector giving class IV AVO gas sand in all blocks scenarios whereas 25 m size has given the strongest reflector compared to block sizes 10 and 50 m. On the other hand, the cap rock at top Fuglen formation shows a strong positive reflector in all block scenarios which give the negative reflectivity in the boundary between the cap and the reservoir rocks. The intercept gradient cross-plot also shows the class IV AVO classes because all points are fallen into the second quadrant.

7.2.2 Effect of bulk density

The effect of fluid substitution on Vp, Vs, density and Poisson's ratio (PR) in the Stø formation in wells 7120/6-2S and 7120/5-1 show a consistent and independent relationship between these petrophysical properties. Vp and Vs are depends on the effective bulk and shear modulus and density of specific rock while Vp/Vs ratio determines the magnitude of the PR. The equation for Vp and Vs are:

$$V_P = \sqrt{\frac{K+\frac{4}{3\mu}}{\rho}} \quad \ldots\ldots\ldots\ldots\ldots\ldots\ldots \quad (7.1)$$

And

$$V_S = \sqrt{\frac{\mu}{\rho}} \quad \ldots\ldots\ldots\ldots\ldots\ldots\ldots\ldots \quad (7.2)$$

Where K, μ and ρ represent the effective saturated bulk modulus, shear modulus and density respectively. Both equation show that Vp and Vs will increase with a decrease in effective density, if all other parameters are kept constant. The shear modulus is insensitive to fluid,

such that the shear modulus of rock frame is same as the shear modulus of same rock saturated with any fluid. Therefore Vs is only controlled by effective density. The fluid properties used for fluid substitution modeling are shown in the Figure 4.9. The density of gas is very low compared to oil and water. Vs however show a slight increase with increasing gas saturation in both wells (Fig. 7.5 & 7.12). The percentage of Vs increase is roughly proportional to the percentage of decrease in density (Fig. 7.6 & 7.14).

On the other hand, effective density and bulk modulus controlled Vp while effective bulk modulus depends on the modulus of mineral materials and modulus of fluid. Gas has much more compressible compared to oil and water. As a result just by adding 10% gas in fully brine-saturated system , leads to a large percentage drop in Vp about 5.5% in the well 7120/6-2S and 21.4% in the well 7120/5-1. This large change is not only depends on the density decrease but also the large change in the effective bulk modulus (K) of the medium.

7.2.3 Effect of saturation

The Table 7.10 shows the change of effective density and fluid modulus with changing fluid saturation. There is a consistent decrease in both parameters with increasing gas saturation (Fig. 7.29). The effective fluid bulk modulus used as an input parameter in the Gassmann fluid replacement modeling is calculated by Reuss harmonic averaging in Hampson Russell software assuming homogeneous saturation. Because of the drop in effective fluid modulus at the 10% gas saturation, the overall effective modulus decreased and Vp is also decreased though the density decrease is insignificant. Increase in gas saturations from 10 to 100% show a very low sensitivities in fluid modulus compared to density. Density is decrease gradually but the fluid modulus remain constant or changed very little and gave the higher Vp in 90% gas saturation in the well 7120/6-2S (Fig. 7.5).

Table 7.10: Effective density and fluid modulus of different fluid saturation condition.

Fluid saturation (%)	Effective Density (g/cc)	Fluid modulus (Gpa)
100% Water	2.5153	2.6308
10%Gas	2.50757	0.3619
50%Gas	2.47666	0.0813
90% Gas	2.44574	0.0458
100% Gas	2.43801	0.0413

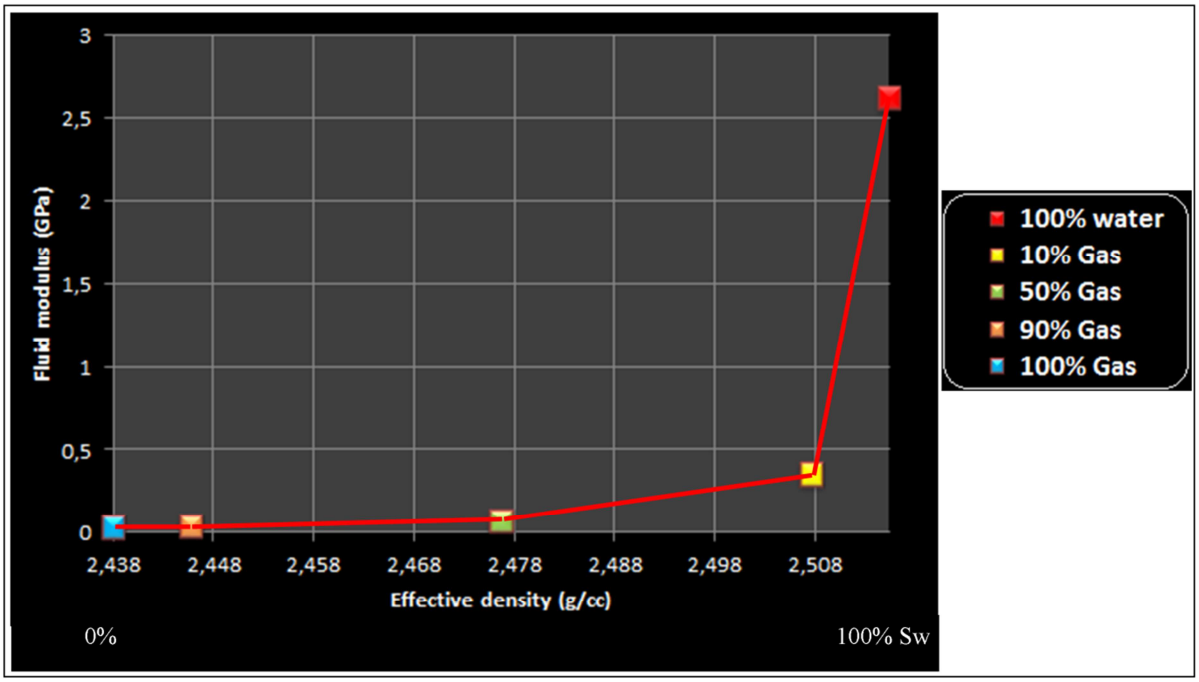

Fig. 7.29: density fluid modulus cross-plot of different fluid saturation in the well 7120/5-1.

The corresponding synthetic seismic data for all fluid saturation scenarios and in-situ water scenario are shown in the Figure 7.20. There is a slight increase in the strength of the internal reservoir reflector. In 7120/6-2S well these internal reflector is more prominent compare to 7120/5-1 because of GOC and OWC effect. After introducing gas into the reservoir, the acoustic impedance contrast increases which also causes an increase in the strength of the reflectors. This change is observed just for the initial 10% gas saturation. With increasing gas saturations, the corresponding synthetic seismics look similar. This is largely because of the decreasing sensitivity of the effective saturated bulk modulus and Vp for progressively higher gas saturation. The percentage of changing Vp is much higher than Vs and density and tend to control the observed synthetic seismic and AVO response for the different saturations.

The top reservoir target reflector shows clearer differences with changing fluid saturations, when comparing the zero offset amplitude for different fluid saturations. The changes in amplitude as expected are larger and larger with increasing gas into water. The largest amplitude has been given by 100% gas saturation because of the increase of acoustic impedance contrast between the reservoir and the cap rock. The maximum percentage of increasing amplitude is given by 10% gas saturation.

7.2.4 Effect of mineralogy

The saturation effect on different mineralogical compositions is dependent on porosity. The clean sandstone (100% quartz) have more porosity compare to quartz-clay (80:20) system which influence on the effective density. The more the gas saturation, the bigger the difference is of density in between these two mineralogical composition units. Vs also follow the density decrease as it increases with decreasing density but the Vp is lower in quartz-clay system compared to pure quartz. Because of high porosity in the pure quartz system, the effect of gas modulus is also higher decreases the effective modulus of the rock and decreases the Vp as well (Fig. 7.7). However it is evident that the gas saturation in the water-gas system from 10% to 100%, leads to a difference of less than 3% change in the corresponding velocity

at 100% gas saturation condition whereas from 0-10% gas saturation leads to 21.42% velocity decreased in the well 7120/5-1.

The Poisson's ratio shows the largest drop with increasing gas saturation. This is just because of large change in Vp while an almost insignificant change in Vs. When the percentage change of all four petrophysical parameters are compared using the same scale, their sensitivity can be ranked in the order: PR > Vp > density > Vs.

Within these two wells as we know from the earlier chapter (chapter 6), the Stø formation in well 7120/6-2S has more shale compared to well 7120/5-1. 7120/6-2S well has higher density compare to 7120/5-1 in all saturation which is responsible for lowering of Vs. The wells 7120/6-2S and 7120/5-1 follow the same rule like quartz and quartz-clay system.

7.2.5 AVO intercept-gradient crossplot

The magnitude of the AVO intercept is controlled by the contrast in the acoustic impedance whereas the AVO gradient is controlled by changing in Poisson's ratio. During comparison of reflectivity using direct measured Vs with calculated Vs (Krief), the intercept is similar because the P-wave acoustic contrast is similar in both cases but the gradient which is depends on PR is different. Decreasing the PR (Vp/Vs) in calculated Vs leads to an increase in gradient (Fig. 7.11). We have to keep it in mind that the Krief (1990) equation is used to calculate Vs for 5 wells where direct measurement is missing.

7.2.6 Combined effect of fluid-saturation-porosity and mineralogy

The acoustic impedance contrast between Stø reservoir and Fuglen cap rock shows different in different wells. Two wells 7121/4-1 and 7121/5-1 show positive zero-offset reflectivity in in-situ gas scenarios whereas wells 7121/4-2, 7120/6-1 and 7120/5-1 showed negative reflectivity and the well 7120/6-2S shown nearly zero reflectivity. Except the well 7120/5-1, all other wells have been gas saturated in-situ conditions which are less dense and reduce the impedance. The impedance depends on the effective velocity and density which is also depends on the combination of different solid and fluid properties. Porosity also involve with this effective velocity and density calculation. Though all wells are gas saturated but because of different thickness and mineralogy of reservoir and cap rocks, the zero-offset reflectivity show positive and negative response within the same reflector (Fig. 7.30).

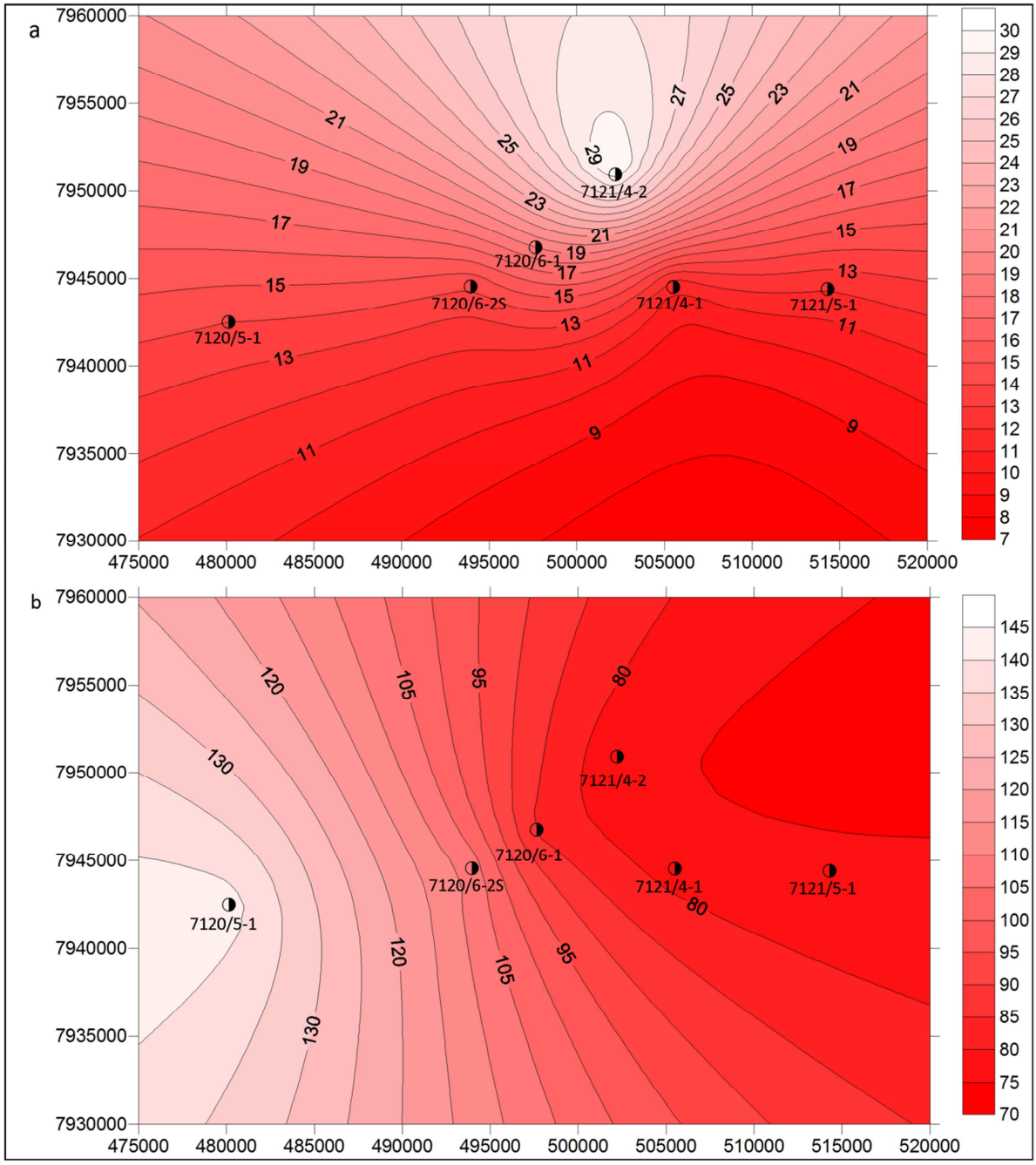

Fig. 7.30: The thickness of the study area (a) Cap rock and (b) reservoir rock.

Figure 7.31 shows the highest negative and positive impedance with reflectivity in wells 7120/5-1 and 7121/5-1. The well 7120/5-1 is a dry but because of mineralogical effect the zero-offset reflectivity is negative whereas in gas bearing 7121/5-1 well shows strong positive reflection. After changing the fluid using fluid replacement algorithm in the dry well from water to gas, the zero offset reflectivity is increased as expected but the change is significantly smaller (-0.063 to -0.069). On the other hand, all gas bearing wells in modeling scenarios (gas replaced by water) giving lower reflectivity compare to in-situ conditions.

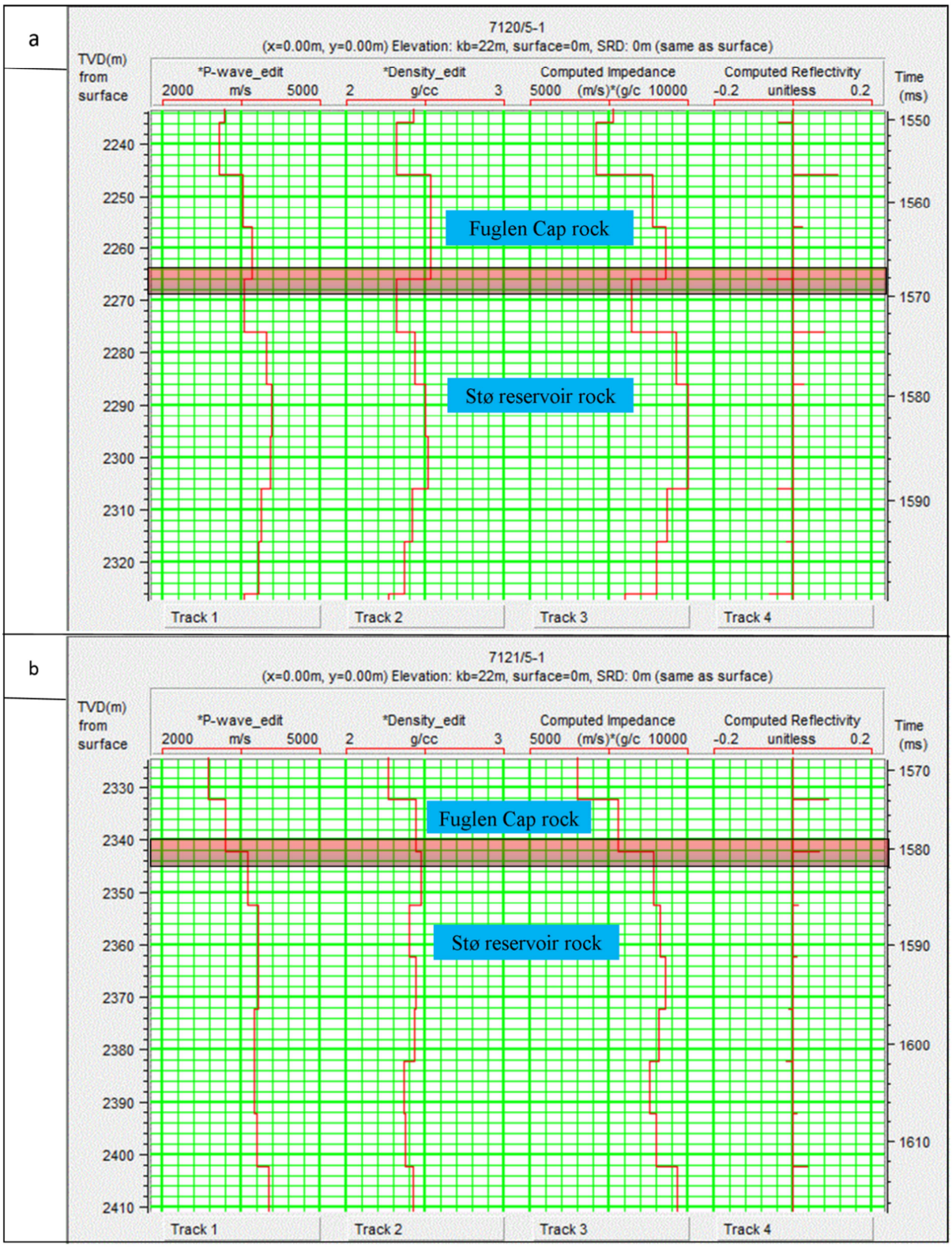

Fig. 7.31: The P-wave acoustic impedance contrast between cap and reservoir rocks in the wells (a) 7120/5-1 and (b) 7121/5-1.

7.2.7 Influence of diagenesis on AVO response

As we know from the chapter 6, the diagenetic history is different for different wells which also explain the different AVO response within the same cap and reservoir rock systems. The

range of reflectivity is very close to zero (0.06 to -0-06) which is because of cemented rock explained by Avseth et al. (2005) (Fig. 7.32). The unconsolidated brine sand and consolidated hydrocarbon saturated sand follow the same trend indicates the important to understand the local geology during AVO analysis. Very little change of reflectivity during AVO modeling is because of low porosity that indicates very low fluid sensitivity in impedance.

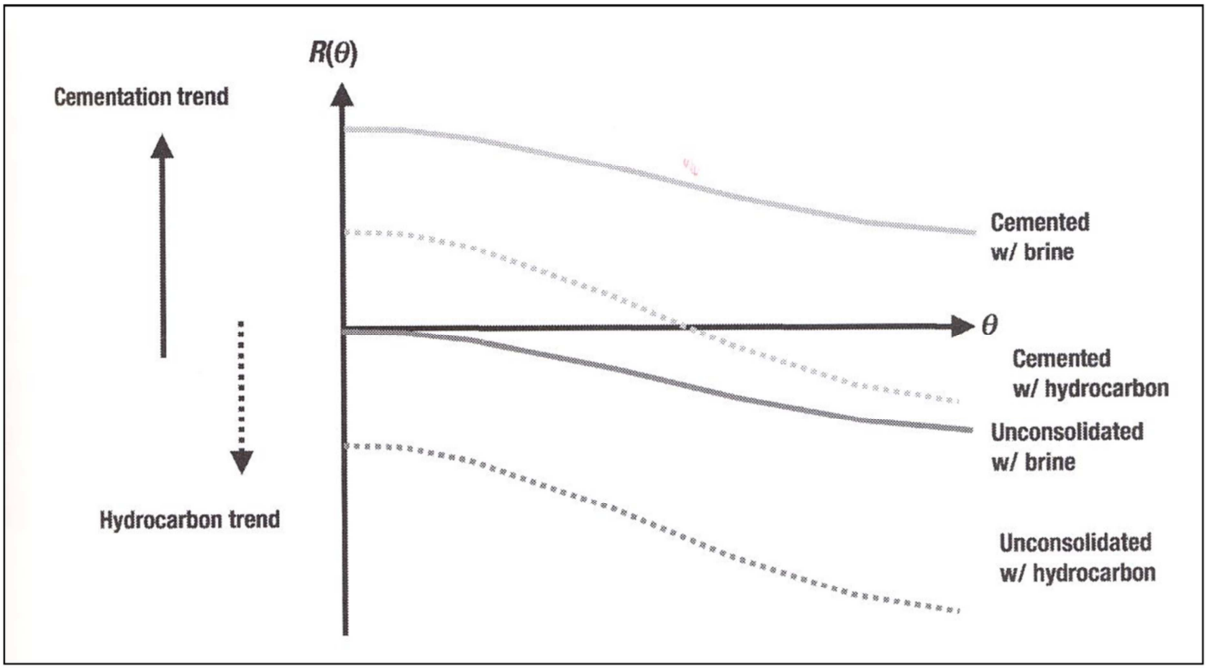

Fig. 7.32: Schematic AVO curves for cemented sandstone and unconsolidated sands capped by shales for brine-saturated and oil-saturated cases (Modified after Avseth et al., 2005).

The cementation or diagenesis depends on many parameters which have a large effect on AVO analysis. The top Stø and Tubeån formation in the well 7120/5-1 have given similar negative zero-offset reflectivity whereas the top Nordmela formation has given positive response though the three reservoir sandstones are water saturated. The deflection of top Nordmela formation is because of lithologic variation. The gamma ray shows this unit is more shaly compare to other two which may responsible for the positive reflectivity at the top and negative reflectivity at bottom of the Tubeån formation which is situated in higher temperature region (Fig. 7.22).

Chapter 8: Seismic Inversion

UNIVERSITY OF OSLO
FACULTY OF MATHEMATICS AND NATURAL SCIENCES

Chapter 8: Seismic Inversion

Seismic inversion involves mapping of physical structure and properties of subsurface of the earth using measurements made on the surface of the earth. In another way we can say it is a technique for creating an earth model using seismic data as an input (Fig. 8.1). As such, it is the opposite of the forward modeling which involves creating a synthetic seismic section based on a model of the earth. We have to understand first the physical processes involved in the creation of seismic data before understand the seismic inversion. The components which we need for inversion from seismic are reflectivity, seismic wavelet and noise. These parameters later invert using different algorithm to a pseudo-impedance section in post-stack seismic inversion workflow.

Thus, in this chapter I run three post-stack seismic inversion model in which I attempt to recover the acoustic impedance from post-stack migrated seismic sections.

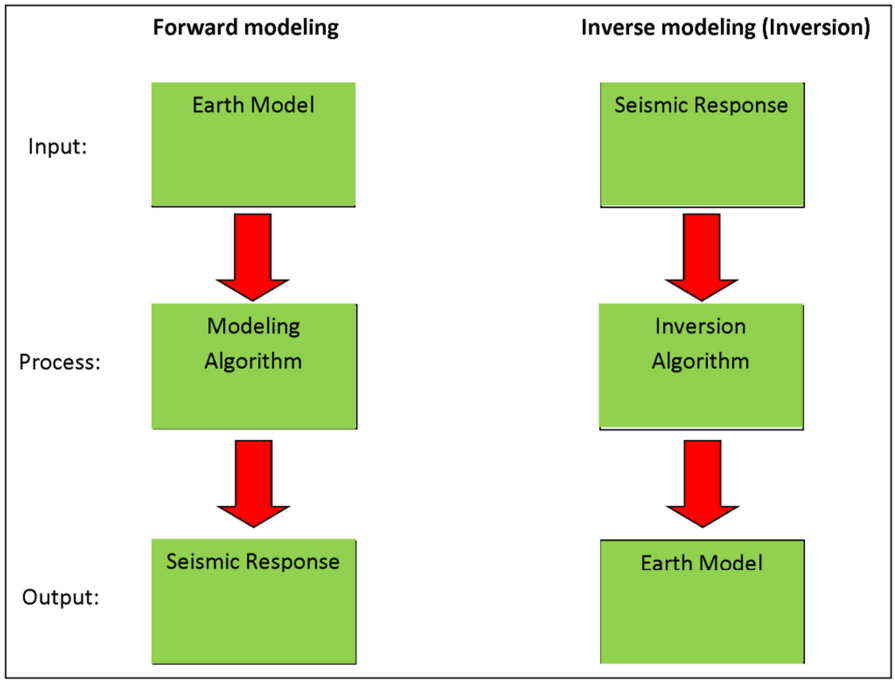

Fig. 8.1: Forward and inverse modeling charts (modified after Russell, 1988).

8.1 Inversion workflow

In inversion workflow, the seismic processed by inversion algorithm to produce earth model. The Figure 8.2 show an example of model based impedance inversion from the seismic line. The seismic first converted into an initial model which is later used for different inversion algorithm to recover the impedance in the target zones. The model based inversion shows different impedance layers within Stø reservoir which are because of lithological variations (dry well).

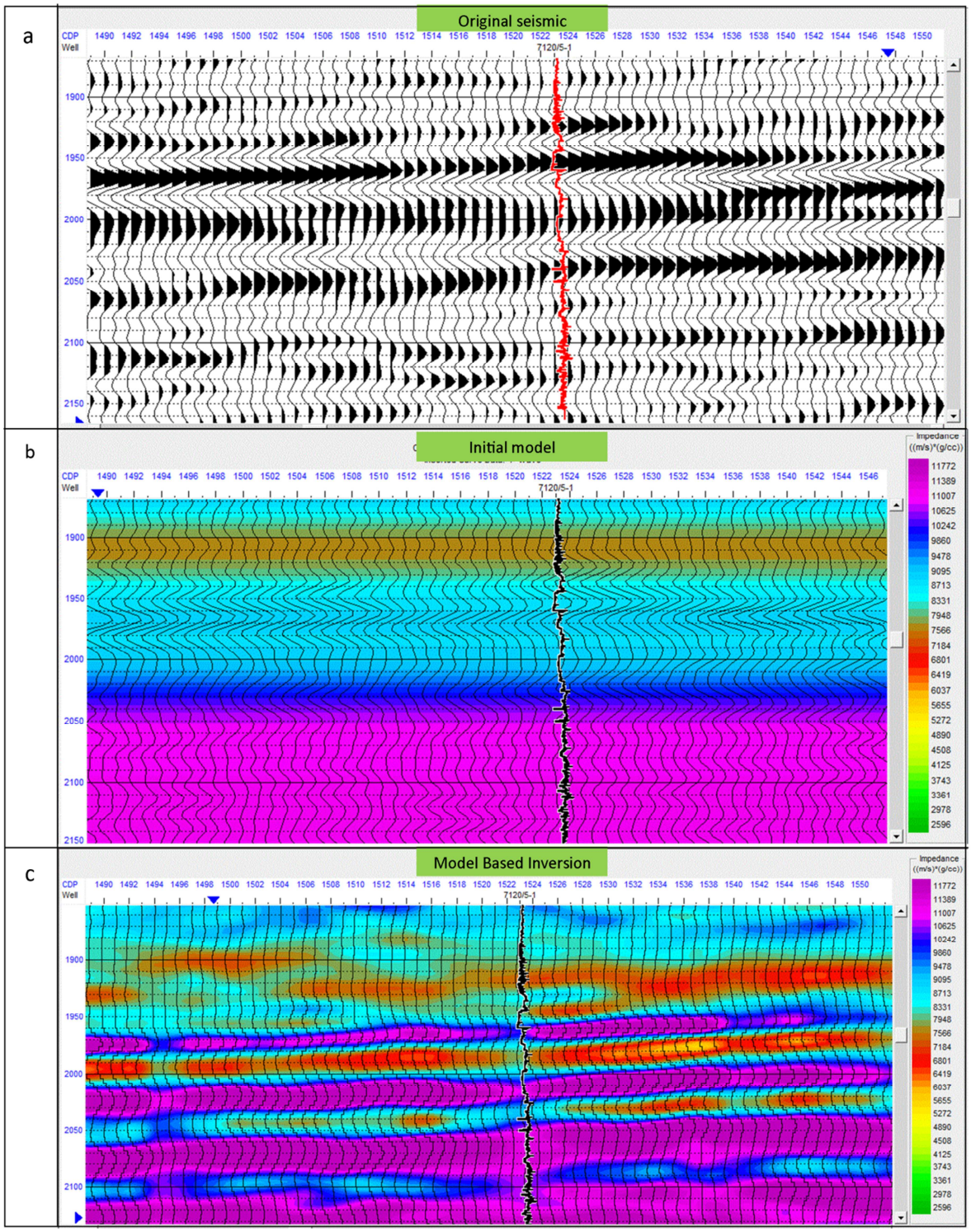

Fig. 8.2: The Stø reservoir section in a 2D seismic line. The well 7120/5-1 ties in the seismic. (a) Original seismic, (b) Initial model for inversion and (c) results of model based inversion.

8.2 Results

The results of three different post-stack inversions and their comparison are shown in this chapter.

8.2.1 Post-stack inversion

Three 2D full-stack seismic lines ST8817-116, ST8817-343 and ST8624-410 are used in this study for post stack inversion. The post-stack inversions have been performed by one of the the Hampson Russell software module STRATA. Four different types of inversion algorithm such as Bandlimited, Model based, Sparse Spike and Neural Network have been applied on the datasets.

Three initial impedance models have been constructed for each dataset to run different inversions. Wells 7121/4-1 and 7121/5-1 have been considered to build the first model for inversion whereas well 7120/6-1 is used to build the second model and the dry well 7120/5-1 is used for the third model. All inversion models have been focused on the target reservoir Stø Formation. The greatest challenge during the inversion workflow was to correlate the respective wells to the target seismic lines. The different inversion results for full-stack datasets are presented below in the Figures 8.3 to 8.7.

8.2.1.1 Model-1 (seismic line ST8817-116 ties with the well 7121/5-1)

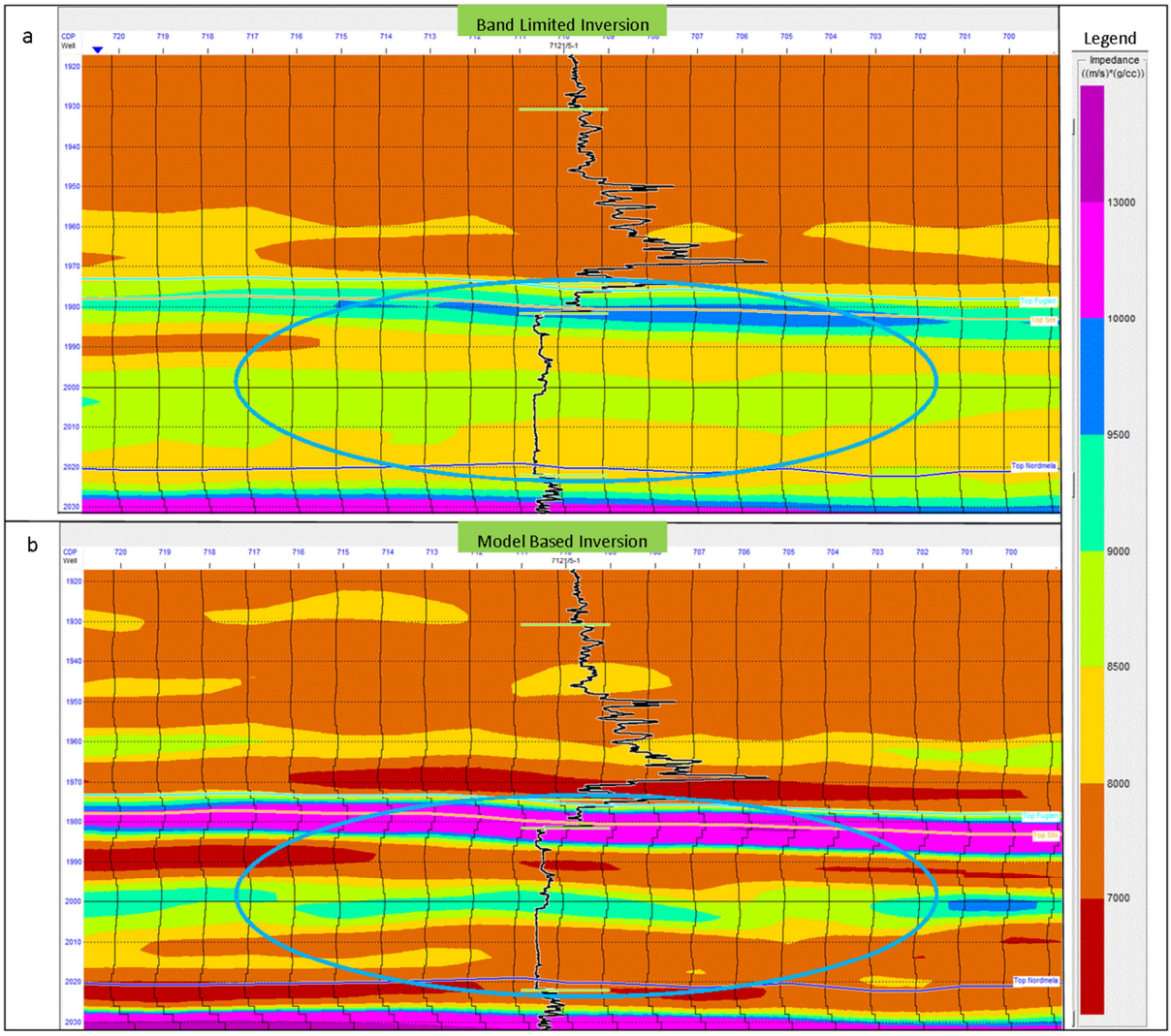

Fig. 8.3: The impedance of Stø reservoir around the well in model-1 on a full-stack data set after (a) Bandlimited and (b) Model based inversion.

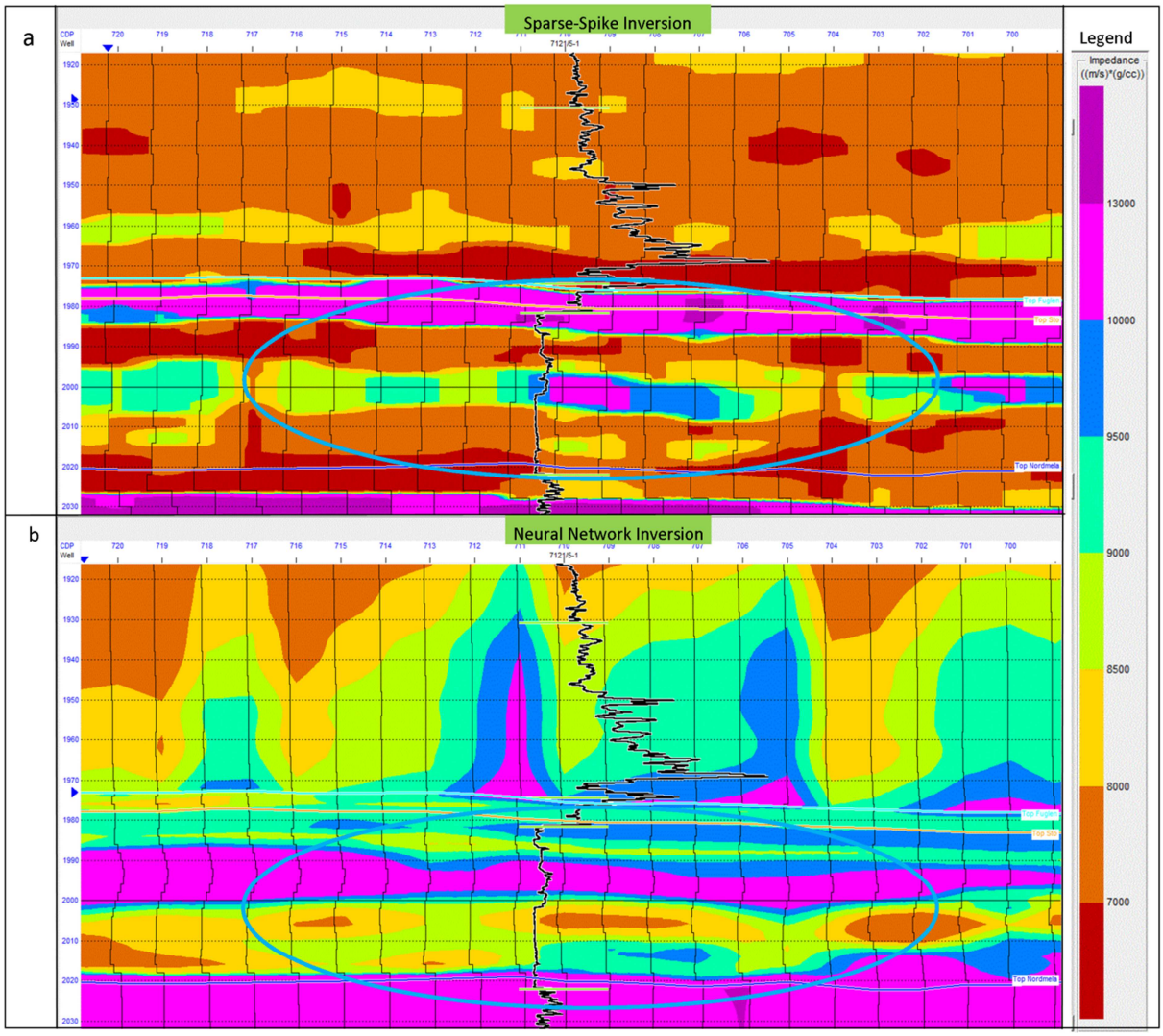

Fig. 8.4: The impedance of Stø reservoir around the well in model-1 on a full-stack data set after (a) Sparse Spike and (b) Neural Network inversion.

8.2.1.2 Model-2 (seismic line ST8817-343 ties with the well 7120/6-1)

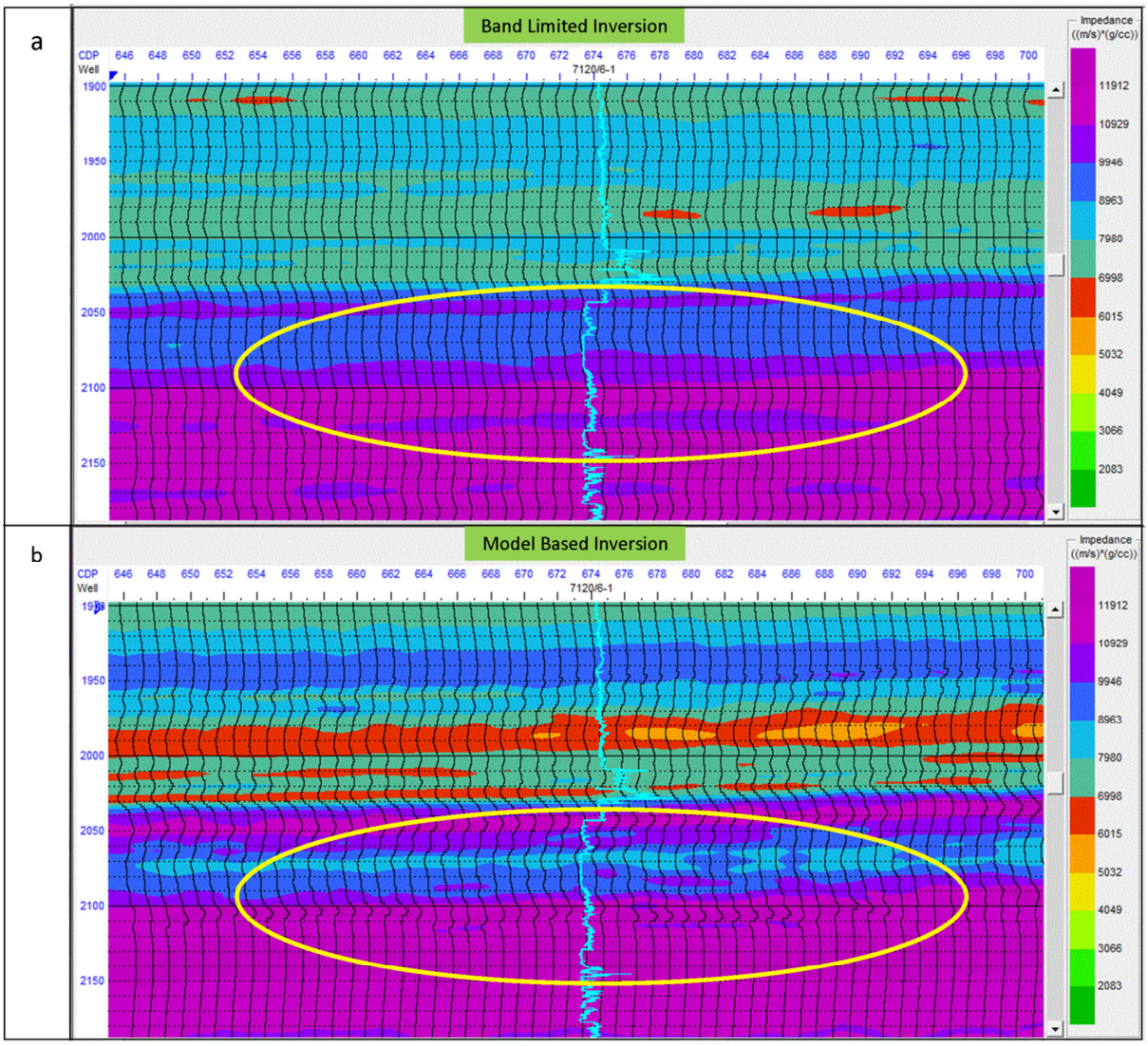

Fig. 8.5: The impedance of Stø reservoir around the well in model-2 on a full-stack data set after (a) Bandlimited and (b) Model based inversion.

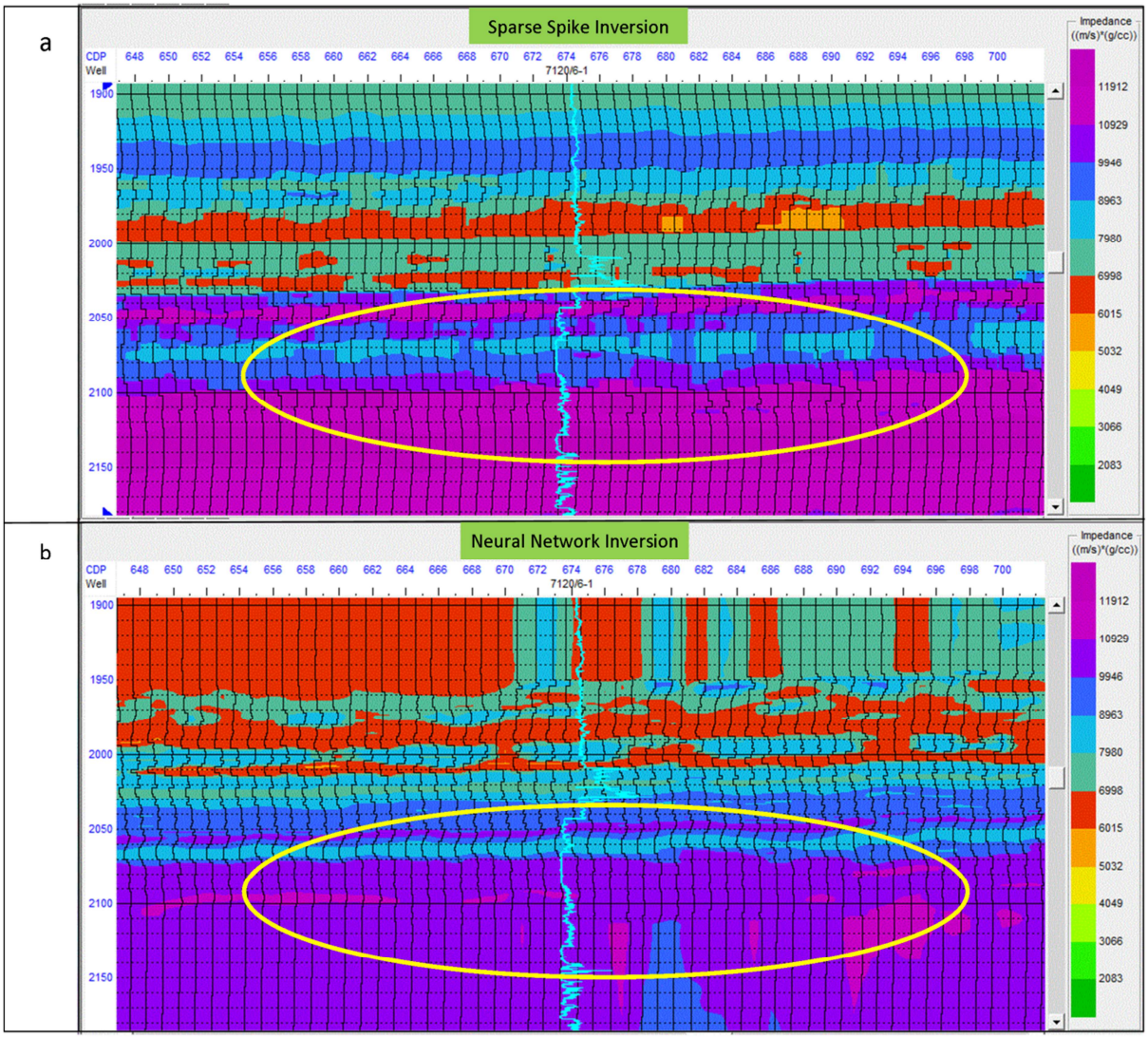

Fig. 8.6: The impedance of Stø reservoir around the well in model-2 on a full-stack data set after (a) Sparse Spike and (b) Neural Network inversion.

8.2.1.3 Model-3 (seismic line ST8624-410 ties with the well 7120/5-1)

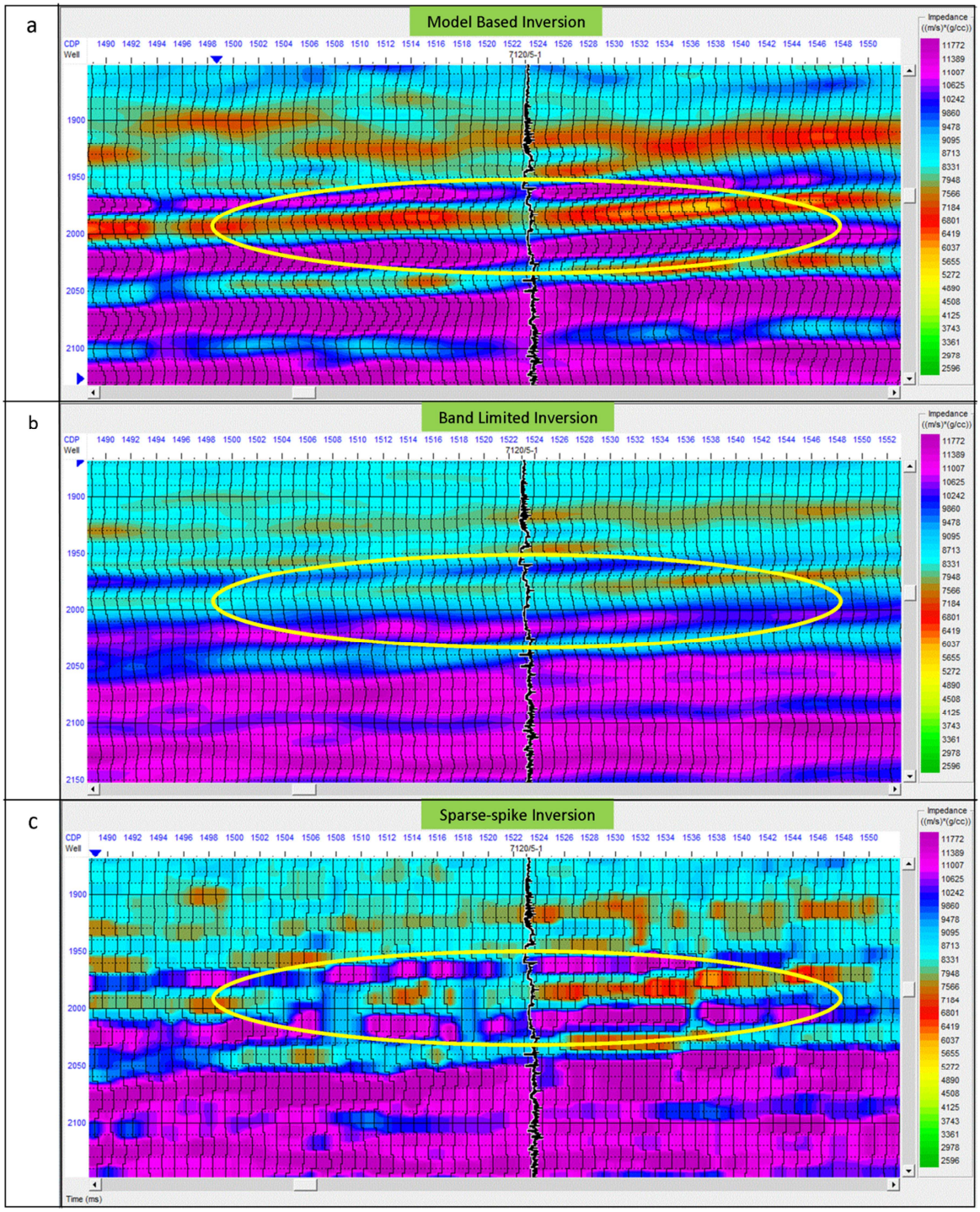

Fig. 8.7: The impedance of Stø reservoir around the well in model-3 on a full-stack data set after (a) Model based, (b) Bandlimited and (c) Sparse Spike inversion.

The Table 8.1 shows the evaluation of different inversion results. From the information it can be concluded that the model based inversions give better results for Stø reservoir compare to the others. The results of sparse spike and bandlimited inversions are also satisfactory but the output of neural network inversion shows relatively poor quality results.

Table 8.1: Evaluation of different inversion results applied on the Stø reservoir.

Full-stack seismic dataset				
Models	Inversion Algorithm			
	Bandlimited	Model based	Sparse Spike	Neural Network
Model-1	Good	Very Good	Poor	Poor
Model-2	Poor	Very Good	Good	Poor
Model-3	Good	Very Good	Good	

8.1.2 Comparison between dry and hydrocarbon bearing wells

Because of better results of model based inversion here I compare the model based inversion of two models (model-1 and model -3). Model-3 is a dry well (Fig. 8.8a) whereas model-1 is gas bearing (Fig. 8.8b). The Stø formation acoustic impedance are different in different wells. Both models have been showing more or less similar impedance range, model-1 (7000-10000 m/s*gm/cc) whereas model-3 (6000-10000 m/s gm/cc). In top Stø in both models started with a lower impedance unit though well in model one is dry. Another lower impedance unit found in both models is the top of clean sandstone unit of Stø formation (Facies-2).

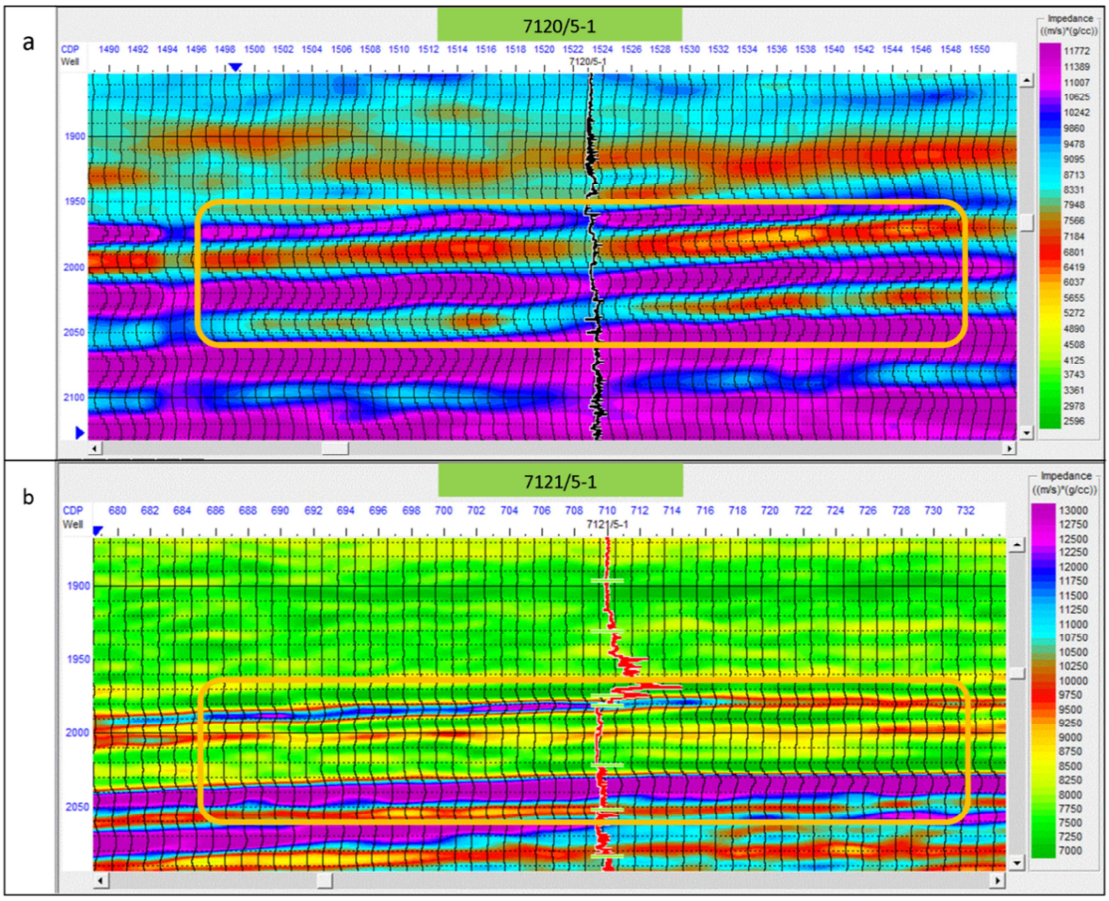

Fig. 8.8: The model based inversion showing the difference impedance in Stø reservoir zone within the (a) 7120/5-1 and (b) 7121/5-1 wells.

8.3 Discussion

The acoustic impedance depends on the velocity and density of the rock which are the summation of mineral and fluid properties. The mineralogical variation within a same reservoir is very common. The Figure 8.9 shows the difference in gamma ray response within the Stø reservoir unit. The model-2 has influence of fine-grained sediments compared to the other models. The lower part of the facies 1 has a transgressive event in all models which influence impedance. Beside depositional changes the diagenetic effect also influences the impedance values which is mostly depends on time, temperature and mineralogy. The temperature distribution over the reservoir varied from well to well because of the location of wells in different structural blocks and depth different of reservoir unit which also influence the impedance within the same reservoir unit. Moreover, the Hammerfest Basin is an uplifted basin and all rock units are over-consolidated reflect very low impedance contrast between cap and reservoir rocks. The fluid effect is very low in compacted rocks because of low porosity but fluid properties are also affected by the diagenetic history and are important for impedance variations.

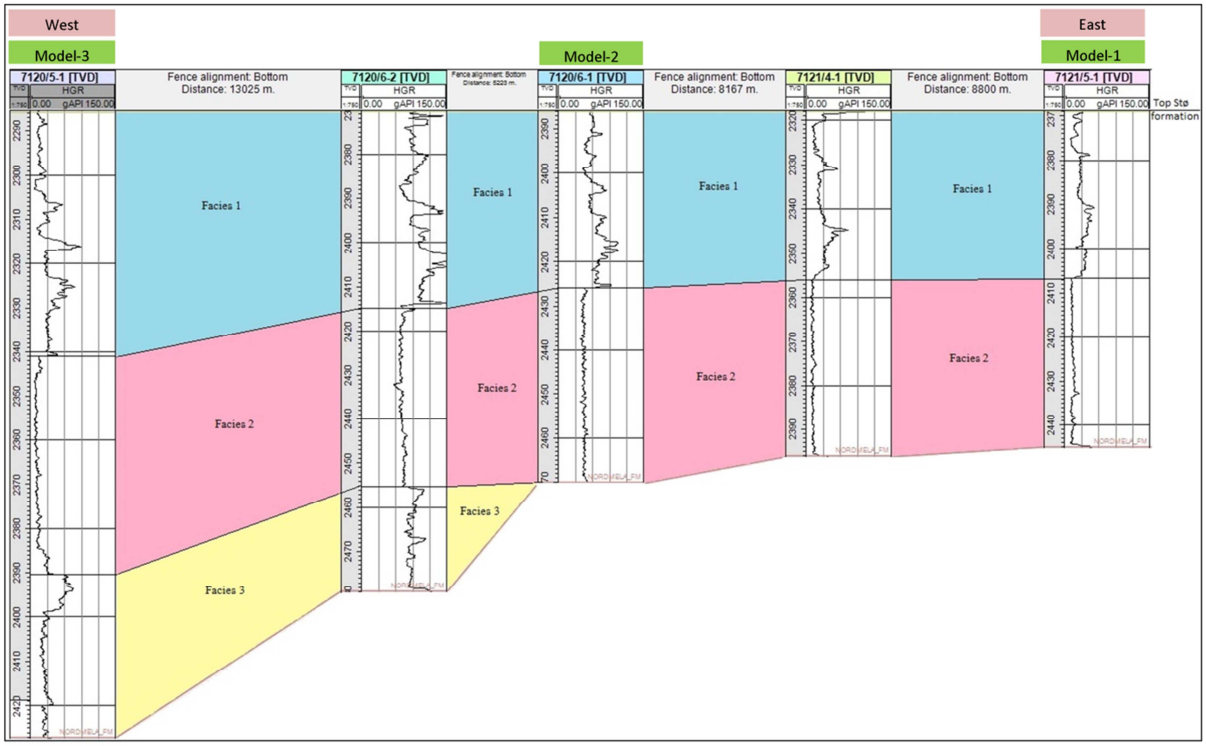

Fig. 8.9: The gamma ray logs of Stø formation showing lithological and thickness variation within different models.

The acoustic impedance of Stø formation calculated from P-wave velocity and density logs is shown in the Figure 8.10. All models start with a low impedance unit, followed by a higher impedance interval and then a lower impedance unit. The model-3 consist of facies 3 has shown the higher impedance value both in inversion results and well logs. Facies 1 is coarsening upward sequence and in the model-1 and model-2 contain gas cause low impedance unit in the top section. This unit also less cemented compare to the lower units. The transgressive units in the lower part of the facies 1 give the higher impedance compare to the upper and lower rocks. The clean facies 2 sand unit shows lower impedance value in all the models because of lower cementation demonstrated in the previous chapter 6. The model-

3 has facies 3. It is diagenetically more cemented compared to the above units and showed higher impedance in the inversion result.

The accuracy of different algorithms is varied model to model which indicate that the accuracy not only depends on the flowchart but also depends on the local geology around the wells. The dry and gas bearing wells are giving more or less similar results in the reservoir units. This could be a limitation of post-stack inversion incase to identify the fluid effect. But the seismic inversion can be used for lithology descrimination within a reservoir and could be very useful to characterize reservoir sandstones.

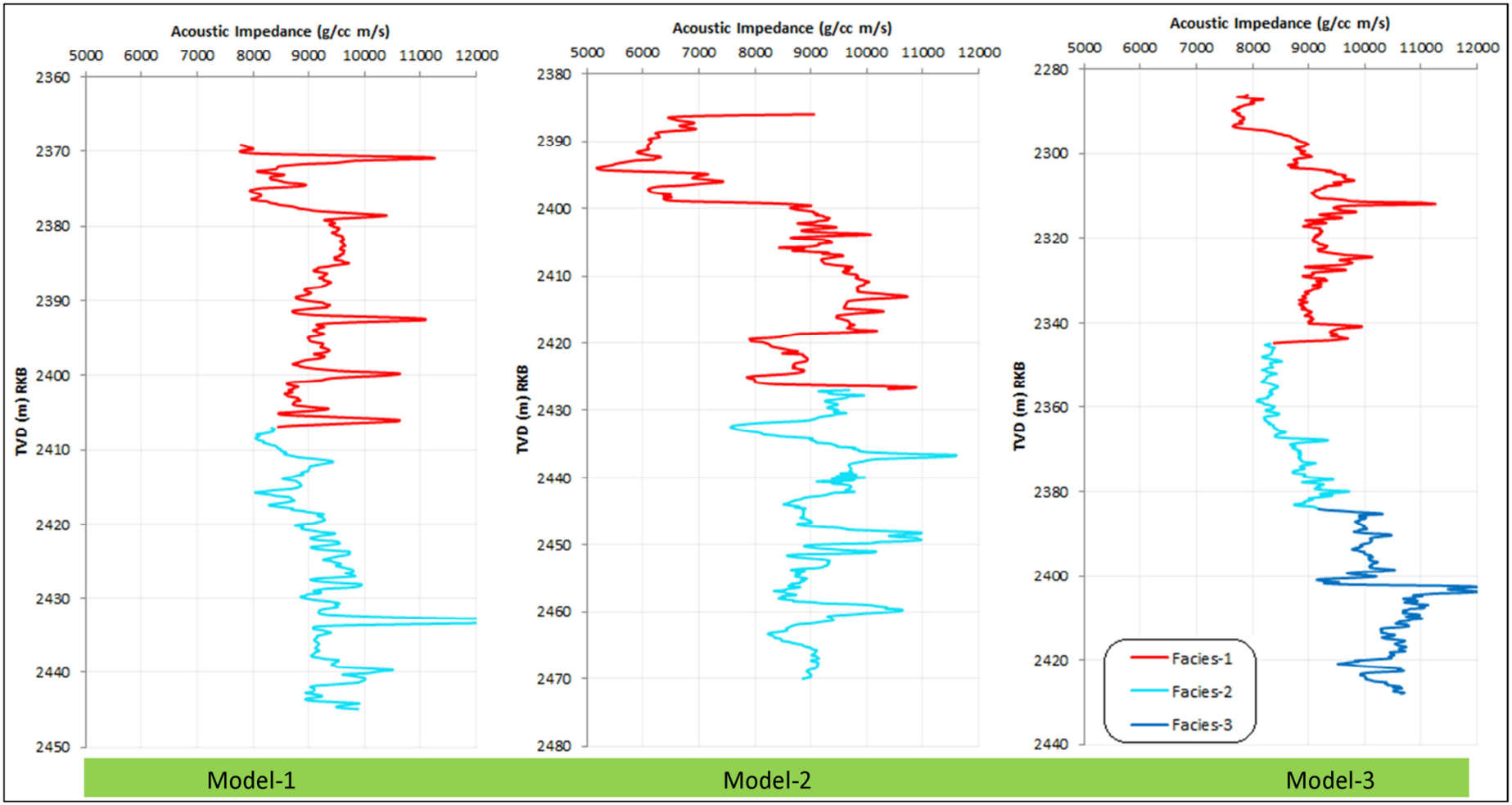

Fig. 8.10: The P-wave acoustic impedance logs of Stø formation with different facies showing variations within models.

Chapter 9: Summary and conclusions

UNIVERSITY OF OSLO
FACULTY OF MATHEMATICS AND NATURAL SCIENCES

Chapter 9: Summary and conclusions

Summary and conclusion

Till now, 94 exploration wells have been drilled in the Norwegian part of the Barents Sea. Recent oil discoveries (Skrugard and Havis) and proven petroleum systems (reservoir, source, trap and seal) exist in the area make future exploration more promising. This area has recorded higher success rate (one in three) than the Norwegian North Sea but because of mostly gas discoveries as well as enormous challenges complexities, it was less attractive for past hydrocarbon exploration. The recent two major oil discoveries are important break-through for the area and obviously will be rejuvenated in future exploration activities. The distance to potential markets, climate, dominant gas products, large water depths and several stages of uplift and erosion pose a lot of challenges for exploration, development and production in the area but modern technologies opened a door to solve many of these problems. The Snøhvit field is such an example that overcomes many challenges and has started production in 2007. Gas production from the Snøhvit field comprises several small discoveries (Snøhvit, Askeladd, Askeladd Vest, Askeladd Sentral and Albatross). This study focuses only on main Snøhvit discover.

Total six exploration wells (7120/5-1, 7120/6-1, 7120/6-2S, 7121/4-1, 7121/4-2 and 7121/5-1) have been drilled in the study area included in this study. Well 7120/5-1 is brine saturated and well 7121/4-2 is gas saturated. Rest of the four wells contains gas, condensate and oil, but oil lag is very thin (not economically producible). In many cases in this study, the brine saturated well used for comparing with hydrocarbon saturated well to evaluate the fluid effect on rock properties. The main reservoir rocks of this area are the Stø, Nordmela and Tubåen Formations where the Stø Formation exposes the best reservoir quality. However, this work lays emphasis on the Stø reservoir including its cap rock the Fuglen Formation.

The main reservoir rock (Stø Formation) is deposited at Lower to Middle Jurassic time. This formation is deposited in a shoreface to nearshore paleo-depositional environment. The provenance direction is E to S-E. Therefore, grains of the Stø Formation are coarse and well sorted in the east than west. Also, the thickness of this formation is decreasing from west to east direction. The Stø Formation has been divided into three different facies. Facies 1 belongs to the upper part of the formation which is poorly sorted and highly bioturbated. Facies 2 is well sorted, fairly bioturbated clean sandstone unit within the Stø Formation. The reservoir quality of facies 2 is better than facies 1. The reservoir quality of facies 3 is in between 1 and 2. In this study, this Stø reservoir is characterized by four different geophysical techniques. The techniques are compaction study, rock physics analysis/diagnostic, AVO modeling and seismic inversion.

Compaction trends and rock properties in the Snøhvit field have been investigated by comparing a suite of petrophysical well logs data and experimental laboratory compaction curves. Vp and density logs have been used for distinguishing the transition zone (MC to CC). Different clay–clay and clay–silt experimental compaction curves have been utilized as a reference. Generally, Vp and density increase as a function of depth, meanwhile the porosity reduces as expected. Several techniques have been used to identify the transition zone between mechanical and chemical compaction (MC to CC). First in the Vp–depth trend, an abrupt increase of velocity has recognized within the same lithology (inferred from the gamma ray log). Incorporating information from a Vp-density cross plot also helps to constrain the depth at which this transition occurs. The present day temperature at transition

zone has been calculated using the bottom hole temperature. The shear modulus-density cross plots helped to constrain the temperature at the transition points. The present day temperature did not fulfill the expected temperature at the transition zone. It shows lower values than expected. This temperature difference is resulted from uplift of this basin. Furthermore, the Vp data shows mismatch with experimental curves which also indicates exhumation of the study area. Different experimental curves compared here to well data to see upper and lower limits of exhumation in well locations. We use gamma ray log as a lithology indicator and calculate V_{sh} for every well. We don't have any mineralogical controlled from direct thin section study. Only shale data points ($V_{sh} \geq 0.75$) and Mondol et al. (2009), Kaolinite-Silt (50:50) experimental curve has been used estimate exhumation in the study area.

Rock physics analysis and diagnostics are carried out by using the data from well 7120/6-2S. This is the only well used in this project has direct Vs measurement. Two RPTs have been used for rock physics diagnostics of the reservoir (Stø Formation) and Kapp-Toscana Group. The cement model (Vp versus porosity plot) is used for evaluating cementation effect on rock properties. Three cement models (contact cement, constant cement and friable sand) have been used as a template. The friable sand model is calculated by using the data from the Stø Formation. On the other hand, saturation model (Vp/Vs versus AI cross plot) is used for evaluating the fluid effect on rock properties. Three saturation models have been calculated. The models are brine, oil and gas saturated pure sandstones. Other potential reservoirs of the Kapp-Toscana Group are also analyzed by using these two rock physics templates.

The FRM of the Stø Formation (main reservoir) provides additional insight into the rock properties of this reservoir rock. The effective rock properties are very much dependent on the properties of different minerals (matrix materials) which constitute the rock. Unfortunately, no mineralogical data is available in this project. The net to gross ratio of the Stø Formation is 0.8. Hence, 80% quartz and 20% clay have been used as matrix materials in all FRM studies. Despite the major limitations and simplifications in the Gassmann fluid replacement model, still it provides a robust approach to evaluate rock properties. On the other hand, the AVO signature is not dependent on the properties of the reservoir alone but also on the overburden. The seismic signal propagates from the surface to the reservoir; hence AVO signatures are also influence by thickness and composition of the overburden. The variations of cap rock properties are also taken into account in AVO modeling. In addition, setting input porosity same as the output porosity removes the effect of pore pressure (MC) which is also an important parameter that may give rise to AVO anomalies. Moreover, the intercept gradient cross plot gives a better understanding of different gas sand classes.

Finally, various post-stack inversion algorithms have been applied on two full-stack 2D seismic lines to predict reservoir properties of the Snøhvit field. The input data for inversion process consists of well logs and 2D seismic data. One important step was to correlate wells with the real seismic before applying inversion algorithms. This is done by examination of correlation between the events on the synthetic traces and the events on the seismic data. This minimizes the misfit function between real seismic data and synthetic traces. Three sets of initial impedance models have been constructed and later inverted by applying Bandlimited, Model Base, Sparse Spike and Neural Network inversion algorithms to predict reservoir characteristics. Finally, the impedance contrast of the reservoir rocks (Stø Formation) in different models has been compared using the model based inversion results.

Despite the number of limitations and simplistic assumptions, the following conclusions can be deduced for the study:

- Two distinct compaction trends are found across the study area that represents the mechanical and chemical compactions of siliciclastic rocks penetrated by wells. In mechanical compaction domain, the velocity-depth trends of six studied wells give more or less a general compaction trend where velocity increases systematically with depth with an exception of Hekkingen formation. The Hekkingen Formation, the main source rocks in the study area, shows abnormally low velocity compared to upper and lower units and deviates significantly from the general compaction trend observed in shallow and deep section.

- In the well 7121/5-1, the porosity reduction by MC dominates down to 1922m (BSF) at present burial depth. This process is governed by vertical effective stress which also depends on the overburden and pore pressures. On the other hand, presently below 1922m (BSF), CC took over the compaction process controlled by a TTI. The compaction gradient of sandstones and shales show difference in different compaction domains. Sandstones show higher compaction gradient than shales in the MC domain, whereas in CC domain it is opposite.

- The present day temperature at transition depth (MC to CC) in well 7121/5-1 is 66^0C. After correcting depth for exhumation, the temperature of that point turns out 93^0C. Accurate determination of this zone is of great value when predicting reservoir quality (porosity, permeability, and cementation) particularly for this study area where temperature information is absent. The very low present day temperature gradient of well 7120/5-1 indicates very low temperature (50^0C) at transition depth after exhumation correction. This temperature is lower than the standard temperature (70^oC) that initiates quartz cementation suggests that the paleo-temperature in the well location may be different than the estimated paleo temperature. The present day temperature distribution is also found different in different wells.

- The magnitude of exhumation has been estimated to fall in the range of 300 to 760 m across the study area without considering the uncertainties that are associated with the application of the method employed in this study. An integrated approach involving several techniques in estimating the magnitude of Cenozoic exhumation will definitely reduce the margin of uncertainty. The exhumation magnitude increases from west to east which follows the previously published exhumation map in the SW Barents Sea.

- The cementation within the reservoir (Stø Formation) is higher in the east than the west. Different texture (size and sorting) within the same reservoir unit is the reason for different cementation. Different facies within the same reservoir (Stø Formation) shows different rock properties. Different facies deposited in different sub environments follow different diagenesis processes within the same reservoir unit.

- Provenance also influences the diagenetic processes. Different sediment sources have given compositional variations in same unit and different wells. Hence, during compaction these sediments behave differently.

- Thickness of the reservoir internally influences the compaction processes.

- The present day effective stress (assuming similar pore pressure) and TTI history are different in different wells. Due to the variation of effective stress the sediment compaction in the MC domain is different. The TTI is giving different diagenetic history in the CC domain. Hence, the rock properties may have varied from well to well.

- It is difficult to differentiate the fluid effect on rock properties in compacted sandstones. The reservoir (Stø Formation) in the studied area is a compacted sandstone unit. Hence, it is very difficult to find out the fluid effect on it. However, the gas saturated shaly sandstones (gas sand 1) has followed the gas saturated line. On the other hand, hydrocarbon saturated clean sandstones (gas sand 2 and oil sand) has not followed the standard saturation model. Moreover, the brine sandstones are violating the robust result in rock physics diagnostics.

- The Kapp-Toscana group follows the standard rules of rock physics diagnostics in both RPTs. But, because of compacted rocks it is very difficult to separate the trends of different formations.

- Averaging (blocking) of petrophysical logs for the AVO modeling is of prime importance such that an inaccurate block size would definitely result in a misleading AVO response. Averaged logs should be representative of the actual geological conditions for the models to be reliable.

- Change of fluid saturation significantly affects both Vp and Vs. Different fluid saturation have different fluid modulus as well as different effective density. Hence, changing the effective modulus of the rock changes Vp. The Vs value has also changed though fluid has no influence on shear wave. Due to change in effective density, the Vs has different for different fluid substitution.

- The mineralogical differences within reservoir rock have given different FRM results. So it is important to know the mineralogy of reservoir rocks for accurate FRM.

- The Stø reservoir sandstones display different sand AVO classes in different wells. Both in-situ and modeled AVO responses are similar but the values change a little bit because of different fluid saturation.

- The thickness of the cap rock also influences AVO response. Thicker cap rock display a lower impedance AVO response. The Stø reservoir sandstones are quite homogenous with good reservoir qualities throughout the study area. However, the disparity in AVO characteristics of the Stø reservoir is largely influenced by the variability in the cap rock properties across the study area. Moreover, different diagenetic conditions of reservoir rocks results different AVO responses.

- All inversion methods in this study show relatively low impedance values within the areas of target reservoir (Stø Formation) compared with upper and lower horizons.

A high quality seismic section as well as well log is essential for obtaining a good inversion result. Also, well correction is important for a good inversion output. A single algorithm does not give the best result in all models. The better results in different models are given by different algorithms. However, it points out that the accuracy of different algorithms not only depends on flowchart but also depends on local geology.

The dry and gas bearing wells show almost similar inversion results within target reservoir (Stø Formation). However, it is difficult to differentiate lithology and fluid effect. This is a limitation in case of fluid characterization, but it could be very useful for rock property characterization. However, these techniques are useful for reservoir characterization in exploration phases as well as monitoring reservoir during production.

Chapter 10: References

UNIVERSITY OF OSLO

FACULTY OF MATHEMATICS AND NATURAL SCIENCES

References

Aki K. and Richards P. G. (1980). Quantitative seismology: Theory and methods. San Francisco: W. H. Freeman and Co.

Asquith G. and Krygowski D. (2004). Basic well log analysis. AAPG methods in Exploration Series 16, 224 pp.

Avseth P., Dvorkin J., Mavko G. and Rykkje J. (2000). Rock physics diagnostic of North Sea sand: Link between microstructure and seismic properties. Geophysics, v. 27, p. 2761-2764.

Avseth P., Mukerji T. and Mavko G. (2005). Quantitative seismic interpretation: Applying rock physics tools to reduce interpretation risk. Cambridge University Press, New York.

Avseth P., Mukerji T., Mavko G. and Dvorkin J. (2010). Rock-physics diagnostics of depositional texture, diagenetic alterations and reservoir heterogeneity in high porosity siliciclastic sediments and rocks-A review of selected models and suggested work flows. Geophysics, v. 75, p. 131-147.

Barclay S. A. and Worden R. H. (2000). Petrophysical and petrographical analysis of quartz cement volumes across oil-water contacts in the Magnus Field, northern North Sea. Spec. Publs int. Ass. Sediments, v. 29, p. 147-161.

Batzle M. L. and Wang Z. (1992). Seismic properties of pore fluids. Geophysics, v. 57, p. 1396-1408.

Berglund L. T., Augustson J., Færseth R., Gjelberg J. and Ramberg-Moe H. (1986). The evolution of the Hammerfest Basin. Norwegian Petroleum Society, p. 319-338.

Bjørlykke K. and Høeg K. (1997). Effects of burial diagenesis on stresses, compaction and fluid flow in sedimentary basins. Marine and Petroleum Geology, v. 14, p. 267-276.

Bjørlykke K., Ramm M., Saigal G.C. (1989). Sandstone diagenesis and porosity modification during basin evolution. Geol Runds 78, p. 243–268.

Bjorlykke K. (1998). Clay mineral diagenesis in sedimentary basins - a key to the prediction of rock properties. Examples from the North Sea Basin. Clay Minerals **33**(1), p. 15-34.

Bjørlykke K., Chuhan F., Kjeldstad A., Gundersen E., Lauvrak O. and Høeg K. (2004). Modelling of sediment compaction during burial in sedimentary basins in Stephansson O., Hudson J. and King L. (eds.), Coupled Thermo-Hydro- Mechanical-Chemical Processes in Geo-Systems. Elsevier, Amsterdam, pp. 699–708.

Bjorlykke K. and Jahren J. (2010). Sandstones and Sandstone reservoirs in Bjorlykke K. (2010), Petroleum Geoscience: from Sedimentary Environments to Rock Physics, Berlin, Heidelberg, Springer-Verlag Berlin Heidelberg, p. 113 – 140.

Bloch S., Lander R. H. and Bonnell L. (2002). Anomalously high porosity and permeability in deeply buried sandstone reservoirs: Origin and predictability. AAPG Bulletin, v. 86, No. 2, p. 301-328.

Boruah N. and Chatterjee R. (2010). Rock physics template (RPT) analysis of well logs and seismic data for lihology and fluid classification. Quarterly Journal of Directorate General of Hydrocarbons, v. III, No. 3, p. 13-27.

Bugge T., Elvebakk G., Fanavoll S., Mangerud G., Smelror M., Weiss H. M., Gjelberg J., Kristensen S. E. and Kåre N. (2002). Shallow stratigraphic drilling in hydrocarbon exploration of the Nordkapp Basin, Barents Sea. Marine and Petroleum Geology, 19, p. 13-37.

Butt F. A., Elverhoi A., Hjelstuen B. O., Dimakis P. and Solheim A. (2001). Modelling late Cenozoic isostatic elevation changes in Storfjorden, NW Barents Sea: an indication of varying erosional regimes. Sedimentary Geology, v. 143(1-2), p. 71-89.

Castagna J. P., Batzle M. L. and Eastwood R. L. (1985). Relationships between Compressional-Wave and Shear-Wave Velocities in Clastic Silicate Rocks. Geophysics, v. 50, p. 571-581.

Castagna J. P., Batzle M. L. and Kan T. K. (1993). Rock physics - The link between rock properties and AVO response, in offset-dependent reflectivity - Theory and practice of AVO analysis, ed. J. P. Castagna and M. Backus. Investigation in Geophysics, No. 8, SEG, Tulsa, Oklahoma, p. 135-171.

Castagna J. P., Herbert W. S. and Douglas J. F. (1998). Framework for AVO gradient and intercept interpretation. Geophysics, v. 63, p. 948-956.

Chi X. G. and Han D. H. (2009). Lithology and fluid differentiation using rock physics template. The Leading Edge, p. 1424-1428.

Chuhan F. A., Bjorlykke K. and Lowrey C. J. (2001). Closed-system burial diagenesis in reservoir sandstones: Examples from the Garn Formation at Haltenbanken area, offshore mid-Norway. Journal of Sedimentary Research, v. 71(1), p. 15-26.

Chuhan F.A., Kjeldstad A., Bjørlykke K. and Høeg K. (2002). Porosity loss in sand by grain crushing. Experimental evidence and relevance to reservoir quality. Marine and Petroleum Geology, v. 19, p. 39–53.

Dalland A., Worsley D. and Ofstad K. (1988). A lithostratigraphic scheme for the Mesozoic and Cenozoic succession offshore mid and northern Norway. Norwegian Petroleum Directorate Bulletin, v.4, p. 65.

Dore A. G. (1995). Barent Sea Geology, Petroleum Resources and commercial potential. Arctic, v. 48(3), p. 207-221.

Dore A. G. and Jensen L. N. (1996). The impact of late Cenozoic uplift and erosion on hydrocarbon exploration: offshore Norway and some other uplifted basins. Global and Planetary Change, v. 12(1–4), p. 415-436.

Dvorkin J., Nolen-Hoeksema R. and Nur A. (1994). The squirt-flow mechanism: macroscopic description. geophysics, v. 59, p. 428-438.

Dvorkin J. and Nur A. (1996). Elasticity of high-porosity sandstones: Theory for two North Sea data sets. Geophysics, v. 61, No. 5, p. 1363-1370.

England P. and Molnar P. (1990). Surface uplift, uplift of rocks, and exhumation of rocks. Geological Society of America, v. 18, p. 1173-1177.

Faleide J. I., Gudlaugsson S. T. and Jacquart G. (1984). Evolution of the western Barent Sea. Marine and Petroleum Geology, v. 1.

Faleide J. I., Solheim A., Fiedler A., Hjelstuen B. O., Andersen E. S. and Venneste K. (1996). Late Cenozoic evolution of the western Barents Sea-Svalbard continental margin. Global and Planetary Change, v. 12, p. 53-74.

Faleide J. F., Bjørlykke K. and Gabrielsen R. H. (2010). Geology of the Norwegian Continental Shelf in Bjorlykke K. (2010), Petroleum Geoscience: from Sedimentary Environments to Rock Physics, Berlin, Heidelberg, Springer-Verlag Berlin Heidelberg, p. 467 –499.

Fawad M., Mondol N. H., Jahren J. and Bjørlykke K. (2011). Mechanical compaction and ultrasonic velocity of sands with different texture and mineralogical compositon. Geophysical Prospecting, v. 59, p. 697-720.

Gading M. (1993). Triassic evolution in the Barents Sea, Norwegian and Russian sectors: a seismic and sequence stratigraphic approach. PhD thesis, Norwegian Institute of Technology, University of Trondheim.

Galius L. J. and Johansen T. A. (2010). Petroleum Geophysics, Unigeo, Bergen.

Gardner G. H. F., Gardner L. W. and Gregory A. R. (1974). Formation velocity and density - the diagnostic basics for stratigraphic traps. Geophysics, v. 39, p. 770-780.
Gradstein F. N., Ogg J. G. and Smith A. G. (eds.) (2004). A geologic time scale 2004. Cambridge: Cambridge University Press.

Glover P. W. J. (2005). Petrophysics MSc course notes (GLG - 66565), Department of Geology, University Laval, Canada.

Han D., Nur A. and Morgan D. (1986). Effect of porosity and clay content on the wave velocities in sandstones. Geophysics. v. 51(11), p. 2093-2107.

Harland W. B. (1973). Mesozoic geology of Svalbard. Mem. Amer. Asso. Petrol. Geol. v.19, p. 135—148.

Hashin Z. and Shtrikman S. (1963). A variation approach to the elastic behavior of multiphase materials. J. Mechanical physics. Solids, v. 11, p. 127-140.

Henriksen E., Ryseth A. E., Larssen G. B., Heide T., Rønning K., Sollid K. and Stoupakova A. V. (2011). Tectonostratigraphy of the greater Barents Sea: implication for petroleum systems. Geological Society, London, Lyell collection, v. 35, p. 163-195.

Håkansson E. and Pedersen S. A. S. (1982). Late Paleozoic to Tertiary tectonic evolution of the continental margin in North Greenland in Embry A. F. and Balkwill H. R. (eds): Arctic geology and geophysics. Canadian Society of Petroleum Geologists Memoir 8, p. 331–348.

Johansson Å., Meier M., Oberli F. and Wikman H. (1993). The early evolution of the Southwest Swedish Gneiss Province: geochronological and isotopic evidence from southernmost Sweden. Precambrian Research, v. 64, p. 361-388.

Krief M., Garat J., Stellingwerff J. and Ventre J. (1990). A petrophysical interpretation using the velocities of P and S waves. The Log Analyst, p. 355-369.

Linjordet A. and Olsen R. G. (1992). The Jurassic Snohvit gas field, Hammerfest basin, Offshore Northern Norway. AAPG Bulletin M 54, p. 349-370.

Marcussen Ø., Thyberg B. I., Peltonen C., Jahren J., Bjørlykke K. and Faleide J. I. (2009). Physical properties of Cenozoic mudstones from the northern North Sea: Impact of clay mineralogy on compaction trends. AAPG Bulletin, v. 93, p. 127-150.

Marcussen Ø., Maast T. E., Mondol N. H., Jahren J. and Bjørlykke K. (2010). Changes in physical properties of a reservoir sandstone as a function of burial depth - The Etive Formation, Northern North Sea. Marine and Petroleum Geology. In press.

Marion D. (1990). Acoustic, mechanical and transpoprt properties of sediments and granular materials. Ph.D. dissertation, Stanford University.

Marion D., Nur A., Yin H. and Han D. (1992). Compressional velocity and porosity in sand-clay mixtures. Geophysics, v. 57, p. 554-563.

Mavko G., Mukerji T. and Dvorkin J. (2009). The rock physics handbook: Tools for seismic analysis of porous media. Cambridge University Press, New York.

Milovak J., (2009). Rock physics modeling of an unconsolidated sand reservoir, Masters Thesis, University of Houston.

Mondol N. H., Bjørlykke K., Jahren J. and Hoeg K. (2007). Experimental mechanical compaction of clay mineral aggregates - Changes in physical properties of mudstones during burial. Marine and Petroleum Geology, v. 24, p. 289-311.

Mondol N. H. (2009). Porosity and permeability development in mechanically compacted silt-kaolinite mixtures. SEG Houston International Exposition and Annual Meeting.

Mondol N. H. (2010). Seismic exploration, in Bjorlykke K. (2010), Petroleum Geoscience: from Sedimentary Environments to Rock Physics, Berlin, Heidelberg, Springer-Verlag Berlin Heidelberg, p. 375 – 402.

Murphy W. F. (1982). Effects of microstructure and pore fluids on the acoustic properties of granular sedimentary materials. Ph.D. dissertation, Stanford University.

Mørk A., Knarud R. and Worsley D. (1982). Depositional and diagenetic environments of the Triassic and Lower Jurassic succession of Svalbard, *in* Embry A. F. and Balkwill H. R., eds.

Arctic Geology and Geophysics: Canadian Society of Petroleum Geologists, Memoir 8, p. 371–398.

Norwegian Petroleum Directorate (NPD) Factpages and Factmaps (www.npd.no). Latest visited 30th of May.

Nyland B., Jensen L. N., Skagen J., Skarpnes O. and Vorren T. (1992). Tertiary uplift and erosion in the Barents Sea: magnitude, timing and consequences, in Larsen R. M., Brekke H., Larsen B. T. and Talleraas E., eds., structural and Tectonic modeling and its application to petroleum geology. Amsterdam, Elsevier, p. 153-162.

Nøttvedt A., Cecchi M., Gjelberg J. G., Kristensen S. E., Lønøy A., Rasmussen A., Skott P. H. and Veen P. M. (1993). Svalbard–Barents Sea correlation: a short review in T.O. Vorren et al. (eds.): Arctic geology and petroleum potential: proceedings of the Norwegian Petroleum Society Conference, 15–17 August 1990, Tromsø, Norway. p. 63–375. Amsterdam: Elsevier.

Ohm S. E., Karlsen D. A. and Austin T. J. F. (2008). Geochemically driven exploration models in uplifted areas: Examples from the Norwegian Barents Sea. AAPG Bulletin, v. 92, p. 1191-1223.

Peltonen C., Marcussen O., Bjørlykke K. and Jahren J. (2008). Mineralogical control on mudstone compaction: a study of Late Cretaceous to Early Tertiary mudstones of the Voring and More basins, Norwegian Sea. Petroleum Geoscience 14(2), p. 127-138.

Peltonen C., Marcussen O., Bjørlykke K. and Jahren J. (2009). Clay mineral diagenesis and quartz cementation in mudstones: The effects of smectite to illite reaction on rock properties. Marine and Petroleum Geology 26(6), p. 887-898.

Polyaeva E., Klarner S., Lowrey C. J. and Zabrodotskaya O. (2011). Depth dependent rock physics trends for Triassic reservoirs in the Norwegian Barents Sea. 73rd EAGE Conference and Exhibition incorporating SPE EUROPEC.

Ramm M. (1991). Diagenesis and porosity evolution of Lower and Middle Jurassic Reservoir sandstones in the Troms I-area, Barents Sea, in Porosity-depth trends in reservoir sandstones: a quantitative study on effects of variations in pore pressure temperature and sandstone petrography on reservoir quality. PhD (Dr. Scient.) thesis, University of Oslo.

Raymer L. L., Hunt E. R. and Gardner J. S. (1980). An improved sonic transit time-to-porosity transform. Trans. Soc. Prof. Well log Analyst, 21st Annual Logging Symposium, paper P.

Ronnevik H. and Jacobsen H. P. (1984). Structural highs and basins in the western Barents Sea, in Petroleum Geology of the North European Margin: Norwegian Petroleum Society, p. 98-107.

Russell B. H. (1988). Introduction to seismic inversion methods. Course notes Series, No.2, Society of Exploration Geophysicist.

Rutherford S. R. and Williams R. H. (1989). Amplitude versus offset veriation in gas sands. Geophysics, v. 54, p. 680-688.

Selley R. C. (1978). Porosity gradients in North Sea oil-bearing sandstones. Journal of the Geological Society, v. 135 (1), p. 119-132.

Selnes A., Dvorkin J., Carr M., Hoffmann J. and Hubert L. (2004). Rock physics diagnostics, effective medium models and analysis of the Stø Formation, Hammerfest Basin, Norway. EAGE 66th Conference &Exhibition-Paris, France.

Shuey R. T. (1985). A simplification of Zoeppritz equations. Geophysics, v. 50, p. 609-614.

Smith G. C. and Gidlow P. M. (1987). Weighted stacking for rock property estimation and detection of gas. Geophysical Prospecting, v. 35, p. 993-1014.

Spencer A. M., Briskeby P. I., Christensen L. D., Foyn R., Kjølleberg M., Kvadsheim E., Knight I., Rye-Larsen M. and Williams J. (2008). Petroleum geoscience in Norden - exploration, production and organization. Episodes, v. 31, No. 1, p. 115-124.

Storvoll V., Bjorlykke K., Karlsen D. and Saigal G. (2002). Porosity preservation in reservoir sandstones due to grain-coating illite: a study of the Jurassic Garn Formation from the Kristin and Lavrans fields, offshore Mid-Norway. Marine and Petroleum Geology 19(6), p. 767-781.

Storvoll V. and Bjorlykke K. (2004). Sonic velocity and grain contact properties in reservoir sandstones. Petroleum Geoscience 10(3), p. 215-226.

Storvoll V., Bjørlykke K. and Mondol N. H. (2005). Velocity-depth trends in mesozoic and cenozoic sediments from the Norwegian shelf. AAPG Bulletin, v. 89, p. 359-381.

Storvoll V. and Brevik I. (2008). Identifying time, temperature and mineralogical effects on chemical compaction in shales by rock physics relations. The Leading Edge, p. 750-756.

Thyberg B., Jahren J., Winje T., Bjørlykke K. and Faleide J.I. (2009). From mud to shale: rock stiffening by microquartz cementation. First Break, v. 27, p. 27-33.

Thyberg B., Jahren J., Winje T., Bjørlykke K., Faleide J.I. and Marcussen Ø. (2010). Quartz cementation in Late Cretaceous mudstones, northern North Sea: Changes in rock properties due to dissolution of smectite and precipitation of microquartz crystals. Marine and Petroleum Geology 1–13.

Vernik L. and Nur A. (1992a). Ultrasonic velocity and anisotropy of hydrocarbon source-rocks. Geophysics, v. 57.

Walderhaug O. and Bjørkum P. A. (2003). The effect of stylolite spacing on quartz cementation in the Lower Jurassic Stø Formation, Southern Barents Sea. Journal of Sedimentary Research, v. 73, No. 2, p. 146-156.

Walderhaug O. (1996). Kinetic modeling of quartz cementation and porosity loss in deeply buried sandstone reservoirs. AAPG Bulletin, v. 80, p. 731-745.

Waples D. W. and Couples G. D. (1998). Some thoughts on porosity reduction - rock mechanics, overpressure and fluid flow. In: S.J. Düppenbecker & J.E. Iliffe (eds.), Basin Modelling: Practice and Progress. Geol. Soc., London, Spec. Pub. 141, p. 73-81.

Wennberg O. P., Malm O., Needham T., Edwards E., Ottesen S., Karlsen F., Rennan L. and Knipe R. (2008). On the occurrence and formation of open fracture in the Jurassic reservoir sandstones of the Snøhvit Field, SW Barents Sea. Petroleum Geoscience, v. 14, p. 139-150.

Worsley D. (2008). The post-Caledonian development of Svalbard and the western Barent Sea. Polar Research 27, p. 298-317.

Wyllie M. J. R., Gregory A. R. and Gardner L. W. (1956). Elastic wave velocities in heterogeneous and porous media. Geophysics, v. 21, p. 41-70.

Ødegaard E. and Avseth P. (2004). Well log and seismic data analysis using rock physics templates. First break, v. 23, p. 37-43.

Appendix

UNIVERSITY OF OSLO

FACULTY OF MATHEMATICS AND NATURAL SCIENCES

Appendix

Chapter 5 Compaction and Rock property evaluation

Shale volume (V_{sh}) calculation:

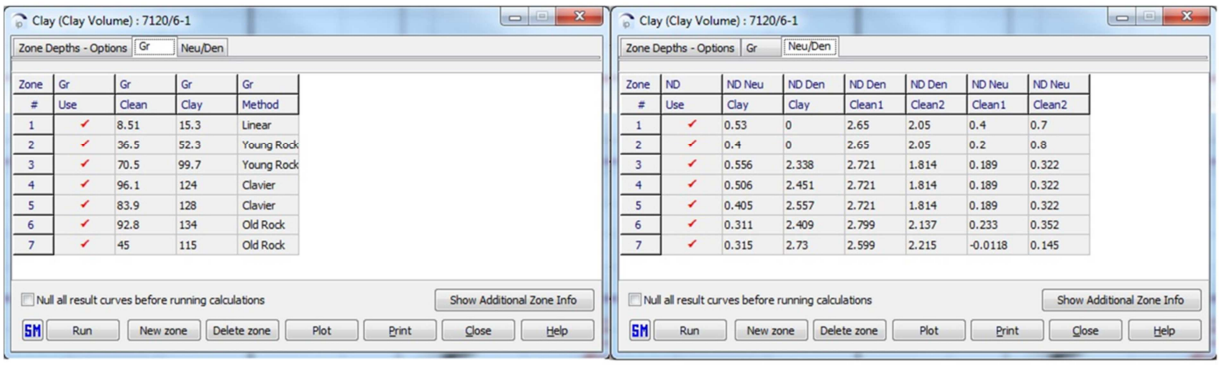

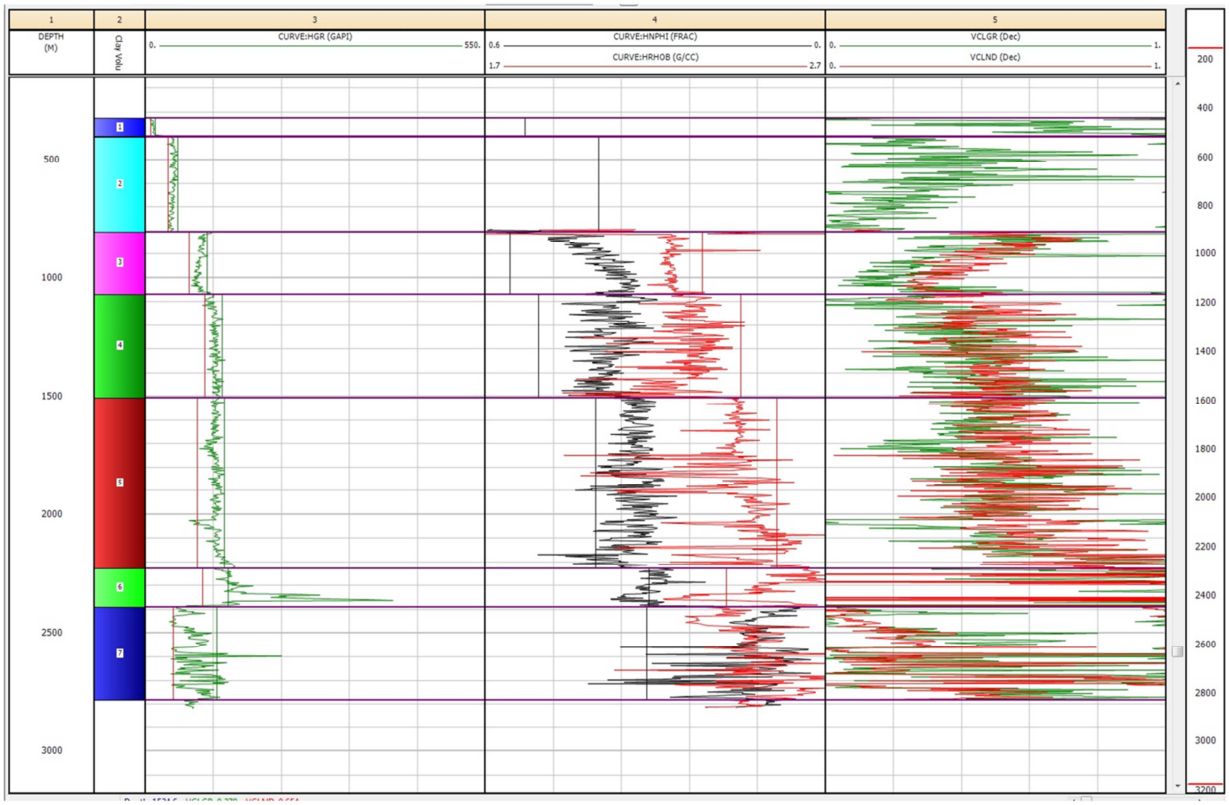

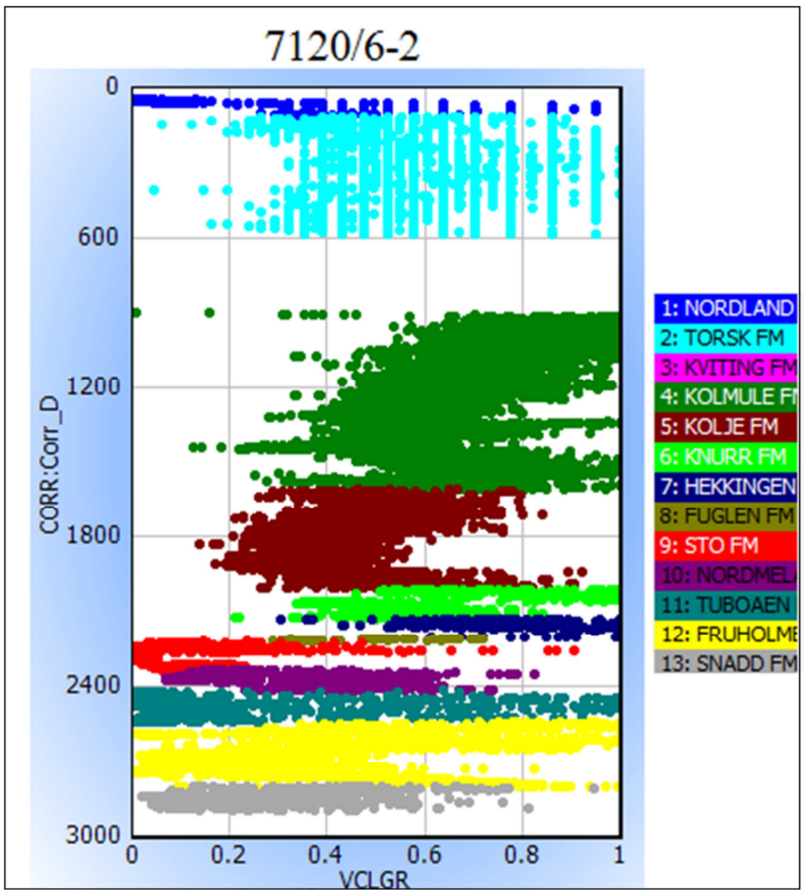
7120/6-2
CORR:Corr_D
0
600
1200
1800
2400
3000
0
0.2
0.4
0.6
0.8
1
VCLGR
1: NORDLAND
2: TORSK FM
3: KVITING FM
4: KOLMULE FI
5: KOLJE FM
6: KNURR FM
7: HEKKINGEN
8: FUGLEN FM
9: STO FM
10: NORDMEL
11: TUBOAEN
12: FRUHOLME
13: SNADD FM

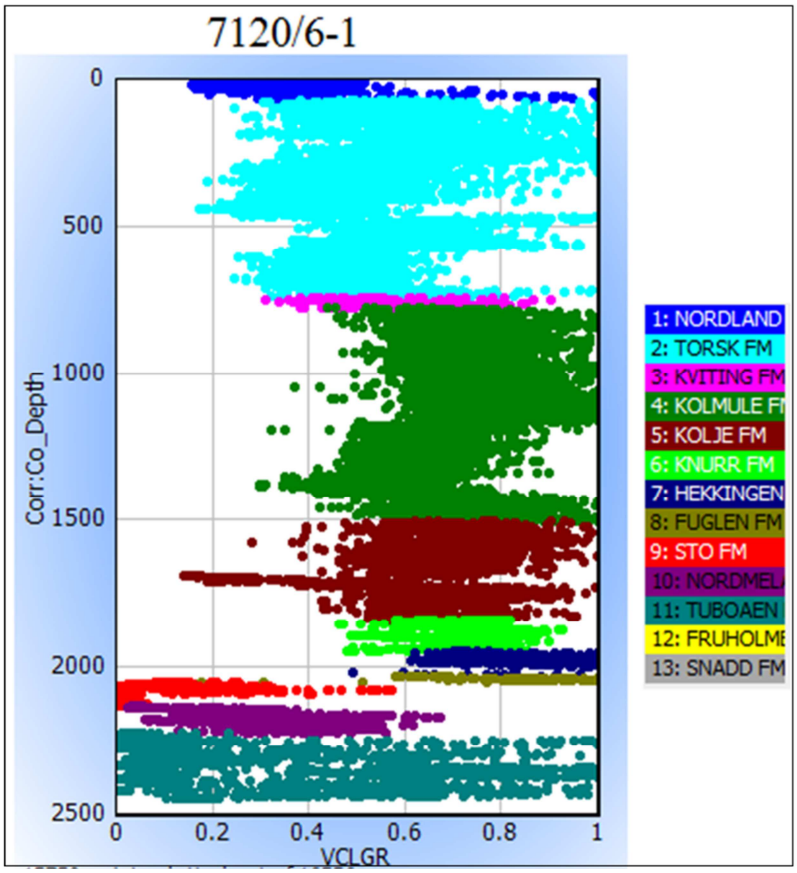
7120/6-1
Corr:Co_Depth
0
500
1000
1500
2000
2500
0
0.2
0.4
0.6
0.8
1
VCLGR
1: NORDLAND
2: TORSK FM
3: KVITING FM
4: KOLMULE FI
5: KOLJE FM
6: KNURR FM
7: HEKKINGEN
8: FUGLEN FM
9: STO FM
10: NORDMEL
11: TUBOAEN
12: FRUHOLME
13: SNADD FM

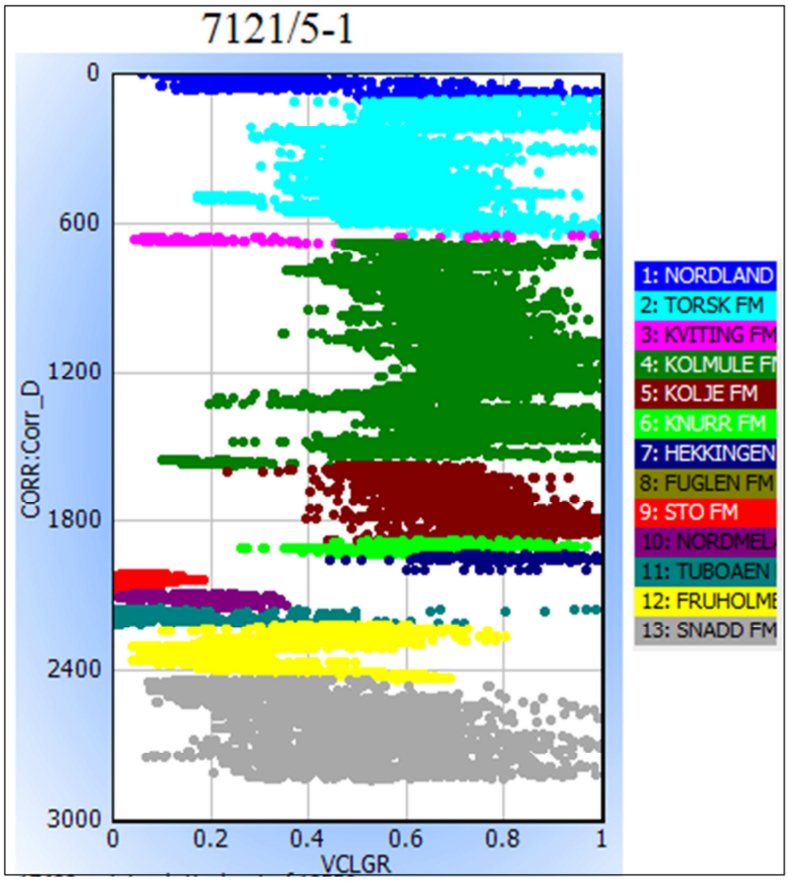
7121/5-1
0
600
1200
1800
2400
3000
CORR:Corr_D
0
0.2
0.4
0.6
0.8
1
VCLGR
1: NORDLAND
2: TORSK FM
3: KVITING FM
4: KOLMULE FM
5: KOLJE FM
6: KNURR FM
7: HEKKINGEN
8: FUGLEN FM
9: STO FM
10: NORDMEL
11: TUBOAEN
12: FRUHOLME
13: SNADD FM

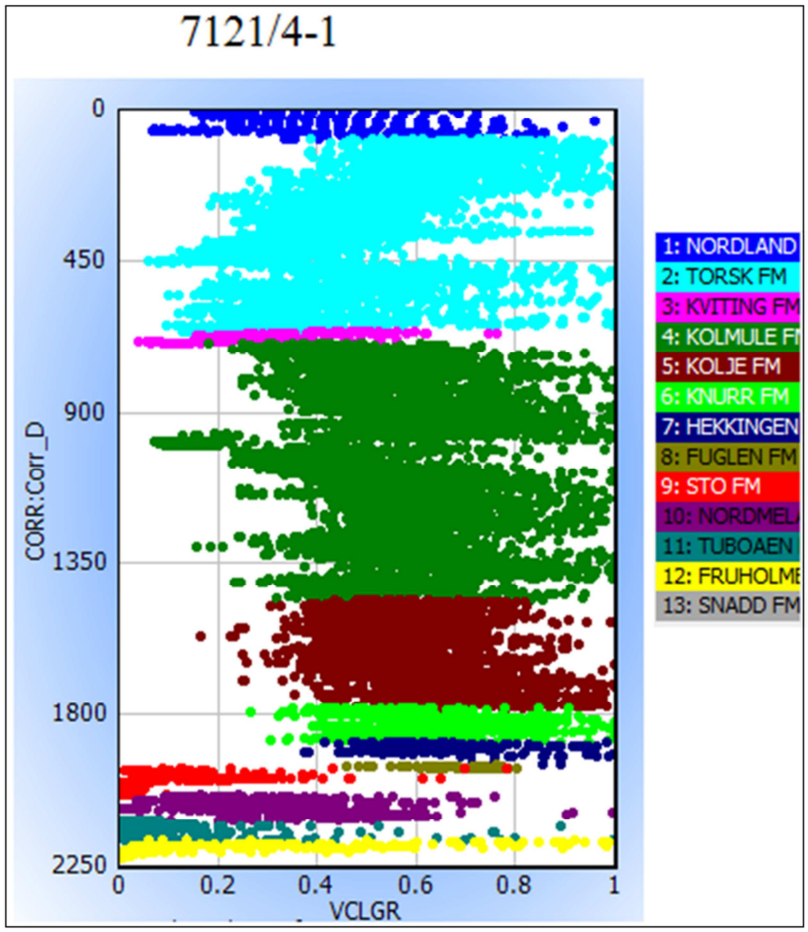
7121/4-1
0
450
900
1350
1800
2250
CORR:Corr_D
0
0.2
0.4
0.6
0.8
1
VCLGR
1: NORDLAND
2: TORSK FM
3: KVITING FM
4: KOLMULE FM
5: KOLJE FM
6: KNURR FM
7: HEKKINGEN
8: FUGLEN FM
9: STO FM
10: NORDMEL
11: TUBOAEN
12: FRUHOLME
13: SNADD FM

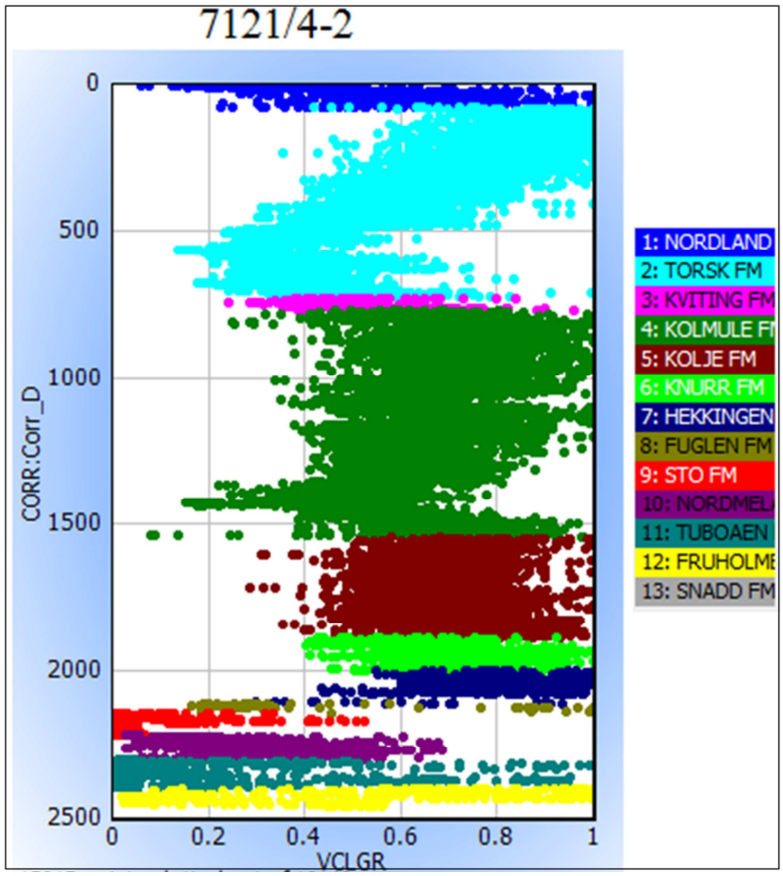

Clay mineral separation using spectral gamma ray:

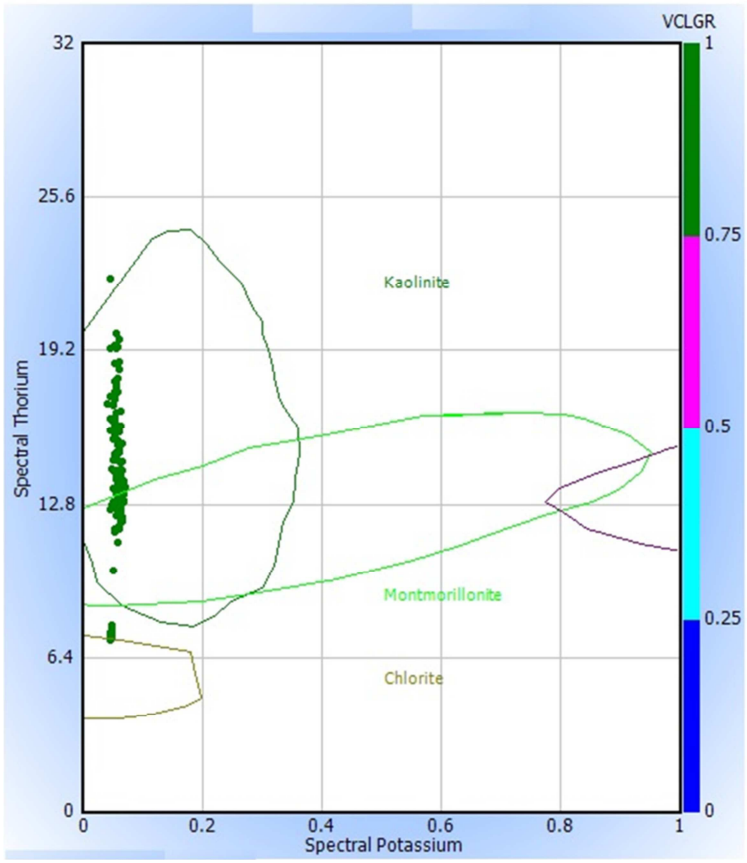

Density-neutron porosity cross plot color coded with photo-electric log and V_{sh}:

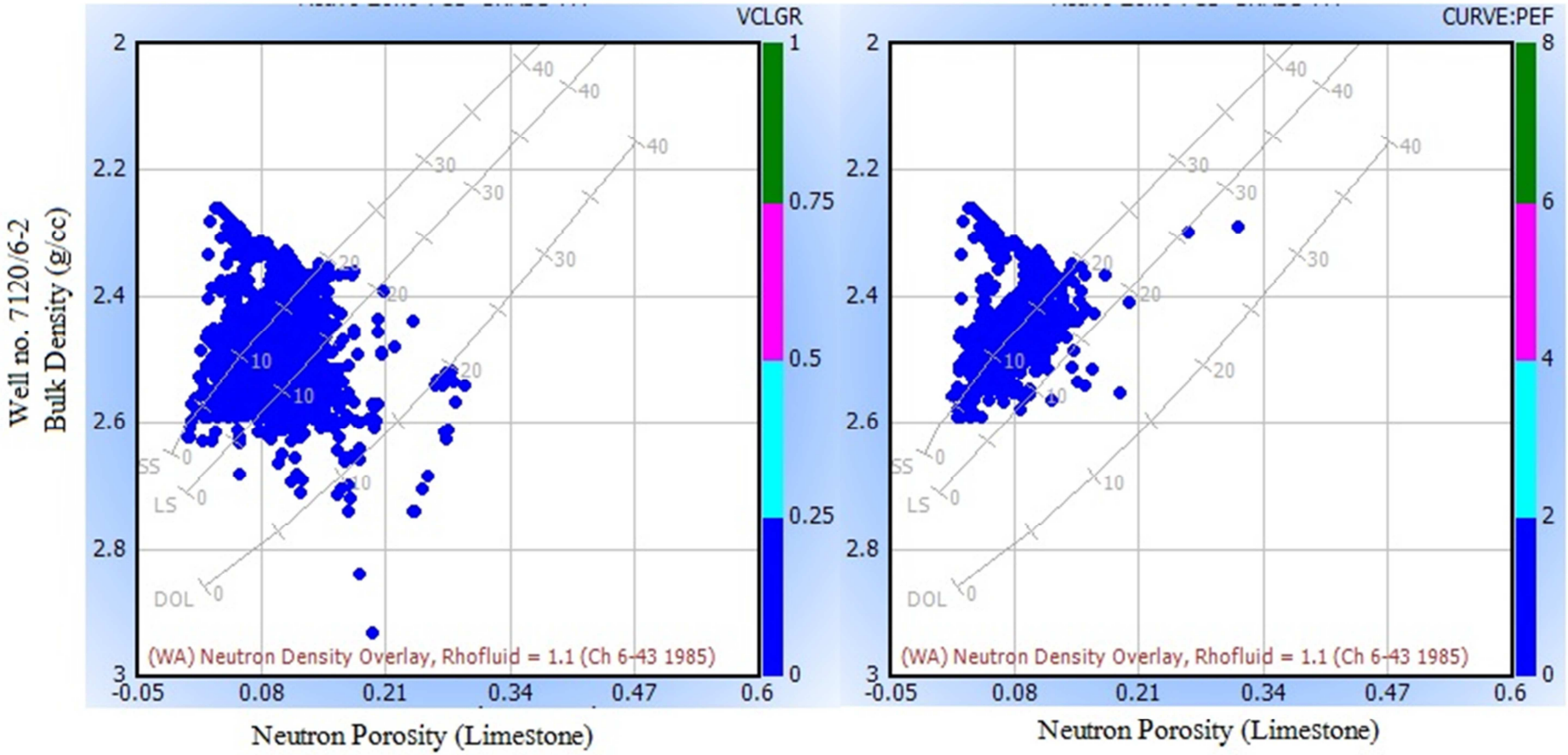

Chapter 6 Rock physics analysis

Rock physics Templates (RPTs):

Data for Gas saturated line						
Porosity (v/v)	K (Gpa)	Mu (Gpa)	Vp (km/s)	Vs (km/s)	Vp/Vs	AI (m/s G/cc)
0,400	1,997	2,784	1,857	1,298	1,431	3,069
0,350	2,683	3,435	2,020	1,390	1,453	3,590
0,300	3,564	4,273	2,205	1,499	1,471	4,194
0,250	4,720	5,390	2,422	1,631	1,485	4,909
0,200	6,303	6,960	2,689	1,799	1,495	5,786
0,150	8,632	9,304	3,038	2,022	1,503	6,915
0,100	12,371	13,202	3,531	2,345	1,506	8,477
0,050	19,362	20,972	4,326	2,882	1,501	10,924
Data for Oil saturated line						
Porosity (v/v)	K (Gpa)	Mu (Gpa)	Vp (km/s)	Vs (km/s)	Vp/Vs	AI (m/s G/cc)
0,400	2,678	2,784	1,843	1,218	1,514	3,461
0,350	3,429	3,435	2,013	1,319	1,526	3,974
0,300	4,388	4,273	2,205	1,436	1,535	4,567
0,250	5,637	5,390	2,431	1,577	1,541	5,268
0,200	7,334	6,960	2,707	1,753	1,544	6,129
0,150	9,797	9,304	3,065	1,985	1,544	7,234
0,100	13,673	13,202	3,565	2,318	1,538	8,760
0,050	20,667	20,972	4,361	2,866	1,522	11,135
Data for Water saturated line						
Porosity (v/v)	K (Gpa)	Mu (Gpa)	Vp (km/s)	Vs (km/s)	Vp/Vs	AI (m/s G/cc)
0,400	7,430	2,784	2,362	1,181	2,000	4,713
0,350	8,542	3,435	2,512	1,286	1,954	5,219
0,300	9,905	4,273	2,687	1,407	1,910	5,801
0,250	11,605	5,390	2,894	1,551	1,866	6,486
0,200	13,784	6,960	3,150	1,731	1,819	7,316
0,150	16,695	9,304	3,477	1,967	1,768	8,360
0,100	20,766	13,202	3,926	2,304	1,704	9,762
0,050	26,867	20,972	4,618	2,858	1,616	11,859

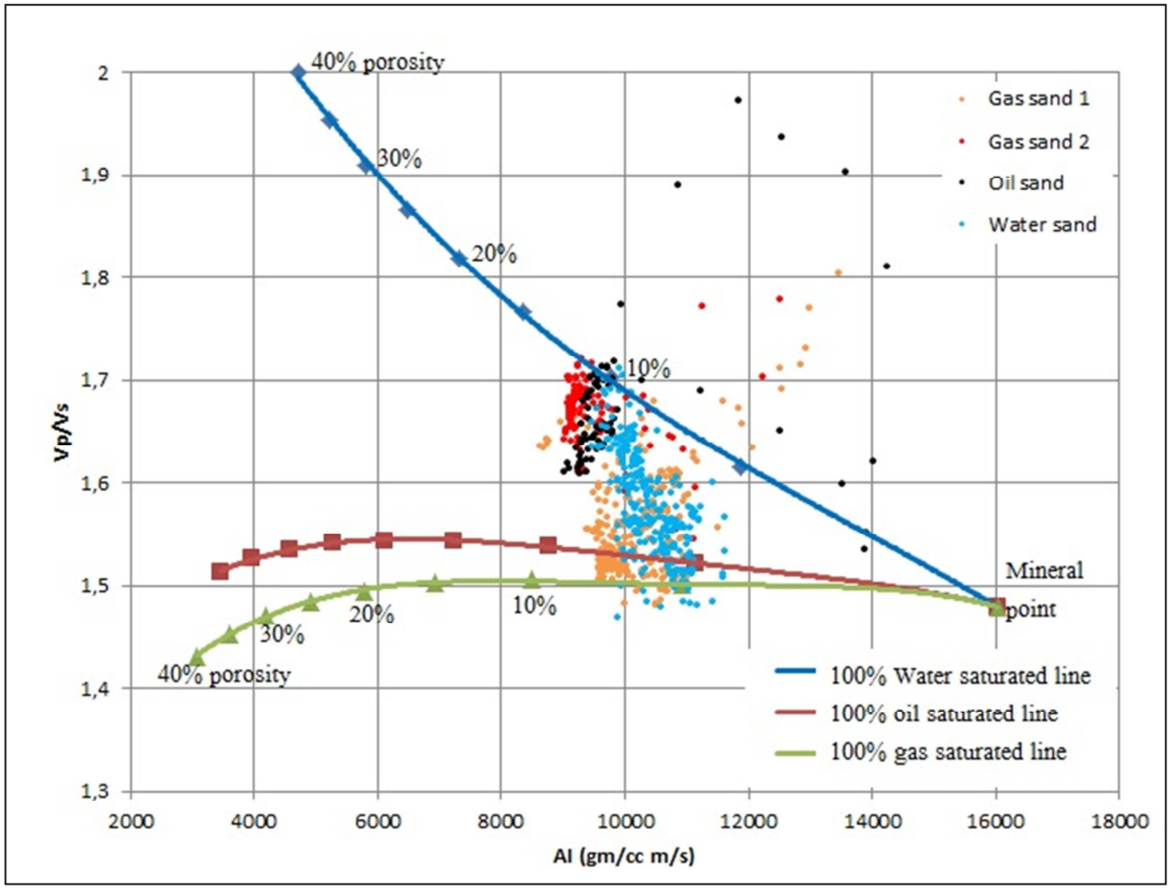

Friable sand model data		Constant cement model data		Contact cement model data	
porosity	Vp	porosity	Vp	porosity	Vp
0	6,05	0,000	6,050	0,000	6,050
0,1	3,926	0,223	3,550	0,302	3,641
0,2	3,151	0,238	3,451	0,325	3,438
0,223	3,035	0,254	3,374	0,342	3,251
0,3	2,688	0,304	3,148	0,376	2,631
0,4	2,36	0,366	2,894	0,387	2,110

Chapter 7 AVO modeling

FRM comparison between wells:

7120/6-2S						
Rock property values					Fluid Influence	
	100% Water	10%Gas	100%Gas		10%Gas	100%Gas
Vp (m/s)	3401,11	2659,29	2553,08		-21,8111	-24,9339
Vs (m/s)	1589,66	1762,08	1781,97		10,84634	12,09756
rho (g/cc)	2,53845	2,53221	2,47599		-0,24582	-2,46056
PR	0,360239	0,108636	0,025026		-69,8434	-93,053

7120_5_1						
Rock property values					Fluid Influence	
	100% Water	10%Gas	100% Gas		10%Gas	100% Gas
Vp (m/s)	3727,83	2929,25	2833,556		-21,4221	-23,9891
Vs (m/s)	2337,46	2341,06	2374,22		0,154013	1,572647
rho (g/cc)	2,5153	2,50757	2,43801		-0,30732	-3,07279
PR	0,176051	0,078072	-0,67826		-55,654	-485,262

Comparison between measured and calculated Vs:

7120/6-2S						
Krief						
	100% Water	10%Gas	100%Gas		10%Gas	100%Gas
Vp (m/s)	3401,11	2659,29	2553,08		-21,8111146	-24,9339186
Vs (m/s)	1589,66	1762,08	1781,97		10,8463445	12,09755545
rho (g/cc)	2,53845	2,53221	2,47599		-0,2458193	-2,46055663
PR	0,360239	0,108636	0,0250258		-69,843354	-93,0530009
Measured Vs						
	100% Water	10%Gas	100%Gas		10%Gas	100%Gas
Vp (m/s)	4108,82	4014,58	4059,18		-2,29360254	-1,20813274
Vs (m/s)	2296,44	2300,29	2335,87		0,1676508	1,717005452
rho (g/cc)	2,476	2,46771	2,39312		-0,33481422	-3,34733441
PR	0,272861	0,255609	0,252453		-6,32263314	-7,479266

Matrix properties calculator:

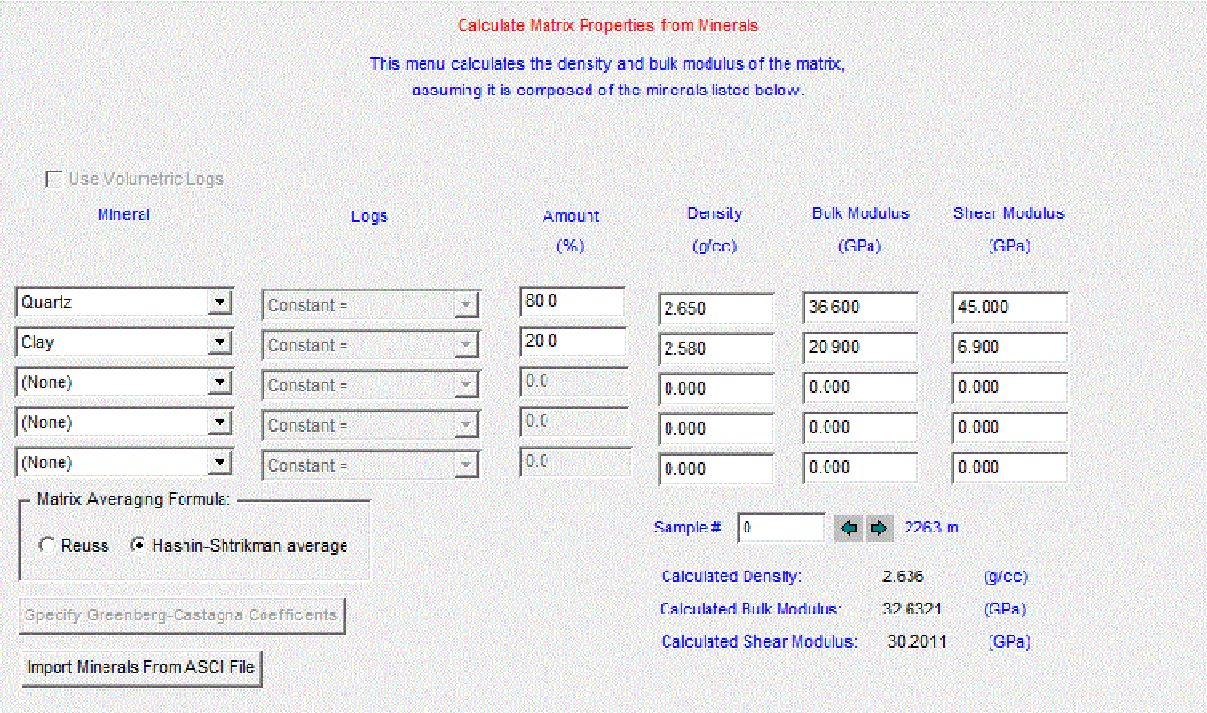

Reflectivity in different wells:

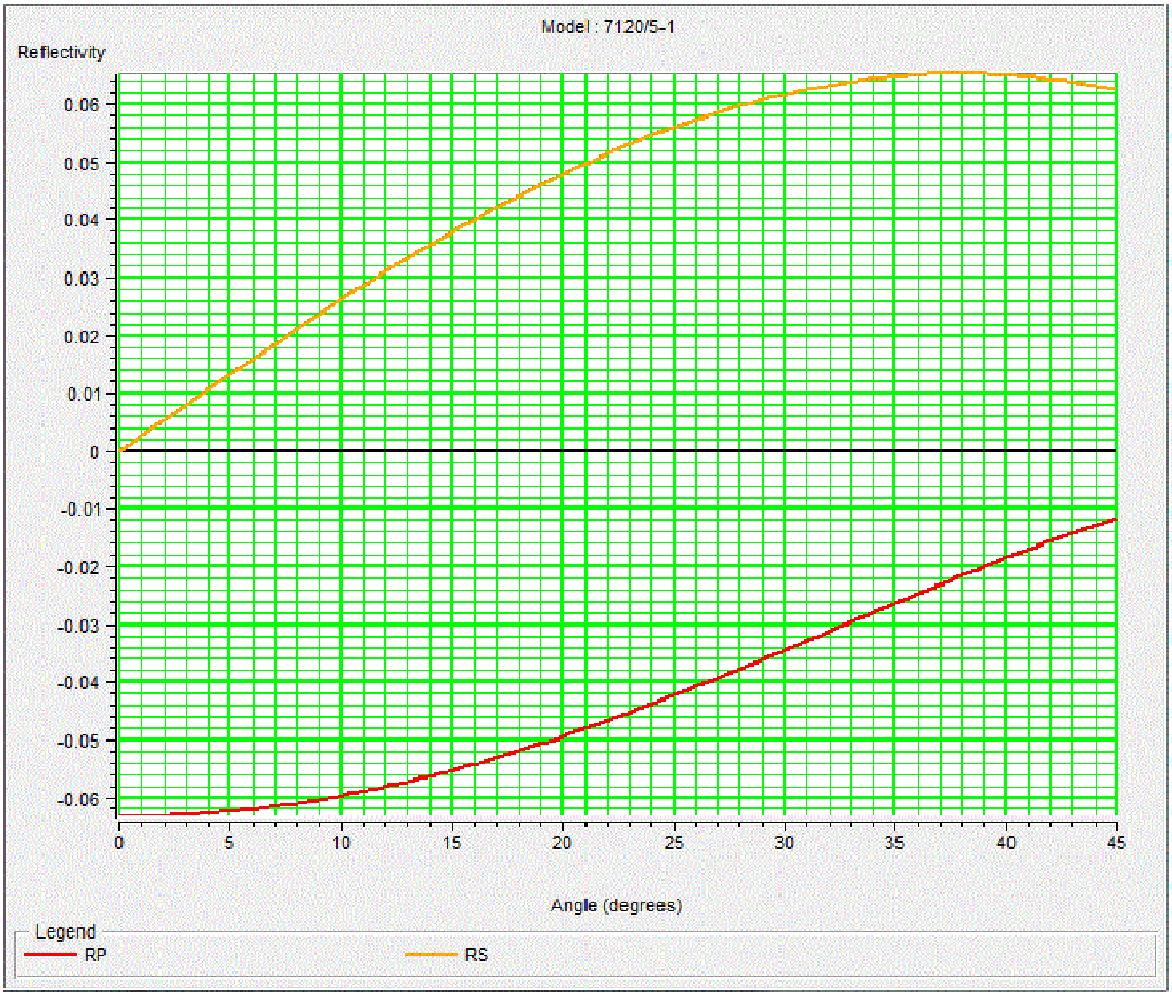

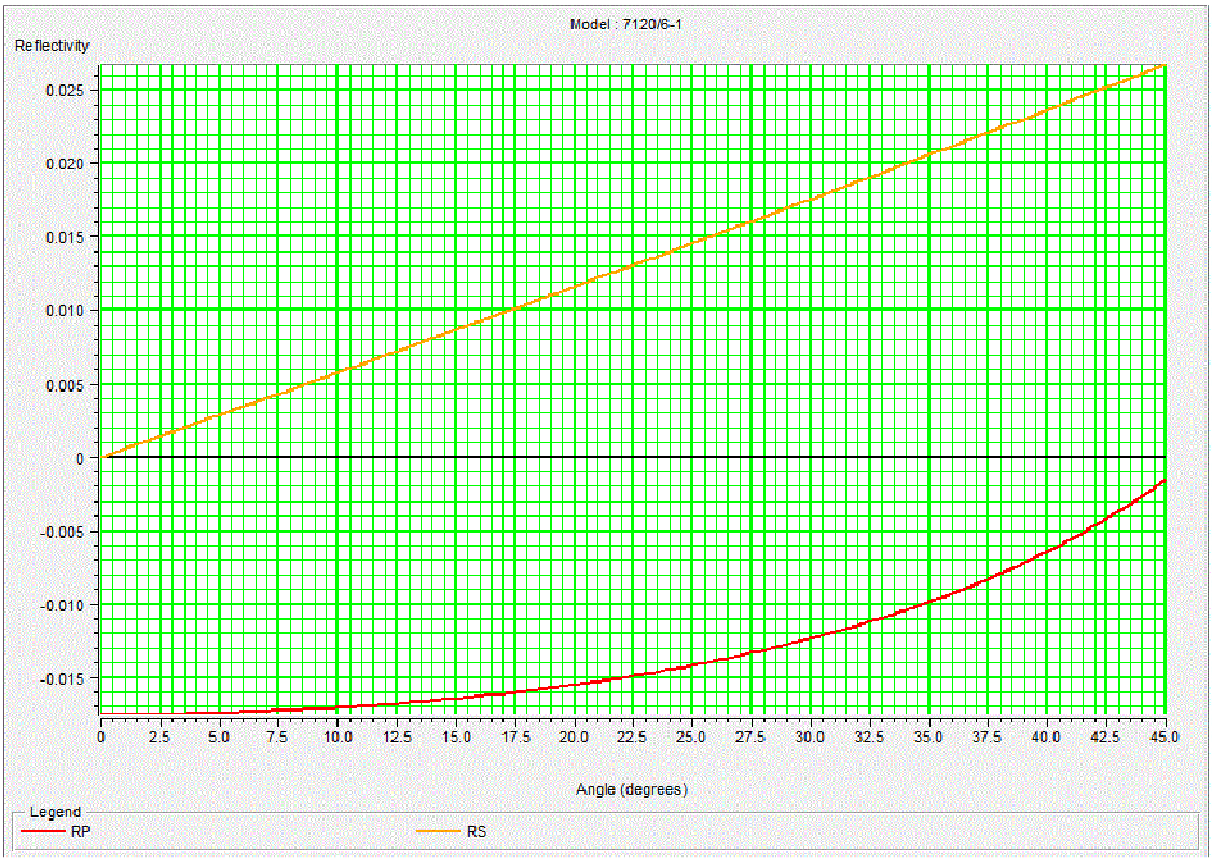
Model : 7120/6-1
Reflectivity
0.025
0.020
0.015
0.010
0.005
0
-0.005
-0.010
-0.015
0 2.5 5.0 7.5 10.0 12.5 15.0 17.5 20.0 22.5 25.0 27.5 30.0 32.5 35.0 37.5 40.0 42.5 45.0
Angle (degrees)
Legend
RP
RS

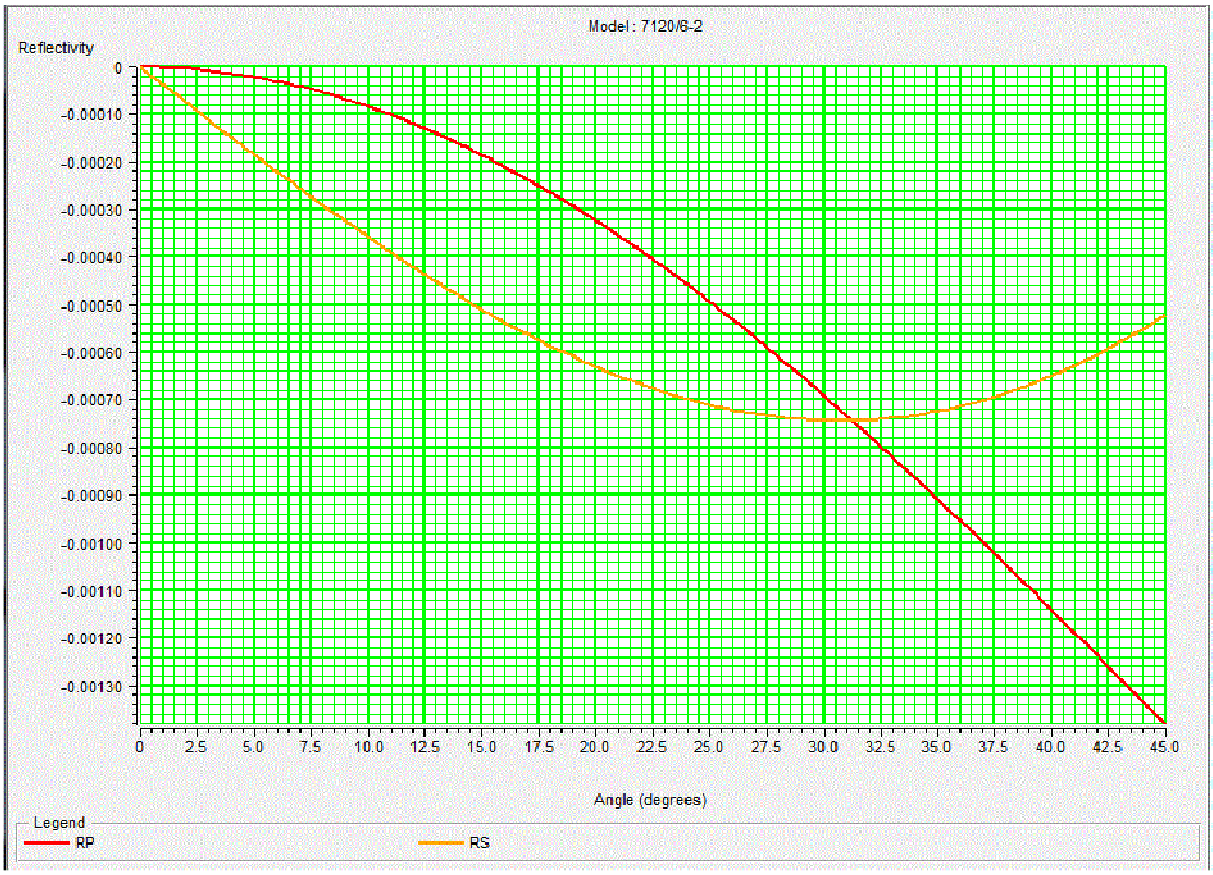
Model : 7120/6-2
Reflectivity
0
-0.00010
-0.00020
-0.00030
-0.00040
-0.00050
-0.00060
-0.00070
-0.00080
-0.00090
-0.00100
-0.00110
-0.00120
-0.00130
0 2.5 5.0 7.5 10.0 12.5 15.0 17.5 20.0 22.5 25.0 27.5 30.0 32.5 35.0 37.5 40.0 42.5 45.0
Angle (degrees)
Legend
RP
RS

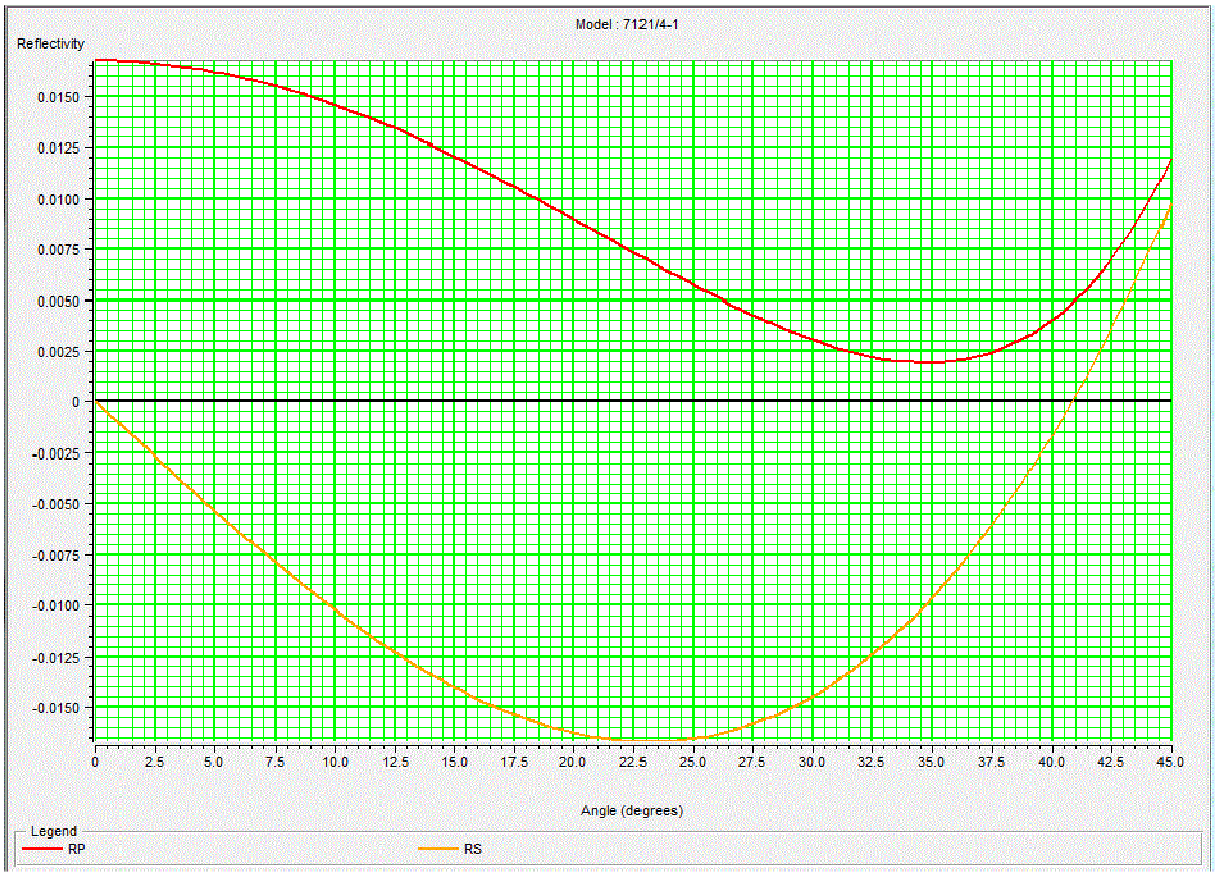
Model : 7121/4-1
Reflectivity
0.0150
0.0125
0.0100
0.0075
0.0050
0.0025
0
-0.0025
-0.0050
-0.0075
-0.0100
-0.0125
-0.0150
0 2.5 5.0 7.5 10.0 12.5 15.0 17.5 20.0 22.5 25.0 27.5 30.0 32.5 35.0 37.5 40.0 42.5 45.0
Angle (degrees)
Legend
RP
RS

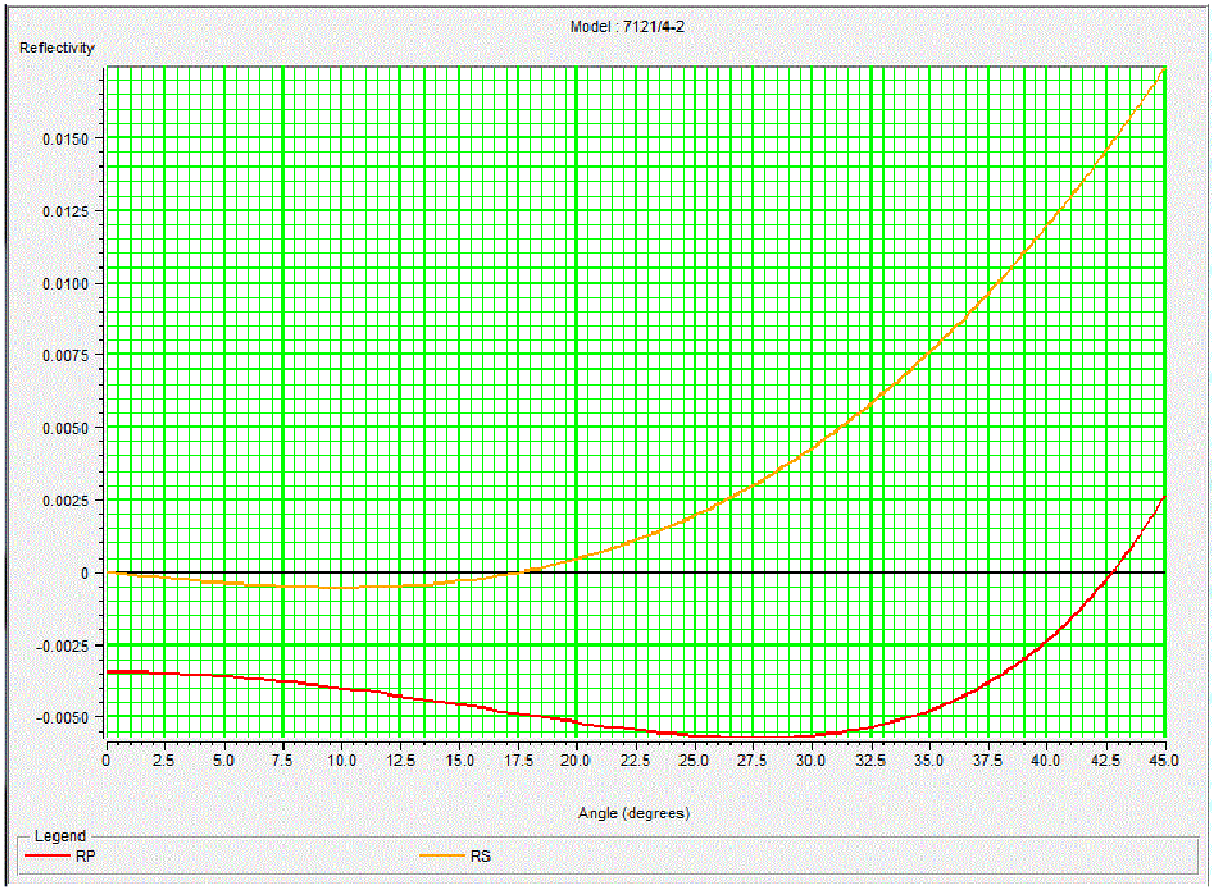
Model : 7121/4-2
Reflectivity
0.0150
0.0125
0.0100
0.0075
0.0050
0.0025
0
-0.0025
-0.0050
0 2.5 5.0 7.5 10.0 12.5 15.0 17.5 20.0 22.5 25.0 27.5 30.0 32.5 35.0 37.5 40.0 42.5 45.0
Angle (degrees)
Legend
RP
RS

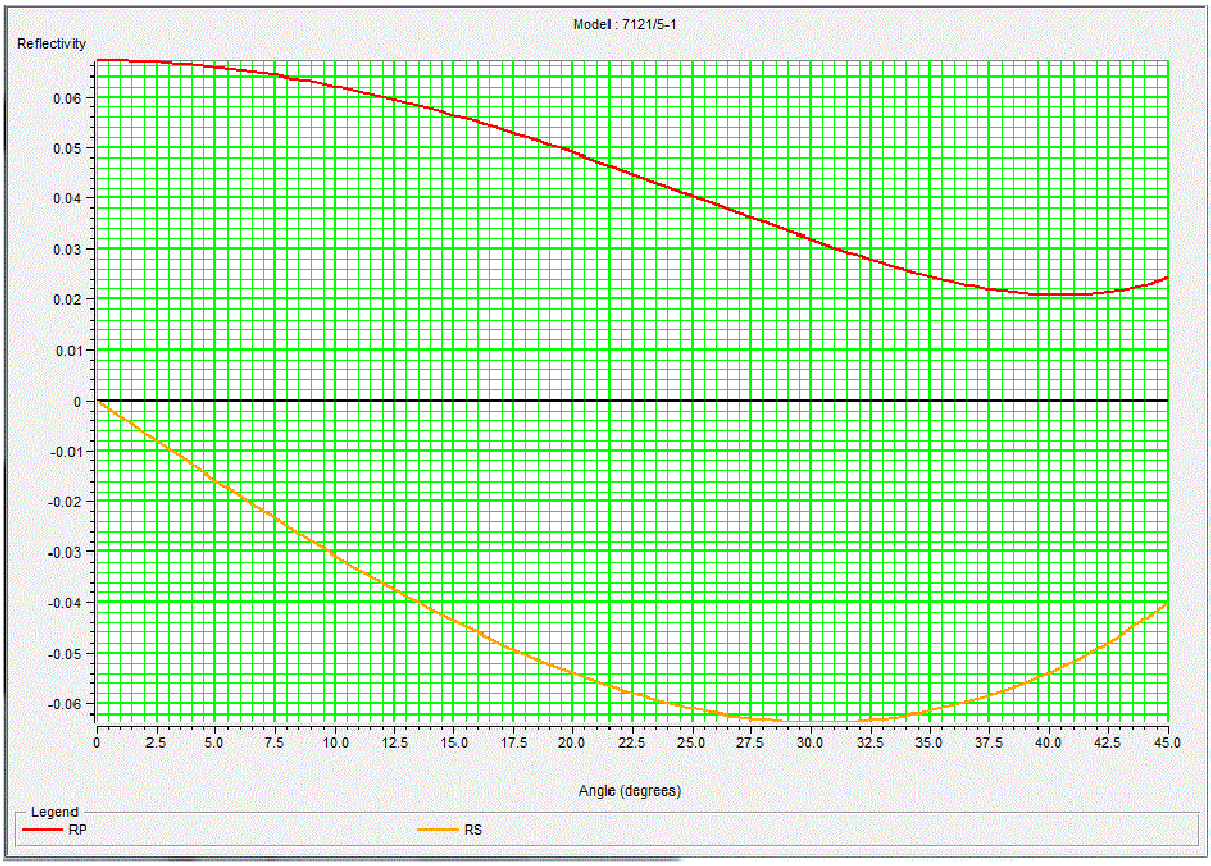

AVO curve: A/B (Two Terms Aki-Richards)

7120/5-1

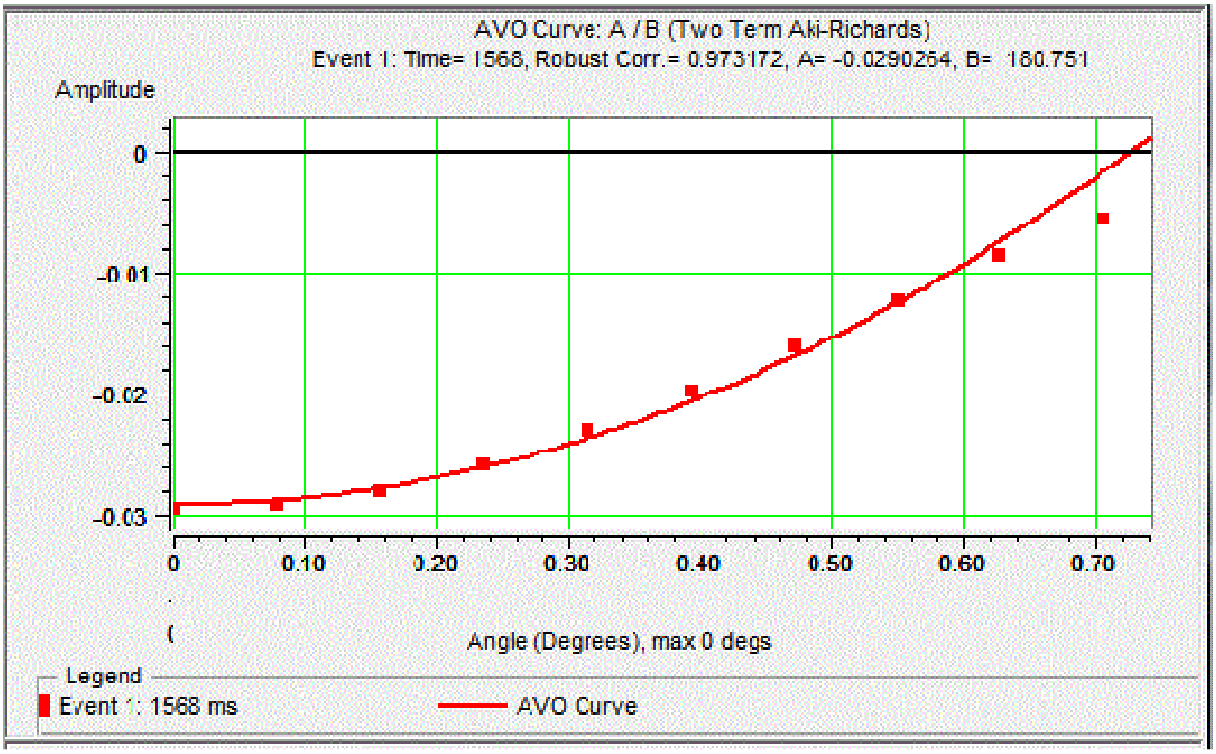

7120/6-1

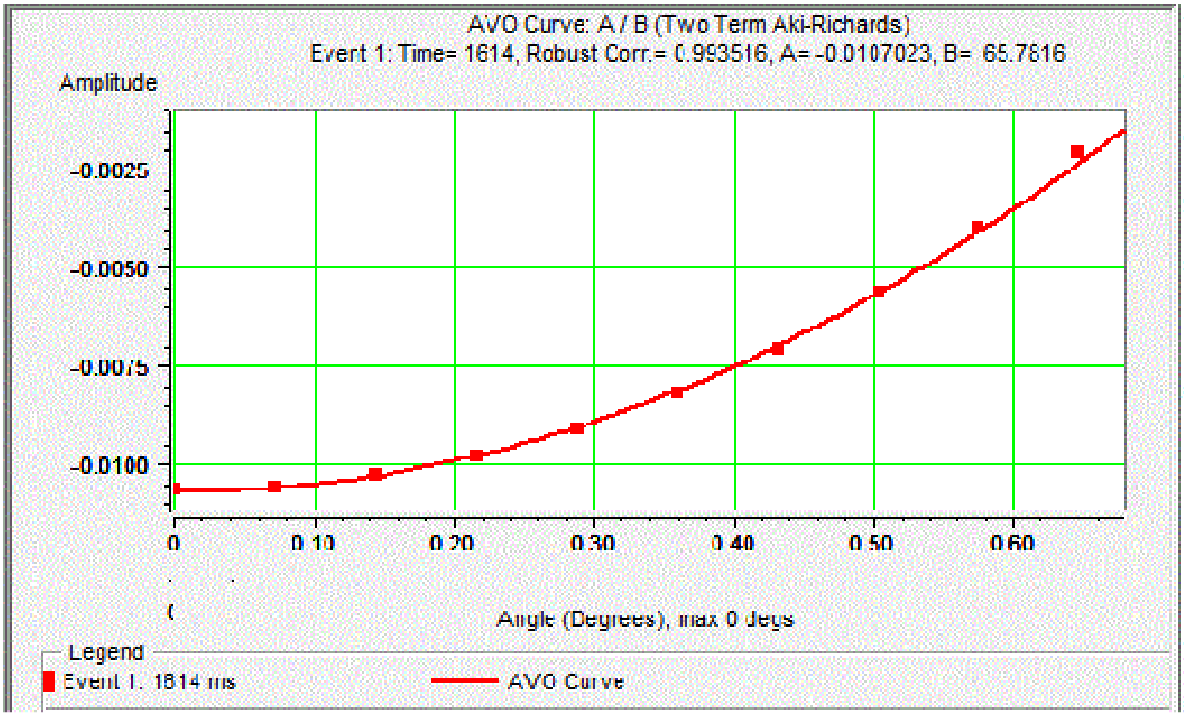

7120/6-2S

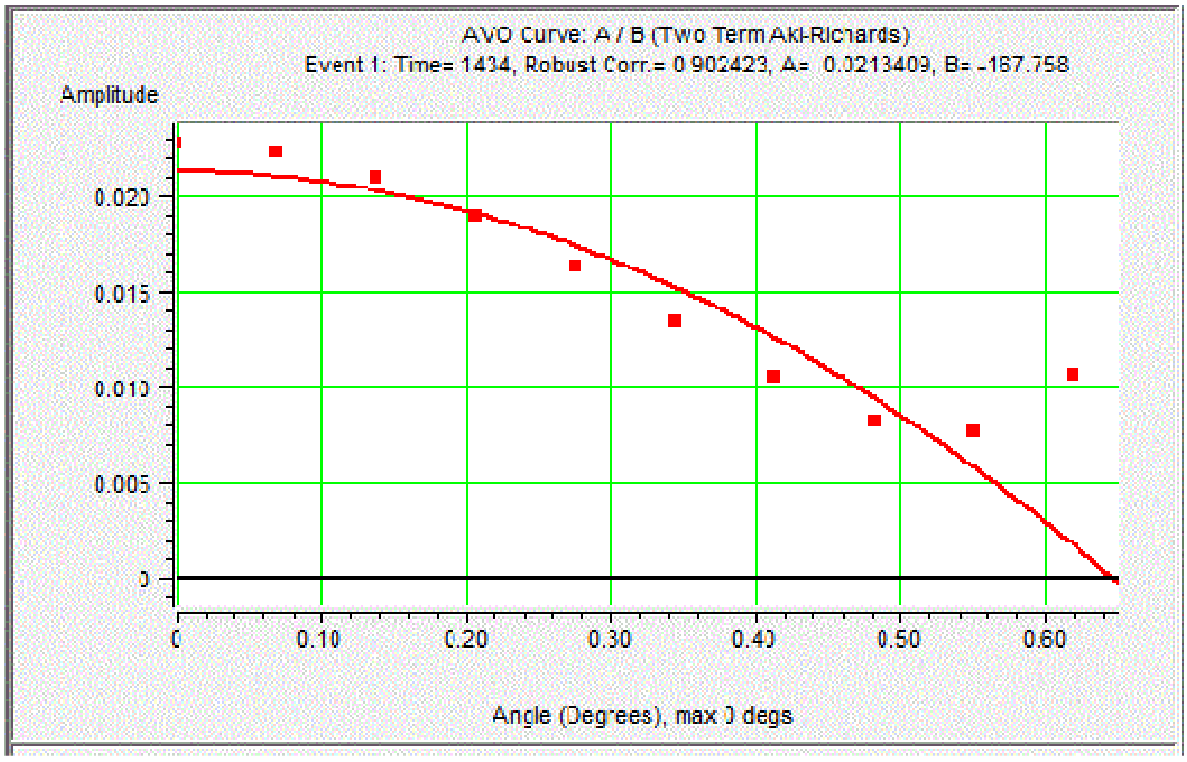

7121/4-1

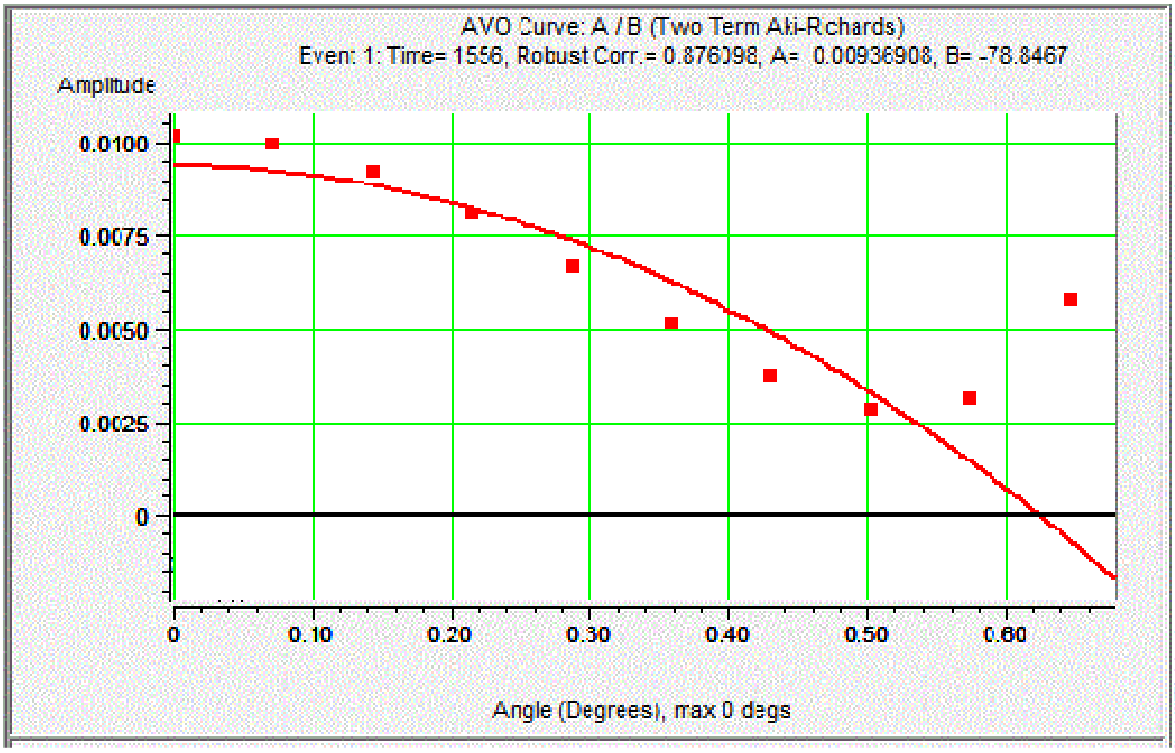

7121/4-2

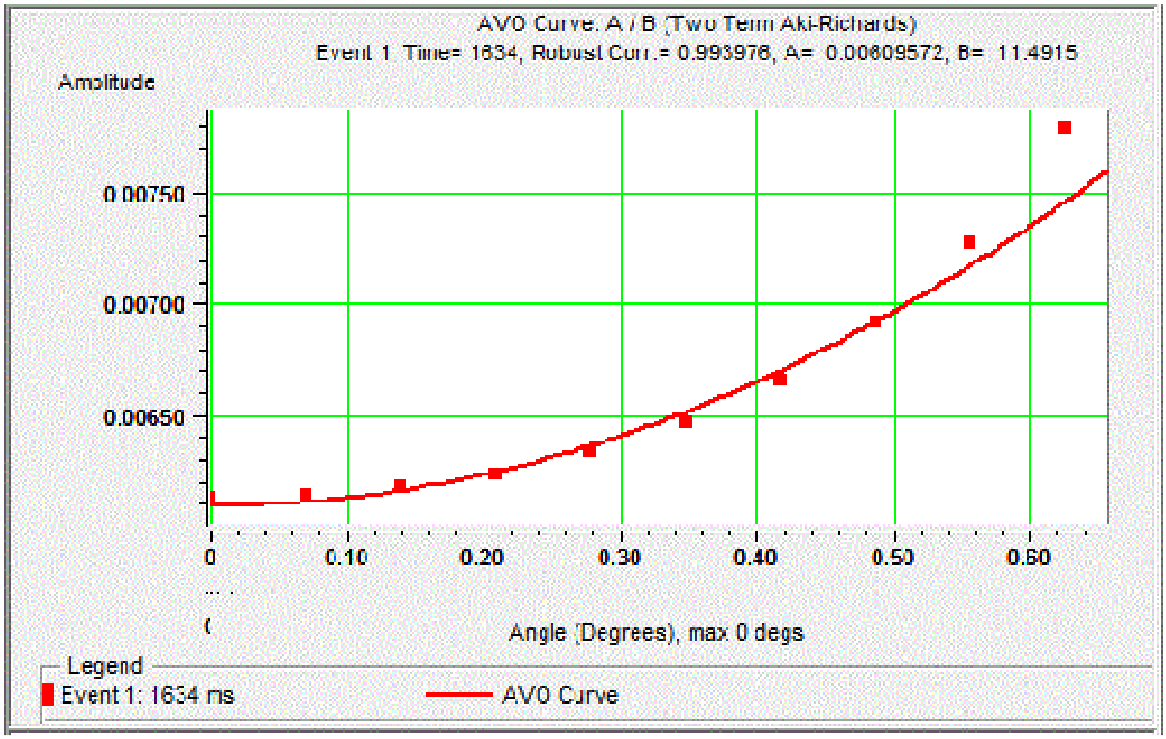

7121/5-1

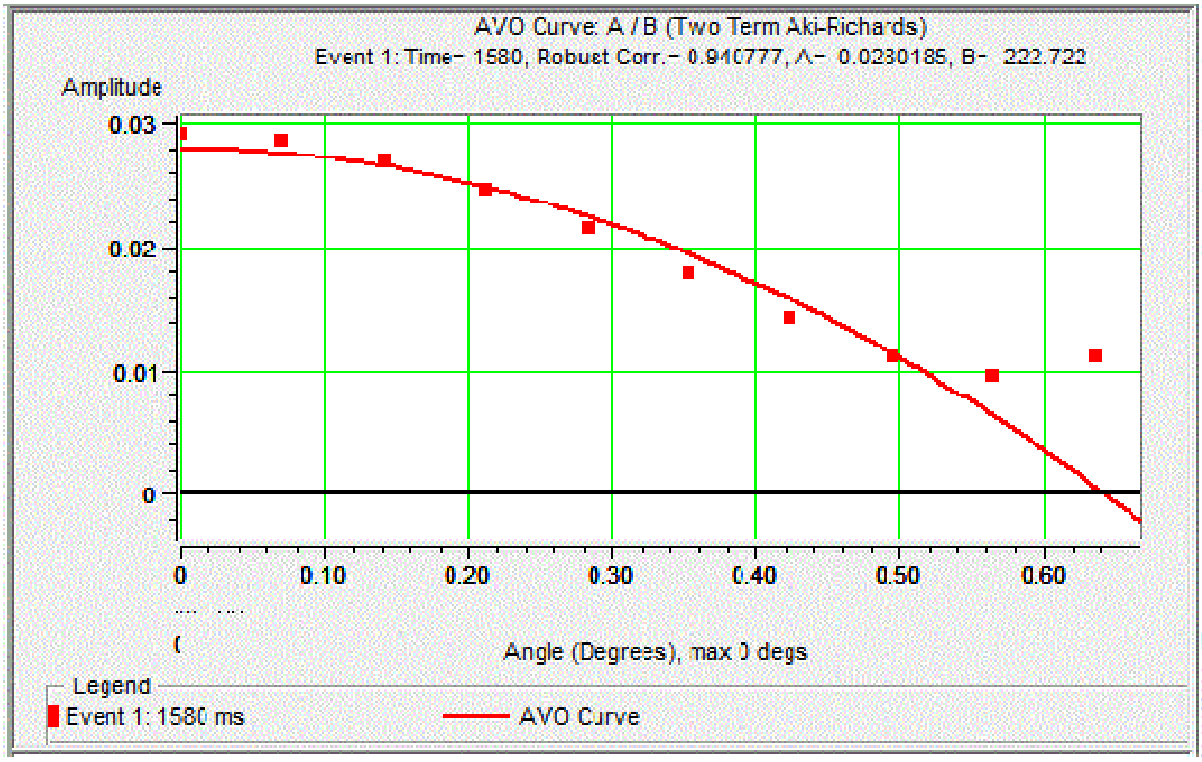
AVO Curve: A / B (Two Term Aki-Richards)
Event 1: Time= 1580, Robust Corr.= 0.910777, A= 0.0230185, B= 222.722
Amplitude
0.03
0.02
0.01
0
0
0.10
0.20
0.30
0.40
0.50
0.60
Angle (Degrees), max 0 degs
Legend
Event 1: 1580 ms
AVO Curve

Chapter 8 Seismic Inversion

Neural Network train window:

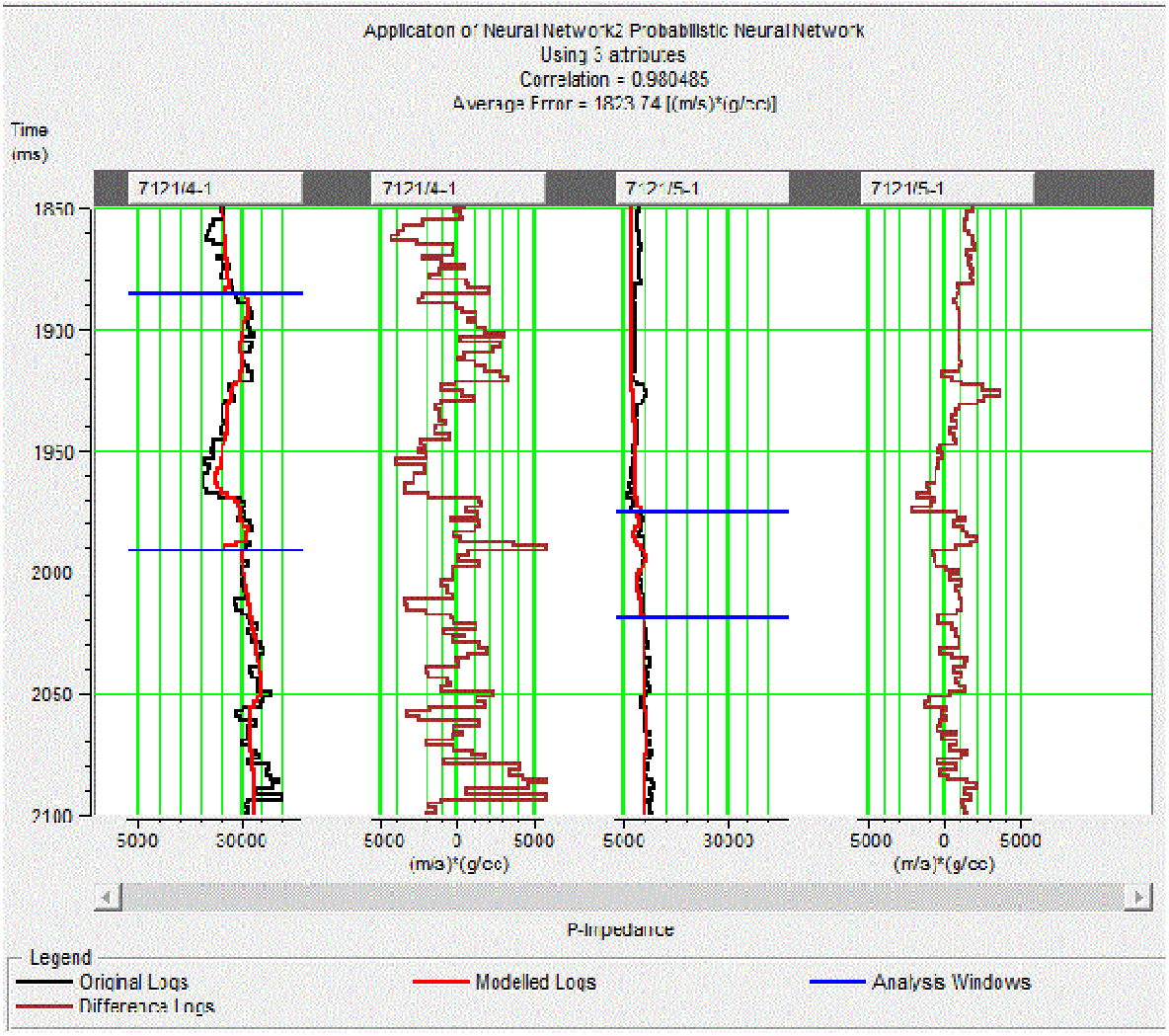

Constraints result window:

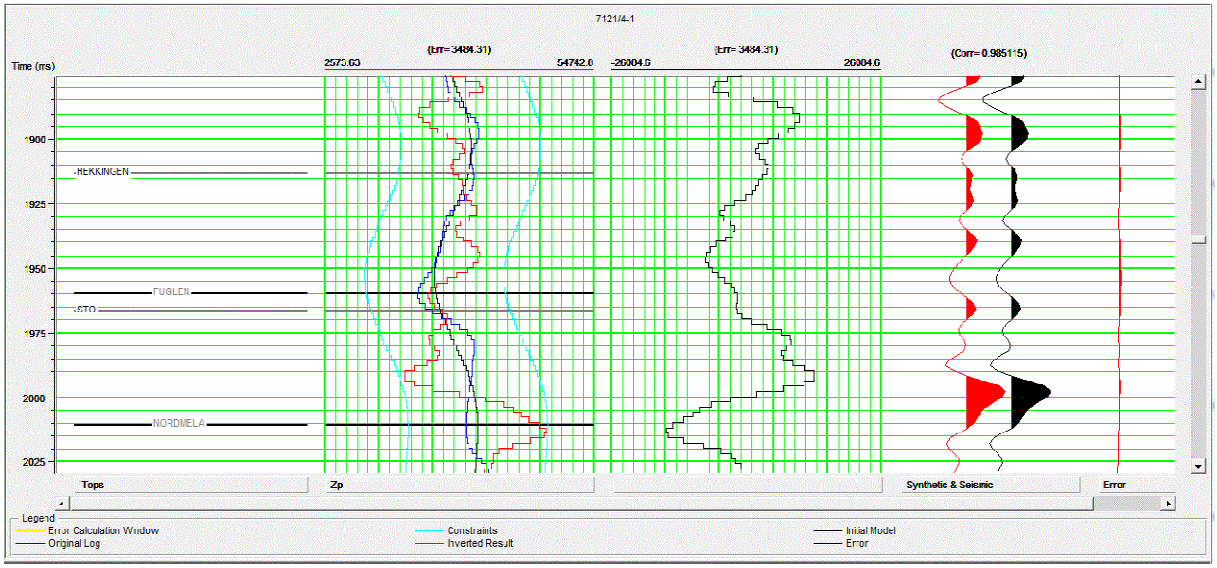

Cross correlation window: